Direct Metal Laser Sintering of Titanium Implant with Tailored Structure and Mechanical Properties

A thesis

submitted in fulfilment

of the requirements for the degree

of

Doctor of Philosophy in [Mechanical Engineering]

at

The University of Waikato

by

IZHAR ABD AZIZ

November 2014

Introduction

The novelty of this work lies in a proposal for a manufacturing procedure using a new design & fabrication technique that can build customised (patient oriented) parts, such as medical implants, with complex structures. The effects of two of the most influencial processing parameters i.e laser power and scan velocity on the as built microstructure and its mechanical properties is described, so that a suitable processing window can be selected for this application. Finally, the gathered knowledge was used to fabricate a new titanium implant with tailored structure & properties.

Direct Metal laser Sintering (DMLS) is widely used as an alternative method for producing customised parts or complex three-dimensional parts by utilising additive layered manufacturing principles. This method applies the use of a moving laser beam to induce surface heating in order to consolidate the metallic powder material. In this research, the principals and processing mechanisms during direct fabrication of titanium alloy parts and their application in the medical field were studied. From a more scientific and academic point of view, the aim of this research was to investigate the laser-titanium powder material interaction thus establishing the process-structure-property relationships. The knowledge could be used to evaluate the potential of extending the process to manufacture tailored structural implants particularly for craniofacial reconstructions.

Expanding the potential of this application in different industries, particularly in the medical field, requires a deep understanding of all the crucial factors that affect the material behaviour during the intricate laser-material interaction. Physical phenomena such as laser absorption, heat transfer, rapid cooling, solidification, oxidation and fluid flow are all happening in a short interaction time which makes the process hard to understand. This thesis aims to reveal those phenomena in order to get a better understanding of the processing parameters and the influence of these on the material properties of the titanium alloy parts manufactured by DMLS.

Scientific Objective of the Thesis

The work done in this research was carefully structured and organised so that a comprehensive knowledge of direct metal laser sintering could be established. Essentially, the work characterises the laser sintering process by revealing the core sintering/melting mechanism, with an emphasis on the thermal history and its crucial processing parameters. The microstructures, along with the corresponding mechanical properties were analysed so that the optimised processing window linking the processing and structural relationships could be developed. Biomedical implants with complex internal structures were fabricated using the knowledge gathered throughout the research work and to justify the newly developed procedure and manufacturing processes.

The outline of this thesis is as follows:

Chapter 2 gives an overview of the experimental procedure and the equipment used in this research. This section is divided into two main categories which are a description of the laser sintering machine and the analysis procedure. The latter involves powder characterisation, the background to the machine, thermal modelling and microstructural characterisation.

Chapter 3 describes the standard fabrication procedure using additive processing, particularly with the EOSINT M270 extended version machine. This chapter gives details about the CAD data acquisition, modelling and simulation techniques, designing a support structure and the post processing procedure used in this research.

Chapter 4 illustrates the core knowledge behind the fundamental principles of an additive manufacturing process by exploring the various phenomena occurring during laser-material interaction. In this chapter, the behaviour of the titanium alloy powder during laser sintering is described through the melt pool morphology and microstructural analysis of as sintered part. Chapter 5 explains the sintering phenomena of a single track on a substrate and remelted layer, of a single layer such as the track morphology, energy absorption and heat transfer.

Chapter 6 investigates the influence of the main processing parameters on as built parts. In this particular chapter the effect of scan spacing and scan speed are studied. The microstructure and mechanical properties is also explained in relation to cubes built on the substrate. In addition to building direction and scanning strategy, DMLS is reported to produce different surface textures on each surface. Therefore, as built specimens were sectioned, ground and etched and a microstructural analysis of three different views i.e top, front and side surfaces was carried out. Tensile testing was performed on standard dog bone specimens and the fracture surfaces were analysed.

In chapter 7, a fabrication framework for manufacturing customised titanium medical implants was established. This includes the manipulation of large amounts of medical data, modelling and simulation of defects, designing and creating lattice structures. In the last few pages, the cost and the production time for producing customised medical implants were analysed. A brief comparison with conventional methods is highlighted. A feasibility study concludes the thesis.

Chapter 8 discusses and interprets the experimental results obtained in chapters 4, 5, and 6 and relates these to the real fabrication work in chapter 7. The effects of processing parameters are the main back bone of this discussion. From here, the critical relationship between processing-structure-properties of DMLS parts is established. This final chapter summarises the main achievements of this thesis. It also includes comment on directions for future research.

Acknowledgement

I would like to thank my supervisor, Professor Brian Gabbitas who gave me a significant amount of assistance throughout the research. With his radiant efforts, excellent suggestions and continuous support, the collaboration with the University Of Wolverhampton, UK took place. It is an honour for me to be able to work with Professor Mark Stanford who is a prominent figure in the world of Additive Manufacturing. My gratitude goes to the engineering department staff at the Telford campus, Ian Lyall, John Rackley and Hayley just to name a few, who provided much support and the warmest welcome during my stay in the UK. With the wonderful assistance of those important persons, I have completed all my specimen fabrications within the schedule.

I would also like to dedicate my work to my family especially to my late mum who passed away during my study in July 2011. She is my inspiration. May Allah bless her soul and place her in heaven. To my dad, Mr Abd Aziz thanks for the great words and the trust that you have in me. The same goes to my sister Azmira and my brother Azri who have been so supportive throughout my journey. My in law family, Dr Abu Asmara, Puan Hasnah, Sophie, Azhad, Hosni, Yan, Mateen, Nabila, Faris, Nadine and Aidid. Thanks for your thoughts & prayers

Huge thanks to my lovely wife, Hanna Zulika who always keeps me moving forward and motivates me when I get exhausted. Words can’t describe how important you are to me and how grateful I am to be with you. To my kids, Aisya Ariana, Adam Qalifh and Ammar Barraq, papa loves you guys.

Special thanks to families in Hamilton, Dr. Sazali, Kak Ija, Dr. Nik, Kak Pica, Nor Azman Zakaria, Syamsul, Ani, Pak Rahman, Cikgu Mat Noor, Mohd Noor, Roslan & family, Khalis& family,Shahril, Kak Fariza, Raakhimi, Kumarcilla, Aruan, Rina and others who have been supporting me throughout this wonderful journey.

My great buddies, Azam, Nazroel, Fadhil, Azman, Azri. May God bless you guys with good health and prosperity.

Abstract

Direct Metal Laser Sintering has attracted much attention over the last decade for producing complex parts additively based on digital models. The capability and reliability of this process has stimulated new design concepts and has widened the manufacturing perspective of product customisation. This research work is designed to gain a deep understanding of laser sintering processing parameters, the corresponding microstructures and the mechanical properties. *The main purpose is to have a body of fundamental knowledge about the laser and titanium powder material interactions, thus establishing the factors that influence the process-structure-properties relationships of the Direct Metal Laser Sintering process.* Finally, a route for manufacturing customised craniofacial implants was described. This is to evaluate the DMLS processing capabilities in medical areas, particularly those parts having porous and lattice design structures.

The interaction between a laser beam and the powder bed creates a distinctive structure; a ball shaped (blob) consists of solid and porous regions. All the blobs have the same shape and morphology which may well suggest that there is a tendency for the powder particles to form a spherical droplet prior to a movingless laser beam. Surrounding the melted core is a sintered region of partially melted powder particles where the powder particles were fused together to form inter-particle necks. There is a linear relation between size, weight and density of a blob and the laser power. The surface temperature obtained exceeds the melting and vaporization temperature of the titanium and this creates a hole on the top part of a blob as a result of a massive temperature rise. Laser power of 140W gives a consistent structure and hardness in a blob. Metallographic analyses of a blob's cross-section show an α+β structure with prior-beta grains. The morphology of the lamellar structure consisted of acicular needles with a basket-weave pattern. The pores were characterised as having flat and spherical features with the size ranging from 2µm to 6µm. The micro-porosity observed may be associated with shrinkage which occurs during solidification or with the presence of entrapped gases from the atmosphere or argon gas from the shrouding environment

Laser power and scan speed are the two most crucial factor controlling the laser-powder interactions. Result shows that laser power is capable of widening the processing parameters particularly the scan speed. Increased laser power causes more powder to melt thus creating a bigger melt pool. Contrary to this, increasing the scan speed reduces the interaction time thus a smaller amount of powder melts. The right combination of these two parameters results in inducing an appropriate exposure time where continuously scanned tracks can be formed. Most of the parts were successfully built using a specific volume energy density of 50Jmm^{-3}, which was considered to be the optimum processing parameter for this research work. The ideal laser-material interaction time was calculated at 0.0008secs.

The microstructural analysis revealed a fully lamellar structure with acicular morphology. XRD analysis confirmed the presence of α' martensite, which explains the thermal history of a high isothermal condition and rapid cooling. The cross section of a solid part exhibited an acicular, needle-like structure with a herring bone pattern, parallel to building direction, due to directional solidification. The microstructure had a high tensile strength but with low ductility. It is also worth mentioning that a slight change in scan speed, with the intention of providing more energy density to the powder, may cause instability in the melt pool and cause deterioration in the mechanical properties. It is therefore confirmed that there is an upper limit and allowable processing window where a good balance of tensile strength and hardness in a DMLS part is achievable.

A framework prior to an implant's fabrication was established and the associated design and manufacturing software are reported. The processing route required software like MIMICS and MAGICS to manipulate the medical images and design data and equitable skills must be acquired to handle the machine in order to successfully fabricate the desired parts. Employing MAGICS new lattice function proved to be more efficient, saving time compared to a manual procedure, especially when dealing with large medical data manipulation. In conclusion, the proposed method from this study is capable of producing a customised part with the highest degree of design complexity compared with other conventional manufacturing methods. This has proved to be very suitable for manufacturing titanium medical implants, particularly craniofacial implants which require a customised and lightweight structure and at the same time still provide good mechanical properties.

Table of Contents

Introduction i
Scientific Objective ii-iv
Acknowledgement v
Abstract vi
Table of Contents vii-xi
Figures and Tables xii-vxii

Chapter 1: Rapid Manufacturing Technologies

- 1.1.1 The Application of RM Technologies 2
- 1.1.2 Rapid Manufacturing framework 4
- 1.1.3 Issues and Advantages pertaining to Rapid Manufacturing 5
- 1.1.4 Rapid Manufacturing Characteristics 6

1.2 Direct Metal Laser Sintering 9
- 1.2.1 Binding mechanism 10
  - 1.2.1.1 Solid State Sintering 11
  - 1.2.1.2 Liquid Phase Sintering 12
  - 1.2.1.3 Full Melting 15
  - 1.2.1.4 Problems in Laser Sintering/Melting 16
- 1.2.2 Physical Phenomena during DMLS 18
  - 1.2.2.1 Wetting behaviour 18
  - 1.2.2.2 Densification rate 20
  - 1.2.2.3 Thermal model 22
  - 1.2.2.4 Microstructure 29
  - 1.2.2.5 Mechanical properties 34
- 1.2.3 Variables affecting DMLS parts 35
  - 1.2.3.1 Machine variables 35
  - 1.2.3.2 Powder properties 37
  - 1.2.3.3 Atmosphere of Sintering 38
  - 1.2.3.4 Powder Deposition 39

1.3 DMLS in Medical Industry

- 1.3.1 Introduction 40
- 1.3.2 RP as a tool for Surgical Planning 40
- 1.3.3 Designing Implant via DMLS 43

1.4 References 47

Chapter 2: Experimental, Fabrication and Analysis Procedure 53
- 2.1 Powder Characterization 54
- 2.2 Density 55

2.3 The Machine – EOS M270 56
- 2.3.1 Technical Data 56
  - 2.3.1.1 Optical System 56
  - 2.3.1.2 Laser 58
  - 2.3.1.3 Scanner 58

2.3.1.4 focussing objective 58
2.3.1.5 Recoating and Elevating system 58
2.3.2 Processing material 59
2.3.3 Processing capabilities 61
2.3.3.1 Software 61
2.3.3.2 Platform Heating module 61
2.4 Analysis Procedure 62
2.4.1 Heat Transfer Analysis 62
2.4.1.1 Assumptions for thermal conditions 63
2.4.1.2 Mathematical model of thermal condition of DMLS 64
2.4.1.3 Laser beam approximations 65
2.4.1.4 Mathematical model solution 66
2.4.1.5 Numerical Model solution 67
2.4.1.6 Governing equation for Thermal model used in MATLAB 68
2.4.1.7 Setting the material properties 69
2.4.2 Microstructural Characterization 72
2.4.2.1 Optical Microscope 72
2.4.2.2 Scanning Electron Microscope 72
2.4.2.3 XRD diffraction 72
2.4.3 Structural Characterization 76
2.4.3.1 Tensile testing 75
2.4.3.2 Fracture Surface analysis 79
2.4.3.3 Microhardness 80
2.4.4 References 81

Chapter 3: Component and Test piece manufacture via DMLS 82
3.1 CAD/CAM modelling
3.1.1 Data Preparation 82
3.1.2 EOS RP Tools 82
3.1.3 Materialise MAGICS RP 83
3.1.4 Support structure and Part Orientation 83
3.2 Machine Set-up 84
3.2.1 Platform preparation 84
3.2.2 Building environment 86
3.2.3 Balancing the recoater blade 87
3.2.4 Machine interface PSW 3.0 88
3.2.5 Scanning strategy 90
3.3 EOS Ti6Al4V Powder Characterisation 91
3.3.1 Particle Size, shape and distribution 91
3.3.2 Compositional analysis 93
3.3.3 Powder Particle Density 95

Chapter 4: Fundamental study on DMLS

4.1 Introduction 96
4.2 Experimental & Processing Conditions 96

4.3 Results 98
4.3.1 Geometrical Characteristics 99
4.3.2 Blob Weight and density 103
4.3.3 Physical Characterization 106
4.3.4 Features and surface of sectioned blob 109
4.4 Heat Transfer Analysis 116
4.4.1 Temperature profile and distribution using the mathematical model 117
4.4.2 Numerical model solution 119
4.4.3 Discussion 125
4.5 Microstructural and Structure Characterization 126
4.5.1 Optical Images 131
4.5.2 SEM Images 131
4.5.3 Porosity 132
4.5.4 Microhardness 134
4.5.6 XRD Characterization 135
4.5.7 Discussion 139

Chapter 5: Single track and Single layer formation

5.1 Introduction 143
5.2 Processing conditions 144
5.2.1 Material and Machine parameters 144
5.2.2 Individual Single tracks 145
5.2.3 Single layer formation 145
5.2.4 Individual track on the remelted layer 146

5.3 Geometrical characteristics of laser induced melting

5.3.1 Laser Induced melting of single line 146
5.3.2 Laser induced melting of single layer 148
5.3.3 Laser induced melting on remelted layer 151
5.4 Heat Transfer analysis 153
5.4.1 Temperature distribution 153
5.4.2 Melt depth 154
5.5 Discussion 156
5.6 References 157

Chapter 6: Microstructure and Mechanical Properties of DMLS parts

6.1 Introduction 158
6.2 Material and Method 159

6.2.1 Processing conditions

6.3 Microstructure characterization

6.3.1 parallel to building direction 163
6.3.2 perpendicular to the building direction 164
6.3.3 XRD characterization 166
6.3.4 Discussion 167
6.4 Mechanical Properties 170

6.4.1 Tensile 171
6.4.2 Fractured Surface analysis 175
6.4.3 Macrohardness 177
6.5 References 179

Chapter 7: Design and fabrication procedure of the Customised Titanium Implants
7.1 Introduction 181
7.1.1 Digital Data Preparation 183
7.1.2 Data Conversion 184
7.1.3 CT Scan Data 185
7.1.4 Thresholding and Segmentation 186
7.1.5 Mirroring Technique and Fixing in MAGICS 187
7.1.6 Generating 3D Solid data & simulation in MAGICS 188
7.2 Designing Porous Structure
7.2.1 Virtual tooling or Puncher 190
7.2.2 Creating Support Structure 192
7.2.3 Result & discussion (Cranio implants) 193
7.2.4 Utilizing Unit Cells Structure 195
7.2.5 Design Parameter for Acetabular cup 196
7.2.6 Processing Conditions 202
7.2.7 Result and discussion 203
7.3 References 205

Chapter 8: Discussion & Future Recommendations
8.1 Introduction 206
8.1.1 The process 206
8.1.2 The Effects of Processing parameters 208
8.1.3 Microstructure and mechanical properties 210
8.1.4 Biomedical applications 211
8.1.5 Future work recommendations 213
8.2 References 215
8.3 Appendix 216

List of Figures

Chapter 1

Fig. 1.1 Application of RM Technologies in 2008 2

Fig. 1.2 Basic Rapid Manufacturing framework 4

Fig. 1.3 The Classification of RM systems based on binding mechanism 8

Fig. 1.4 Laser Based Consolidation mechanism 9

Fig. 1.5 Type of sintering 10

Fig. 1.6 Liquid phase sintering mechanism 13

Fig. 1.7 Different combinations of the powder particles 14

Fig. 1.8 Densification process 19

Fig. 1.9 Good and wetting behaviour based on the contact angle The contact angle is associated with the balance of three interfacial energies $\gamma_{\text{sv (solid-vapor)}}$,$\gamma_{\text{sL(Solid-liquid)}}$ and $\gamma_{\text{LV(liquid-vapour)}}$. 20

Fig. 1.10 The Geometry of laser irradiation explained by S.Z. Shen *et al* 25

Fig. 1.11 Physical model DMLS 26

Fig. 1.12 Ti6Al4V microstructure evolution 29

Fig. 1.13 Microstructure of Ti6Al4V (a) lamellar structure (b) equi-axed structure (c) bimodal structure 32

Fig. 1.14 Ti 6Al 4V Optical & TEM images of material made by additive manufacturing 32

Fig. 1.15 Factors affecting DMLS 35

Chapter 2

Fig. 2.1 Gas Pycnometry apparatus 55

Fig. 2.2 EOS M270 Extended version machine 56

Fig. 2.3 Gaussian beam profile and distribution on the powder bed 66

Fig. 2.4 The Geometry of laser irradiation 67

Fig. 2.5 Thermal properties used in the MATLAB 71

Fig. 2.6 Bragg diffraction 73

Fig. 2.7 E8-04 Tensile standard dimensions 76

Fig. 2.8 Dog Bone shaped tensile specimen specimen 76

Fig. 2.9 Vicker's Hardness Identation 80

Chapter 3

Fig. 3.1 Digital data transfer format 82

Fig. 3.2 Customised mini plate and its associated apparatus 86

Fig. 3.3 Standard substrate/platform used for M270 86

Fig. 3.4 components associated with the machine 87

Fig. 3.5 Levelling of the recoater using a clock gauge 88

Fig. 3.6 PSW processing interface 89

Fig. 3.7 Type of scanning pattern 91

Fig. 3.8 EOS Ti6Al4V powder 91

Fig. 3.9 Graph shows the particle distribution of EOS Ti64 92

Fig. 3.10 SEM images of the EOS Ti6Al4V powder 93

Fig. 3.11 EDS data for the EOS Ti6Al4V powder 94

Chapter 4

Fig. 4.1 The features a blob showing a hole and cross section 98

Fig. 4.2 Top and Side Views of the blob (100W) 99

Fig. 4.3 Dimension used for measuring the sintered blobs 101

Fig. 4.4 Blob size variations prior to increasing laser power 102

Fig. 4.5 Radial distance from the centre point 103

Fig. 4.6 weight in relation to laser power. Differences in weight with Stepped increases in laser power of 20W 104

Fig. 4.7 Inner (melted) and outer diameter of the blobs 108

Fig. 4.8 SEM Images of the core region of 200W blob (a)(b) 109

Fig. 4.9 SEM images of the outer region (b) 110

Fig. 4.10 The Area where partially melted particles were analysed 111

Fig. 4.11 Type of necks formation observed in the porous region 112

Fig. 4.12 Neck size measured at the neck of the each blob 113

Fig. 4.13 Particles in the intermediate region where the melted core and sintered particles are divided. (a) & (b) are SEM images of 200W blob 114

Fig. 4.14 Agglomerated powder particles and pore structure 115

Fig. 4.15 Heat flux generated within the beam radius (Wmm^{-2}) 117

Fig. 4.16 Temperature in Solid(blue) 118

Fig. 4.16a Surface temperature on the powder bed for 20W 118

Fig. 4.17 20W laser exposure for 0.001sec (Temperature profile) 121

Fig. 4.18 20W laser exposure for 0.1 sec (Temperature profile) 121

Fig. 4.19 20W laser exposure for 10sec (Temperature profile) 122

Fig. 4.20 Peak temperature and Isothermal condition of 200W, t=10s 124

Fig. 4.21 Experimental and simulated results for temperature distribution 125

Fig. 4.22 Optical images of blob (100W) cross section surface 127

Fig. 4.33 120W Blob surface texture at different magnifications 128

Fig. 4.24 140W Blob surface texture at different magnification 129

Fig. 4.25 160W Blob cross section surface 129

Fig. 4.26 180W Blob cross section surface 130

Fig. 4.27 200W Blob cross section surface 130

Fig. 4.28 SEM Images of the blob showing the increase size α and β lath with increased laser power 131

Fig. 4.29 Increased size of α and β lath with increased laser power 132

Fig. 4.30 Micrographs of 100W and 200W blobs surface. Black spots show porosities 133

Fig. 4.31 Pore size and morphology 134

Fig. 4.32 Microhardness on 100W blob polished surface at different textures 135

Fig. 4.33 Microhardness on 140W blob polished surface at different textures 135

Fig. 4.34 XRD Data of the blobs (100W to 200W) 136

Chapter 5

Fig. 5.1 A synthesized single track on a Titanium substrate/platform 143

Fig. 5.2 Laser induced melting on the single track 146

Fig. 5.3 Optical images of laser induced on single track 147

Fig. 5.4 SEM images of the individual track

Fig. 5.5: Single layer formation. (a) The arrow shows the laser stripe width. scanning strategy for this particular layer and (b) the laser end point 148

Fig. 5.6 Optical micrograph of single layer 149
Fig. 5.7 weakly bonded particle on a single layer 150
Fig. 5.8 SEM images of a single layer melted depth and unmelted particles 151
Fig. 5.9 SEM images of the individual track built onto the solidified layer 151
Fig. 5.10 Temperature field and melting depth after 0.001sec 154
Fig. 5.11 Temperature field and melting depth after 0.1sec 155

Chapter 6

Fig. 6.1: Surface for metallographic analysis. The top view indicates a cross-hatching technique using zig-zag vectors 160
Fig. 6.2 S1 polished surface obtained at scan speed of 750mm/s 161
Fig. 6.3 The OM images of S2 polished surface obtained at scan speed of 1000mm/s 162
Fig. 6.4 The OM Images of S3 polished surface obtained at scan speed of 1250mm/s 163
Fig. 6.5: Top view for S1(750mm/s), S2(1000mm/s) and S3(1250mm/s) 164
Fig. 6.6: SEM micrographs of a side view (A) and top view (B) of S1 165
Fig. 6.7: XRD spectra of laser sintered titanium alloy parts at different scan speed 167
Fig. 6.8: columnar grains of S1, S2 and S3 168
Fig. 6.9 Stress vs Strain graph for group 1,2 and 3 174
Fig. 6.10 Fractured surface of G1 176
Fig. 6.11 Fractured surface of G2 176
Fig. 6.12 Fractured surface of G3 176

Chapter 7

Fig. 7.1 Image processing work flow 183
Fig. 7.1a Fabrication process flow 184
Fig. 7.2 CT scan images of an infected mandibular due to ameloeblastama 184
Fig. 7.3 The area of interest (segmentation) is selected via tresholding 185
Fig. 7.4 CT scan images and simulation in MAGICS 189
Fig. 7.5 mandible implant with titanium mandible tray assembly 190
Fig. 7.6 Virtual Puncher designed in SolidWorks 191
Fig. 7.7 Boolean operation used to create pores on the mandible 192
Fig. 7.8 Support Structure on the implants 193
Fig. 7.9 Frontal and mandible implants 194

Fig. 7.10 optical and SEM images of the cubes showing detail of the structure built for each of the CAD files 198
Fig. 7.11 Load vs displacement graph for different unit cell structures 198
Fig. 7.12 Utilizing the unit cell structure on the acetabula cup 202
Fig. 7.13 Acetabula cups with lattice structure produced by DMLS 204

List of Tables

Chapter 1

Table 1.1 Mechanical properties of Ti6Al4V 34
Table 1.2 Near net shape manufacturing methods for producing medical devices from titanium 42

Chapter 2

Table 2.1 Technical data of M270X Machine 57
Table 2.2 Specification of laser used in the EOS M270 machine 58
Table 2.3 Material data Sheets 61
Table 2.4 Technical data Sheets for processing capabilities 61
Table 2.5 Thermophysical properties of Titanium used in the simulation 64
Table 2.6 Dimensionless absortance value for titanium 65
Table 2.7 Material Data used in MATLAB programming 70
Table 2.8 Lattice parameter restriction 73
Table 2.9 Instron machine set parameters 75
Table 2.10 Tensile specimen dimensions 76
Table 2.11 Groups of different scan speed and scan spacing 77
Table 2.12 PSW interface used to set up the scanning strategy 78
Table 2.13 Parameter for Skin and Core Exposure 80

Chapter 3

Table 3.1 Standard EOS processing parameters 89
Table 3.2 Particle size distribution 92
Table 3.3 Compositonal analysis of EOS Ti6Al4V Titanium alloy powder 93

Table 3.4 EDX compositional test result compared to ISO and ASTM standards 94
Table 3.5 EOS Ti6Al4V powder density 95

Chapter 4

Table 4.1 Blob measurements collected after 10sec laser irradiations 100
Table 4.2 Solid and porous parts of the blobs 101
Table 4.3 The weight and density of the blobs 103
Table 4.4 weight and density of the blobs prior to increasing laser power from 100W to 200W 104
Table 4.5 Differences in weight of the blobs prior to laser power 105
Table 4.6 Cross sections surface of the blobs 106
Table 4.7 Inner and outer dimensions of the blobs 108
Table 4.8 Neck Width of the blob 112
Table 4.9 Time for surface to melt 116
Table 4.10 Maximum Surface heat flux and temperature with corresponding laser power 119
Table 4.11 Vickers Hardness with variations in laser power 134
Table 4.12 Indexing the XRD data 138

Chapter 5

Table 5.1 Processing parameters used for the experiment 144

Chapter 6

Table 6.1 Processing condition for each group 160
Table 6.2: XRD diffraction data for S1, S2 and S3 167
Table 6.3: Yield strength of different groups 171
Table 6.4 Stiffness value for different scan speed and spacing 172
Table 6.5 Elongation value for different scan speed and scan spacing 172
Table 6.6 Average Tensile properties for Each group 173
Table 6.7 Macrohardness value for Group 1,2 and 3 177

Chapter 7

Table 7.1 Image processing work flow 182
Table 7.2 CT scan specification 185

Table 7.3 Thresholding values for bones and Tissues 187

Table 7.4 Design parameters for the acetabula cup 195

Table 7.5 The weight, volume and density of the cubes 196

Table 7.6 The pore volume and porosity of the 15mm cubes 197

Table 7.7 Load and stiffness values for the titanium cubes 198

Table 7.8 Cup volume and porosities 201

Equations

(1) Good and poor wetting equation based on contact angle associated with interfacial energies 21

(2) Contact angle equation 21

(3) Laser energy density Input 22

(4) Dimensional Analysis Solution 22

(5) Volume Energy Density 23

(6) Heat Conduction during laser heat treatment 23

(7) First analytical solution for moving heat source 24

(8) Temperature profile and melting depth(S.Z. Shen et al) 25

(9) Densification Equation (Simchi & Pohl) 36

(9.1) Specific Energy Input(Simchi&Pohl) 36

(9.2) Relative Density of porous material 36

(10) Relative Density of Porous material 45

(11) Density Equation 55

(12) Laser Beam approximation/surface heat flux 65

(13) Surface Temperature Equation 65

(14) MATLAB Equation 69

(15) Relation between d spacing and miller indexes 75

(16) Laser energy density 105

(17) Laser Beam intensity based on Gaussian distribution 119

(18) Bragg’s Equation 135

(19) Porosity equation 196

Chapter 1 Rapid Manufacturing Technologies

Rapid Manufacturing has emerged from the advent of rapid prototyping in order to produce models and prototypes through a concept of additive manufacturing[1, 2]. This is in contrast to traditional cutting, forming or casting methods. It belongs to the more general category of Rapid Prototyping (RP) systems, which are used for various kinds of applications during early product development in order to verify design and manufacturability, through concept evaluation, prototype models for presentation, as well as functional testing. The use of prototype model alone has had a tremendous effect on business values [2]. The continuous improvement of RP in the area of alloy powders and sintering/melting technologies has pushed the limits of this system towards direct fabrication of functional parts in a small batch, which is known as Rapid Manufacturing and Rapid Tooling (for tooling and mould fabrication)[3].

For clarification, a simple definition of Rapid Prototyping and Rapid Manufacturing is given below [4];

a. **Rapid Prototyping** – refers to a group of commercially available process which are used to create solid 3D parts from CAD through a technique known as a Layer Manufacturing technique or Additive Fabrication
b. **Rapid Manufacturing** – uses this Layer manufacturing technique or additive fabrication to directly manufacture solid 3D parts for the end user either as parts of assemblies or as standalone products
c. **Rapid Tooling** – uses this layer manufacturing technique to directly fabricate tooling and moulds without the aid of any machining processes

There are still arguments regarding the definition of RP and RM. For some, RM means quick direct production of end-use parts by any manufacturing method and for others, it requires the use of layer manufacturing techniques somewhere along the production chain. However Terry Wohlers, a prominent additive manufacturing industry consultant defined RM as the direct manufacturing of finished products through an RP device [5]. This technique uses additive processes to deliver finished products from digital data which eliminates all tooling. RM is still an emerging set of technologies that have been gradually evolving from mere prototyping tasks to the final and fully functional manufacture of parts and products [6]. In a regional context, RM is defined as a set of techniques, technologies and methods that provide rapid and flexible manufacturing for a variety of applications: prototypes, moulds, dies, general tooling and final product (www.rmplatform.com).

1.1.1The Applications of RM technologies

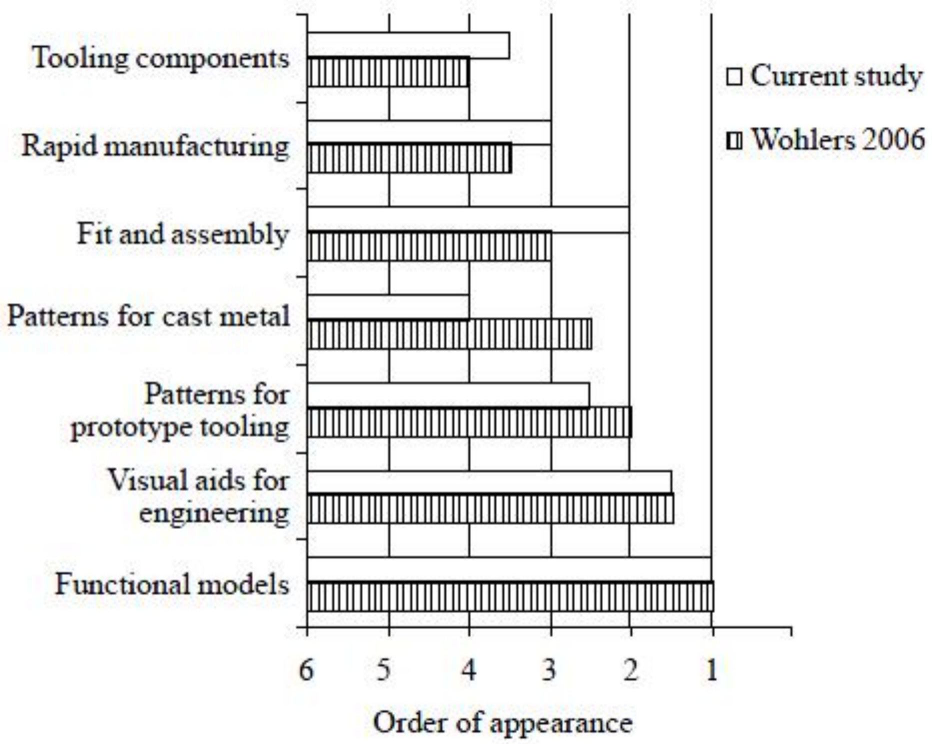

Figure 1.1: Application of RM technologies in 2008 [7]

A survey, shown in figure 1.1, was done to investigate the extensive use of RM tecnologies and in 2008 the result was compared to the Wohlers Report. From this it was shown that the application of Rapid Manufacture for functional models was the main purpose for having RM equipment and Rapid Manufacturing was ranked sixth on the list. It is well known that DMLS is best suited to production of a few parts with high complexity. This technology has evolved from making prototype models to producing functional parts as a result of the great advances in materials and laser technology. These improvements have been well suited to the mould and die industry where complex tool inserts were required to fabricate parts within a day. Maria Grazia Violante *et al* reported the use of RM technologies to manufacture fixtures and others have used SLS as one of the hybrid tooling methods to quickly produce multi component parts for tooling applications [8, 9]. It was suggested that the most effective way to utilise hybrid manufacturing systems may be through the use of direct metal laser sintering [10]. Beside rapid tooling applications, other potential applications are in aerospace, motorsport, medicine, denstistry, automotive and electronics[11] .

The applications have also expanded steadily into the medical field which mainly requires customised design and light structures [12, 13]. The use of RPM technology for medical applications, particularly in customised medical devices has attracted a lot of attention. Most of the work has been in the evaluation of the microstructures and mechanical properties of parts built using an additive principle. Ti 6Al 4V-Eli test specimens produced by layered processing were fabricated in an effort to investigate their metallurgical constitution and to compare the mechanical properties with those specified for similar materials produced in more conventional ways. They concluded that these test pieces showed comparable and in several cases superior properties to those specified in the ASTM standard [14].

As far as digital and automated fabrication are concerned, many works in this field have proposed multi platform and integrated systems combining a layered manufacturing technique with other virtual tools. A significant development is the use of a virtual reality environment with direct metal fabrication in order to improve the surgical output of customised medical implants. The use of such an automated method reduces the time to performing an implant by 50%, compared with technologies involving casting or machining and provides higher geometrical accuracy [15].

1.1.2 Rapid Manufacturing Framework

Rapid manufacturing offers the fastest path for bringing functional end products to the market. This is because the data is transferred digitally from the design platform to the end of fabrication platform. Many have agreed that it shortens the product development cycle [6, 16]. One of the profound findings is that this procedure does not required a lengthy mould fabrication process but builds a part directly based on the digital design data provided. Therefore the time to market is significantly reduced at reasonable production cost.

Figure 1.2: Basic Rapid Manufacturing Framework [17]

CAD data is digitally transferred to the RM machine. The machine builds the final product without any tooling or moulding. During intermediate phases, the CAD data is transformed to a triangulation data format and then sliced for generation of the 2D scanning path. A secondary process such as machining and heat treatment is performed depending on the requirements of the intended application. Because this technique gives full melting, the parts are fabricated to near full density so that RM systems have the capability of producing parts with good mechanical properties thus eliminating the post processing phase.

1.1.3 Issues and Advantages pertaining to Rapid Manufacturing

Hopkinson *et al* [18] highlighted three major issues pertaining to RM. They also concluded that the high cost of RM materials is generally acceptable and it is not the major driver for materials' selection. It is satisfying the requirements of a product that is most important. The following issues will affect the growth of Rapid Manufacturing ;

1. Material properties
2. Quality Control
3. Identification of suitable product to be produced by RM technologies

In the early development of DMLS, the material was tuned to suit the technology. Due to the limited availability of materials, the technology was initially restricted to tooling applications as commonly, in tooling fabrication one of the only concerns is functional requirement. Later, inspired by the rapid part manufacturing philosophy, the technology was developed to utilize the same material as those used in more conventional processing such as casting, forging or machining. Parallel with this advancement, powder metallurgy has evolved to produce alloy powders suited to this requirement. Nowadays, many parts can be built directly with the same material but by using different manufacturing routes [19].

The material properties of parts produced by rapid manufacturing have been compared to those made by injection moulding. It is known that the material properties of RM parts sometimes do not match those of parts made by injection moulding but a lot of research has been carried out to enhance the material properties of RM parts [20]. RM systems also face the issue of quality control as the parts produced by RM normally have high surface roughness and a stair effect on the surface[21, 22]. This means that post process machining is required which can be costly and time consuming.

An extensive analysis was undertaken and a comparison made to justify the use of RM systems as a new production technique, to replace the conventional methods. The published work confirmed the intuitive concept of producing mixed components in one building space via RM systems to effectively reduce the cost of each component [23]. Although there are quality control issues with this approach, RM has distinct advantages:

a. Complicated geometries can be made
b. A reduction in the number of parts that require separate manufacture because assemblies can be made in one process
c. The realization of concurrent engineering
d. High integrity products for low volume outputs
e. Reduced cost, lead time and improved quality

1.1.4 Rapid Manufacturing Characteristics

Rapid Manufacturing Systems all share a similar procedure for producing 3D parts. This is because the development of RM systems happened simultaneously. Major differences amongst these sophisticated systems are the type of materials that can be processed and the binding mechanism that fuses the powders within and between each layer. Essentially, RM systems have the following procedure;

a. They utilise fine powder particles
b. The powder is spread in a very thin layer (100um or less)
c. The powders are fused according to a CAD design by applying thermal energy via laser or electron beams
d. The process is repeated to build stacking layers
e. Post process to increase density

There are numerous RM systems commercially available on the market as mentioned earlier. There are also RM systems capable of producing metal parts using powder technologies such as Electron Beam Melting (EBM). EBM forms the core technology for machines made by Arcam AB which is marketed in the US by a company called STRATASYS. Similar to DMLS processes, EBM fuses metallic powder with its highly focused beam in a vacuum chamber. The machine can process metallic materials such as Titanium (Ti 6Al4V, Ti 6Al 4V ELI, ASTM F75) and cobalt chrome. The various systems and mechanisms have been discussed elsewhere [24, 25].

Another approach is known as powder deposition where powder is delivered by nozzles directly to the point where a focused laser melts the powder, fusing it into a part line by line, layer by layer[26]. This technique offers a larger working area compared to the powder bed method and has the advantage of being able to repair existing parts. The machine system is known as a Laser Engineered Net Shaped System (LENS) and was originally developed by Sandia National Laboratories before being commercialised by Optomec Inc. The LENS 850R system has a working chamber off 900mm x 1500mm x 900mm with positional accuracy of ±0.25 mm across the working area and linear resolution of ±0.025 mm according to Optomec. Argon gas is purged throughout the fabrication process to control the oxygen level which stays below 10 parts per million. With moving nozzles and tilt-rotate table capability, the machine can not only build parts but can also repair existing parts by adding thin layers where parts are worn or damaged.

Considering the practicality of the moving working table which is not suitable for heavy and huge parts, POM Group in the United States improved the laser cladding system by using a sophisticated five axis laser and powder metal head. They mounted cameras onto the head so that the melt pool height can be well monitored. A patented feedback control system using information from the cameras modulates the laser energy to maintain the melt pool height at predetermined levels. There are two standard machine configurations with the working dimension of 1219 x 600 x610 mm and 813 x 508 x 381 mm respectively This machine equipped with a 1 or 2kW fibre coupled-diode laser with positioning accuracies of ±0.098 mm/m. The layer thickness which controls the finished part resolution is in the range of 40 to 100µm[27].

Besides the powder deposition system, the process can be divided into a few groups based on the binding mechanism. The binding method of each machine can be distinguished based on the available processing materials and the type of binding. As shown in figure 1.3, the powder consolidation method is divided into a chemical process, sintering and gluing. In 2007, Kruth *et al* published the consolidation mechanism used in laser and powder bed layered manufacturing and classified the processes according to the different types of sintering used:

Solid State Sintering (SSS), Liquid Phase Sintering (LPS), Full melting (FM) and Chemically induced melting (CI) [28]. The materials used in laser sintering include plastic, wax, nylon/glass composites, ceramics, metal-polymer powders, metals, alloys and polymers. The machine was then divided into deposition for fused deposition modeling, photocuring or light sensitive polymers for SLA, selective laser sintering, 3D Printing and layer object manufacturing.

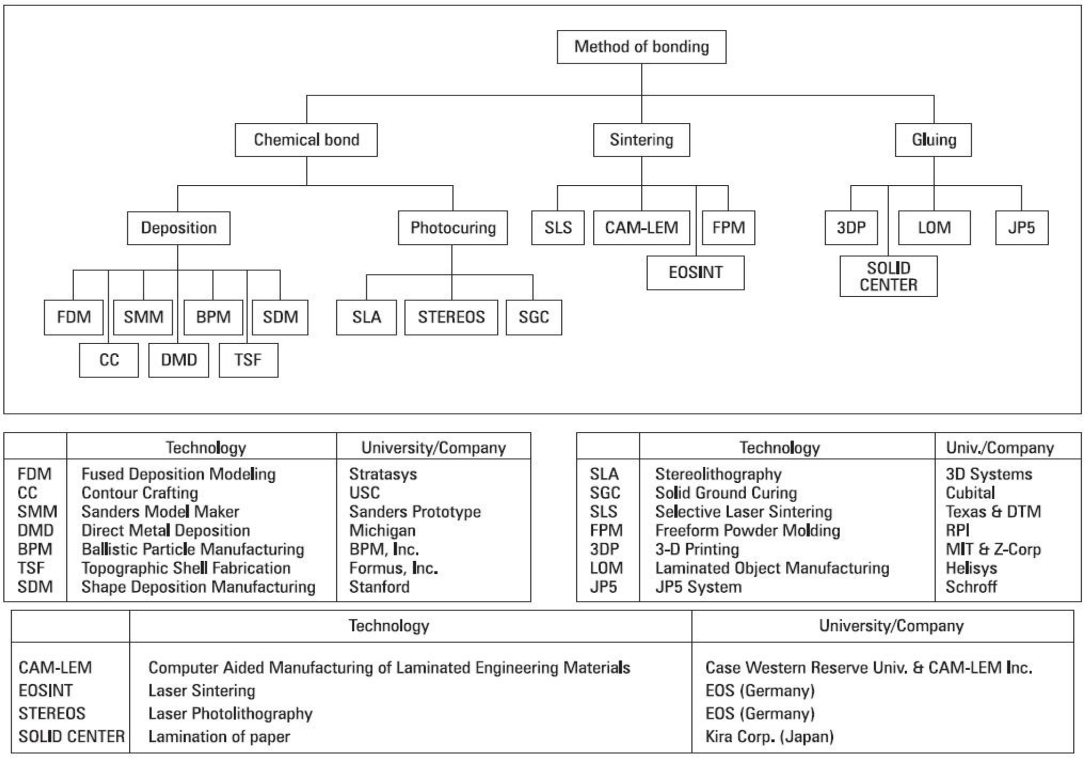

	Technology	University/Company
FDM	Fused Deposition Modeling	Stratasys
CC	Contour Crafting	USC
SMM	Sanders Model Maker	Sanders Prototype
DMD	Direct Metal Deposition	Michigan
BPM	Ballistic Particle Manufacturing	BPM, Inc.
TSF	Topographic Shell Fabrication	Formus, Inc.
SDM	Shape Deposition Manufacturing	Stanford

	Technology	Univ./Company
SLA	Stereolithography	3D Systems
SGC	Solid Ground Curing	Cubital
SLS	Selective Laser Sintering	Texas & DTM
FPM	Freeform Powder Molding	RPI
3DP	3-D Printing	MIT & Z-Corp
LOM	Laminated Object Manufacturing	Helisys
JP5	JP5 System	Schroff

	Technology	University/Company
CAM-LEM	Computer Aided Manufacturing of Laminated Engineering Materials	Case Western Reserve Univ. & CAM-LEM Inc.
EOSINT	Laser Sintering	EOS (Germany)
STEREOS	Laser Photolithography	EOS (Germany)
SOLID CENTER	Lamination of paper	Kira Corp. (Japan)

Figure 1.3: The Clasification of Rapid Manufacturing Systems based on binding mechanism[29].

1.2 Direct Metal Laser Sintering

Sintering is manifested by the bonding between the contacting particles subjected to a localised heat treatment. Many ideas were proposed in order to bind the powder particles with the aim of having a good functional part. With the advances in laser technologies such as shorter laser wavelength with greater laser power, sintering or melting of the powder metallic particles became attainable. In another area, the physical and chemical properties of the metallic powders were improved so that better laser-powder interaction could be stimulated. All this was with the aim of having greater bonding specifically for additive processes where inter-layer and inter-track bonding is of primary concern.

As discussed in the earlier sections, laser sintering technologies can be classified as being in a different category based on the binding mechanism applied by the machine to form a solid 3D part. Different manufacturers have an identical technique to binds each layer. Generally, SLS can be classified into four categories but this classification is not absolute and the borders are not very clear especially between SLS and SLM.

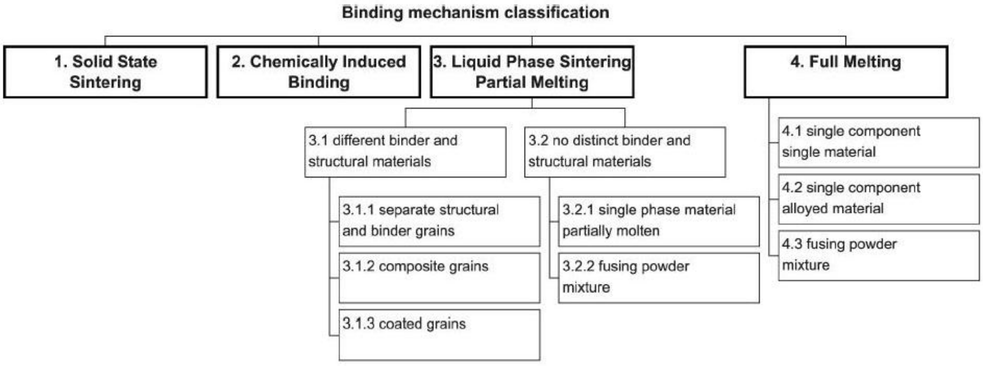

Figure 1.4:Laser based powder consolidation mechanism *[28]*

In this research work, the DMLS process is considered to be selective laser melting rather than selective laser sintering even though the latest DMLS machine is fully capable of synthesising the powder particle to be either sintered or melted. In this work, the aim was to use DMLS to fabricate all parts to be fully dense which required the processing parameters to be set accordingly. This can cause confusion but bearing in mind that the parts fabricated in this process are near to fully dense, it is more appropriate to utilise powder fusion by melting rather than sintering.

In Figure 1.4 the consolidation mechanism is divided into four categories: Solid state sintering, chemically induced binding, liquid phase sintering/partially melting and full melting. The applicability of the consolidation process is dependent on the processing materials. For the chemical induced binding method, binder and composite grains can be used and a single component and metallic powder is processable via full melting. These four types of binding will be used as the critical boundary feature in order to distinguish the type of binding mechanism in DMLS of this particular machine in this research work.

1.2.1 Binding mechanism

As shown in above figure, laser sintering process can be classified based on its binding mechanism. Generally, there are two types of sintering; solid state sintering (SSS) and liquid phase sintering (LPS). Solid state sintering occurs when the powder compact is densified wholly in a solid state at sintering temperature, while liquid phase sintering occurs when liquid is present in the powder during densification [30, 31]. The important changes taking place during sintering are densification and grain growth. In this section, various types of sintering are briefly explained but with more on liquid phase sintering as it this is close to describing the consolidation of metallic powder during the additive process used in this particular research work.

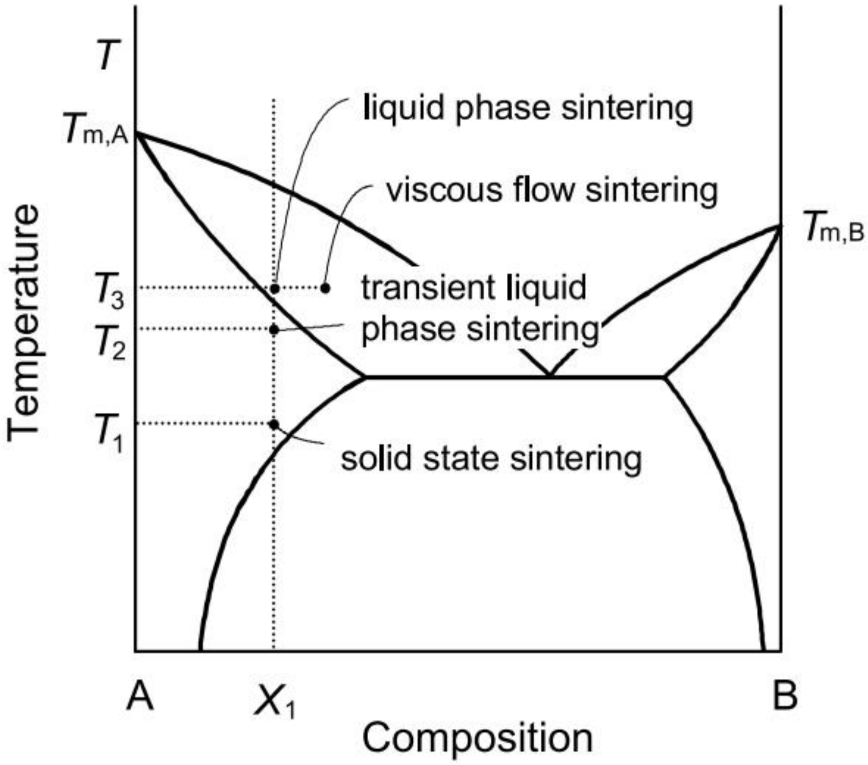

Figure 1.5: Type of Sintering[32]

1.2.1.1 Solid state sintering (SSS)

Solid State Sintering (SSS) is a thermal process which fuses the powder particles by creating a neck between the particles. The advantage of this sintering technique is the capability to sinter a broad range of powder materials as long as enough energy is provided to give sufficient heat to bind the particles. All powders are consolidated via diffusion of atoms i.e surface, volume and grain boundary diffusion. The temperature needed to induce sintering between two particles depends on the material and particle shape, size and distribution. For a crystalline material a grain boundary grows at each contact point to replace initial solid-vapour interfaces. Normally, a two sphere model is used to describe the sintering process. During prolonged sintering the grain boundaries migrate and the particles coalesce into a single sphere with a final diameter equal to $2^{1/3}$ times the original diameter. This physical diffusion happens slightly below the melting temperature [32]. This binding mechanism is rarely used since the process is slow and not practical because of the high laser scan speed. This would contribute to higher costs and lower productivity. However, this technique is best suited for consolidating ceramics' parts and is sometimes used for post processing after partial laser consolidation of metallic parts during solid state sintering.

1.2.1.2 Liquid Phase Sintering

Liquid phase Sintering (LPS) is defined as a process for forming high performance, multi-phase components from powder sintered under conditions where solid grains coexist with a wetting liquid [32]. A typical LPS condition is to have a liquid phase present and for the solid grains to be soluble in the liquid. Under these circumstances the liquid wets the solid and provides a capillary force that pulls the grains together. Figure 1.6 illustrates the related events taking place during liquid phase sintering such as solid state sintering, rearrangement, solution precipitation and final densification [30]

LPS is also explained by the melting of a low melting point phase which is known as the binder while a higher melting point structural phase remains solid. Therefore, powders are mostly a mixture of particles of a high and low melting point material but composite grains or coated grains are also applicable. One of the advantages over solid state sintering is that the formation of liquid gives faster sintering. However, complications can exist with single component powders since it is necessary to understand the process parameters to ensure sufficient surface melting whilst avoiding core or structural particle melting [33].

Tolockho *et al* state that the 'balling' phenomenon is one of the problems obstructing successful performance of single component laser sintering. In the case of two components, there is a clear distinction between the structural material, as the main component with a high temperature capability and the binders [33]. In the work of Tolockho *et al* the laser irradiation was adjusted to a level that exceeded the binder's melting temperature where the liquid binder wets and binds the structural particles. Normally, the binder components are smaller than the structural particles favouring higher solubility leading to better wetting and spreading for good densification.

There are three main concerns during the liquid phase sintering process; rearrangement, solution re-precipitation and final phase sintering.

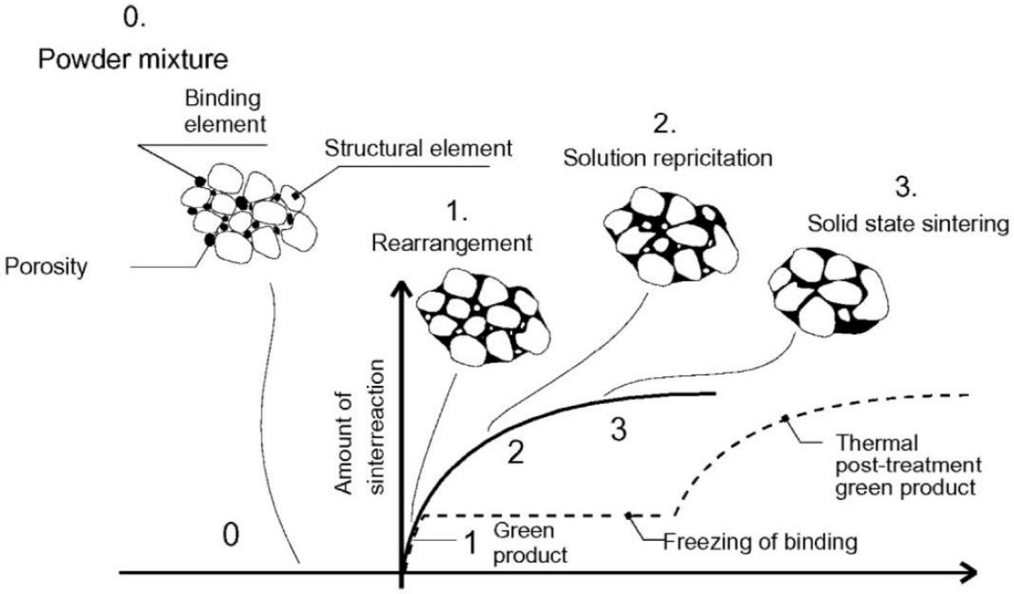

Figure 1.6:Liquid Phase Sintering Mechanism *[32]*

Liquid phase sintering can be simplified into three stages. The first stage is a rearrangement of particles when the liquid forms and wets the solid structure. The second step occurs when solution re-precipitation becomes active leading to pore elimination by grain shape adjustment and the third step is microstructural coarsening, where the mean grain and pore sizes increase continuously. The post processing or debinding process such as furnace treatment, HIP or infiltration are normally required in this process to eliminate the 'green' parts in order to increase the density of the parts.

The density of a part is closely related to the inter-particle space or voids. These inter-particle voids are initially caused by inhomogeneous particle packing that later creates the porosity in a solid part. In a review led by R.M German, pores exist between the grains and these are wetted by the liquid[34]. Through capilliary action the liquid preferentially fills the smaller pores. As the smaller pores fill, the mean pore size increases while the overall porosity and number of pores decreases.

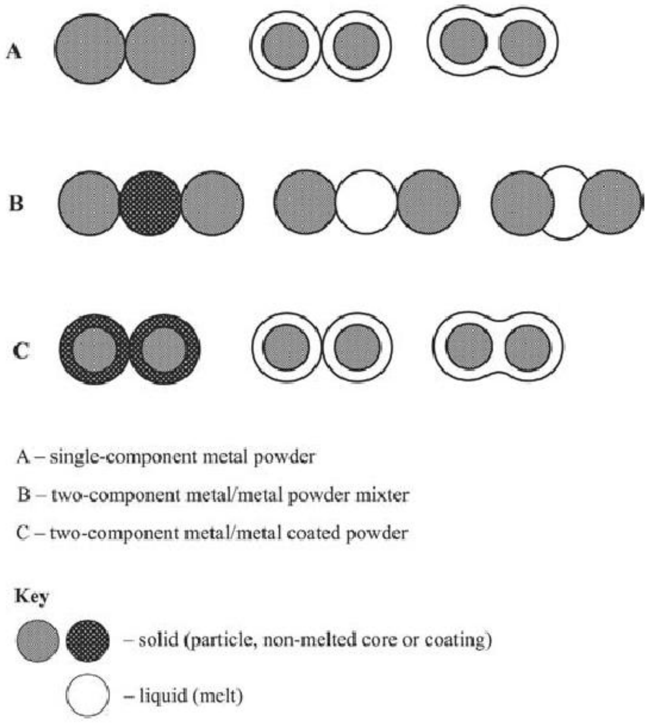

Figure 1.7: Different combinations of the powder particles

There are three different combinations of powders that can be used for this technology [35];

1. *Separate grains* – this technology separates the core and binder components. The binders have a smaller size and lower melting temperature compared to core components which have a higher melting temperature. The core can be a ceramic or metal but the binder is mostly metallic.
2. *Composite grains* – through the mechanical alloying process, the structural powders and binders are repeatedly milled, fractured and welded together. In turn, the composite grains consist of two different powders in one individual powder grain.
3. *Coated grains* – the structural grains are coated with the binder component. The laser irradiation scans and melts the binders first and the structural component remains solid throughout the process.

1.2.1.3 Full melting

The development of full melting processes such as selective laser melting was driven by a requirement to have fully dense parts with optimum mechanical properties. The ability to achieve almost 99.8% part density through completely melting the powders has eliminated those lengthy post processing treatments[19, 36]. Polymers as well as metals can be made fully molten by this process. However there is a limitation on the metallic materials that can be processed by this technique. The presence of a liquid pool makes the process more difficult to control and furthermore at high processing temperatures careful control of the atmosphere is required in order to avoid oxidation. Another difficulty encountered during a full melting process is the presence of high thermal stresses which cause shrinkage, cracking, curling and delamination.

This complete melting process is achievable because of significant improvements in laser energy density. Nowadays, a shorter wavelength laser Nd:YAG (1.06um) is used to provide greater laser energy with a smaller spot size compared to previous CO2 laser sources. Fischer *et al*[37] reported the use of a Nd:YAG laser for pure Titanium powder. R Morgan *et al* used the nanosecond pulse of Nd:YAG to sinter metallic powders [38]. In addition, the absorbance of laser energy in metallic materials is greater for a shorter wavelength laser rather than in a long wavelength CO2 laser. However, studies have shown that there are drawbacks when using a full melting process, such as part distortion due to internal stresses and high surface roughness caused by a ‘balling’ phenomenon [39]. Therefore, details which aid our understanding of the process parameters and suitable preheat treatments are mentioned in several research works in order to minimize these effects.

Partial melting – here there is no distinction between the structural and binder components which means it can be a single phase component. However, there is a clear distinction between molten and non-molten areas throughout the process. The laser energy input is adjusted to ensure that insufficient energy is supplied and only the outer shell of the particles are melted rather than complete particle melting. The molten materials act as a binder to join the core particles which remain unaffected.

Chemically induced process

This process is rarely utilized for commercially available sintering machines but has proved to be feasible to sinter ceramics, metals and polymers. IPT Achen in Germany have used this technique to sinter SiC ceramics' parts. SiC powders will partially disintegrate into Si and C during heating. A reaction with oxygen will then form SiO which will then act as a binder to fuse the SiC particles. Finally post processing via Si infiltrants is used to achieve fully dense parts.[35]

1.2.1.4 Problems in Laser Sintering/Melting

SLS/SLM technologies offer a promising technique for producing parts that would be difficult or impossible to build using traditional tools. Despite the benefits of laser sintering, there could be problems during material consolidation involving reactive metallic materials such as titanium and aluminium. The consolidation process involves an intricate interaction between the powder and the laser beam let alone the processing environment. Problems during consolidation are summarized below;

a. There is a short time for laser-powder interaction which may lead to short material heating times relative to the time required for fully melting the powder particles. Tolockho *et al* mentioned that during laser processing, sintered, semi-sintered/semi melted or fully melted material can be formed [40]. Dai and Shaw, investigated the transient thermal effects on the fabricated parts [41].
b. The melt pool must wet the previously processed layer and when it solidifies it must be flat enough to enable the next thin layer to be deposited. Since the reaction is mainly based on capillary forces, the wetting characteristics of liquid over the solid particles are critical [42].
c. The intermediate handling of the powders, especially during the consolidation process is of prime importance to avoid powder contamination which would be detrimental to laser-powder interaction. Oxide layers, trapped gas and impurities within the powders have been identified as sources of contamination [43, 44]

d. Two component SLS processes require careful control of process parameters to sufficiently melt the desired powders. A problem can occur if the two components have similar melting points with both components can become liquid[35].

1.2.2 Physical phenomena during DMLS

DMLS is steadily becoming popular for the fabrication of functional metal parts with high geometrical complexity. Research and commercial interest in this area are increasing every year. Unfortunately, there remain many gaps in our understanding of the process mechanism and process parameters let alone the effects of this processing method on a materials microstructure and properties. This is indeed a challenging task due to a multitude of phenomena taking place in a very short time and the non- linear characteristics of the process.

It is known that during the localised interaction of the laser beam with metallic powders, the high energy deposition causes the powder particles to melt and create a molten pool [45]. In an ideal case, the liquid pool created during DMLS should be well spread over the underlying solid and remain continuous along the direction of the laser beam. However, it is reported in many publications that the behaviour of this liquid pool is often far from ideal and there is a need to understand the factors that influence and are responsible for controlling the liquid pool behaviour. In this section a brief explanation of the physical mechanism taking place during DMLS is presented. An understanding of these physical phenomena is essential for further process development and process control.

1.2.2.1 Wetting Behaviour

In DMLS, when a laser beam strikes the powder surface, the powder undergoes densification by sintering leading to a volume reduction. As additional laser energy is absorbed by the sintered powder, it eventually undergoes melting and further volume reduction as additional powder is dragged into the melt pool under the action of surface tension. Under this short laser exposure, heat transfer by conduction and radiation takes place from the laser processed zone into the surrounding powder and by radiation and convection into the space above the melt pool. The wetting behaviour of a liquid on a solid substrate is of prime importance in DMLS since it determines the spreading behaviour of a melt and affects the infiltration characteristic of the system[28, 35].

For a good wetting to take place, a reduction in the amount of surface oxides is of prime importance providing a clean metal to metal interface. In most liquid phase sintering systems there is only a weak chemical reaction between the constituents. Thus surface tension from the liquid phase is a significant factor in determining the sintering rate. In such cases, the three main concerns are solid solubility in the liquid, wetting of the liquid on the solid grains and solid phase diffusion in the liquid [32]. The Kingery model explains the densification process by dividing it into three main stages; rearrangement, solution precipitation and final stage sintering. Based on this model, if there is a high liquid level, then full density can be achieved via rearrangement upon liquid formation. On the contrary, at low liquid level, the solid skeleton slows densification by solid state sintering.

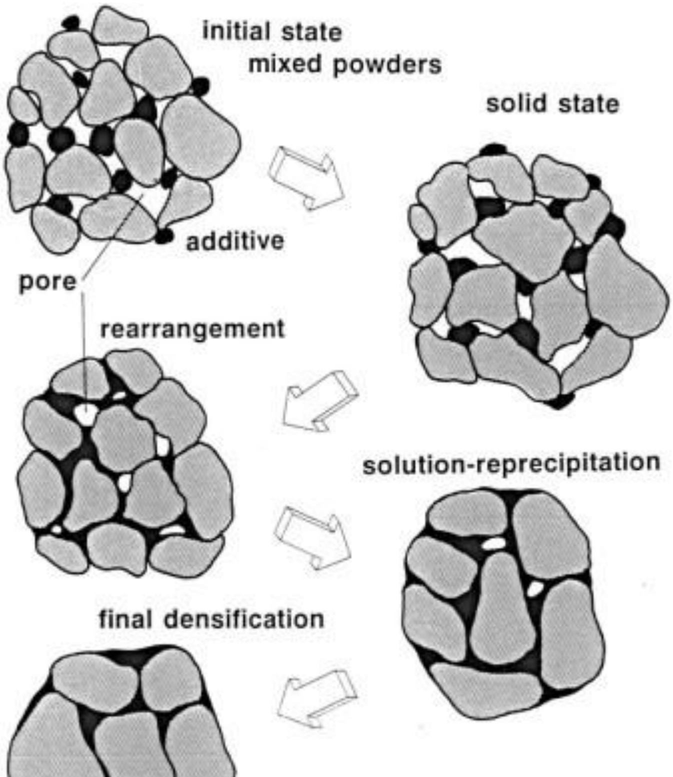

Figure 1.8: Densification Process

In principal, prior to liquid phase sintering, the solid is soluble in the liquid at the sintering temperature. This solubility causes the liquid to wet the solid providing a capillary force pulling the grains together. Also the high temperature further assists densification. After liquid formation, the compact consists of three phases which are solid, liquid and vapour. When the liquid spreads across the solid, it replaces the solid-vapor interfaces with liquid-solid and liquid-vapor interfaces. The solid particles can be rearranged by this liquid flow. At the same time, there are some melted particles which become pores because of the liquid flow into fine capillaries between solid particles. The elimination of these pores governs the overall densification process and microstructural coarsening.

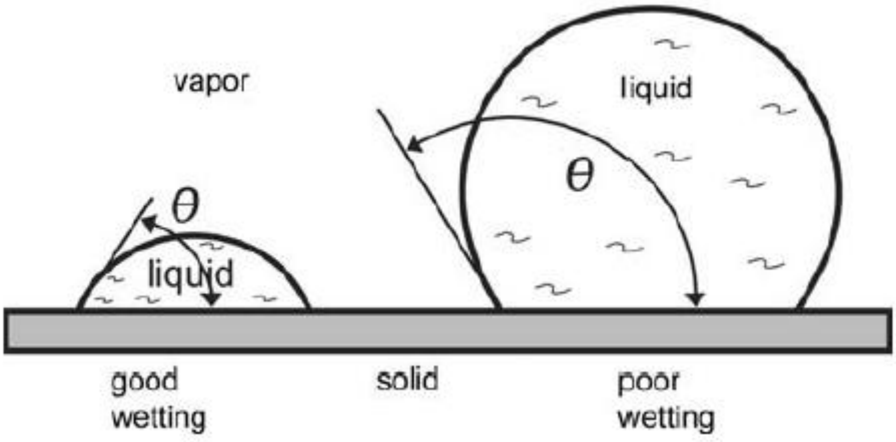

Figure 1.9: Good and poor wetting based on the contact angle. The contact angle is associated with the balance of three interfacial energies $\gamma_{sv\ (solid\text{-}vapor)}$,$\gamma_{sL(Solid\text{-}liquid)}$ and $\gamma_{LV(liquid\text{-}vapour)}$.

For a constant solid-vapour surface energy, the contact angle depends on the relative interfacial energies. A low contact angle induces liquid wetting over the solid grains providing a capillary attraction that helps to densify the powder. A liquid which wets the powder moves to occupy the lowest energy configuration so it preferentially flows to the smaller grains and pores. This gives rise to rearrangement densification. A high contact angle indicates poor wetting so the liquid retreats from the solid. This causes swelling and liquid exuding from pores. Therefore, liquid formation causes either densification or swelling. In practice, a broad range of capillary conditions exist since the microstructure is composed of a range of grain and pore sizes and shapes, each with different capillary behaviour[29, 46].

The equation as follows: The importance of a low contact angle leading to good wettability is illustrated by the following equations[46]:

$$\gamma_{SV} = \gamma_{SL} + \gamma_{LV}\cos\theta \qquad (1)$$

where subscripts S, L and V represent solid, liquid and vapour respectively. Rearrangement of equation 1 gives the contact angle as a function of the relative surface energies.

$$\theta = \arccos\left(\frac{\gamma_{SV}}{\gamma_{LV}} - \frac{\gamma_{SL}}{\gamma_{LV}}\right) \qquad (2)$$

As shown in the above schematic (figure 1.8) of the microstructure during liquid phase sintering, a common situation is for the liquid to wet the solid. At this point, the newly formed liquid penetrates between the solid grains, dissolves the sintered inter-particle bridges and induces grain rearrangement. Due to better solid solubility in the liquid, the liquid improves transport rates responsible for grain coarsening and densification[46]

1.2.2.2 Densification rate

Considering the process of DMLS, the temperature of the powder bed can easily exceed the melting temperature leading to a full melting of particles. It is also possible that the high energy density exposed to the powder might be high enough to cause the material to evaporate. DMLS is therefore prone to suffer from instability of the molten pool due to the full melting mechanism used. This is a normal phenomenon in persistent liquid phase sintering where at the sintering temperature the solid is soluble in the liquid. On cooling, the liquid solidifies to produce a dense microstructure with good mechanical properties

The DMLS process is known to have an extremely high temperature gradient and rapid solidification occurs as a consequence of this. This contributes to a unique microstructural evolution[47]. Additionally, shrinkage and high residual stresses tend to occur in processed components because of the rapid interaction which creates a high temperature gradient[48]. Furthermore, the high residual stresses accumulating in each single track and layer can cause distortion and delamination on the final parts[49].

Many factors influence the densification of metal powders during a laser sintering process. These factors can be divided into two main categories which are processing parameters and material properties. The processing parameters are those variables that have a great influence and control on the DMLS process. In other words, processing parameters can be considered as the variables that determine the amount of energy density transferred to the powder [50]. Material properties include the chemical constituents and the purity of the powder material, method of alloying (elemental or pre-alloy), and particle characteristics (size, shape and distribution) [51]. By assuming constant material properties, the melting/solidification process is influenced by the specific laser energy density which determines the densification rate and the resultant microstructure [52]. The parameters that are most influential in governing the intensity of the laser beam and the amount of energy delivered to the powder bed are laser power (P), scan speed or scan velocity (v), hatch spacing (HS) and the layer thickness (LT). Others have also added the influence scanning strategy, even though the effect of this parameter is proved to be marginal [53].

The laser energy density used to assess the laser energy input on the powder bed is calculated based on the following equation;

$$\mathrm{LED} = \frac{\text{laser power (Watt)(P)}}{\text{beam diameter (mm)}} = \frac{\mathrm{J}^{\mathrm{s}-1}}{(\pi \mathrm{r}^2)\mathrm{mm}^2} \tag{3}$$

$$\frac{\mathrm{J}}{\mathrm{m}^2} = \frac{\mathrm{J}}{\mathrm{s}}\,\mathrm{x}\,\frac{1}{\mathrm{m}^2}\,\mathrm{x}\,\frac{\mathrm{s}}{\mathrm{m}} = \mathrm{Jmm}^{-3}(\text{dimensional analysis}) \tag{4}$$

where LED = laser energy density, P= laser input. This equation is solved by using the dimensional analysis method. One can also use the volume energy density (VED) by adding layer thickness and hatch spacing to the equation (Jmm^{-3})

$$\mathrm{VED} = \frac{\text{laser Power(P)}}{\text{Layer ThicknessxHatch SpacingxScan Speed}} \tag{5}$$

1.2.2.3 Thermal model

One of the key objectives of this research is to analyse the sintering/melting mechanism during laser-powder interaction and to understand this interaction by investigating the thermal history. This chapter elaborates on the previous work on DMLS which involves the development of a thermal model with regard to the temperature distribution due to surface heat flux, the laser beam characteristics, the energy produced and the powder absorption coefficient, the sintering/melting mechanism and briefly the heat transfer mechanism.

However, to model the SLS/SLM process in a way to enable an understanding of its thermal history is a challenging task as it involves phase-change problems (powder-liquid-solid). These phase-changes cause many key variables, such as powder bed density, thermal conductivity, heat capacity and thermal diffusivity to change with time and temperature creating a non-linear thermal system which requires a comprehensive analytical approach. The fundamentals of heat transfer during melting and solidification have been studied intensively and are well documented [54, 55]. The fundamental equation used for heat conduction during laser heat treatment is:

$$\rho C_p \frac{\delta T}{\delta t} = \lambda \nabla^2 \mathrm{T} + \alpha \mathrm{I}(\mathrm{x,y,z,t}) \tag{6}$$

Where ρ is the density, C_p the specific heat, T the temperature, λ the thermal conductivity, α the fraction of the radiant energy absorbed per unit time t and unit volume of metal and I (x,y, z, t) is the intensity of the laser irradiation in W/m^2. Rosenthal derived the first analytical solution for a moving heat source in a semi finite substrate for 3D heat distribution[56]

$$T(\zeta, y, z) - T_o = \frac{\alpha P}{4\pi\lambda R} exp\left(-\frac{V\zeta}{(2\delta)} - \frac{VR}{2\delta}\right) \tag{7}$$

$$R^2 = = \zeta^2 + y^2 + z^2 \tag{7.1}$$

$$\zeta = x - Vt \tag{7.2}$$

Where T_o is the temperature at a large distance from the heat source, P the incident laser power, V the velocity of the heat source in the positive X-direction and δ is the thermal diffusivity. This solution does not take into account the latent heat due to melting or solidification and only gives a good prediction of the temperature profile at a large distance from the source[57].

The two most widely used methods are enthalpy and temperature-based equivalent heat capacity methods. Both methods in this group have certain advantages and drawbacks. Few researchers are agreed on specific conditions, especially for long irradiation time for which the DMLS process is best investigated numerically by applying three dimensional transient heat balance equations. Some researchers were satisfied mathematically with a simple closed-loop analytical solution[58]. Various physical and thermal models and their analysis methods have been reviewed[59].

A simple analytical solution was presented by Shen *et al* [60] to solve the problems of laser induced melting in four materials: titanium, aluminium, fused quartz and copper. Certain assumptions, such as a requirement for the laser beam diameter to be large enough compared with the molten region and the material's thickness to be much greater than the thermal penetration depth, were made in order to offer stability. Shen *et al* also highlighted that it is necessary to assume that the thermal properties (conductivity, diffusivity & density) of the material are independent of time thus allowing a linear system solution. Their findings elucidated an overestimation of the calculated melt depth size for the longer irradiation time and that the developed thermal model was reasonably accurate at the beginning of the irradiation process in which vapour and plasma effects were not strong. Finally, they derived an equation to get the temperature profiles and the melting depth:

$$S(t) = \frac{k_l}{A_l\, I}\left[\frac{2\lambda_l {A_l}^2 I^2}{{k_l}^2} t + C_o\right]^{1/2} + \ln\left[\frac{\frac{2\lambda_l {A_l}^2 I^2}{{k_l}^2} t + C_o}{T_m}\right]^{1/2} \qquad (8)$$

The time for the surface reaching the melting point T_m is:

$$T_m = \frac{(T_m - T_o)^2 \; C_s \rho_s \kappa_s}{2(A_s I)^2} \tag{8.1}$$

And the time for the surface reaching the vaporization point is:

$$T_v = \frac{(T_v - C_o)^2 \; {\kappa_l}^2}{2(A_l I)^2 \lambda_l} \tag{8.1}$$

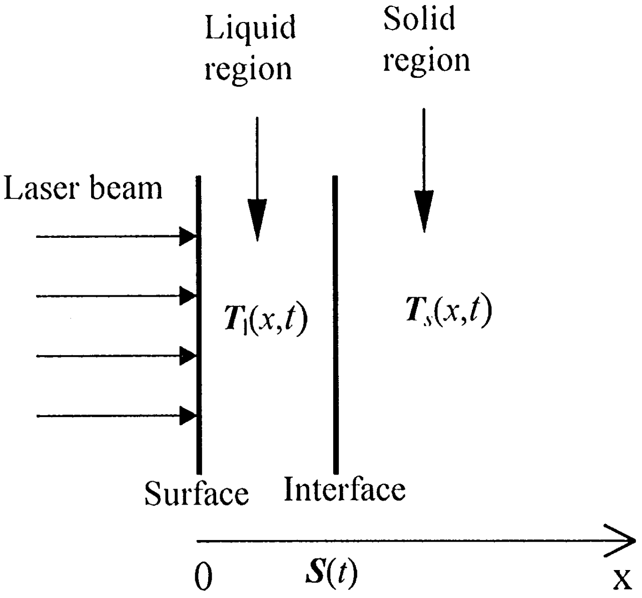

Figure 1.10: The Geometry of laser irradiation explained by S.Z Shen *et al*

Xiao and Zhang [61], later presented an analytical solution for a rapid melting and solidification process using an integral approximation solution. This method allows the calculation of a surface temperature field, the location of interfacial zones (liquid, mushy zones) and the solid fraction on the surface in relation to the effects of various processing parameters.

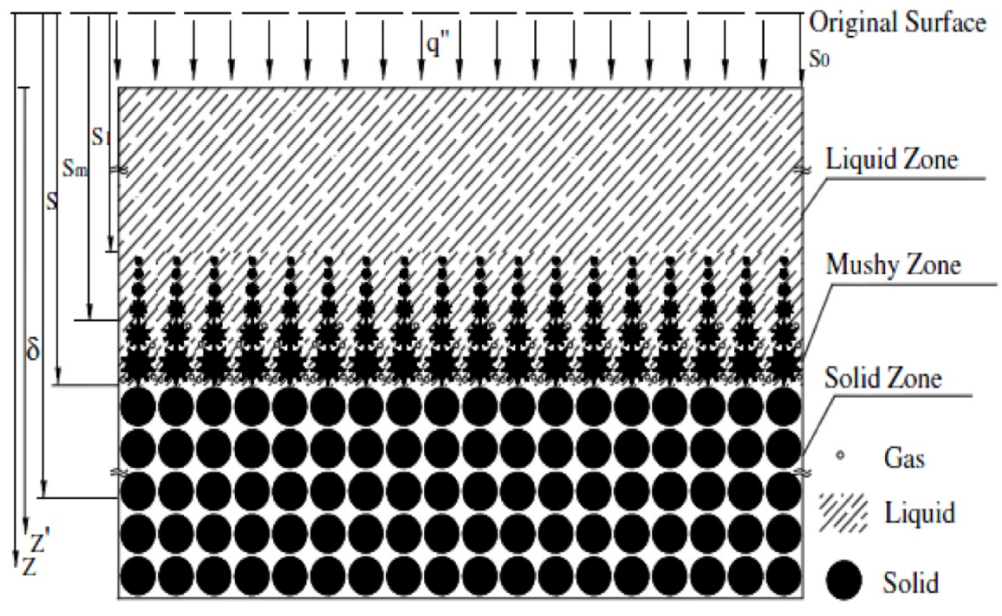

Figure 1.11: Physical model of DMLS

The thermal model can also be demonstrated by solving classical Stefan problems provided that boundary conditions were chosen appropriately [62]. In this paper, a numerical model based on the finite volume method is developed to perform computations for different beam diameters, scan speeds, substrate temperatures and power input profiles. From the results of these computations, the relationships giving the time to initiate melting, the time to reach maximum melting depth and the total melt re-solidification time were derived. This method allowed a comparison of the surface temperature history for the three different power input profiles with approximate closed-loop form solutions.

An important study to model the laser sintering process was carried out by Tolockho *et al* [40]. This work gives a comprehensive theoretical understanding of the sintering/melting formation during DMLS. Their work has shown that DMLS is capable of not only producing sintered or partially sintered parts but fully melted parts having near to full density if sufficient energy density is provided. In this study, a Nd;YAG stationery laser beam with a 1.06μm wavelength and regarded as a Gaussian beam was used. The powder bed, filled with loose titanium powder underwent a laser strike for 10secs. The formation of various hemispherical (in shape) sintered samples were analysed prior to gradually increasing the laser power and changing the types of powder investigated. It was found that the loose titanium powder, which represents a single metallic component, is sintered under the influence of the laser beam as a result of surface melting of the particles and by subsequent joining of the solid non-melted cores of particles. This numerical study which was based on an enthalpy method showed that the heat transfer mechanism is governed by thermal radiation that determines the front propagation velocity. The characteristics of the powder i.e density, shape and size is reported to have a significant influence on the thermal contact radiation. An in depth explanation of the thermal contact radiation in the powder bed has been given by [63]. The mapping and modelling of single scan track formation is emphasised in the work of Childs et al [64]. They used a CO_2 continuous laser beam to investigate the influence of laser power and scan speed in several metallic powders. They also analysed the geometry and stability of a melt pool which was mainly controlled by the laser power and scan speed. Another similar study was undertaken by Y K Song [65]. Song reported that there exists a great temperature gradient from the surface of the powder bed to the substrate/platform used and the maximum depth of the molten powder layer is about 45µm under the specific condition of 110W laser power and $0.2ms^{-1}$ scan speed. He also investigated the influence of scan speed on the part’s microstructure where he reported that with an increased scan rate, the part exhibits more porosity and the interlayer bonding is more visible.

Chen and Zhang [59] investigated the SLS process using a moving Gaussian beam through three dimensional modelling coupled with a finite volume method for a mixture of metal powders, each with distinct melting points, with melting induced by laser irradiation . The method used successfully modelled the sintering depth or liquid pool and the heat affected zone. Based on this technique, the results indicated that the sintering depth and shape of the heat affected zone significantly increases with increasing laser beam intensity and decreasing moving laser beam scanning velocity. Zhang further improved the thermal model using a stationery laser beam [66]. In another study [67] laser melting was described as a complex physicochemical metallurgical process involving phase transformation, mass and heat transfer in a short period of time.

A similar approach to that used in previous described above was used, but more variables such as laser power scan speed, scan interval and preheating temperature to stimulate the temperature field were taken into account. The simulation results showed that a lower thickness, narrower scan interval and a slower scan velocity tend to improve the temperature profile in the powder bed. Moreover, the parameter range in which the maximum temperature in the powder bed could reach the melting point of tungsten (about 3,420°C) was obtained.

Verhaeghe *et al* chose a different approach from the aforementioned work [68]. Their aim was to have a simple, pragmatic and flexible model taking into account all phase transitions including evaporation by using an enthalpy formulation. They successfully established a thermal model which could determine melt pool depth and width and the surface temperature. The simulated surface temperature given by the model was up to 12000˚C for 80W laser power input and this was unlikely to happen without evaporation taking place. The simulated melt pool widths which represent lateral heat transfer were in good agreement with the experimentally observed behaviour at 20W. However, they noticed that the simulation results were different from the experimental data once the energy density increased[68].

They outlined a few possibilities which might explain the differences. Firstly, the Marangoni convection effects. Secondly, temperature gradients in the melt pool which give rise to surface tension. Thirdly, evaporating material can create a recoil pressure on the melt pool, flattening the melt pool and pushing out the liquid in the lateral direction. Finally, the beam radius is not a constant because at higher laser power, the system optics give a larger beam radius. These are some of the phenomena which were not being considered in this experiment but were highlighted as having equally important effects on the process. It was concluded that although the model is relatively simple and contains certain limiting assumptions, insight about the SLM process can be gained by analysing the simulation results and comparing with experimental data. Work needs to be done, however, to improve the agreement between model and experiment, especially at higher power inputs. In the future, the model will be applied to process control to obtain, for example, a stable bath width when making a transition from dense to powder substrates.

1.2.2.4 Microstructure

The microstructure of titanium alloys depends strongly on processing history and heat treatment which directly influence their mechanical properties. Depending on these conditions, titanium alloys can have many types of microstructure such as duplex or bi-modal structures. Duplex structures consist of primary alpha and transformed beta. The primary α forms on cooling through nucleation and growth and its morphology can vary from elongated plates to an equiaxed globular morphology where the latter is a result of recrystalization. It is also known that the formation of globular alpha not necessarily through deformation or recrystalization but is also due to slow cooling rates from above the α+β phase field[69].

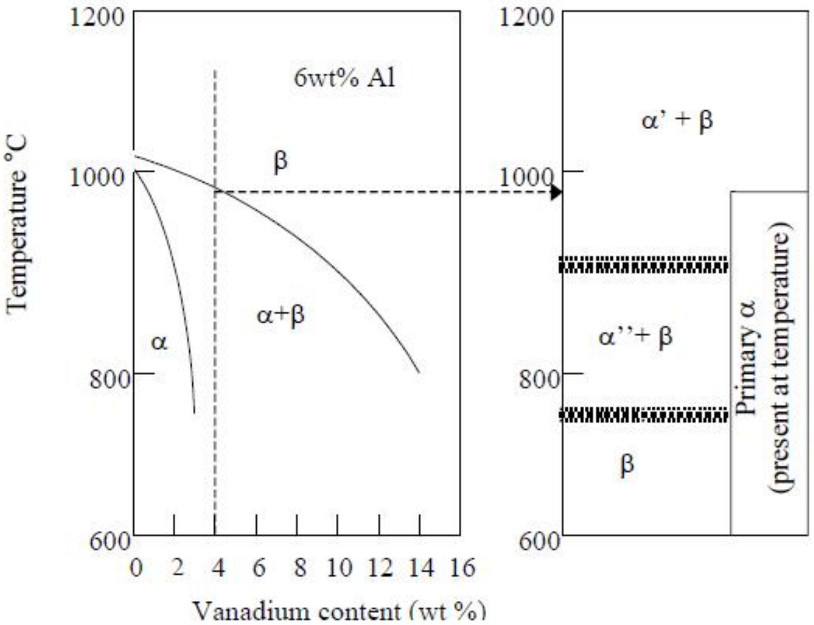

Figure 1.12: Ti 6Al 4V microstructure evolution after quenching from different temperature[69]

A common and prominent feature of a laser sintering/melting process is that the thermophysical interaction between the laser and material involves a highly focused energy input or high working temperature over very short times. This produces extremely high cooling rates which have been reported to be between 10^3 to 10^8 K/s [70]. This process is characterised by high temperature with very high cooling rates and this distinguishes the microstructure from those found in other processing methods [71]. Yong AK Song *et al* elucidated that SLS processing is based on melting and not on diffusion, so the process closely resembles liquid phase sintering [65]. The main processing parameters, such as laser power, scan speed, scan spacing and layer thickness, exert huge influences not only on the microstructure, but equally importantly on the part properties. Lore Thijs *et al,* who investigated the microstructural evolution of Ti 6Al 4V SLM processed parts, established the process-structure relationships given below [72];

1. Fast cooling gives rise to a martensite phase.
2. Due to partial re-melting of previous layers, the microstructure contains elongated grains of several hundred micrometres in length.
3. The direction of the elongated grains depends on the local heat transfer condition which is determined by the scanning strategy (and the part geometry).
4. Segregation of Al, due to rapid solidification, and the heating effect caused by the scanning of subsequent layers, led to the precipitation of an intermetallic Ti_3Al phase. This makes the melt pool boundaries visible on etching. The amount of precipitation increases if a lower scanning speed is applied.

Due to line and layer wise building principles, SLM of metals creates different type of microstructures depending on the building direction. Perpendicular to the building direction, very fine acicular martensite was found which is also known as α' phase with a hexagonally close packed structure [73]. Front and side views showed elongated grains with heights of several micrometers, which form because of epitaxial solidification and which are much longer than the layer thickness. As a consequence of the building strategy, the microstructure of SLM parts is reported to be affected by the heat flow direction. It has been found that the microstructure shows columnar grains of the primary β phase oriented according to the heat flow direction [47]. The material used for this experiment was Ti-6Al-7Nb alloy powder sintered using a continuous wavelength of Ytterbium fibre laser. H.P Qu *et al* described the SLM process as having an ultra-high temperature gradient in the melt pool which creates high heat conduction along the longitudinal direction. Fully lamellar grains of different grain size were observed and they also reported that the top surface, which is perpendicular to the building direction, experienced a higher solidification rate with finer microstructure as a result [74].

Besides the building direction, the microstructure of SLM parts is also dependant on the processing parameters. A comprehensive investigation was executed in order to look at the microstructural evolution of high laser energy density (LED) and diverse scanning speed [70]. In this study, it was found out that the phase transformation in SLM processed Ti powder changes from a β phase bcc crystal structure to an α phase hexagonal structure at scanning speeds equal to 100mms^{-1} and from β phase to martensite α’ at scanning speeds larger than 200mms^{-1}. Additionally, the authors found that at lower scanning speeds, when the energy density is relatively high leading to a higher SLM temperature, a complete transformation of β to α phase occurs on solidification.

The solidification rate of the liquid front within the melt pool increases with low energy density. This enhances both thermal and kinetic undercooling leading to a formation of very fine acicular martensitic α’ phase in the final solidified Ti parts. This is in agreement with the work of other researchers who carried out a post laser sintering heat treatment to modify the microstructure [75]. It was suggested that slow cooling rates result in the formation of more alpha with a lamellae microstructure and that fast cooling rates, from water quenching, result in a martensitic transformation.

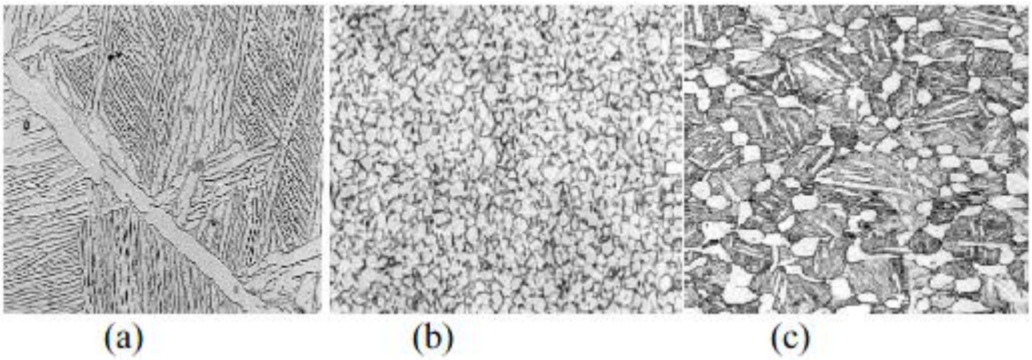

Figure 1.13: Microstructure of Ti6Al4V (a) lamellar structure (b) equi-axed structure (c) bimodal structure [75]

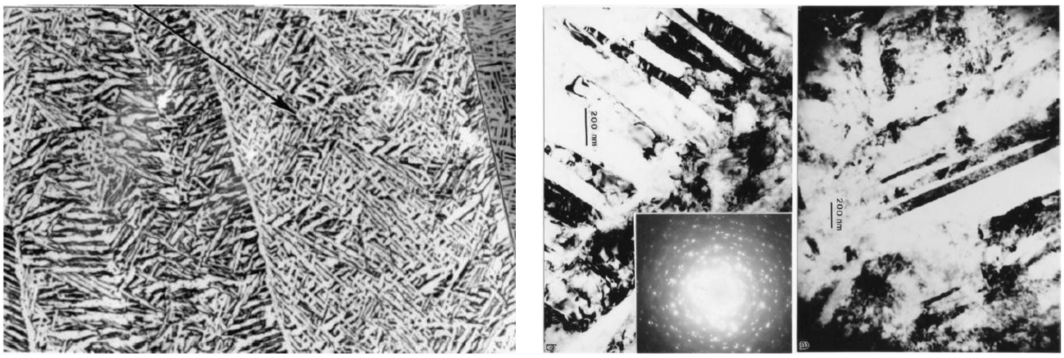

Figure 1.14: Ti 6Al 4V Optical & TEM images of material made by additive manufacturing [76]

Ben Vrancken *et al* described the SLM process as a quick interaction between laser and powder involving high energy input which leads to steep thermal gradients, rapid solidification and fast cooling [77]. They elucidated the influence of designated heat treatments on as built SLM parts. They reported that the original martensitic α’ phase found in as built SLM parts was converted to an α + β lamellar microstructure, while maintaining the original grain structure when heat treated at temperatures below the β transus temperature. When heat treated above the β transus temperature, extensive grain growth occurred and large β grains were formed which transformed to lamellar α+β upon cooling.

1.2.2.3 Mechanical properties

Microstructural homogeneity plays a crucial role in achieving good and consistent mechanical properties. One of the commonly encountered problems in laser sintering is the variation of grain size along the building direction. Research efforts have demonstrated the potential from laser sintering to achieve microstructures and mechanical properties equivalent or superior to those obtained in bulk material after a post-processing treatment [76-78]. Table 1.1 gives an overview of the results from mechanical testing. The mechanical properties of DMLS specimens are compared with those for bulk materials obtained from the literature.

As built specimens show slightly lower density and hardness compared with solution treated and annealed samples. They have the highest tensile yield strength, tensile strength and the lowest elongation to fracture. The tensile properties of as built Ti 6Al 4V satisfied the ISO 5832-3 standard requirements (TS >780MPa, UTS >860MPa) but the elongation to fracture was below the limit accepted by the standards (>10%). The microhardness of as built specimens is 320HV [79]. The mechanical properties of laser sintered parts also depend on the binding mechanism as a weak type of binding exhibits lower levels of mechanical properties [35].

	As built	Hipped	STA	Annealed
Density (kg/m^3)	4319	-	4430	4430
Hardness (HV)	320	312	395	350
Young's Modulus (GPa)	117	117	110	110
Tensile Yield Strength (MPa)	970	795	920	920
Ultimate Tensile Strength (MPa)	1122	870	1000	1000
Elongation at Rupture (%)	4	-	10	12

Table 1.1:Mechanical Properties of Ti6Al4V parts,*[42]*, [80]

1.2.3 Variables affecting DMLS parts

Processing parameters in DMLS can be defined by an array of machine parameters including laser power, scan speed, scan spacing, layer thickness, building conditions and material based input parameters. These parameters have a large influence on the process and are essential for determining the integrity of the as built parts. However, this process-material relationship is not always clear and requires a more scientific understanding. In order to do this, many researchers have started to reduce DMLS to its bare bones where the principal mechanisms i.e single strike, single track and single layer formation have been analysed [81, 82]. This is because the foundation for building a 3D part in layer manufacturing relies on the stability of its single tracks and its layer formation. Selecting a suitable processing window is of prime importance in DMLS so that fully dense parts can be manufactured.

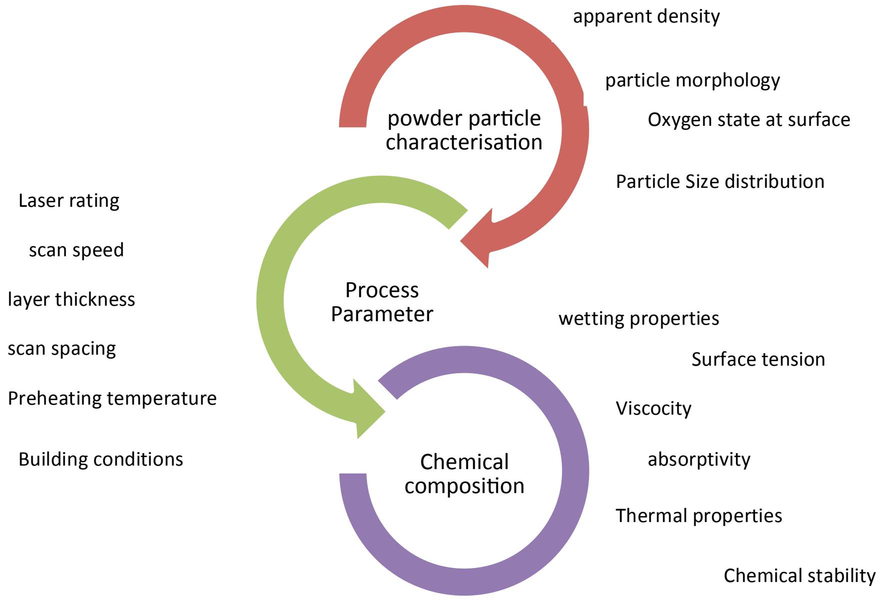

Figure 1.15: Factors affecting DMLS

Published work has indicated the crucial factors affecting the quality of DMLS parts [83]. Most of these factors do not require further research as they have nearly the same effect in all sintering processes, regardless of the material, the deposition technique or software used. However, some variables are dependent on material and processing parameters and in these cases little or no previous research exits. Some of these variables may have a great influence on a part's density and be important in controlling the final microstructure and some may have a minimal effect. Below shows the important variables which could have an effect on the final parts.

1.2.3.1 Machine variables

There is general agreement among researchers that in DMLS there are four crucial parameters that may control the final microstructure thus the part properties [52, 84]. These are laser power, scanning velocity, scan spacing and layer thickness. These are the principal parameters that are of prime importance in influencing the final parts made by DMLS. The specific energy input of the machine profoundly affects the densification process and this derives from these four crucial parameters. Simchi and Pohl reported that the laser energy input has a linear relationship with the part density [52]. This means that an increase in laser power, decreasing laser speed, a reduction in the layer thickness and an increase in the degree of overlapping between tracks all contribute to higher density parts. This can be explained by the densification equation below, which links part density to the specific energy input[52]:

$$\rho = C_1 - C_2 \exp(-K\varphi) \qquad (9)$$

where ρ is the sintered density, φ is the specific energy input (kJmm^{-3}) and C_1, C_2 and K are constants. The specific energy input is given by the relationship:

$$\varphi = \frac{P}{v\,d\,h} \qquad (9.1)$$

Where P is the input power, v is the scan speed, d is the beam diameter, h is the scan spacing

Yadroitsev *et al* concluded that the SLM process has its own optimum processing window where successful parts can be built through an analysis of the molten pool stability due to differences in scan speed [49]. The range of optimum scanning speeds is larger for higher laser power[81]. In this work a brief reference to the optimal processing parameters used to build good Ti64 parts using the continuous laser mode was published as follows: 42W laser power, 200mms^{-1} scanning speed with a scan spacing of 75µm and a 30µm layer thickness. As for iron powder, Simchi and Pohl reported that there is an upper limit to the laser power at which a sound 3D iron part can be produced. If excessive energy input is used, the residual stresses would be significant, causing delamination or weak inter-layer bonding. Rombouts *et al* added that at high scan speed, insufficient overlap between neighbouring scan tracks formed porous zones positioned along the building direction [44].

1.2.3.2 Powder properties

Powder size and morphology have an effect on powder layering, packing density and flowability. The smallest particles can fill small voids between larger particles and thus increase the packing density [43, 85]. It is known that finer particles provide a larger surface area thereby absorbing more laser energy. Greater absorption of laser energy leads to higher temperatures and better sintering kinetics. In DMSL, greater packing density is of prime importance in order to have good layer adhesion and therefore lower porosity parts [86]. It has been reported that a lower mean particle size produces parts with better surface as well as a shorter melting time [43, 87]. Therefore, every batch of new powder is sieved at a specific value in order to have a range of small powder particles during the process.

Previous studies have shown that higher oxygen content is an impediment to the formation of a continuous molten pool[88]. This is known as a balling effect. Powder with a high oxygen content and when exposed to a high energy density has a larger temperature gradient and surface tension gradient causing a single line to break up into spherical droplets. Besides that, too high a laser scan speed or excessive laser power can caused the same problem[89].

A study on different types of Ti64 powder particles used for DMLS was done by B Engel *et al* [43, 88]. They reported that once the powder has been exposed to the atmosphere, water vapour or moisture is the variable of concern as it can easily become attached to the powder. The presence of hydrogen gas was also reported and this has only a slight effect and it is not problematic at all. The study highlighted the need for a degassing process as a pre-processing procedure prior to the removal of water vapour or moisture.

1.2.3.3 Sintering Atmosphere

Any sintering of metal powder, particularly reactive metals such as titanium, must be processed under an inert atmosphere[90]. For atmosphere sintering, the building environment is the composition of the atmosphere itself during the DMLS process. In order to provide an inert atmosphere, nitrogen or argon gas is flushed continuously during fabrication under a vacuum. The use of nitrogen as a protective gas has been shown to give slightly lower density compared with argon, but is cheaper to use. However, in an experiment comparing nitrogen and argon atmospheres, the recorded difference in density is less than 1% of theoretical density [76]. Besides an inert atmosphere, another variable that may have a significant influence is the oxygen content of the atmosphere, particularly in the sintering of a reactive powder such as titanium[44]. However there is a lack of information in this area. During the sintering time, the oxygen content in many commercial machines is controlled to be less than 0.04%.

it’s The final microstructure[91] of a laser sintering part also can be influenced by the building chamber temperature . During sintering this can be explained by associating the high working temperature and rapid cooling with high thermal stresses during a sintering/melting process. Cooling of a section or a layer directly after sintering is impractical. Therefore controlling the whole building chamber may perhaps reduce high thermal stresses. Without proper control, a part may have problems such as cracking or bad warpage and shrinkage. A study in which a building temperature of 230°C was used for sintering Ti64 alloy powder was reported to have been successful in reducing thermal stresses in a part and eliminates the need for a post heat treatment. However, increasing the building chamber temperature may be detrimental to the lifetime of the base plate and other associated machine components [92].

1.2.3.4 Powder Deposition

The deposition of the powder is controlled by the re-coater and the gap between the re-coater and the base plate. In the case of titanium powder, the layer thickness is set at 30µm which means that after every scan the base plate lowers by this specific amount. Ensuring the right gap between the re-coater and the base plate is one of the hardest tasks since it requires manual observations and good judgement. On top of that, the powder needs to be evenly distributed on the platform to make sure the final part has good relative density[85].

The layer thickness as mentioned before has an important effect on the densification of the powder. The layer thickness, or the height of the deposited powder, determines the energy per mm^3 and it therefore controls the degree of powder densification. From practical observation, the first five layers are crucial before the process reaches stability and builds a part. The manual levelling of the base plate has been noted to be a problem in at least one article [51]. It seems to be very difficult to ensure a completely flat surface. A gauge clock is normally used to do the levelling and this is sometimes time consuming. It also has been observed that the re-coater sometime vibrates during its motion across the powder bed. A good re-coater provides smooth movement and levels the powder evenly.

1.3 DMLS in the Medical Industry

1.3.1 Introduction

In this chapter, the current developments of biomedical implants particularly craniofacial implants made from titanium powders and fabricated via laser sintering are reviewed. This section is divided into two main categories; the fabrication procedures and the design capabilities. In the first section a brief background on the application of rapid prototyping technologies in the medical field is explained. Later, the fabrication procedure for a customised implant and the innovative design capabilities of DMLS are described. There are a few methods which can be used to produce craniofacial implants. Previously, one of the preferred methods used by cranio-maxillofacial surgeons was the use of titanium mesh (perforated) plate or the preformed implants [93]. The mesh plate is normally used to reconstruct the bones at the frontal area and the latter (preformed) for the mandibular. From using the aforementioned method, various problems were identified, mainly because of the difficulties to conform to the unique shapes of the human bones. Thus, it consumes longer surgery time and is highly exposed to human errors as the surgeons are required to bend and form the plate manually to fit the defective area[94]. Due to these limitations and difficulties, only a few straight forward cases can be attained by the surgeons and others which have greater complexity were left unsolved.

1.3.2 RP as a tool for Surgical Planning

In late 1980's, a new approach was embraced by surgeons where advanced computer imaging and cutting-edge manufacturing equipment were brought together [95]. This sophisticated computer imaging not only provided greater improvement on the computer tomography (CT) scan data by offering 3D visualisation but also made it handy to process and translates into different CAD platforms or analysis software tools. With the aid of this 3D visualisation and simulation, the correct and necessary information pertaining to the defects are at the surgeon's fingertips and this can be retrieved digitally for quantitative analysis. Therefore, evaluation and surgical planning no longer require an in-situ procedure but can be more comfortably performed outside of the operating theatre.

Rapid prototyping (RP) on the other hand has evolved enormously. Many complex parts, mainly made from polymers, are manufactured successfully with great detail and accuracy and with no tooling required [96]. With these attributes, RP is used to replicate human bones by directly processing the CT scan data of a patient. The model is made from photosensitive resin and is known as a stereolithography (SL) model. This replica model of a patient is really important for a high risk case where great understanding and information are required for precise planning. A simulation of a real operation can be done using this model to increase confidence and skills [97].

Recently, the integration of computer imaging and RP technology are potentially promising in this new area. Medical imaging is manipulated to not only give a better visualisation aid for surgeons but extends to the possibility of simulation to carry out virtual surgery. This not only increases surgeons' confidence but also increases the quality and the accuracy of the surgical outputs. On top of this the surgical time is also significantly reduced, as the time consuming in-situ planning procedure is eliminated [98]. There are many manufacturing methods and processes used for producing implant devices from titanium material [93].

	Investment casting	**Forging**	**Machining**	**EBM**
Microstructure	Coarse acicular α+β, thick prior beta grain	Dependent on processing parameters.	Dependent on process parameters. No beta grain boundaries.	Fine acicular α+β, thin prior beta grain boundaries. Slightly elongated prior beta
Strength	Adequate strength	Typically higher strength	High strength	Moderate high strength
Tooling	Initial high	Initial high	Initial	No Cost – no

requirements	cost	cost – long lead times	moderate cost-moderate lead times	lead time-minimal programming
Process intensity and lead Time	Multiple operation-very labor intense	Moderate operation-fast production	Moderate process time-minimal labor	Moderate process time-minimal labor
Product surface finish-for further processing	Fine orange peel finish-gate removal grind	Fine smooth finish-flash parting-line remowal grind	Moderate machine finish-deburr grind removal	Course ripple finish-fixture support removal
Porous coating application	Added processing Time-retain adequate strength	Added processing time-lose high strength-some coatings	Added processing time-lose high strength-some coatings	No added processing time- retain adequate strength

Table 1.2: comparison of near net shape manufacturing for implant devices[14]

With digital fabrication, the process has received more attention and confidence from other industries. This method uses advanced manufacturing techniques such as direct metal fabrication to build customised implants made from stainless steel or hard to process materials such as titanium. With this approach, the implant could be tailored physically to suit complex human anatomy and mechanically prior to strength [99]. Solid freeform fabrication techniques such as DMLS offer fast implant fabrication without using any tooling or moulds. Medical data captured from a CT scan machine is easily transferred to commercial 3D biomedical software in order to build a 3D digital data on the computer screen. This 3D digital data is directly processed from a CT scan gives better visualisation of the defects and more flexibility in converting from 2D to 3D and vice versa when it is necessary to do so. In a complex case which requires more information about the defects, one can fabricate a patient’s skull and use it for detailed planning. Trials on a patient’s replica can be done and a new implant could be well justified before the real operation take place. This has led to improvements in medical services particularly in the area of 3D visualisation of a specific anatomy, surgical planning, implant design and manufacturing [95].

Apparently, RP techniques allow the manufacture of accurate anatomical models from CT scans [16]. However, the implant is traditionally designed by marking up a physical bio-model. Subsequently, the model is reverse engineered to transfer the design of the implant to a software environment and cast with a mold. This route consists of CT scan conversion, rapid prototyping (RP), 3D CAD and biomodelling, rapid manufacturing (RM), reverse engineering (RE) and finite element analysis.

1.3.3 Designing implant via DMLS

It is well known that titanium is an attractive material for biomedical application due to its high strength, lightweight and high corrosion resistance. Oxygen easily adheres to the surface of a bulk titanium material forming a thin layer of TiO_2 which characterise its biocompatibility features[100]. Some examples of biomedical applications are craniofacial implants i.e frontal and mandibular tray, hip stems, joints and osteosynthesis material such as screws and plates. Manufacturing of these implants is known to be an expensive and labour-intensive process let alone the fabrication of customised devices. On top of that, any implants need to meet stringent requirements for safety purposes and avoiding surgical intervention. The implanted material should be strong and durable enough to withstand the physiological loads over many years [101].

One of the critical features of a good implant is that it has to have a suitable balance between strength and stiffness so that it best matches the behaviour of bone[102]. Human bones consist of cortical and cancellous bone with a Young’s modulus of 10-20GPa while the metallic implant is reported to have a Young’s modulus of about 110-200GPa [103]. Due to this mechanical mismatch, bone becomes insufficiently loaded and becomes stress shielded. This is a major concern in the fabrication of metallic implants where a new design approach which uses a foam or porous structure is introduced. Therefore, a standard manufacturing technique no longer suits the fabrication of this new innovative implant concept, a more efficient and flexible manufacturing approach is required where the highest degree of geometry complexity can be fabricated.

For the last 20 years different methods for producing porous titanium and titanium alloy implants have become available including the CAD/CAM procedure, sintering of particles or plasma spraying of the powder onto implant surfaces [104, 105]. However none of these conventional techniques is capable of producing a completely controlled geometry and complex external morphology in one step. Furthermore, in cases requiring a re-creation of complex anatomy models and implants, the process could involve many steps, which prolongs the fabrication time. To save time, an optimum manufacturing process needs to be used where steps, inaccuracy and errors can be minimized.

Bone is typically a complex structure consisting of an inner spongy cancellous bone and an outer dense cortical bone with an elastic modulus of 0.5GPa and 20GPa respectively [106]. The anistropic nature of bone adds more complexity to this variable. The outer dense cortical bone has a density in the region of 1.990 gcm^{-3}. Implants are normally made of stainless steel, titanium and cobalt chrome which are heavier than bone. As an example the most popular biocompatible material is titanium, with good strength to weight ratio, high resistance to corrosion and has a density of $4.43gcm^{-3}$ which is twice the density of bone [93]. This effect which is known as 'stress shielding' due to a difference in stiffness of the implant material and bone, causes bone loosening and it affects the implant's lifetime [107].

Direct metal laser sintering is a rapid prototyping technology employing layer by layer manufacturing using a highly focused laser beam by which it is possible to directly generate 3D objects with defined structure and shape. In addition, it allows the use of titanium and its alloys as starting powders that are completely fused under a laser irradiation resulting in comparable mechanical strength when compared with other manufacturing means [14]. This technique also allows fabrication of a very thin layer (0.02mm0.06mm) thus permitting unmachinable and unmold-able geometries to be created. The manufacturing advances of this technique provide a good platform for producing innovative implant designs such as functionally graded structural implants. Implants with controlled gradient porosity along a desired axis introduce difference material density and therefore variable stiffness. This new design approach has the potential to have the same bone tissue stiffness at the implant-bone interface. Many authors have identified that new designs should have the characteristics given below: [42, 108];

1. A 3D highly porous and interconnected pore network, enabling cells to enter, attach and migrate through the structure
2. Biocompatible materials
3. A suitable surface structure and chemistry for cell attachment, proliferation and differentiation
4. Mechanical properties to match those of the tissue of site implantation
5. Easy to make into a variety of shapes and sizes with a controlled internal structure

According to Ashby, the Young's modulus of the porous material depend strongly on the relative density of the porous material [93]

$$\frac{E^p}{E^s} = C\left(\frac{p^p}{p^s}\right)^2 \tag{10}$$

Where E^p is the Young's modulus of the porous material, E^s is the Young's modulus of the dense material. P_p/P_s the relative density and C a constant.

Varying mechanical properties in different regions of a single implant are paramount especially for load bearing capability, especially important in mandible implants [109]. This could be done by applying different density in different regions or by effectively reducing weight without compromising its functionality. For example, for load bearing implants, at the joint or at the fixation region it would be a requirement to have a dense region while the body of an implant could be made to be more porous. Many academic articles suggested that a cellular structure is the path to explore where reduction of weight could be optimized[109]. Voids generated in the design of the internal structure can effectively reduce the weight of the implant with a sufficient trade-off in strength [106, 110].

Cellular structures can be classified into two types based on their void arrangement. Periodic cellular structures have repeating interconnected unit cells in all three directions (x, y, z) with cell dimensions ranging from tens of micrometers to tens of millimetres. Sandwich, honeycomb and truss structures are some examples of these periodic type cellular structures. On the other hand, random void arrangements are known as stochastic cellular structures. A stochastic type of structure showed lower mechanical properties compared to periodic structures. Generally, cellular structures have good energy absorption, thermal and acoustic insulation properties. Their mechanical properties are dependent on the shape and size of the struts forming cell walls and pores [111].

The hypothesis to be tested in this research work is that an optimized set of processing parameters can be developed, which enables the manufacturing of both fully dense and porous titanium alloy parts with complex internal structures. In particular, the aim of the research is to develop, demonstrate and characterize the techniques for designing and fabricating such porous structures utilizing a reactive material, in this case Ti6Al4V titanium alloy powder, through a direct metal laser sintering method. When fully developed, it is expected that this manufacturing route will enable the fabrication of customised porous implants with an intended microstructure and mechanical properties which suits the intended biomedical applications. This work also evaluates the current 3D medical imaging processing technique with the aim of developing a patient specific implant through the laser sintering process.

References

1. Yusuf, S.O.O.a.Y.Y., *RP Technology: Applications and benefits for rapid product development.* Journal of Intelligent Manufacturing, 1999. **10**: p. 11.
2. Smith, P.G., *The Business of Rapid Prototyping.* Rapid Prototyping Journal, 1999. **5**(4): p. 7.
3. Levy, G.N., R. Schindel, and J.P. Kruth, *Rapid Manufacturing and Rapid Tooling with Layer Manufacturing (Lm) Technologies, State of the Art and Future Perspectives.* CIRP Annals - Manufacturing Technology, 2003. **52**(2): p. 589-609.
4. P.Dickens, N.H., *Rapid Prototyping for Direct Manufacture.* Rapid Prototyping Journal, 2001. **4**(7): p. 6.
5. Wohlers, T., *Direct Digital Manufacturing*, in *Manufacturing Engineering*2009. p. 8.
6. Kochan, A., *Rapid prototyping gains speed, volume and precision.* Rapid Prototyping Journal, 2000. **20**(4): p. 5.
7. Munguía, J., J.d. Ciurana, and C. Riba, *Pursuing successful rapid manufacturing: a users' best-practices approach.* Rapid Prototyping Journal, 2008. **14**(3): p. 173-179.
8. Violante, M.G., L. Iuliano, and P. Minetola, *Design and production of fixtures for free-form components using selective laser sintering.* Rapid Prototyping Journal, 2007. **13**(1): p. 30-37.
9. Mognol, P., et al., *A first approach to choose between HSM, EDM and DMLS processes in hybrid rapid tooling.* Rapid Prototyping Journal, 2007. **13**(1): p. 7-16.
10. Morey, B., *Building Parts Directly*, in *Manufacturing Engineering*2008.
11. Sebastian Storch, D.N., Guenther Schaefer and Rolf Reiter, *SLS qualifying analysis of metal based powder systems for automotive application.* Rapid Prototyping Journal, 2003. **9**(4): p. 12.
12. Akova, T., et al., *Comparison of the bond strength of laser-sintered and cast base metal dental alloys to porcelain.* Dent Mater, 2008. **24**(10): p. 1400-4.
13. Bandyopadhyay, B.V.K.W.X.S.B.A., *Engineered Porous Metals for Implants.* Journal of Manufacturing, 2008. **60**(5): p. 4.
14. Andy Christensen, A.L., Ryan Kircher, *QUALIFICATION OF ELECTRON BEAM MELTED (EBM) Ti6Al4V-ELI FOR ORTHOPAEDIC IMPLANT APPLICATIONS.* p. 8.
15. Alida Mazzoli, M.G., Roberto Raffaeli, *Direct fabrication through electron beam melting technology of custom cranial implants designed in a PHANToM-based haptic environment.* Materials and Design, 2009. **30**: p. 7.
16. Oh, Y.T. and G.D. Kim, *A benchmark study on rapid prototyping processes and machines: quantitative comparisons of mechanical properties, accuracy, roughness, speed, and material cost.* Proceedings of the Institution of Mechanical Engineers, Part B: Journal of Engineering Manufacture, 2008. **222**(2): p. 201-215.

17. Prashant K. Jain, K.S., Pulak M. Pandey, P. V. M. Rao. *ADVANCES IN MATERIALS FOR POWDER BASED RAPID PROTOTYPING*. in *Advances in Materials and Processing*. 2006. Coimbatore, India.
18. Dickens, N.H.a.P., *rapid prototyping for direct manufacture.* Rapid Prototyping Journal, 2001. **7**(4): p. 6.
19. Shellabear, M., *Direct Metal Laser-Sintering of Titanium.* ProQuest Science Journals, 2008. **32**(5): p. 42.
20. Dalgarno, K.W. and R.D. Goodridge, *Compression testing of layer manufactured metal parts: the RAPTIA compression benchmark.* Rapid Prototyping Journal, 2004. **10**(4): p. 261-264.
21. Gu*, X.Y.a.P., *A review of rapid prototyping technologies and systems.* Computer Aided Design, 1996. **28**(4): p. 307-318.
22. A. Lamikiz, J.A.S.n., L.N. Lo´ pez de Lacalle, J.L. Arana, *Laser polishing of parts built up by selective laser sintering.* International Journal of Machine Tools & Manufacture, 2007. **47**: p. 11.
23. Hague, R. and M. Ruffo, *Cost estimation for rapid manufacturing — simultaneous production of mixed components using laser sintering.* Proceedings of the Institution of Mechanical Engineers, Part B: Journal of Engineering Manufacture, 2007. **221**(11): p. 1585-1591.
24. Parthasarathy, J., et al., *Mechanical evaluation of porous titanium (Ti6Al4V) structures with electron beam melting (EBM).* J Mech Behav Biomed Mater, 2010. **3**(3): p. 249-59.
25. Li, X., et al., *Fabrication and characterization of porous Ti6Al4V parts for biomedical applications using electron beam melting process.* Materials Letters, 2009. **63**(3-4): p. 403-405.
26. L.E Weiss, R.M., F.B.Prinz, G. Neplotnik, P.Padmanabhan, K.Ramaswami, *Shape Deposition Manufacturing of Heterogeneous Structures.* Manufacturing Systems, 1997. **16**(4): p. 10.
27. Costa, L. and R. Vilar, *Laser powder deposition.* Rapid Prototyping Journal, 2009. **15**(4): p. 264-279.
28. J.-P. Kruth, G.L., F. Klocke, T.H.C. Child, *Consolidation phenomena in laser and powder-bed based layered manufacturing.* CIRP Annals - Manufacturing Technology, 2007. **56**(2): p. 30.
29. Mukesh Agarwala, D.B., Joseph Beaman, Harris Marcus and Joe Barlow, *Direct Selective Laser Sintering of Metals.* Rapid Prototyping Journal, 1995. **1**(1): p. 11.
30. Kang, S.-J.L., *Sintering: Densification; grain growth and microsturcture*. Vol. 1. 2005: Elsevier.
31. Atsuko Shimosaka, Y.U., Yoshiyuki Shirawa, Jusuke Hidaka, *Sintering Mechanism of two spheres forming a Homogenous Solid Solubility Neck.* KONA, 2003. **21**(2003): p. 15.
32. German, R.M., *Sintering theory and Practice*, 1996, John Wiley and Sons.
33. Tolochko, N., et al., *Selective laser sintering of single- and two-component metal powders.* Rapid Prototyping Journal, 2003. **9**(2): p. 68-78.
34. Randall M German, P.S.a.S.J.P., *Review: Liquid Phase Sintering.* Journal of Materials Science, 2009. **44**: p. 39.
35. Kruth, J.P., et al., *Binding mechanisms in selective laser sintering and selective laser melting.* Rapid Prototyping Journal, 2005. **11**(1): p. 26-36.

36. Yang, J., H. Ouyang, and Y. Wang, *Direct metal laser fabrication: machine development and experimental work.* The International Journal of Advanced Manufacturing Technology, 2009. **46**(9-12): p. 1133-1143.
37. Fischer, P., et al., *Sintering of commercially pure titanium powder with a Nd:YAG laser source.* Acta Materialia, 2003. **51**(6): p. 1651-1662.
38. R. Morgan, C.J.S.a.W.O.N., *experimental investigation of NdYAG laser.* Rapid Prototyping Journal, 2001. **7**(3): p. 14.
39. Tolochko, N.K., et al., *Selective laser sintering and cladding of single-component metal powders.* Rapid Prototyping Journal, 2004. **10**(2): p. 88-97.
40. Nikolay K. Tolochko, T.L., Maxim K. Arshinov, Andrey V.Gusarov, Victor I. Titov and Ludo Froyen, *Mechanism of selective laser sintering and heat transfer in Ti Powder.* Rapid Prototyping Journal, 2003. **9**(5): p. 13.
41. Dai, K. and L. Shaw, *Thermal and mechanical finite element modeling of laser forming from metal and ceramic powders.* Acta Materialia, 2004. **52**(1): p. 69-80.
42. Vandenbroucke, B. and J.-P. Kruth, *Selective laser melting of biocompatible metals for rapid manufacturing of medical parts.* Rapid Prototyping Journal, 2007. **13**(4): p. 196-203.
43. Bourell, B.E.a.D.L., *ti alloy powder preparation.* Rapid Prototyping Journal, 2000. **6**(2): p. 10.
44. Rombouts, M., et al., *Fundamentals of Selective Laser Melting of alloyed steel powders.* CIRP Annals - Manufacturing Technology, 2006. **55**(1): p. 187-192.
45. N.K Tolochko, S.E.M., N.V Sobolenko, Yu V. Khlopkov, I.A Yadroitsev and V.B Mikhailov, *Main relationships Governing Laser sintering.* Journal of Advanced Materials, 1995. **2**(2): p. 151-157.
46. Das, S., *Physical aspect of process control in SLS.* Advanced Engineering Materials, 2003. **5**(10): p. 11.
47. Chlebus, E., et al., *Microstructure and mechanical behaviour of Ti—6Al—7Nb alloy produced by selective laser melting.* Materials Characterization, 2011. **62**(5): p. 488-495.
48. Mercelis, P. and J.-P. Kruth, *Residual stresses in selective laser sintering and selective laser melting.* Rapid Prototyping Journal, 2006. **12**(5): p. 254-265.
49. Yadroitsev, I. and I. Smurov, *Selective laser melting technology: From the single laser melted track stability to 3D parts of complex shape.* Physics Procedia, 2010. **5**: p. 551-560.
50. Olakanmi, E.O., R.F. Cochrane, and K.W. Dalgarno, *Densification mechanism and microstructural evolution in selective laser sintering of Al–12Si powders.* Journal of Materials Processing Technology, 2011. **211**(1): p. 113-121.
51. M.W Khaing, J.Y.H.F., L.Lu, *Direct Metal laser sintering for rapid tooling: processing and characterisation of EOS parts.* Materials and Processing Technology, 2001. **113**: p. 4.
52. Simchi, A. and H. Pohl, *Effects of laser sintering processing parameters on the microstructure and densification of iron powder.* Materials Science and Engineering: A, 2003. **359**(1-2): p. 119-128.

53. Simchi, A., *Direct laser sintering of metal powders: Mechanism, kinetics and microstructural features.* Materials Science and Engineering: A, 2006. **428**(1-2): p. 148-158.
54. Wen-Shu Jiaung, J.-R.H.C., *Lattice Boltzmann Method for the Heat Conduction Problem with Phase Change.* Numerical Heat Transfer, Part B: Fundamentals, 2001. **39**(2): p. 167-187.
55. Adrian Bejan, A.D.K., *Heat Transfer Handbook*, 2003, John Wiley & Sons, Inc.
56. Rosenthal, D., *The theory of Moving Source of heat and its applications to metal transfer.* Trans. ASME, 1946. **43**(11).
57. Darmadi, D.N., J.Tieu, A.Kiet, *Analytic and finite element solutions for temperature profile in welding using varied heat source model.* World Academy of Science, Engineering and Technology, 2011. **81**: p. 154-162.
58. Argyropoulos, H.H.a.S.A., *Mathematical modelling of solidification and melting: a review.* Modelling Simulation Materials Science Engineering, 1996. **4**.
59. Zhang, T.C.a.Y., *THERMAL MODELING OF METAL POWDER-BASED SELECTIVE LASER SINTERING.* 2005.
60. Z.H. Shen, S.Y.Z., J. Lu, X.W. Ni, *Mathematical modeling of laser induced heating and melting is Solids>.* Optics & Laser Technology, 2001. **33**(2001): p. 533-537.
61. Xiao, B. and Y. Zhang, *Analysis of melting of alloy powder bed with constant heat flux.* International Journal of Heat and Mass Transfer, 2007. **50**(11-12): p. 2161-2169.
62. Das, H.C.a.S. *Scaling Laws for Melting and Resolidification in Direct Selective Laser Sintering of Metals*. in *Solid Freeform Fabrication Symposium Proceedings*. 2001. The University of Texas, Austin.
63. A.V. Gusarov , T.L., L. Froyen , V.I. Titov *Contact thermal conductivity of a powder bed in selective laser sintering.* International Journal of Heat and Mass Transfer, 2003. **46**: p. 7.
64. Childs, T.H.C., C. Hauser, and M. Badrossamay, *Mapping and Modelling Single Scan Track Formation in Direct Metal Selective Laser Melting.* CIRP Annals - Manufacturing Technology, 2004. **53**(1): p. 191-194.
65. Song, Y.-A. and W. Koenig, *Experimental Study of the Basic Process Mechanism for Direct Selective Laser Sintering of Low-Melting Metallic Powder.* CIRP Annals - Manufacturing Technology, 1997. **46**(1): p. 127-130.
66. Yuwen Zhang , A.F., C. W. Buckley, T. L. Bergman, *Three-Dimensional Sintering of Two-Component Metal Powders With Stationary and Moving Laser Beams.* Journal of Heat Transfer, 2000. **122**: p. 9.
67. Zhang, D.Q., et al., *Select laser melting of W–Ni–Fe powders: simulation and experimental study.* The International Journal of Advanced Manufacturing Technology, 2010. **51**(5-8): p. 649-658.
68. Verhaeghe, F., et al., *A pragmatic model for selective laser melting with evaporation.* Acta Materialia, 2009. **57**(20): p. 6006-6012.
69. Pedersen, R., *Microstructure and Phase Transformation of Ti6Al4V*, in *Department of Applied Physics and Mechanical Engineering, Division of Engineering Materials*2002, Lulea University of Technology.

70. Gu, D., et al., *Densification behavior, microstructure evolution, and wear performance of selective laser melting processed commercially pure titanium.* Acta Materialia, 2012. **60**(9): p. 3849-3860.
71. Kąc, S. and J. Kusiński, *SEM and TEM microstructural investigation of high-speed tool steel after laser melting.* Materials Chemistry and Physics, 2003. **81**(2-3): p. 510-512.
72. Thijs, L., et al., *A study of the microstructural evolution during selective laser melting of Ti–6Al–4V.* Acta Materialia, 2010. **58**(9): p. 3303-3312.
73. J.-P. Kruth, M.B., E.Yasa, J. Deckers, L. Thijs, J. Van Humbeeck, *Part and material properties in selective laser melting of metals.* 16th International Symposium on Electromachining (ISEM XVI): p. 12.
74. Qu, H.P., Wang, H. M., *Microstructure and mechanical properties of laser melting deposited γ-TiAl intermetallic alloys.* Materials Science and Engineering: A, 2007. **466**(1-2): p. 187-194.
75. M E Ramosoeu, H.K.C., A S Bolokang, G Booysen and T N Ngonda, *ADDITIVE MANUFACTURING: CHARACTERIZATION OF TI-6AI-4V ALLOY INTENDED FOR BIOMEDICAL APPLICATION.* Light Metals Conference 2010, 2010: p. 8.
76. Murr, L.E., et al., *Microstructure and mechanical behavior of Ti-6Al-4V produced by rapid-layer manufacturing, for biomedical applications.* J Mech Behav Biomed Mater, 2009. **2**(1): p. 20-32.
77. Vrancken, B., Thijs, Lore,Kruth, Jean-Pierre,Van Humbeeck, Jan, *Heat treatment of Ti6Al4V produced by Selective Laser Melting: Microstructure and Mechanical properties*, in *Journal of Alloys and Compounds*2012.
78. Bellini, A. and S. Güçeri, *Mechanical characterization of parts fabricated using fused deposition modeling.* Rapid Prototyping Journal, 2003. **9**(4): p. 252-264.
79. AbdAziz, I., *Microstructure and Mechanical Properties of Titanium Alloy powder produced by Direct Metal Laser Sintering*, in *School of Science and Engineering*2010, Waikato University: New Zealand.
80. Luca Facchini, E.M., P Robotti, A Molinari, *Microstructure and Mechanical Properties of Ti6Al4V produced by Electron Beam melting of pre-alloy powder.* Rapid Prototyping Journal, 2009. **15**(3): p. 8.
81. Yadroitsev, I., et al., *Factor Analysis of Selective laser melting process parameters and geometrical characteristics of Synthesized single tracks.* Rapid Prototyping Journal, 2012. **18**(3): p. 9.
82. M. Matsumoto, M.S., K. Osakada, F. Abe, *Finite element analysis of single layer forming on metallic powder bed in rapid prototyping by selective laser processing.* International Journal of Machine Tools & Manufacture, 2002. **42**: p. 61-67.
83. Klingbeil, J.B.a.N., *The Role of Process Variables in Laser-Based Direct Metal Solid Freeform Fabrication.* Journal of Manufacturing, 2001.
84. Ruidi Li, Y.S., Jinhui Liu, Huashan Yao, and Wenxian Zhang, *EFFECTS OF PROCESSING PARAMETERS ON THE TEMPERATURE FIELD OF SELECTIVE LASER MELTING METAL POWDER.* Powder Metallurgy and Metal Ceramics,, 2009. **48**(3-4(466)): p. 10.
85. Marcu, T., et al., *Effect of surface conditioning on the flowability of Ti6Al7Nb powder for selective laser melting applications.* Applied Surface Science, 2012. **258**(7): p. 3276-3282.

86. Simchi, A., F. Petzoldt, and H. Pohl, *On the development of direct metal laser sintering for rapid tooling.* Journal of Materials Processing Technology, 2003. **141**(3): p. 319-328.
87. Spierings, A.B., N. Herres, and G. Levy, *Influence of the particle size distribution on surface quality and mechanical properties in AM steel parts.* Rapid Prototyping Journal, 2011. **17**(3): p. 195-202.
88. Marleen Rombouts, J.-P.K., Ludo Froyen, *IMPACT OF PHYSICAL PHENOMENA DURING SELECTIVE LASER MELTING OF IRON POWDERS.* Fabrication, Materials, Processing, Properties TMS (The Minerals, Metals & Materials Society), 2009. **1**.
89. Tolochko, N.K., et al., *Balling processes during selective laser treatment of powders.* Rapid Prototyping Journal, 2004. **10**(2): p. 78-87.
90. B Ferrar, L.M., E. Jones, R. Stamp, CJ Sutcliffe, *Gas Flow Effects on Selective Laser melting (SLM) manufacturing performance.* Materials and Processing Technology, 2012. **212**: p. 11.
91. Zaeh, M.F. and M. Ott, *Investigations on heat regulation of additive manufacturing processes for metal structures.* CIRP Annals - Manufacturing Technology, 2011. **60**(1): p. 259-262.
92. Bertol, L.S., et al., *Medical design: Direct metal laser sintering of Ti–6Al–4V.* Materials & Design, 2010. **31**(8): p. 3982-3988.
93. Bram, M., et al., *Implant surgery: How bone bonds to PM titanium.* Metal Powder Report, 2006. **61**(2): p. 26-31.
94. Igor Drstvensek, N.I.H., Tadej Strojnik, Tomaz Brajlih, Bogdan Valentan,Vojko Pogacar, Tjasa Zupancis Hartner, *Applications of Rapid Prototyping in Cranio-Maxilofacial Surgery Procedures.* INTERNATIONAL JOURNAL OF BIOLOGY AND BIOMEDICAL ENGINEERING, 2008. **2**(1).
95. Leiggener, C., et al., *A selective laser sintering guide for transferring a virtual plan to real time surgery in composite mandibular reconstruction with free fibula osseous flaps.* Int J Oral Maxillofac Surg, 2009. **38**(2): p. 187-92.
96. Ibrahim, D., et al., *Dimensional error of selective laser sintering, three-dimensional printing and PolyJet models in the reproduction of mandibular anatomy.* J Craniomaxillofac Surg, 2009. **37**(3): p. 167-73.
97. Liu, Q., M.C. Leu, and S.M. Schmitt, *Rapid prototyping in dentistry: technology and application.* The International Journal of Advanced Manufacturing Technology, 2005. **29**(3-4): p. 317-335.
98. S. Lohfeld, P.M., D. Serban,D.Boyle, G. O'Donnell, N. Peckitt *Engineering Assisted SurgeryTM: A route for digital design and manufacturing of customised maxillofacial implants.* Journal of Materials Processing Technology, 2007. **183**(2007): p. 6.
99. M. Wehmoller, T., P.H. Warnke, C. Zilian, H. Eufinger, *Implant design and production—a new approach by selective laser melting.* International Congress Series, 2005. **1281**: p. 6.
100. Fox, P., et al., *Interface interactions between porous titanium/tantalum coatings, produced by Selective Laser Melting (SLM), on a cobalt–chromium alloy.* Surface and Coatings Technology, 2008. **202**(20): p. 5001-5007.

101. Ryan, G., A. Pandit, and D.P. Apatsidis, *Fabrication methods of porous metals for use in orthopaedic applications.* Biomaterials, 2006. **27**(13): p. 2651-70.

102. SJ Hollister, C.L., E Saito,CY Lin, RD Schek, JM Taboas, JM Williams, B Partee, CL Flanagan, A Diggs, EN Wilke, GH Van Lenthe, RMuller, T Wirtz ,S Das, SE Feinberg, PH Krebsbach, *Engineering craniofacial scaffolds.* Orthod Craniofacial Res, 2005. **8**: p. 162-173.

103. Niinomi, M., *Mechanical properties of biomedical titanium alloys.* Materials Science and Engineering, 1998. **A243**: p. 231-236.

104. Cronskar, M., *The use of Additive Manufacturing in the Custom Design of orthopaedic implants*, in *Technology and Sustainable Development*2011, Mid Sweden University: Sweden.

105. Sameer R. Paital, N.B.D., *Calcium phosphate coatings for bio-implant applications: Materials, performance factors, and methodologies.* Materials Science and Engineering R, 2009. **66**: p. 70.

106. Krishna, B.V., S. Bose, and A. Bandyopadhyay, *Low stiffness porous Ti structures for load-bearing implants.* Acta Biomater, 2007. **3**(6): p. 997-1006.

107. Pattanayak, D.K., et al., *Bioactive Ti metal analogous to human cancellous bone: Fabrication by selective laser melting and chemical treatments.* Acta Biomater, 2011. **7**(3): p. 1398-406.

108. Wailan D. Chan, M.H.P., DDS, PhD;, P.G.K.H. Harvey A. Goldberg, PhD; S. Jeffrey Dixon, DDS, PhD;, and D. Gildo C. Santos Jr., PhD; Amin S. Rizkalla, PhD, PEng, *Tissue Engineering Scaffolds for the Regeneration of Craniofacial Bone.* JCDA, 2009. **75**(5): p. 372-376.

109. Murr, L.E., et al., *Next-generation biomedical implants using additive manufacturing of complex, cellular and functional mesh arrays.* Philos Transact A Math Phys Eng Sci, 2010. **368**(1917): p. 1999-2032.

110. Shishkovsky, I.V., et al., *Porous biocompatible implants and tissue scaffolds synthesized by selective laser sintering from Ti and NiTi.* Journal of Materials Chemistry, 2008. **18**(12): p. 1309.

111. Hollister, S.J., *Scaffold design and manufacturing: from concept to clinic.* Adv Mater, 2009. **21**(32-33): p. 3330-42.

Chapter 2: Experimental, Fabrication & Analysis Procedure

There is a close relationship between the densification of metal powders due to laser irradiation with the processing parameters and material properties. The influential processing parameters in DMLS are laser power, scanning rate, layer thickness and scan spacing while the powder properties consist of the powder particles size, shape, distribution and its chemical constitutions. It was found that, as the laser energy input increases (higher laser power, lower scanning speed, lower scan spacing and lower layer thickness), better densification achieved [1, 2]. Besides the influence of processing parameters, the sintering process is strongly affected by the powder properties where powders with high packing density, high flow rate and low oxygen content are preferred [3, 4].

2.1 Powder Characterisation

Titanium pre-alloy powders, Ti6Al4V (6% of aluminium, 4% of Vanadium) was used for laser sintering. This titanium alloy powder was produced through a gas atomization technique and theoretically would be spherical and small in size. The powder was supplied by EOS and is known as EOS Titanium Ti64 powder. It is known that smaller particles have high surface area and more energy per unit volume, which promotes faster sintering.

Malvern Particle Sizer

The powder particle size and distribution was determined using a laser diffraction method, which is more accurately known as Low Angle Laser Light Scattering (LALLS). This method is used in many industries for particle characterisation and quality control. The method relies on the fact that the diffraction angle is inversely proportional to the particle size. The machine used in this work is a Malvern MasterSizer.

Particle Shape Characterisation

The simplest way to characterize the shape of profile of particles is to evaluate their geometric shape. The British standard institute (ISO 3252) has prepared the standard glossary of terms used in the description of the appearance of powder grains[5];

a. Acicular – needle shaped
b. Angular – having a sharp edge or roughly polyhedral deriving from poly, meaning many and hedra meaning a base; therefore polyhedral is understood to be a geometric shape having many faces each of which can act as a base
c. Crystalline – a geometric shape freely developed in a liquid
d. Dendritic – a branched crystalline shape
e. Fibrous – regularly or irregularly threadlike
f. Flacky – no formal definition in the standard
g. Lamellar – platelike
h. Granular – approximately equidimensional but irregular shape
i. Modular – rounded, irregular shaped
j. Irregular – lacking any symmetry
k. Spherical – globular shaped

2.2 Density

A Quantachrome Instrument, Ultrapycnometry 1000 was used to calculate the density of the laser sintered part. The operation of this instrument is based on Archimedes principle which is a gas displacement and volume pressure relationship known as Boyle's Law. Nitrogen gas was used instead of Helium which can penetrate the finest pores of the sample near to 0.25nm.

Figure 2.1: Gas Pycnometry apparatus

The density measurement of complex part was also done using the Archimedes principle with a modified weight balance. The weight of the piece is measured in air (digital weight) w_a and in water w_w. The density is calculated using the equation below:

$$\rho = \frac{w_a}{w_a - w_w}(\rho_w - \rho_a) + \rho_a \qquad (11)$$

with ρ_w the density of water and ρ_a the density of air.

However problems occur when dealing with porous specimens with open porosity. In this case, water or gas penetrates into the specimens and causes the weight to be bigger than it should be. The result is that the density is over estimated and can sometimes be more than that of the bulk material.

2.3 The Laser Sintering Machine –EOSINT M270

In this research work, an EOSINT 270 extended mode machine was used for components and test piece manufacture. This machine, commissioned in 2006, was manufactured by Electro Optical System (EOS) and is known as Direct Metal Laser Sintering (DMLS) machine. EOS was founded in 1989 and is today the world leading manufacturer of laser sintering systems.

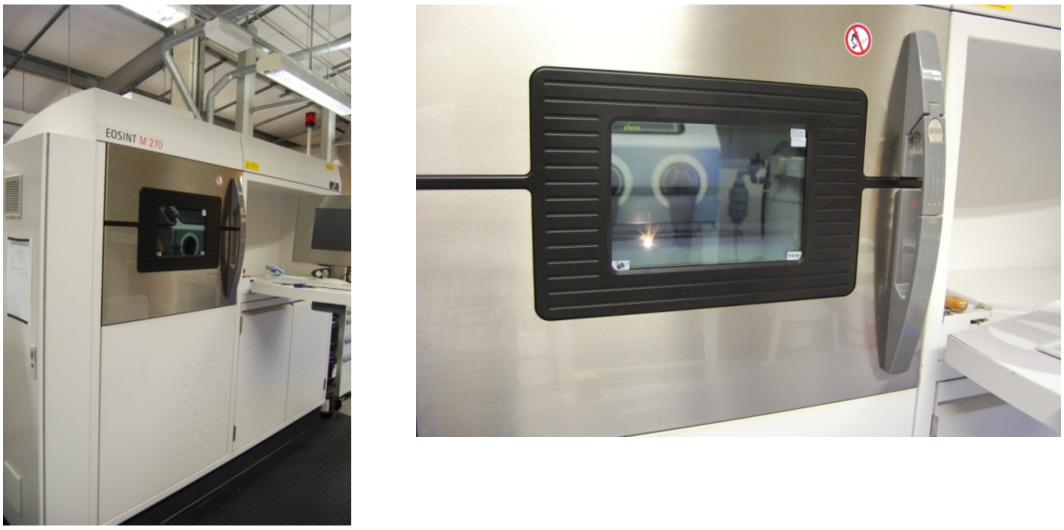

Figure 2.2: EOSINT M 270 machine

The M270 is specifically designed for the fabrication of 3D metal parts. The system is equipped with a solid state 200 watt laser which provides exceptionally high quality parts during the building process. The system operates in a protective argon atmosphere, allowing a wide range of materials to be used ranging from light alloys and steels to titanium alloys, super-alloys and composites. The EOSINT M270 offers a number of powdered metal materials with corresponding parameter sets and standardized property profiles. In addition, all materials are subjected to an intensive process development procedure and constant quality assurance

2.3.1 Technical data

The EOSINT M270 has a bigger processing platform compared to the previous model M250 and capable to process reactive materials such as titanium powder. The machine compromises of many inter-related subsystems as follows:

1. A processing chamber with a recoating system
2. An elevating system and platform heating module
3. A Laser with an optical system
4. A gas management system
5. Process control software

Standard Installation Mode

In this mode the EOSINT M 270 is set up for optimum, safe and cost effective processing of all EOS powders such as StainlessSteel, MaragingSteel and CobaltChrome materials. Processing is done under a nitrogen atmosphere created by a nitrogen generator integrated into the machine frame which generates the nitrogen from an external compressed air supply.

Xtended installation Mode

The machine used in this research work is on an Xtended installation mode. In this mode the EOSINT M 270 system is set up to operate using an inert argon atmosphere. Reactive metals such as EOS Titanium and Alumunium powders may only be processed using this installation mode. Most other materials such as nickel alloys and steels can also be processed under an argon atmosphere.

Dimension (w x d x h)	**2000mm x 1050mm x 1940mm**
Weight	Approx 1130 kg (without powder)
Main supply (three phase system)	400V + 6%-10% at 50/60Hz
Main fuse protection	3 x 32A
Maximum power consumption including cooler	5.5 kW
Compressed air consumption	Approx. 20m^3/h at 7 bar

Table 2.1: Technical data of the machine M 270

2.3.1.1 Optical system

The function of the optical system is to create and position the laser beam in order to fuse, melt or otherwise solidify the powder material depending on the given energy density. The laser emits a laser beam which is guided by an optical fibre, a beam expander optic, the scanner mirrors and a focusing objective. All optical surfaces have special coatings to guarantee effective beam guidance.

2.3.1.2 Laser

Type	**Yb (ytterbium) fibre laser**
Wavelength	1060 – 1100 nm
Nominal powder	200W
Power in the building area	195W

Table 2.2: laser specification used in M270x machine

2.3.1.3 Scanner

The scanner is a high speed scanner unit comprising

1. precision galvanometer scanners with temperature compensation
2. actively cooled ultra high reflection mirrors
3. integrated servo and interface electronics
4. digital data transfer from the system's control computer and signal processing

The system also uses an integrated home-in sensor, which detects and corrects any scanner drift at regular intervals. A high position stability of the laser beam is thereby maintained even under varying environmental conditions or with high thermal loading due to long exposure times and large building jobs.

2.3.1.4 Focussing objective

The machine used in this work has attached to it a dual focus laser beam system in which the sharper focused laser gives an accurate exposure of contours and the other one gives a broader focus for fast exposure of large areas. The dual system allows the focused beam to switch automatically during a scanning process according to the scanning strategy. The focussing objective is known as an F-theta objective which focuses the laser beam onto a flat field. The lens surface is kept away from dirt with a pneumatic lens protection device on its protective glass.

In order to get the laser beam focused on horizontal planes which represent the working surface, an F-theta lens has been used in this machine. Equipped with a special optical design, the F-theta lens allows the beam to be focused on the powder bed according to the entry angle of the laser beam when the mirror is rotated. This condition is exposed to a slight error which causes the barrel shaped distortions of the image. There is also distortion associated with processing parameters and other configurations that require correction and calibration. In this study, all the errors were corrected and compensated for by the software.

2.3.1.5 Recoating and Elevating system

The function of the re-coating and elevating system is to deposit metallic powder evenly onto a building platform layer by layer. The re-coating system comprises a re-coating element, a re-coater arm and a linear drive, which moves the re-coater arm in the horizontal direction. For titanium materials a high speed steel blade is used for re-coating and for other materials a wear-resistant ceramic blade is utilized. The re-coater moves horizontally at a speed of 40 to 500mm per second.

The elevating system compromises a dispenser, building and collector systems. It moves the building platform in the vertical direction in predefined steps which is the layer thickness. The part is built on this building platform which is mounted in a platform carrier. The building platform carrier has a three point mounting and two motorised adjustment screws for simple and exact adjustment of the platform. In combination with a measurement tool, which is mounted on the recoater arm, this allows a quick and easy alignment of the platform at the start of each job. It also includes reference positioning holes for precisely and reproducibly locating the build platform with corresponding positioning pins.

The building system has two parallel guide rails with backflash free guides for highest positioning accuracy and long operating lifetime. The tolerance for the position repeatability is ≤± 0.005mm with maximum build height of 215mm including building platform

2.3.2 Processing Materials

A number of materials are available for use with EOSINT M270 machine offering a broad range of rapid manufacturing applications. Of particular interest in this research work is EOS Ti64 powder. EOS Titanium Ti64 is a Ti6Al4V alloy. This is a well -known light alloy with excellent mechanical properties and high corrosion resistance combined with low specific weight and biocompatibility. EOS also provides an extra low interstitial powder (ELI) which has high purity. This powder material is mainly used for aerospace and biomedical applications

	properties	**application**	**standard**
AlSi10Mg	High strength and hardness, good dynamic properties, good thermal properties and low weight	Functional prototypes, parts subject to high loads, Automotive, engineering, Pneumatics, Motor racing	
EOS Cobalt Chrome MP1	Excellent strength and hardness, high corrosion and temperature resistance	Dental and medical implants. High temperature engineering	Fulfils the mechanical and chemical specifications of ISO 5832-4 and ASTM F75
EOS Maraging steel MS1	Martensite-hardeable steel, excellent strength and high toughness, easily machine-able, good thermal conductivity	Injection moulding, high volume production, aluminium die casting, high performance parts-aerospace	Chemical composition – US 18% Ni Maraging 300, European 1.2709 and German X3NiCoMoTi 18-9-5
EOS Nickel Alloy IN625	High tensile, creep and rupture strength, good corrosion	Applications in Maritime industry, chemical industry parts, aerospace	Chemical compositions UNS N06625,AMS

	resistance	and motor sport	5666F, AMS 5599G, W.Nr 2.4856, DIN NiCrMo9Nb
EOS Stainless Steel GP1	Good mechanical properties, excellent ductility	Functional prototypes, small series product, spare parts (high toughness and cutility)	Chemical composition corresponds to US 17-4, European 1.4542, German X5CrNiCuNb 16-4

Table 2.3: Material Data Sheet (www.gpiprototype.com) These materials are used for specific purposes with specific processing parameters

2.3.3 Processing capabilities

Building area	**220mm X 228mm X 190mm**
Minimum feature size	0.38mm
Minimum wall thickness	0.3mm – 0.4mm
Layer thickness	20 or 40µm
Beam spot	0.1mm
Surface roughness (As built)	Ra 4 - 8µm, Rz 20-45µm

Table 2.4: Technical data sheet of the processing capabilites for M 270

The DMLS M270 machine can process various types of materials from stainless steel to reactive materials such as titanium. One needs to use the valid operating instructions using the parameters set by EOS. The machine has a capability of sintering titanium alloy metallic powder at a volume rate of 1.2mm^{3}s^{-1} or 2.6in^3 per hour. Volume rate is a measure of build speed during laser exposure. The total build speed depends on the average volume rate, the recoating time and other factors pertaining to DMLS processing parameters.

2.3.3.1 Processing Software

The machine comes with its own processing PSW software. This software controls the build process, the building environment and the machine's components. It requires an industry type of desktop to run the software with minimum specifications as shown below;

- Processor – at least Pentium 4 with at least 2 GHz
- At least 1 GB main memory capacity
- More than 10GB hard disk
- Data interface at 10/100 Mbit Ethernet

Using the process PSW software, the building process (job) is prepared, protocolled and filed. Data can also be displayed in a graphical layer format directly on the machine using this software.

2.3.3.2 Platform heating module

The platform heating module reduces temperature gradients between the building platform and the part to reduce internal stresses and ensure good bonding of the first layer. It also removes any moisture from the powder and helps to maintain the part at a constant temperature during any interruptions in the building process to ensure maximum process reliability. The operating or working temperature is set around 40 to 80°C.

2.4 Analysis Procedure

In the first section of the analysis procedure, the laser sintering mechanism is explained based on the heat transfer analysis. A mathematical solution and numerical model using MATLAB software were used to explain and describe the optical and thermal behaviour of the laser sintering process

2.4.1 Heat transfer analysis

In this work thermal modelling was used to describe and illustrate the isothermal conditions during DMLS by applying two different methods. The first method uses a closed loop formed analytical solution for multi-dimensional heat conduction. In this mathematical model solution, 2D heat transfer analysis based on work carried out by SH Zhen *et al* was utilized[6]. The second method uses a numerical solution by employing the MATLAB V6.5 laser toolbox function. These two results were compared with the experimental results of a stationery laser beam and were used to explain the thermal history during the laser sintering process. There are two main objectives for analysing the thermal history during DMLS;

1. To illustrate the laser beam intensity distribution on the temperature distribution in the powder bed. The ideal shape used for the laser beam in this study is a normal or Gaussian distribution
2. To investigate the effects of laser power variations on temperature distribution and sintering depth.

2.4.1.1 Assumptions made for the thermal condition

The heat transfer analysis in this study was performed by making a few important assumptions as follows:

1. The system used is homogeneous where the powder particles are assumed to be all the same size and have homogeneous physical properties in all directions. A control volume is a fixed region in space bounded by a specific control boundary through which energy and matter may enter or exit. The specific control boundary is considered to be the control surface of the system
2. Convection in the building chamber is a natural convection and since the chamber is enclosed, it is very small and thus negligible. The radiation and convection from the surface are neglected thus explaining how the excess heat builds up on the surface of the particle and is dissipated in the form of conduction
3. The laser power is constant throughout the process and it is responsible for the initial light intensity. The diameter of the laser beam used in this work was 100µm for all experiments.
4. It is assumed that the liquid phase is incompressible and the melting point of the metal is not affected by changes in pressure. Significant density change prior to shrinkage during solidification is neglected.
5. During laser irradiation on the powder bed, a liquid pool is formed under the laser beam and the molten metal infiltrates the unsintered powders driven by capillary and gravitational forces. A densified heat affected zone (HAZ) is formed after the laser moves away and the liquid pool solidifies.

A moving coordinate system of which the origin is fixed at the centre of the heat source is employed.

6. All of the solutions presented are based on Fourier's Law of heat transfer in one dimension. A semi finite approximation of the substrate is utilized to obtain closed-form solutions.

2.4.1.2 Mathematical model of Thermal condition in DMLS

In this study, the laser beam is assumed to have a Gaussian distribution and moves at a constant velocity over a surface of a two dimensional metal powder layer. As explained before, a closed form three dimensional solution to induce melting of a substrate by a moving surface flux is used in the first method. Convection heat loss through the surface of the powder bed, temperature dependant material properties and phase change are not included in this calculation. This analysis focuses only on the early stages of the laser/powder-particle interaction in order to find out the speed of heat transfer and its distribution.

In order to simplify the non-linearity problems in a thermal model of the DMLS process, the thermophysical properties of the powder material is assumed to be temperature independent. Therefore, the physical parameters of the material such as density, thermal conductivity, thermal capacity and optical absorptivity were kept constant using the values for the various parameters as shown in table 2.5

	unit	Titanium
Density in solid	ρ_s (kg/m^3)	4500
Density in liquid	ρ_l (kg/m^3)	4110
Specific heat in solid	C_s(J/kg.K)	528
Specific heat in liquid	C_l(J/kg.K)	700
Thermal conductivity in solid	K_s (W/ m.K)	21.6
Thermal conductivity in liquid	K_l (W/ m.K)	20.28
Melting temperature	T_m(K)	1940

Vapour Temperature	T_v (K)	3558
Latent heat	L_v ($10^5 kg^{-1}$)	3.65
Thermal diffusivity in solid	m^2s^{-1}	184.1
Thermal diffusivity in liquid	m^2s^{-1}	119.1

Table 2.5: Thermo-physical properties of Titanium used for the simulation[6-8]

The absorptance value of the EOS Ti6Al4V powder used in this research is based on that for pure titanium and re[ported in work carried out by T.L. Nikolay *et al* [9]

Absorptivity	**Titanium**
Solid	0.257
Liquid	0.433

Table 2.6: Dimensionless absoptance value for Titanium[9]

In this study the absorptance (A) is defined as a ratio of the absorbed radiation to the incident radiation. Reflectance is the ratio of reflected radiation to the incident radiation. Absorptance of a single component is calculated based on the simple formulation A = (1-R). In the work of Nikolay *et al*. it was concluded that the absorptance coefficient of single component titanium powder is dependent on the laser wavelength and the value as shown in table 2.6.

2.4.1.3 Laser beam approximation

The laser source power as a function of the source position is assumed to be Gaussian and is given by the equation[10]:

$$P = \frac{2}{\pi r^2} exp\left[-2\frac{(X - Xs)^2 + (Y - Ys)^2}{{r_b}^2}\right] \tag{12}$$

in which P is the laser power, r_b is the beam radius and (x_s,y_s)the position of the source. The laser energy can be regarded to be in the form of surface heat flux imparted into the powder bed which obeys the Gaussian heat source distribution:

$$q\ (x, y)\ =\ \frac{2AP}{\pi\omega^2}\exp\left(-\frac{2(x^2+y^2)}{\omega^2}\right) \tag{12.1}$$

$$q\ =\ \frac{2AP}{\pi\omega^2}\exp\left(-\frac{2((-Vt+x)^2+y^2)}{\omega^2}\right) \tag{12.2}$$

where ω is the equaivalent radius of the laser beam and the distance is from the centre of the laser beam area to the point with heat flow density mitigated to the $1/e^2$. A is a powder bed absorptivity to the laser beam. The absorptivity value for Ti6Al4V powder is referred to the value in Table2.6.

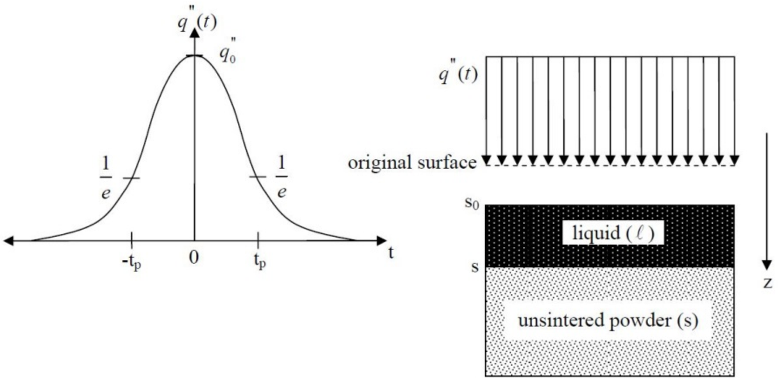

Figure 2.3: Gaussian beam profile and distribution on the powder bed

Figure 2.3 illustrates a cross-sectional profile of the laser beam intensities. In this work, only a Gaussian beam shape is considered. The total energy incident on a point (x,y) in this model will be equal to that calculated in equations 12.1 and 12.2. The Gaussian beam has two normal spatial components x and y which can be considered separately with regard to their effect on heating of the powder bed. The Y-component has no functional limitations because the penetration depth is in the z direction and the beam moves in the x-direction. The x-component must be of a form that can solve the Fourier's law of heat transfer. Thus, the y component of the beam approximation can be taken to be the ideal Gaussian form. The first approximation for the beam assumes that the total beam energy is irradiated to the substrate by a surface flux.

2.4.1.4 Mathematical model Solution

The mathematical thermal model used in this research work is based on the work of Z.H Shen [6]. The principal used in this study is that when a high power laser strikes the powder surface, a part of the laser is absorbed and conducted into the interior of the material. The isothermal condition of the powder is determined by the given energy density. If it is high enough, the given energy may cause the powder to melt and even vaporise. The whole process of laser induced melting is divided into two steps: before melting and after melting

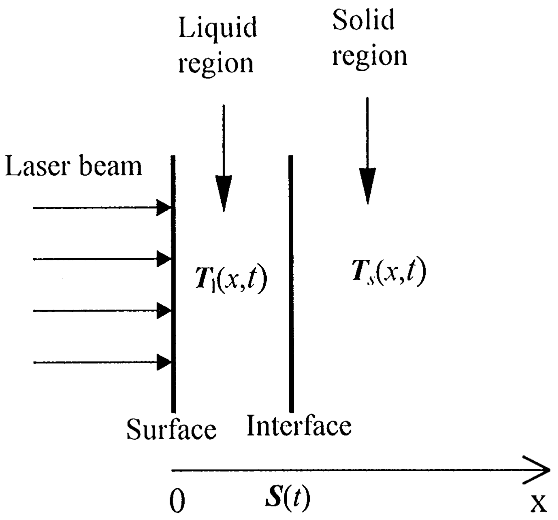

Figure 2.4: the geometry of laser irradiation[11]

Before melting the temperature profile is given as:

$$T_s(x,t) = T_w(t)e^{-x/\delta(t)} \tag{13}$$

where T_w represents the temperature of the surface and $\delta(t)$ is a temporal function representing the temperature penetration depth in the solid. The boundary conditions as follows;

$$T_s(x,t) = T_o, x \to \infty \tag{13.1}$$

$$T_s(x,t) = T_o, t = 0 \tag{13.2}$$

According to the Shen *et al* the following relations are obtained from the derivations;

$$T_w(t) = \left[\frac{2\lambda_l A^2{}_l l^2}{k^2{}_l} + C_0\right]^{1/2} \tag{13.3}$$

$$\delta_l(t) = \frac{k_l}{A_l I}\left[\frac{2\lambda_l A^2{}_l I^2}{k^2{}_l} t + C_0\right]^{1/2} \tag{13.4}$$

$$\delta_s(t) = \frac{\rho_s L}{A_l I T_m}\left(\lambda_s + \frac{T_m k_s}{\rho L}\right)\left[\frac{2\lambda_l A^2{}_l I^2}{k^2{}_l} t + C_0\right]^{1/2} \tag{13.5}$$

$$S(t) = \frac{k_l}{A_l I}\left[\frac{2\lambda_l A^2{}_l I^2}{k^2{}_l} t + C_0\right]^{1/2} ln \frac{[2\lambda_l A^2{}_l I^2 t / k^2{}_l]^{1/2}}{T_m} \tag{13.6}$$

$$C_0 = {T_m}^2 - \frac{\lambda_l k^2{}_l A^2{}_l}{\lambda_s k^2{}_s A^2{}_s}(T_m - T_0)^2 \tag{13.7}$$

The time for the surface to melt and vaporise is given by below equations;

$$t_m = \frac{(T_m - T_0)^2 c_s k_s \rho_s}{2(A_l I)^2 \lambda_l} \tag{13.8}$$

$$t_v = \frac{(T_v - C_0){k_l}^2}{2(A_l I)^2 \lambda_l} \tag{13.9}$$

2.4.1.5 Numerical Model Solution

MATLAB is a high level interpreted language and interactive environment for algorithm development, data visualization, data analysis, and numerical computation developed by MathWorks Inc. (http://mathworks.com). One of the many toolboxes available in MATLAB is the laser toolbox which is a collection of special purpose MATLAB functions and scripts. This was created to further extend the MATLAB environment to solve particular classes of problem. In this study, the laser toolbox is used to analyse the thermal induced by the laser interaction with the powder.

2.4.1.6 Governing equation for the Numerical model in MATLAB (v6.5)

The temperature model is described using the surface heat source function. This can be done by assuming a semi-infinite substrate with constant material properties and surface heat source defined by the power density moving over the substrate's surface. The surface heat source will induce a temperature rise in the substrate when it is moving at a constant velocity in the x-direction relative to the surface. This temperature rise is given by:

$$T(x,y,z,t) = \int_{-\infty}^{\infty}\int_{-\infty}^{\infty} AI(x',y')W(x,y,z,x',y',v)U(R,t,v)dx'dy' \qquad (14.0)$$

where

$$R = \sqrt{x^2 + y^2 z^2} \qquad (14.1)$$

$$W(x,y,z,x',y',v) = \frac{1}{2\pi KR} exp\left[-\frac{v}{2k}(x - x' + R)\right] \qquad (14.2)$$

and

$$\begin{aligned} U(R,t,v) &= \frac{v}{\sqrt{\pi}}\int_{1/\sqrt{k}}^{\infty} exp\left[-\frac{(\vartheta\xi^2 - \frac{v}{k})^2}{4\xi^2}\right] d\xi \\ &= \frac{1}{2}\left[1 - erf\left(\frac{R - vt}{2\sqrt{kt}}\right) + e^{\vartheta v/k}\left(1 - erf\left(\frac{R + vt}{2\sqrt{kt}}\right)\right)\right] \end{aligned} \qquad (14.3)$$

in which K denotes the thermal conductivity and k the thermal diffusivity of the material. This expression is evaluated using the Fast Fourier Transform (FTT). For simplicity a steady state situation is considered and for this when U=1, t→∞.

A basic condition for the two dimensional Fourier transformation is that the function to be transformed is periodic in the x-y plane. This is not the case for the intensity profile I and the function W and will introduce errors in the evaluation of the temperature distribution. These errors are introduced by the truncation of I and W. If the grid size is too small, then for $|x|>L$ and $|y|>L$, $W(x,y) \neq 0$ and $I(x,y) \neq 0$. To reduce errors, the region of calculation was set sufficiently large where $L>3d$, d is the diameter of the laser beam.

2.4.1.7 Setting the material properties

The materials' properties can be defined using the Microsoft Access or data structs in MATLAB. The material's parameter was then saved in this workspace. The data structure used in this programming is as shown below. To simplify the simulation and avoiding the non-linearity equation in transient temperature distribution, constant material properties were utilized. In this simulation, the material properties are assigned to the substrate. Therefore, solid Ti6Al4V properties are used consistently throughout the simulation. Once the properties were decided, the data was stored in MATLAB data structure format (.mat). This can be retrieved easily with the specific programming function.

Name	EOS Ti64 (Identifier, string)
Absorptivity	Absorptivity, ((vector of) double (s))
lambda	(laser wavelength [m] for which A is defined, (vector of) double (s))
K	Thermal conductivity [W/(m*K), double]
rho	(density [kg/m^3], double)
Cp	Thermal heat capacity [J/kg*K]], double)
Kappa	Thermal diffusivity [m^2/s], double)
T	Temperature [K] for which the above parameters are defined, double)

T_m	Melt temperature [K], double)
T_v	(vaporisation temperature [K], double

Table 2.7: Materials data used in MATLAB programming

Figure 2.5 shows the data structure stored in MATLAB programming interface. The thermomechanical properties for Ti6Al4V collected from a few published works were used in this simulation work[6-9]. The material data structure was defined and the temperature profile scripts were called to simulate the temperature profile of the specific laser conditions.

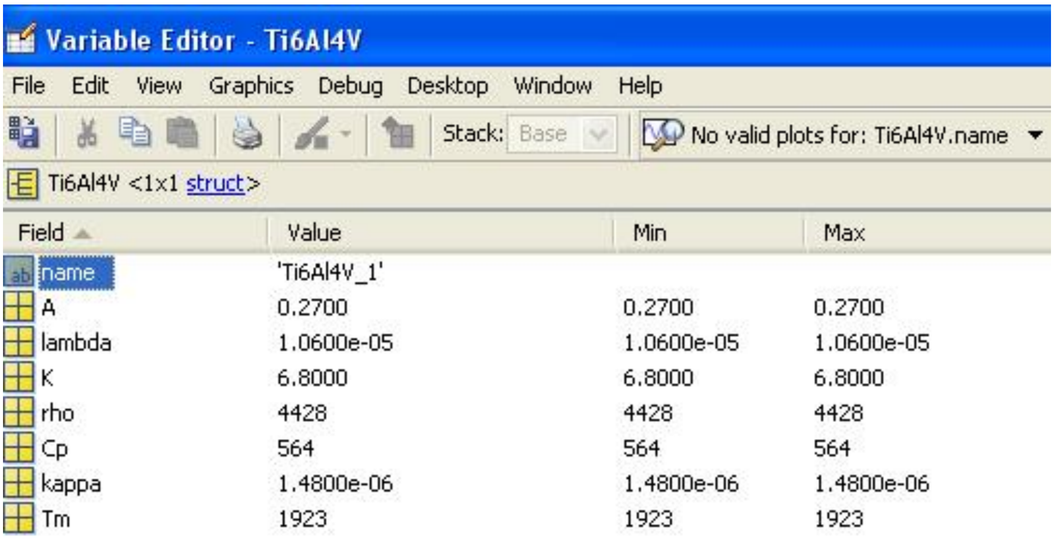

Field	Value	Min	Max
name	'Ti6Al4V_1'		
A	0.2700	0.2700	0.2700
lambda	1.0600e-05	1.0600e-05	1.0600e-05
K	6.8000	6.8000	6.8000
rho	4428	4428	4428
Cp	564	564	564
kappa	1.4800e-06	1.4800e-06	1.4800e-06
Tm	1923	1923	1923

Figure 2.1: Thermal properties used in MATLAB simulation

2.4.2 Microstructural Characterisation

The microstructural analysis was performed based on the standard procedure established for processing titanium alloy specimens. The specimens were sectioned, ground, polished and etched accordingly for optical microscopy. The microstructures obtained were compared with other published work in the discussion section.

2.4.2.1 Optical Microscope

Optical images were captured using an Olympus BX 60 Digital Optical Microscope. The specimens were ground, mounted in resin, polished using SiC papers up to 4000 grit and etched with Kroll's reagent solution. Olympus stream v1.7 software was used to acquire, process and measure images thus providing valuable data and reports.

2.4.2.2 Scanning Electron Microscopy

The size, shape and the chemical constitution of the Ti6Al4V powders used for laser sintering were evaluated using scanning electron microscopy. The shape of the individual powder particles was evaluated based on standard shapes such as spherical, cylindrical and acicular. A Hitachi S-4700 Scanning Electron Microscope was used to run the analysis. A portion of the Ti6Al4V powders used for specimen fabrication was used to carry out an analysis by optical and scanning electron microscopy of synthesized laser sintered spots, tracks and layers. Scanning Electron Microscope (SEM)

2.4.2.3. X-ray Diffraction

X ray powder diffraction is a useful tool for characterizing material structures. Diffraction patterns can be analysed for phase identification in order to determine what crystalline substances are present in a tested sample. It is known that, each crystalline substance has a unique diffraction pattern. XRD data are normally analysed based on the angular position of peak intensities. The number of observed peaks is related to the symmetry of a unit cell where higher symmetry gives fewer peak reflections.

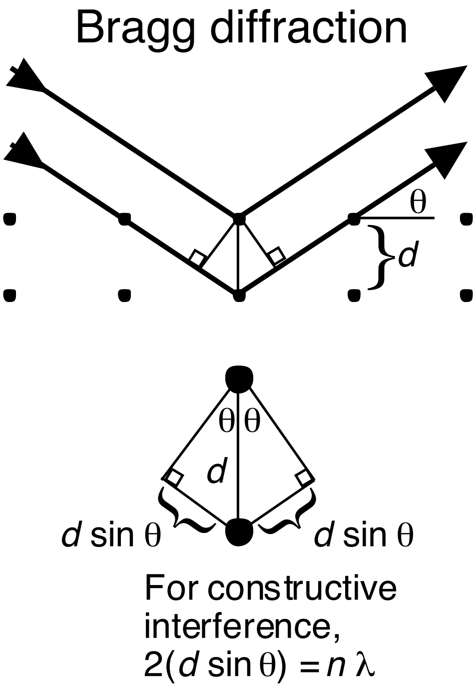

Figure 2.6: Bragg diffraction

From Bragg’s equation, the d-spacing can be calculated. The d-spacing of the observed peaks are related to the repeating distances between planes of atoms in the structure. These three features of a diffraction pattern; the number of peaks, the position of the peaks and the intensities of the peaks define a unique fingerprint X ray pattern for every crystalline material. In more quantitative work, the peak positions can be used to define the lattice parameters for a given unit cell. Unit cells of three dimensional repeating structures have different shapes based upon the symmetry of the structure. In all cases, the unit cells are parallelepipeds but the different shapes arise depending on restrictions placed on the lengths of the three edges (a, b,and c) and the values of the three angles (α, β and γ)

Crystal System	Lattice parameter Restrictions
Cubic	$a = b = c, \alpha = \beta = \gamma$=90˚
Tetragonal	$a = b \neq c, \alpha = \beta = \gamma$=90˚
Orthorhombic	$a \neq b \neq c, \alpha = \beta = \gamma$=90˚
Monoclinic	$a \neq b \neq c, \alpha = \gamma$=90˚ $\beta \neq 90$
Triclinic	$a \neq b \neq c, \alpha \neq \gamma \neq \beta \neq 90$
Hexagonal	$a = b \neq c, \alpha = \beta = 90, \gamma = 120$
Trigonal	$a = b \neq c, \alpha = \beta = 90, \gamma = 120$

Table 2.8: Lattice parameter restrictions

Determining the lattice parameters of the unit cell from the XRD data requires knowing how to assign the Miller indices (h k l) to each diffraction peak through a process known as pattern indexing. Normally for a known material, this is done by referring the data to that reported in the literature or in a database of diffraction patterns known as JCPDS. The Miller indices relate the peak positions or d-spacing to the lattice parameters by an equation specific to the crystal system. As an example for hexagonal and orthorhombic unit cell the relationship between d spacing and miller indices is given by the following equation;

$$\frac{1}{d^2} = \frac{4}{3}\left(\frac{h^2 + hk^2 + k^2}{a^2}\right) + \frac{l^2}{c^2} = \frac{4\, sin^2\Theta}{n\lambda^2} \qquad (15.0)$$

$$\frac{1}{d^2} = \frac{h^2}{a^2} + \frac{k^2}{b^2} + \frac{l^2}{c^2} \qquad (15.1)$$

where a, b and c are the lattice parameters of the unit cell and hkl are the Miller indices identifying the repeating planes causing the diffraction peak with spacing d_{hkl}. In the cubic system, one peak position, d, can be used to determine the lattice parameter provided the Miller indices can be assigned. However, a better way to obtain the parameter is to input all of the peak positions that can be indexed and refine the lattice parameters using a number of data points and regression analysis.

X-ray Diffraction patterns of the blobs and blocks manufactured via laser sintering were acquired from a Philip Expert X-ray diffractometer equipped with Cu-Kα radiation. The X-ray source was a conventional sealed 2500 watt x-ray tube operated at 40kV and 40mA. Incident and diffracted beam slits were at 1 and 4 degrees respectively, chosen for high intensity. Data were collected by step counting at 0.02 deg intervals for 2 seconds per data point. In this experiment two types of scanning was performed.

a. Full scan of 2Θ = 30 -90˚; step size
b. Specific Peaks scan at 2Θ = 30 -41.5, step size;

2.4.3 Structural Characterisation

2.4.3.1 Tensile testing

Tensile testing was carried out using an Instron 4204 machine following the ASTM E8M standard and according to the ISO 6892 standard indication. A 0.25 mm/min cross head speed was applied. An axial extensometer was employed for measuring the elongation. In particular, the ASTM E8M standard for the tensile specimen's geometry was followed. The specimens had a rectangular shape with an overall length of 110mm and a reduced section length of 50mm with the thickness of 4mm

Tensile machine	Setting
Interface type	4200/4300/4400
Machine parameters	standard
sample rate (points/secs)	100
cross head speed (mm/min)	0.25
Extensometer switch value	50mm

Table 2.9: Instron machine set parameters

Tensile testing was conducted on three different groups of specimens. Each group had predefined processing parameters. The first group consisted of nine (9) tensile specimens produced with a consistent scan speed at 1250 mms^{-1} and scan spacing of 0.05mm, 0.08mm and 0.1mm respectively. Each specimen was marked and labelled. This process was repeated with a lower scan speed at 750mms^{-1} and 1000mms^{-1} respectively. All samples were tested in accordance to ASTM E8 for metallic materials. The samples were strained at a rate of 0.3mm sec^{-1} through 0.2% yield followed by a rate of 0.25mm sec^{-1} until fracture.

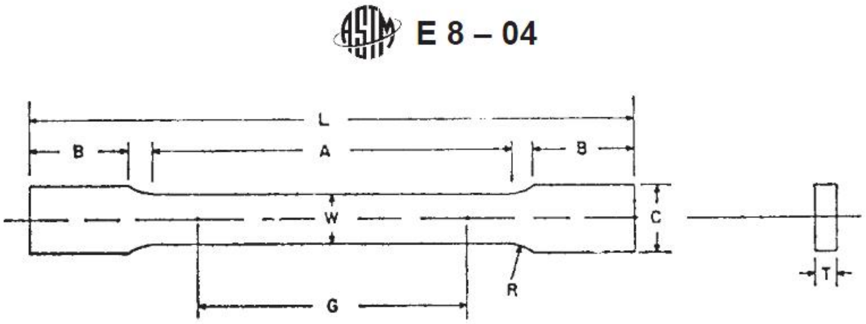

Figure 2.7: E8-04 Tensile specimen standard dimensions

Dimension	mm
Gauge Length (G)	50
Width (W)	10
Thickness (T)	4
Radius of fillet (R)	7
Overall length (L)	110
Reduced length (A)	64
Reduced width (B)	23
Width of grip section (C)	25

Table 2.10: Tensile specimens dimension

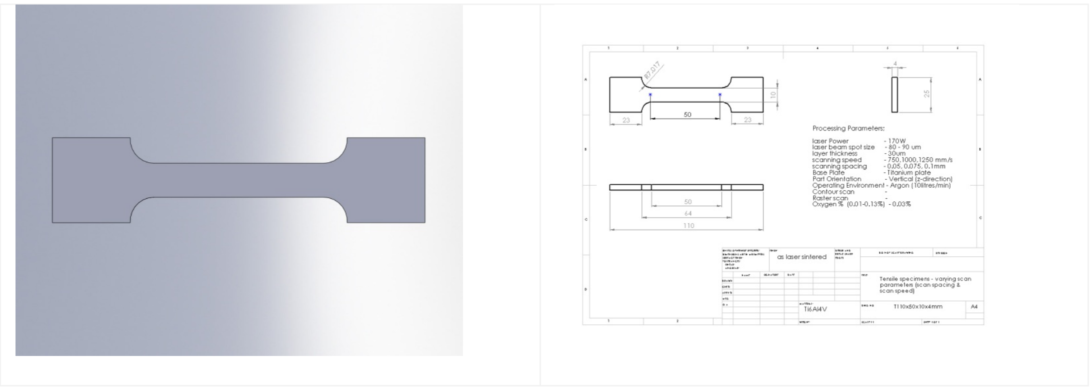

Processing Parameters:

laser Power - 170W
laser beam spot size - 80 - 90 um
layer thickness - 30um
scanning speed - 750,1000,1250 mm/s
scanning spacing - 0.05, 0.075, 0.1mm
Base Plate - Titanium plate
Part Orientation - Vertical (z-direction)
Operating Environment - Argon (10litres/min)
Contour scan -
Raster scan -
Oxygen % (0.01-0.13%) - 0.03%

Figure 2.2: Dog bone shaped tensile specimen

As shown in table 2.11, a total of 27 dog –bone shaped specimens were fabricated for the tensile testing. The two variables in this experiment were the scan spacing and scan speed. The specimens were divided into G1, G2 and G3 for scan speeds of 1250mms^{-1}, 1000mms^{-1} and 750mms^{-1} respectively. The different scan spacing was denoted by S1, S2 and S3 for 0.05mm, 0.08mm and 0.1mm scan spacing respectively. The combination of different scan speed and spacing was labelled accordingly and three tensile specimens were fabricated for each group.

Group	Scan speed(mm/s)	Scan spacing	Quantity
G1S1	1250	0.05	3
G1S2	1250	0.08	3
G1S3	1250	0.1	3
Group	Scan speed(mm/s)	Scan spacing	
G2S1	750	0.05	3
G2S2	750	0.08	3
G2S3	750	0.1	3
Group	Scan speed(mm/s)	Scan spacing	
G3S1	1000	0.05	3
G3S2	1000	0.08	3
G3S3	1000	0.1	3

Table 2.11: Groups prior to the different scan speed & scan spacing

The processing parameters were set manually so that the Core and Skin input was according to the desired setting. The setting involved the main parameters such as laser power, scan spacing, scan speed, beam offset and scanning strategy. The scanning strategy was divided into Core and Skin. The detailed scanning strategy parameters were as shown in table 2.12. The beam offset was used to compensate for the beam errors due to image distortion and the rotating motion of two mirrors. The value of 0.015mm is based on the EOS standard processing parameters. There is no pre-exposure for each layer which means that the laser scanned the layer once only and a new thin layer of powder was then subsequently deposited.

Processing parameter (DP1)	**G1S1_0.05**
Scan speed	1250mm/s
Scan spacing	0.05mm
Laser Power	170W
Beam offset	0.015
Hatching	X, Y Rotated
Stripe width	5mm
Stripe overlap	0mm
Skywriting	Yes
Offset	Yes
Processing parameter (Skin/Core)	
Pre-Exposure	No Exposure
Skin Exposure	G1S1_0.05
Post Exposure	Contours
Core Exposure	No Exposure
Skin Thickness (x,y)	100mm
Skin thickness (z)	100mm
Base Radius	0mm
Hatching	X, Rotated

Table 2.12: PSW interface used to set up the scanning strategy

As mentioned before, the scanning strategy on each layer was divided into two areas: Core & Skin. Hatching determines the scanning pattern on each layer. In this setting, the laser first scans in the X-direction followed by the Y direction and is then rotated by 60˚. This is to make sure that the laser scans the whole predefined area in each layer.

Processing parameter		
Updown	Upskin	Downskin
Distance	0.09 mm	0.09mm
Speed	1000 mm/s	1000 mm/s
Power	120 W	120 W
Thickness	0.09 mm	0.06 mm
Overlap with skin	0.00 mm	
Min Length	0.30 mm	
Hatching	X, Y	X,Y

Table 2.13: Parameters for Skin & Core Exposure

2.4.3.2 Fracture surface morphology

The fracture surfaces of the tensile specimens were analysed using a Hitachi S-4700 Scanning Electron Microscope. There were nine groups of specimens with different processing parameters as mentioned in the specimen fabrication. From each group three tensile specimens were prepared. The specimens were sectioned and mounted on a small aluminium stub to keep the fracture surface clean. A careful examination of the fracture surface was carried out at low magnification for the purpose of identifying:

a. The dominant fracture surface features/topography/morphology
b. The regions of microscopic crack initiation
c. The nature and characteristics of early crack growth.
d. The final fracture where the region of overload can be observed and compared with other groups with different processing parameters.

The examination was also done at gradually increasing magnification in the centre region or overload region with the purpose of identifying the nature and severity of damage initiation. The fine scale features on the fracture surface for each different group was observed.

2.4.3.3 Microhardness Test

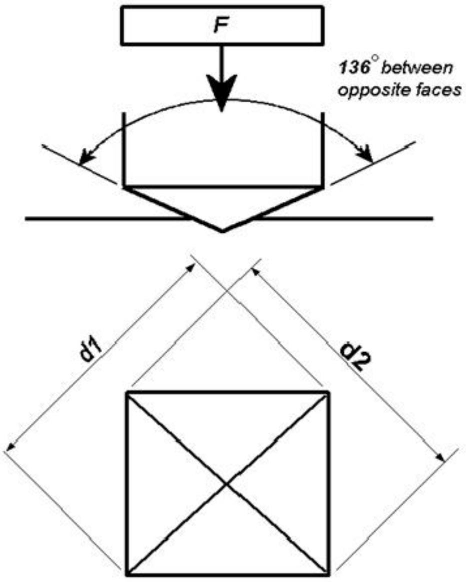

Figure 2.9: indenter for Vicker's hardness Test, source; (www.wikipedia.com)

The Vickers hardness test method consisted of indenting the test material with a diamond indenter, in the form of a right pyramid with a square base and an angle of 136 degrees between opposite faces subjected to a load of 1 to 100 kgf. The full load is normally applied for 10 to 15 seconds. The two diagonals of the indentation left in the surface of the material after removal of the load were measured using a microscope and their average calculated. The area of the sloping surface of the indentation was calculated. The Vickers hardness is the quotient obtained by dividing the kgf load by the square mm area of the indentation. The conditions used for the microhardness test are shown below:

a. Load = 50kgf
b. Holding time = 15s
c. Number of readings = 15

References

1. Simchi, A., *Direct laser sintering of metal powders: Mechanism, kinetics and microstructural features.* Materials Science and Engineering: A, 2006. **428**(1-2): p. 148-158.
2. Olakanmi, E.O., R.F. Cochrane, and K.W. Dalgarno, *Densification mechanism and microstructural evolution in selective laser sintering of Al–12Si powders.* Journal of Materials Processing Technology, 2011. **211**(1): p. 113-121.
3. Simchi, A., F. Petzoldt, and H. Pohl, *On the development of direct metal laser sintering for rapid tooling.* Journal of Materials Processing Technology, 2003. **141**(3): p. 319-328.
4. Prashant K. Jain, K.S., Pulak M. Pandey, P. V. M. Rao. *ADVANCES IN MATERIALS FOR POWDER BASED RAPID PROTOTYPING*. in *Advances in Materials and Processing*. 2006. Coimbatore, India.
5. Oleg D Neikov, S.L., Irina V Frishburg, Dina V, *Handbook of Non Ferrous Metal Powders: Technologies and Applications*, 2009, Elsevier: England.
6. Z.H. Shen, S.Y.Z., J. Lu, X.W. Ni, *Mathematical modeling of laser induced heating and melting is Solids>.* Optics & Laser Technology, 2001. **33**(2001): p. 533-537.
7. Wiria, F.E., K.F. Leong, and C.K. Chua, *Modeling of powder particle heat transfer process in selective laser sintering for fabricating tissue engineering scaffolds.* Rapid Prototyping Journal, 2010. **16**(6): p. 400-410.
8. Daryabeigi, K., *Thermal Properties for Accurate Thermal Modeling*, 2011.

9. Nikolay K. Tolochko, T.L., Yurii V. Khlopkov, Sergei E. Mozzharov, Victor I. Titov and Michail B. Ignatiev, *Absorptance of powder materials suitable for laser sintering.* Rapid Prototyping Journal, 2000. **6**(3): p. 155-160.
10. Romer, G.-w., *Matlab Laser Toolbox User Manual*, 2010.
11. S. Ahn, J.M., J. Ramos, and J. J. Beaman, *PHYSICAL MODELING FOR DYNAMIC CONTROL OF MELTING PROCESS IN DIRECT-SLS.*

Chapter 3: Component and test-piece manufacture via DMLS

In this chapter, the experimental procedure and the techniques used to fabricate specimens is reported. In the beginning, the Ti 6Al 4V powder, supplied by EOS, used in this research work was characterised. All parts were directly manufactured using an EOSINT M270 extended version machine by utilizing the EOS Ti6Al4V powder material. This machine implies the layered manufacturing principles by fusing various metallic powders layer by layer into a solid part by melting it locally using a focussed laser beam. The manufacturing process for this research work, which consisted of producing mechanical testing specimens and implant specimens using DMLS, was divided into a few main categories. In this chapter, the details of these are explained.

3.1 CAD & CAM Modelling

Generally, the laser sintering process begins with the creation of 3D CAD data in various types of CAD software such as Solidworks, Unigraphic and Inventor. Most of the software is capable of producing 3D data and most important is the capability for converting the 3D data to stl format. **STL** (Standard Tessellation Language) is a file format native to the stereolithography CAD software created by 3D Systems. This file format is supported by many other software packages; it is widely used for rapid prototyping and computer-aided manufacturing. STL files describe only the surface geometry of a three dimensional object without any representation of colour, texture or other common CAD model attributes. The STL format specifies both ASCII and binary representations. Binary files are more common, since they are more compact.

3.1.1 Data Preparation

Once the design is completed, the CAD data must be converted to a readable machine format. This conversion is necessary to create the specific layer interface (SLI) data which are required for the building process. At this stage, three dimensional data is converted into a sequence of two dimensional data called ‘slices” consisting of many layers.

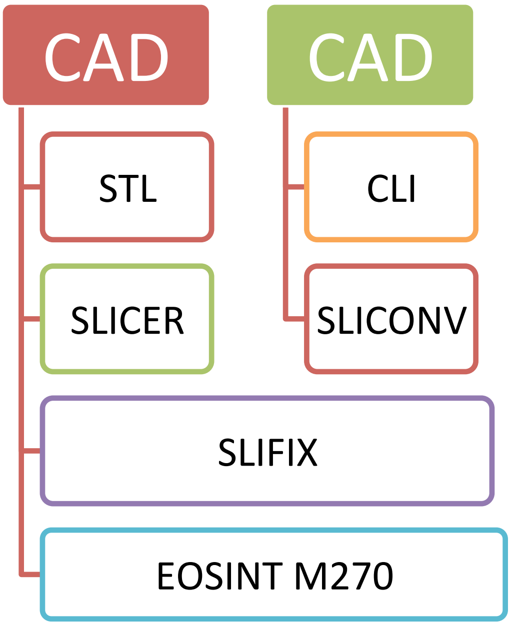

Figure 3.1: Digital data transfer format

An STL file describes a raw unstructured triangulated surface using the unit normal and the vertices (ordered by the right-hand rule) of the triangles using a three-dimensional Cartesian coordinate system. This translation is necessary to allow the data to be processed in a Computer Aided Manufacturing (CAM) platform as shown in figure 3.1 This means that all the design, regardless of what type of CAD (computer aided design) software was used in initial design stage, the final step must be ended with the translation to a readable CAM format. Beside the ‘stl’ format, there are a few more options that can be used such as ‘igs’, ‘iges’ etc. For this research work only ‘stl’ format was used in each of the fabrication processes. A simple part also can be designed using MAGICS instead of the aforementioned CAD software, as MAGICS provides basic design functions.

3.1.2 EOS RP Tools

The EOS RP Tools software is used to convert either STL data or common layer interface (CLI) data to EOS specific layer interface (SLI) which is required for the subsequent building process. Layer data or solid bodies can be separated into skin and core data to facilitate process optimisation.

The EOS RP Tools consist of the following modules;

- SLIVIEW – graphical user interface for visualising layer data
- SLICER – generates two dimensional layer data out of three dimensional STL data
- SLIFIX – automatic repair of the most common errors in layer data such as overlaps, double contours and inverted polygon orientation
- SKINCORE – separate massive part data into one data set for a definable Skin and a Core on a two dimensional basis
- SLICONV – automatic data conversion from CLI to SLI and vice versa (ASCII or binary)
- RADIUS – create a fillet radius between the upper surface of the building platform and the part to improve the platform part connection and allows generation of a SKIN and CORE structure which is open to the building platform.

3.1.3 Materialise Magics RP

Magics RP version 15 is used in this research work. One of the many advantages of using Magics is that it provides effective visualisation of parts in STL format. Huge files, such as for example, a file that has been converted from CT scanning data is easily manipulated in Magics software. Magics RP is a software package for data pre-processing based on STL data. Besides the bespoke functions, Magics RP is also used for repairing and editing purposes. Parts are assembled in Magics and once completed the new assembled parts can be imported to IGES or CATIA for further finite element analysis. The additional or upgraded module provides more sophisticated functions such as STL reinforcements, building supports and a library of lattice structures' unit cells.

3.1.4 Support Structure and Part Orientation

Before sintering any of the part geometry, a support structure was built on the tray and then the bottom of the part developed before building the part from the bottom up. The absence of a support structure over an appropriate area causes parts to severely warp. The support structures were created using integrated Magics-EOS RP Tools software. The geometry of the part, which in this case was the mandible, was carefully analysed, paying particular attention to all the down facing surfaces and the area where there is a large volume of material. The support structures were placed manually rather than automatically to avoid unnecessary and massive support structures which lead to longer production time. The mandible implant was first orientated in different positions in order to get the best possible building orientation. Consideration of building height and the removal of the support structures after completion were important when selecting the best building orientation. The part and the support structures were sliced at 30µm intervals and saved in .sli format. This was done by using the EOS RP tools software.

3.2 Machine Set Up

The machine set up included the platform/substrate preparation, building condition (use of argon gas for flushing), powder refilling in the powder container, selecting the appropriate re-coater blade and levelling it with the platform. In this research, a mini plate and standard plate were used as the substrate depending on the size and quantity of the intended specimens. There is a strict procedure which needs to be followed for machine set up, sample handling and a post processing procedure which require special tools and attire as shown in fig 3.4.

3.2.1 Platform preparation

The machine has two identical platforms which are known as a mini plate and standard plate. The mini plate is 110mm (L) x 110mm(W) x 10mm(T) in size. Four tapered holes were placed at the four corners and the surface was milled to give a reasonably flat and smooth surface. The surface was wiped with acetone to ensure it was clean, then the mini plate was attached to the machine’s platform which is specially designed to cater for the size of this small plate. This platform moves up and down at precise incremental values equal to the desired powder layer thickness. The standard plate (270mm x 250mm x 50mm) is normally used for big parts or smaller parts manufactured in a larger quantity. The same procedure is applied for the standard plate.

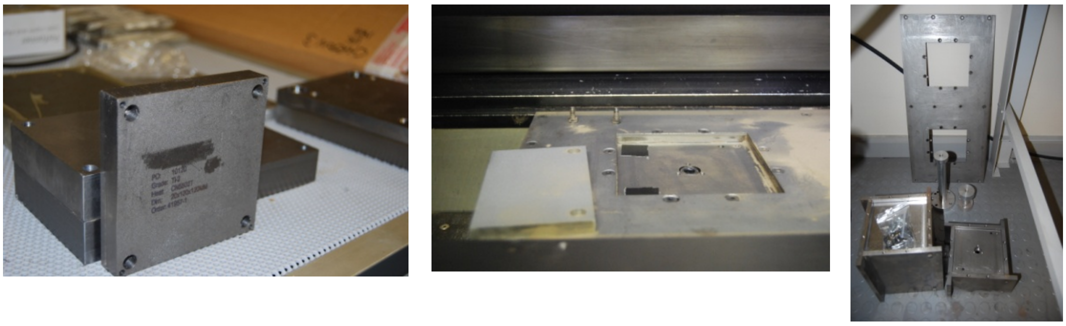

Figure 3.2: Customised mini plate and its associated apparatus

The parts were built on a building platform which can either be integrated into the part for tooling inserts or separated from the part after the building process. The separation is done using an EDM wire cutting machine. The building platform is then re-machined to ensure a smooth and flat surface before reusing it. When using Ti6Al4V alloy powder, a DirectBase Ti25 solid platform is used. The building platform is attached to the elevating system, particularly the carrier plate in the process chamber, by four 8mm corner screws. For large or massive parts, a thicker building platform is used which is about 36mm in thickness.

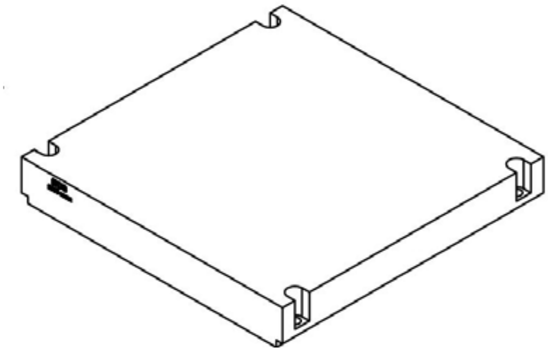

Figure 3.3: Standard plate for M 270

3.2.2 Building Environment

The building environment is referred to as the building chamber condition of the machine. One of the main concerns is to reduce the oxygen level. The M270 machine has a sealed process chamber which enables a high purity of protective gas to be maintained, thereby enabling the equipment to process a wide range of materials including reactive metals, such as titanium. In this work, argon gas was used to control the oxygen levels inside the chamber and act as a protective gas.

The Oxygen concentration was controlled to between 0.01 % to 0.13%. The machine fills at 40 litres /min and drives the O_2 down to 0.03% and then goes into hold mode where the chamber is fed with argon at 10 litres/min. The argon enters the chamber around the theta lens assembly to keep the lens glass free from products generated by the sintering. The argon that is in the chamber is driven through a filter and returned to the chamber again around the lens cover. Every time, before processing took place, the building chamber was cleaned to ensure that the chamber was protected and because of the high reactive materials interaction, had a safe environment for the high intensity laser beam. .

b. The building chamber Siever (Titanium 63µm)

c. The argon gas bottles Special hover

Figure 3.4: Components associated with the machine

3.2.3 Balancing the re-coater blade

The appropriate re-coater is used for a specific design and operating condition. In this research work, a blade re-coater made from stainless steel was used for fabrication of all specimens. Once the re-coater was fixed onto the holder, a clock gauge was used to do the levelling. This is quite an important procedure to ensure that a sufficiently large enough gap was placed in between the re-coater and the platform. This will make sure that the blade is not touching the raised platform prior to its movement, particularly in the horizontal axes while depositing a new thin layer of powder. The levelling is also essential in order to have evenly distributed powder particles on the platform. The re-coater needs to be firmly attached as any vibration would affect the powder layer.

Figure 3.5 Levelling of the re-coater using the clock gauge

3.2.4 Setting up the Processing Parameters using PSW 3.0

These part and support structure files which are known as specific layer interface files (SLI) were then saved and retrieved at the machine's desktop using the machine's processing interface. The software is known as PSW version 3.3. This software was used to virtually place the desired parts and their support structures onto the machine's building platform. The software allows the user to control the machine's processing parameters such as laser power, scan speed, scan spacing and powder layer thickness.

Normally, the default factory setting was used for a standard job. The setting is shown in Table 3.1 and the software's interface is as shown in figure 3.6. This software also provides information about the current state of the building environment such as the chamber current temperature and oxygen level. It also senses the movement of both the building platform (vertically, up and down) and the powder deposition blade (horizontally, back and forth). The powder deposition onto a building plate is maintained as a uniform distribution for every single movement of the deposition blade. Once everything is finalised, the start button is pressed to initiate the laser sintering process.

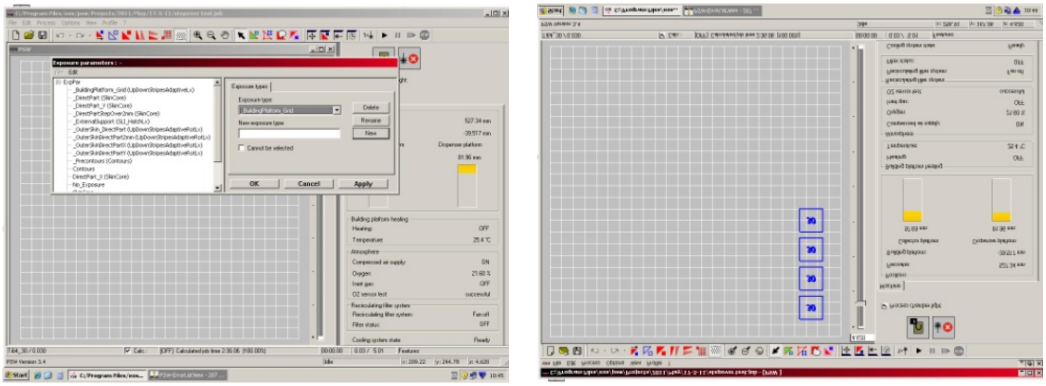

Figure 3.6: PSW version 3.3 software’s processing interface

The PSW software is installed at the machine. Once the slicing data is ready, the data is imported to the machine using this PSW software, the job is named and the orientation is set accordingly. The interface shows the one to one dimension of the building area in the process chamber.

Process Parameter	EOS Standard Setting
• laser power	• 200W
scan speed	1250mms^{-1}
Scan Spacing	100µm
• Layer Thickness	• 30µm
Beam diameter	100µm
Post -Treatment	• none

Table 3.1: Standard EOS processing parameters for EOS Ti64 powder

Table 3.1 provides the standard processing parameters suggested by EOS for EOS titanium alloy powder. This is the default setting for titanium alloys used in this machine and those parameters can be changed within the acceptable range of values. The allowable parameters are laser power, scan spacing, scan speed, scanning strategy (stripe width, overlaps) and layer thickness. In this research work, the testing and specimen fabrication of titanium alloy parts was based on these standard parameters.

3.2.5 Scanning strategy

In DMLS, a 3D part is constructed by consecutively sintering/melting powder layers. The laser beam moves in the x and y directions in order to scan all the predefined 2D area. The area can be scanned with individual single lines or using a raster scanning method. The raster pattern consists of individual scan lines, each overlapping the previous one to form a continuous layer. The fundamental processing unit of the DMLS process is single scan line.

The Skin & Core scanning strategy was used for all of the parts fabrication in this work in order to standardise the scanning method. In the Skin & Core method, the parts are divided into two regions. The material is first contoured around the cross-section using a focused beam with 0.1mm diameter at a speed of 1250mm/s and a power of 150watts. The cross-section is then raster scanned at 1250mm/s at 170watts with a step over of 0.09mm. Once a layer is completely built, a roller then evenly adds a new 30-micron thin layer of powder over the top of the previously cured (or formed) part. The process is then repeated until the part is complete.

The EOS GmbH M270 machine has a huge advantage by offering a controllable scanning strategy, which means that the scanning of a part can be divided into different regions or areas with a different scanning parameter. The machine's process software can split the model into two types of build area, 'Skin' (outer shell) and 'Core' (inner). This can speed up fabrication times by defining different laser scan speeds and layer thicknesses. Each experiment may require different skin and core settings as explained above.

The scanning strategy used in this research work is shown below (fig 3.7):

a. *Contour scan* – The material was first contoured around the cross-section using a focused beam of 0.1mm diameter at a speed of 1250mm/s at 150watts.
b. *Raster scan* - The cross-section was then raster scanned at 1250mm/s at 170watts with a stepover of 0.09mm

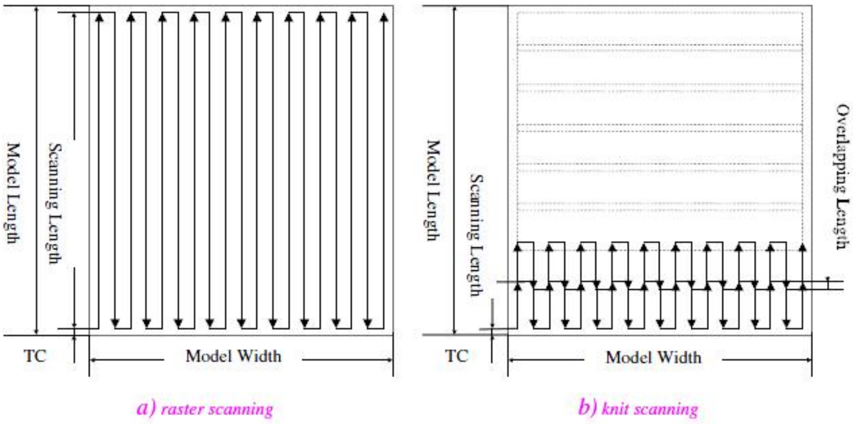

Figure 3.7: Type of scanning pattern

3.3 EOS Ti6Al4V Powder Characterisations

The powder used in this research work was EOS Ti64 powder. One of the main criteria for a good flow-ability and distribution of the powder during the sintering/melting process is to have small, spherically shaped powder. A 63µm sieve was used and placed on the top of the powder container. Titanium powder, which comes in sealed bottles, was tipped out of the bottle onto the net and a scraper was used to distribute the powder uniformly. This step was repeated until the container had a sufficient amount of powder.

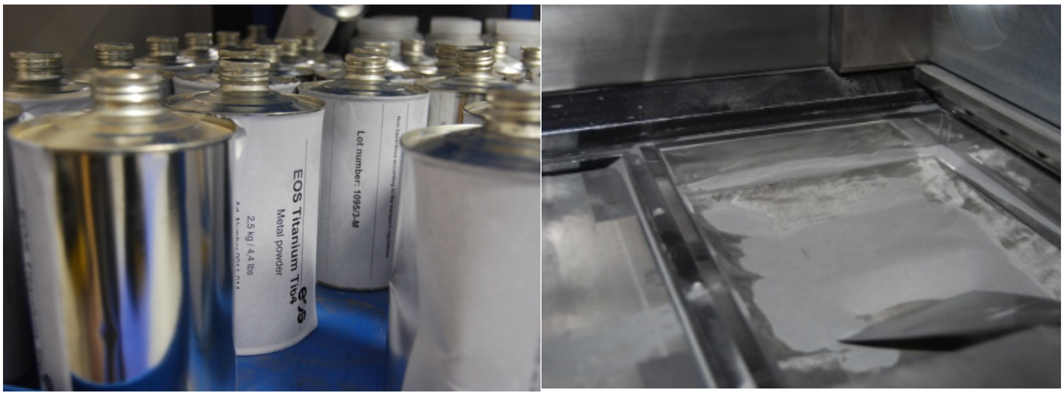

Figure 3.1: EOS Ti6Al4V powder

3.3.1 Particle Size, Shape and Distribution

The powder particles were in a range of 10 to 100 micron (fig 3.9). The analysis showed that the average particle size was $37.93\ \mu m$ with the lowest percentile (0.1) reported at $24.45\mu m$ and highest percentile (0.9) at $58.05\mu m$. The specific area of the powder particles was $0.168m^2/g$. The results also showed that the size distribution of the powder particles produced by a gas atomisation technique were generally small and lower than 100μm (Table 3.2). The powder particles also had a tighter average size distribution range of about 40 μm.

Parameter	
Powder Particle	Ti6Al4V
Particle Reflective index (RI)	2.22
Dispersant Name	Water
Dispersant Reflective Index (RI)	1.33
Obscuration	12.83
d(0.1)	24.48 um
d(0.5)	37.93 um
d(0.9)	58.05 um
Mean	39.82 um
Standard deviation	13.04 um

Table 3.2: Particle size distribution of EOS Ti64 powder

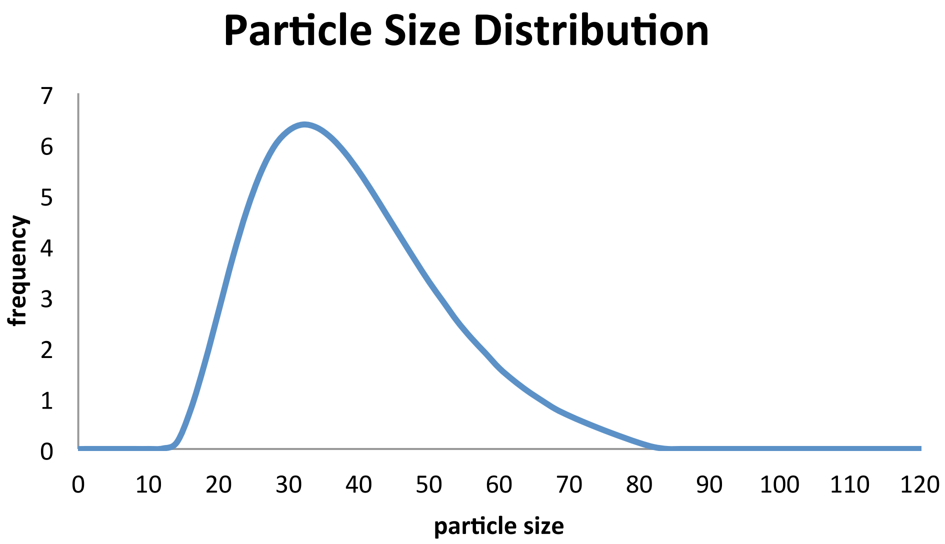

Figure 3.9: Graph of the particle size distribution

Morphology and Chemical compounds

The morphology of the Ti6Al4V gas atomized powder was examined using optical microscopy and scanning electron microscopy. The chemical compounds were investigated using Electron Dispersive Spectroscopy (EDS).

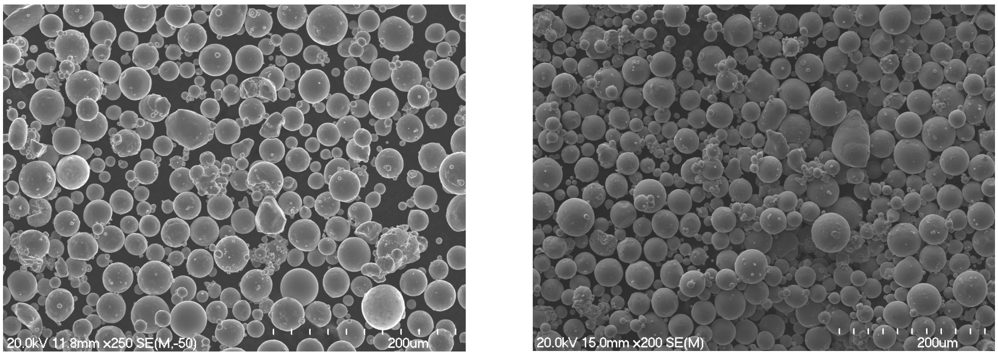

Figure 3.10: SEM images of the EOS Ti64 powder

Generally, all the powder particles were spherical. A few irregular particle shapes were seen in the powder sample due to vibration and rough handling. It also noted that the powder particles were of small size with an average size of 50microns.

3.3.2 Compositional analysis

From the elemental analysis, there were no other elements detected besides titanium, aluminium and vanadium confirming a lack of chemical contamination on the surface.

Table 3.3: Compositional analysis of EOS Ti64 titanium alloy powder

Ti6Al4V	Raw powder	mounted with epoxy resins
Aluminium	5.76	4.91
Vanadium	4.66	4.84
Titanium	balance	balance

The interstitial elements were not investigated since the sample powder received from the fabricator was not carefully sealed. Some contamination was expected.

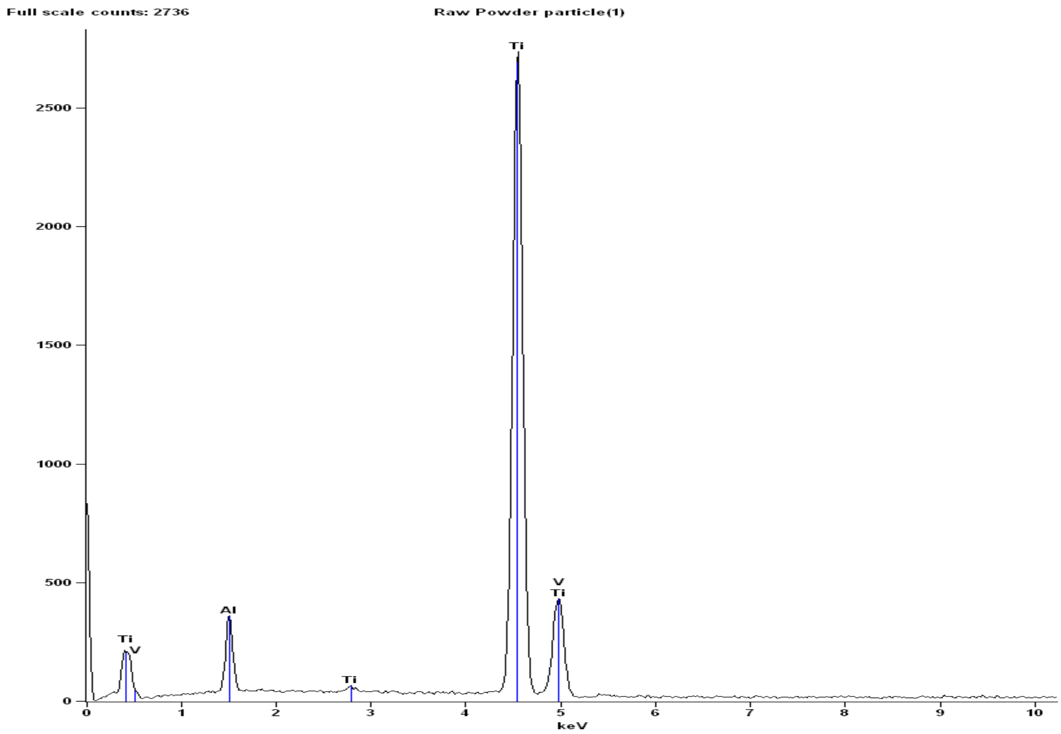

Figure 3.11: EDS Data of the EOS Ti6Al4V

Ti6Al4V	Wt %	Error	ISO 5832-3	ASTM F1472(%)
Ti	89.57	±0.67	balance	balance
Al	5.76	±0.15	5.50/6.75	5.50/6.75
V	4.66	±0.43	3.50/4.50	3.50/4.50

Table 3.4: EDX compositional test results compared with ISO & ASTM standards

Figure 3.11 shows that the composition of the Ti6Al4V gas atomised powder, examined with the Ti6Al4V powders mounted in epoxy resin, has the lowest aluminium percentage (4.91%) compared with ISO and ASM standards, but with an acceptable vanadium percentage (4.84%). The aluminium and vanadium content of un-mounted Ti6Al4V powder was 5.76% and 4.66% respectively. Table 17 confirmed that the percentage of aluminium and vanadium is within the range of the ASM and ISO Standards. The gas atomized powder used for the laser sintering process had 5.76% aluminium and 4.66% vanadium respectively. The percentage set by the standard is 5.50 to 6.75 % aluminium and 3.5 to 4.5%

vanadium. The powder is supplied by EOS specifically for use in the EOSINT M270 machine.

3.3.3 Powder Particle Density

The powder density was calculated using gas pycnometry apparatus. Three consecutive readings were performed to calculate the mean and standard deviation. The results are as shown below;

	Ti6Al4V
Powder Mass	89.21g
Average Volume	20.26cc
Average Density	4.4025 g/cc
Volume SD %	0.0047

Table 3.5: EOS Ti64 powder density

Relative density = $\frac{4.40}{4.46} x\ 100$

= 98.65%

Based on the Ti6Al4V reference density of 4.46gcm^{-3} the atomized Ti6Al4V powder has a relative density of 98.65% which is considered to be near to full powder density.

Chapter 4: Fundamentals study on DMLS

Stationery laser spot on the powder bed

The aim of this chapter is to elucidate the effect on geometrical characteristics of a focussed laser beam at various laser power outputs on a Ti 6Al 4V powder bed. Experiments were carried out to analyse the influence of DMLS parameters particularly laser power on the melt pool size and morphology of the synthesized laser spot. A stationery Nd:YAG laser beam with power varying from 20W to 200W was struck on loose Ti6Al4V powder for ten seconds. A period of ten seconds was selected as this will produce specimens with measureable size even at the lowest laser power. The as built structure due to this condition was reported and analysed prior to a powder consolidation mechanism. Results showed that at each laser power a blob structure or a spherical droplet was formed consisting of a melted core and surrounded by incompletely sintered powder particles similar to a hemispherical shape. The specimen sizes varied from 1mm to 8mm in diameter with increasing laser power. Metallographic analysis showed that the neck size between powder particles varied with the laser power depending on the location and distance from the centre of the laser beam spot. The spherical droplets or blobs had a bigger radial distribution compared with their depth with increasing laser power.

4.1 Introduction

Direct metal laser sintering (DMLS) is considered to be a feasible way of producing complex parts for low production runs. Many studies have shown that this technique, which employs additive manufacturing principles, is capable of producing functional parts with mechanical properties comparable to more conventionally made parts[1-4]. Therefore, much of the research on sintering processing was directed towards extending the use of this technology in critical areas such as aerospace and biomedical applications where customised design is of prime importance. However, the emphasis of many of the studies was more on the applications rather than on fundamental studies of the sintering mechanism, particularly on laser-material interaction. This is because, many researchers had difficulty understanding the sintering process which involves a large number of mutually influential, complicated parameters [1, 5].

Based on typical laser sintering definitions, a sintered structure consists of particles bonded by necks where only partial or surface melting has occurred (binding at the interfacial grain contact area). However, with the advances in laser and powder technologies, the DMLS process is indeed capable of producing fully density parts where the powder particles are fully melted during the process. Of particular interest is the heat transfer mechanism where, during laser-material interaction, a sufficient amount of energy (heat) is absorbed by the powder which causes phase changes from solid powder to liquid and finally back to solid. This interaction happens very quickly, within microseconds, depending on the processing parameters. Subsequently, residual stresses develop in a laser sintered part and this influences the integrity of the part[6, 7]. With a greater understanding of process-microstructure relationships, one can modify and manipulate the process parameters so that desired properties can be achieved.

4.2 Experimental & Processing Conditions

The loose titanium alloy powder used is known as EOS Ti6Al4V with an average particle size of 40µm. The powder was sieved using a 63µm filter and placed in the powder container in the building chamber with a layer height of 10mm and without any substrate. This was to provide a sufficiently large enough processing zone without the influence of a substrate. Argon gas was flushed through until the oxygen level dropped to 0.01% and the chamber temperature was set 80˚C throughout the experiment. Powder scanning was accomplished using a Nd:YAG laser beam (1.06µm wavelength). The processing parameters were adjusted so that the laser strike on the powder bed was accomplished in accordance with the set parameters.

There was a long enough gap between each laser strike so that each sintered structure, corresponding to its laser power, could be distinguished. The scan speed was set to zero which means that the laser was kept motionless during the experiment and the time duration for each strike was 10 seconds. As-built specimens were collected and labelled corresponding to the laser power used.

A Quantachrome Instrument, Ultrapycnometry 1000 was used to calculate the density of the laser sintered part. The operation of this instrument is based on Archimedes principle and Boyle’s Law. Nitrogen gas was used instead of Helium which can penetrate the finest pores of the sample near to 0.25nm.

Microstructural examination was performed using an optical microscope and Scanning Electron Microscope (SEM) equipped with an EDS analysis system. Phases were identified determined by the XRD method using the Philip X-Ray Diffractometer. Microstructural examination was carried out on the polished cross-section of specimens, etched with the Kroll’s reagent (100ml of distilled water, 3ml of HF, 6ml of HNO_3). Measurement of the cracks, particle sizes and other structural features were made using the Image Analysis software on the optical microscope.

4.3 Results

A crucial aspect of the DMLS process is the heat flow from a laser strike on the powder bed with a highly focused beam occurring predominantly downwards through the previously solidified layer or substrate. In this experiment, the powder bed was set at 10mm thick in order to avoid the influence of the substrate. Within this relatively long exposure time, the material is continuously heated to above or below the β transus temperature with each laser beam pass. Therefore, the microstructure occurring in a layered structure may be complex and the degree of complexity will depend on the thermal history.

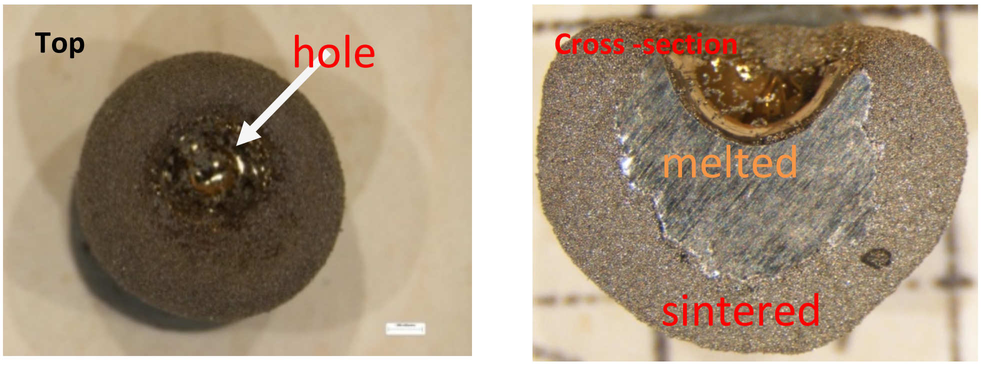

Figure 4.1: The features of a blob, showing a hole and cross section

4.3.1 Geometrical Characteristics

All the samples collected after the 10seconds laser irradiation shared a similar shape but with various sizes as predicted. The shape could be best described as a ball shape or blob with a small hole on the top. The hole had a shiny surface surrounded by agglomerated powder particles. The cross-section of the samples provided in more detail the features of the irradiated structure, and clearly showed that for each of the laser power levels applied, there are two distinct regions comprising solid and porous material.

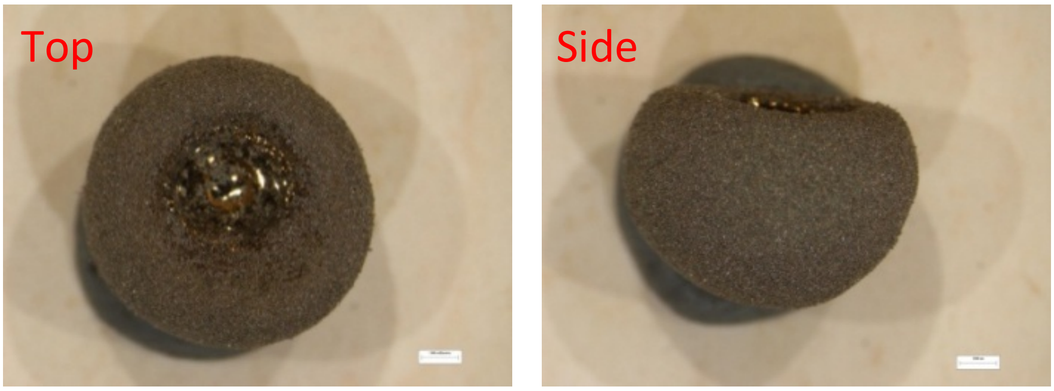

Figure 4.2: Top and side view of the blob (taken from a 100W blob)

Figure 4.1 and 4.2 show top and side views of a blob. The figure shows that the as-sintered structure resembles a spherical droplet or a ball shape. All the blobs have the same shape and morphology which may well suggest that there is a tendency for the powder particles to form a spherical droplet prior to a movingless laser beam. Cross-sections of the blobs show the feature of the laser-material interaction in more detail. The blobs can be divided into a solid core or inner part and a porous outer part.

At the core or inner part, a solid surface is observed which resembles a half-moon shape. This shiny flat inner structure is surrounded by weakly bonded powder particles. The size of the structure gradually increases with higher laser power and so does the size of core/inner region. The boundary dividing these two regions is visible but is not a sharply delineated feature. Surrounding the melted core is a partially sintered zone or a region of partially melted particles where the powder particles were fused together to form inter-particle necks.

There were no pores or micro cracks observed in the melted region. All of the blobs had a small hole on the top where the laser first struck the powder bed. The diameter of the hole for each blob is quite similar ranging from 0.8mm to 1.2mm. This may indicate that the high energy density associated with each of the laser powers used causes the powder particles to evaporate and splash thus creating a small empty space. This might be the reason for all the blobs having a hole or space on the top surface. The form of the hole appears to be consistent for each of the laser powers used. It was only at 140W that the hole on the collected blob appeared to be very small.

Laser Power (W)	**Sintered region (Outer)**		**Melted Region (Inner)**	
	Depth (mm)	Width(mm)	Depth(mm)	width(mm)
20	1.9	2.6	1.0	1.3
40	1.9	3.6	0.8	1.4
60	3.3	4.1	1.5	2.1
80	3.7	5.4	2.3	2.9
100	3.4	6.1	1.6	3.7
120	5.2	6.0	3.3	3.6
140	5.2	6.7	3.4	3.8
160	5.8	7.1	2.8	4.2
180	5.8	7.3	3.6	4.7
200	5.8	7.3	3.8	4.7

Table 4.1: Blob measurements collected and measured by Optical Microscopy after 10 seconds laser beam exposure

The data in table 4.1 shows the relationship between laser power and the measured size of the blobs after the powder bed had been exposed for 10 seconds to form a single laser spot. The spot size was maintained at 100µm throughout the experiment. Therefore, the effects of variations in spot size diameter can be neglected. In the present investigation, smooth, flat, and shiny surfaces are observed in all the laser processed specimens. Each of the different laser powers produces close to a ball shaped structure or blob with two distinct regions consisting of solid and porous regions even when the power is as low as 20W. The solid region or melted zone depth increases with increased laser power and the depth of the melted core region, similar to a half-moon shape, also increases with increasing laser power.

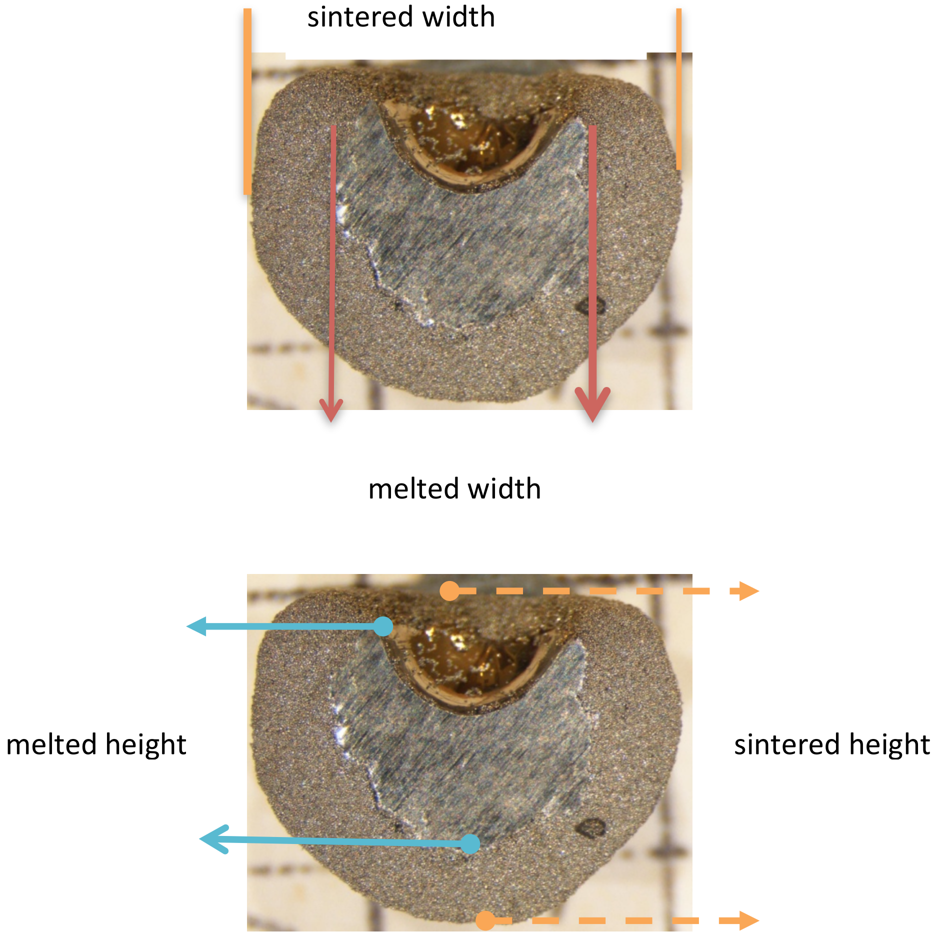

Figure 4.3: The dimensions used for measuring the sintered blobs

	20	40	60	80	100	120	140	160	180	200
Solid	√	√	√	√	√	√	√	√	√	√
porous	√	√	√	√	√	√	√	√	√	√

Table 4.2 : Solid and porous part on the blobs

The table and figure 4.3 above confirm that each blob consists of two distinctive features: a solid part and a porous structure. The solid core represents the fully melted area where sufficient energy was absorbed by the powder to form a molten pool which then solidified. The molten pool also moves downward and infiltrates the powder particles beneath. This is visible at the boundary between the solid and porous area where no sharp boundary is noticeable. The molten pool was also spotted outside the melted core region which suggests that the high beam intensity has splashed a small amount of the molten pool outside the core region (fig. 4.13).

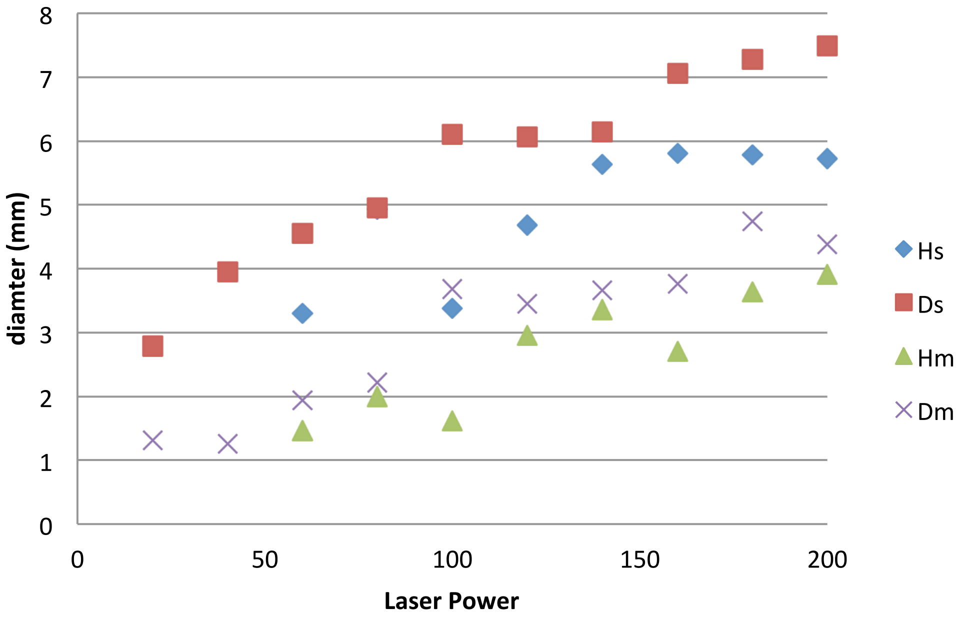

Figure 4.4 Blob size variations prior to increasing the laser power

The data indicates that the laser power has a linear relationship in terms of size, weight and density of an as built structure (fig 4.4). The size, weight and density of an as-built structure varies almost linearly with laser power. The blobs have a diameter (radial distance) bigger than their depth (height) with respect to the centre of the blob. The radial distance was measured at the centre of the cross section rather than at the top surface (fig 4.5). This is because there is an empty space (hole) at top surface, like a crater which makes it difficult to select the correct centre point.

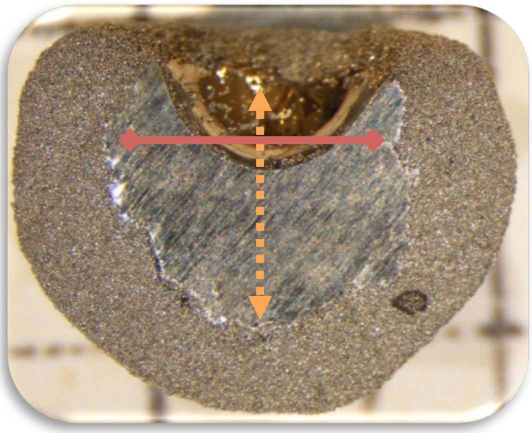

Figure 4.5: Shows the radial distance from the centre point

Therefore, the data shows a bigger radial distribution even though one can see that there is only a slight difference in measurements. There is a huge increase in depth between 100W to 120W giving a depth increase of about 2mm. When the laser power exceeds 120W, there is only a slight increase in height and diameter.

4.3.2 Blob Weight & Density

Each of the samples was weighed and its density calculated using a digital weighing machine and gas pycnometry equipment respectively. The results show that the blobs' weight and density have a linear relationship with the laser power. The weight varied from 0.02g at 20W to 0.56g at 200W. The density of the sample at 20W was 1.69gcm^{-3} and it increased gradually to 4.02gcm^{-3} at 200W.

Laser Power	weight	density
20W	0.02g	1.69 g/cm^3
40W	0.07g	3.02 g/cm^3
60W	0.14g	5.43 g/cm^3
80W	0.21g	5.46 g/cm^3

Table 4.3: The weight and density of blobs for laser power from 20-80W.

The relative density was measured using Archimedes' principle using gas pycnometry apparatus. For each sample, the average of three readings was taken. These values are useful for comparing the different samples, but one should be aware of the possible overestimation for DMLS samples. When there are larger pores within the samples, particularly at 60W to 100W, the samples can be filled with unmolten powder particles during the process and these will wrongly contribute to the total amount of bulk material.

Laser Power	weight	density
100W	0.27g	5.51 g/cm^3
120W	0.33g	3.76 g/cm^3
140W	0.39g	4.29 g/cm^3
160W	0.48g	3.74 g/cm^3
180W	0.54g	3.65 g/cm^3
200W	0.56g	4.02 g/cm^3

Table 4.4: Weight and density of the blobs for increased laser power from 100W-200W.

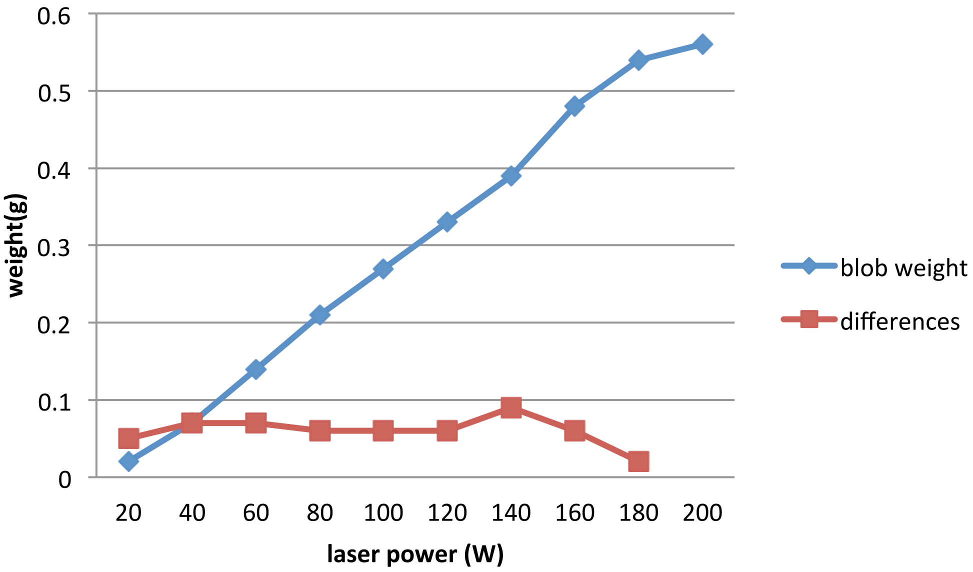

Figure 4.6: Weight in relation to laser power. Differences in weight with stepped increases in laser power of 20W

Based on tables 4.4 and 4.5 and the graph in figure 4.6, it is clear that an increase of laser power causes an increase in the size, weight and density of the deposited blobs. At lower laser power the laser energy density is low and therefore the sintered volume is small. With higher laser power, the energy density is higher and therefore the sintered particles are bigger. It is also clear from fig. 4.6 that the difference in weight is minimal from 20W to 120W and becomes a maximum at 140W and then falls when increased further to 180 W. This suggests that an optimum laser-material interaction occurs at a laser power of 140 W, where a bigger melted core and larger amount of sintered particles were observed. Contrary to this, at 180W and 200W, the differences in weight fall to 0.06g and 0.02g respectively, even though the laser power is higher.

The laser energy density for a stationery laser beam can be calculated as shown below:

$$laser\ energy\ density\ (LED) = \frac{Laser\ Power(J/s)}{laser\ beam\ diameter(m)} \tag{16}$$

The energy per volume was obtained by dimensional analysis (Jm^{-3}). The energy density unit is Joules per square mm. From this equation, 20W gives an energy density of 25461 Jmm^{-1} while 200W produces ten times the energy density at 20W. It is clear that by increasing the laser power gradually to 20W has caused a slight increase in weight. The highest recorded weight difference and the highest density were given at a laser power of 140 W. This suggests that an optimum energy density was absorbed by the powder bed at a laser power of 140 W. This is also reflected in the size and morphology of the blob at 140W, where the hole/space at the top is smaller and the melted top is flat. It should also be noted that the density of the 140W blob reaches the theoretical full density which is 4.29gcm^{-3} .

	Laser Energy Density (kJ/m^{-3})	**Differences in weight (g)**	**Blob's density (g/cm^3)**
20	25.5	0.05	1.69
40	50.9	0.07	3.02
60	76.4	0.07	5.43
80	101.9	0.06	5.47
100	127.3	0.06	5.51
120	152.8	0.06	3.76
140	178.2	0.09	4.29
160	203.7	0.06	3.74
180	229.1	0.02	3.65
200	254.6		4.02

Table 4.5: Weight differences and density of the blobs in relation to laser power.

4.3.3 Physical characterisation of a blob

Blobs were sectioned in order to investigate the surface of an internal cross section. Only selected blobs were sectioned due to difficulties in holding and cutting them. The cross-sections are shown below. The images in Table 4.6 were taken using an optical microscope at lower magnification. Red and yellow circles are used to generalize the diameter of the sintered blobs and melted core respectively. A circle was drawn to best represent the diameter of the core and the blob.

It can be seen that for a blob the cross section consists of two distinct features which are a melted zone and sintered powder particles. The sintered particles completely surrounded the melted core. For all of the blobs, except for that in specimen C, the melted core region is more like a half moon shape where the top region is an empty space. There is no sharp boundary separating these two regions.

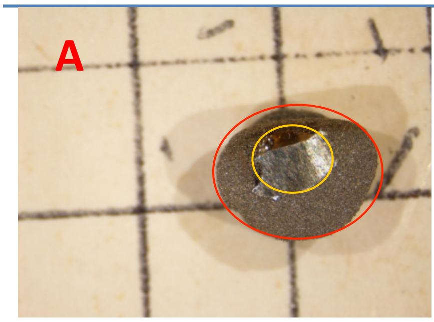	Laser Power : 100W Blob size:6.1mm Melted core diameter:3.7mm
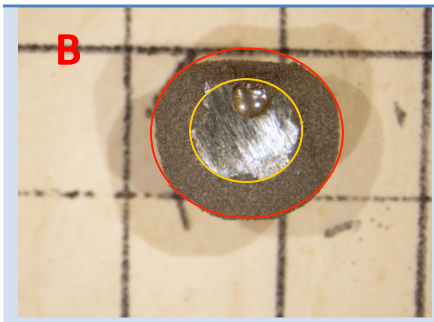	Laser Power : 120W Blob size:6.0mm Melted core diameter:3.6mm

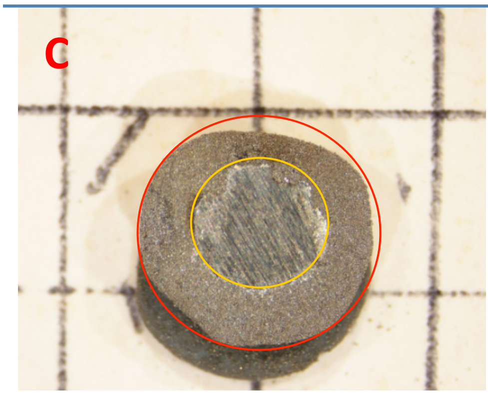	Laser Power : 140W Blob size: 6.7mm Melted core diameter: 3.8mm
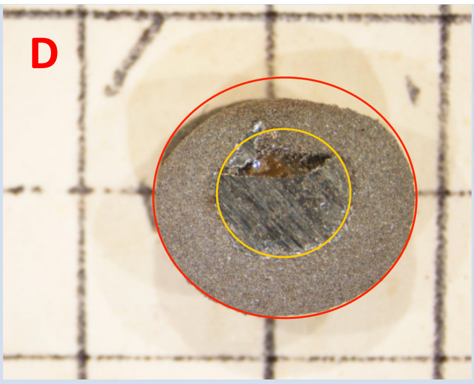	Laser Power : 160W Blob size:7.1mm Melted core diameter:4.2mm
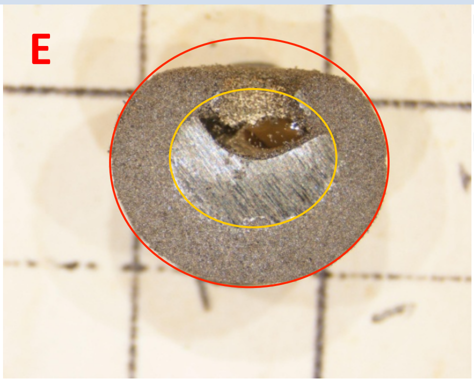	Laser Power : 180W Blob size:7.3mm Melted core diameter:4.7mm
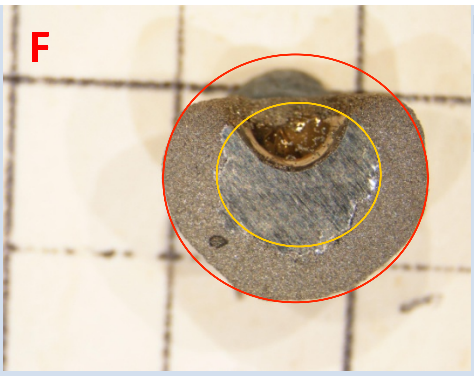	Laser Power : 200W Blob size:7.3mm Melted core diameter:4.7mm

Table 4.6: cross section surface of the blobs (100W-200W)

It is clear from the images in table 4.6 that the size of the blobs or the spherical droplets increases with increasing laser power. The red and yellow circles were used to compare graphically the gradual increase in diameter of the inner and the outer parts. It can also be seen that the ratio of the inner diameter to outer diameter is consistent regardless of the increased laser power. This is one of the significant similarities shown by the blobs particularly for A to F.

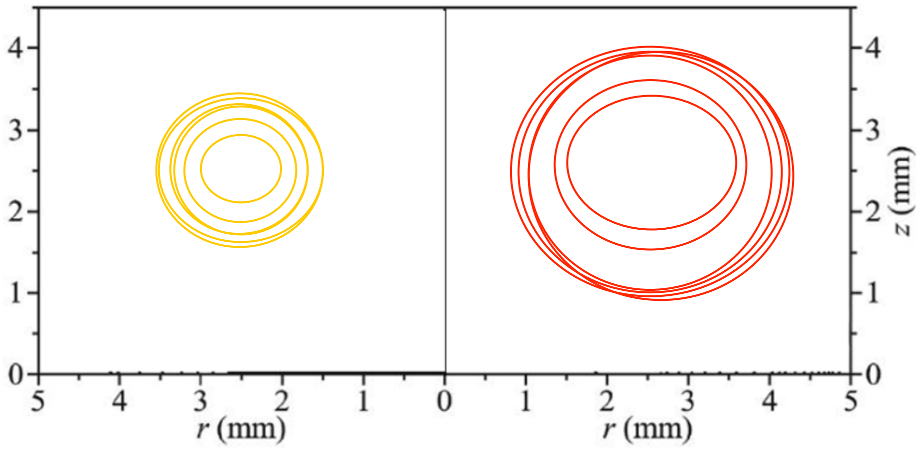

Figure 4.7: Inner (melted) and outer diameter of the blobs

Figure 4.7 shows the increase in the inner and outer diameters relative to the radius. Table 4.7 provides the inner and outer diameter measurements for the blobs and the corresponding ratio. There is a significant difference of 0.7 mm in the outer diameter when the power input changes from 120W to 140W. The average outer to inner diameter is 1.6 and the highest recorded ratio at 140W is 1.8.

	Inner diameter (mm)	Outer diameter (mm)	Ratio
100W	3.7	6.1	1.6
120W	3.6	6.0	1.7
140W	3.8	6.7	1.8
160W	4.2	7.1	1.7
180W	4.7	7.3	1.6
200W	4.7	7.3	1.6

Table 4.7: Inner and outer diameter of the blobs

The data in table 4.6 and 4.7 show that there is a consistent relationship between the laser, the powder and its exposure time. The blobs obtained provide a good indication of the molten pool and the heat affected zone. It is also worth highlighting that there are no geometrical differences in the melted core and sintered region for a laser power level of more than 180W.

4.3.4 Features & Surface of the sectioned blob

Scanning electron microscopy was used to characterise the sectioned blobs. The surface of sectioned blobs was not polished or etched in order to maintain the as-sintered features. The purpose was to investigate the two distinctive features associated with the blobs which are the melted core in the inner part and the partially melted particles surrounding the melted core. The blobs have important features which can be divided into three main regions

1. The inner part
2. The outer part
3. The boundary (intermediate)

Core (Inner Region)

At the core or inner region, the particles are fully melted which means that the powder particles experience a high laser temperature. The surface of a cross section is very rough due to the high speed cutting that has left many scratch lines on the surface. At each of the laser powers used (20W-200W) the blobs produced consisted of a melted core with the size increasing from 1mm to almost 5mm in diameter.

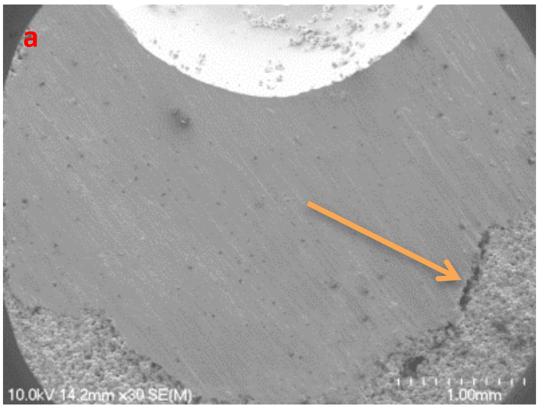

Fig. 4.8 SEM image of the core region of 200W blob (a)(b)

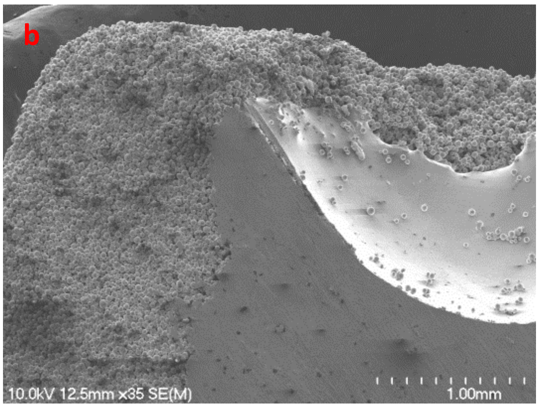

The core region consisted of a solid area where the powder particles were fully melted forming a shape like a half moon. There is a curvature (empty space/hole) at the upper part (crater) where the laser strikes the powder bed. A small amount of sintered powder can be seen on the top surface In the intermediate region, indicated by the arrow, there is a boundary separating the melted and sintered region. The melted powder particles have infiltrated the sintered region mostly at the upper part. There are no pores or micro cracks visible on the surface.

Outer Region (sintered region)

The outer region consisted of weakly bonded powder particles which have been partially melted. Due to heat radiation and conduction through the powder bed, the high temperature spreads through the powder particles but not high enough to melt them. The hot melted core acts as a source of heat transfer to the surroundings. This resulted in many weakly bonded powder particle agglomerates which together formed a larger partially sintered structure around the melted core.

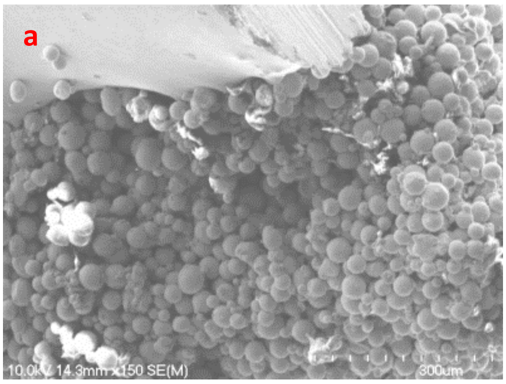

Fig. 4.9 SEM images of outer region of 200W fibre laser (a)

The less effectively sintered region encompasses the core region and this had a uniform radius except for the upper part. In this region the powder particles were bonded together through the formation of necks. The neck size varied depending on their location and distance from the core. At higher magnification agglomerates and inter-agglomerate particles were also visible near to the core.

A brief analysis was carried out in order to investigate how the particles were bonded at the outer region. An area situated at 1mm to 10mm from the edge of the core region was analysed. The observation showed that the partially melted powder particles were connected via neck formation.

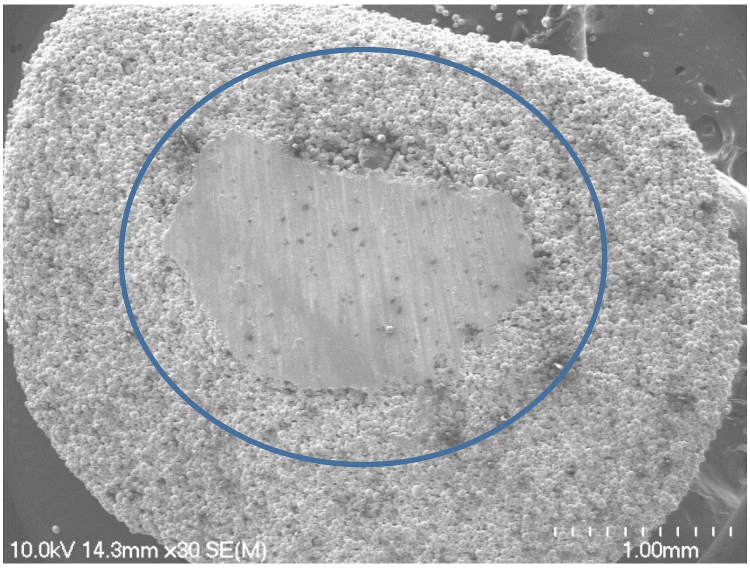

Figure 4.10: The area where partially melted particles were analysed (200W Blob)

The size (width) of the necks also varies depending on the laser power used and the location away from the melted core. The widths of 15 measurable necks on blobs from each of the laser power inputs were calculated and the average is presented in Table 4.8 below:

Laser Power	Neck size range	Laser Power	Neck Size range
20W	3 µm to 6 µm	**120W**	12µm to 15.5µm
40W	3.5 µm to 8 µm	**140W**	12 µm to 16 µm
60W	6 µm to 10.5µm	**160W**	13.5 µm to 15.5 µm
80W	10.5 µm to 12.5µm	**180W**	12.5 µm to 15.5 µm
100W	13.5 µm to 16 µm	**200W**	10 µm to 13.5µm

Table 4.8: Necks width of the each blob

The data collected shows that the width of a neck increases with the laser power. At low laser power, the powder particles were weakly bonded with the formation of narrow necks. The particles were also further apart. At higher laser power the necks became wider and the distance between the particles was smaller.

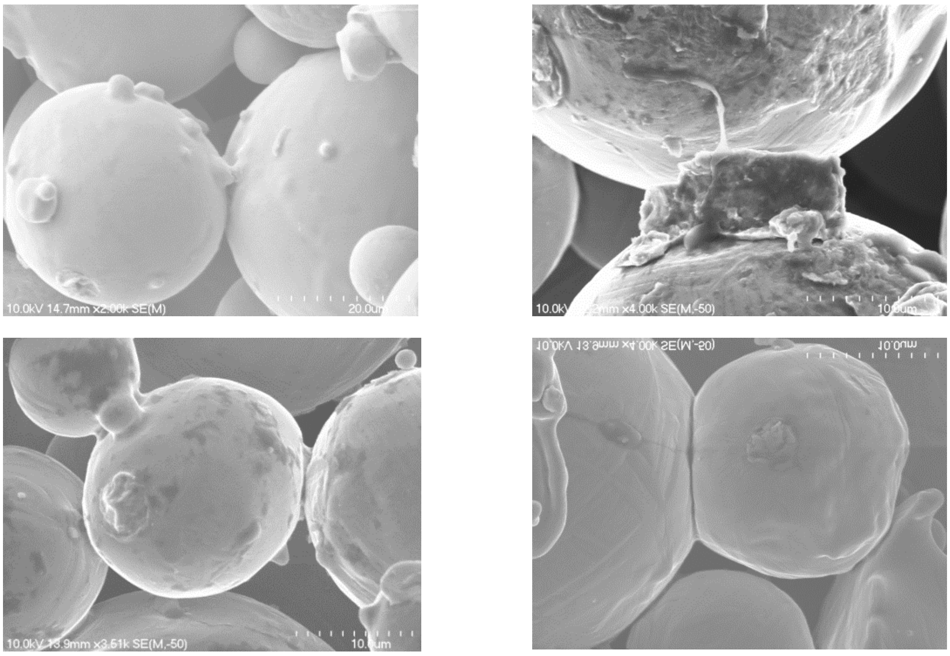

Figure 4.11: Type of necks formation observed in the porous region

The image below shows how the width of the neck was measured for each of the blobs. The measurements were performed within a predefined area which was 1 to 10mm from the edge of the melted core. The distance between the two connected particles was also measured.

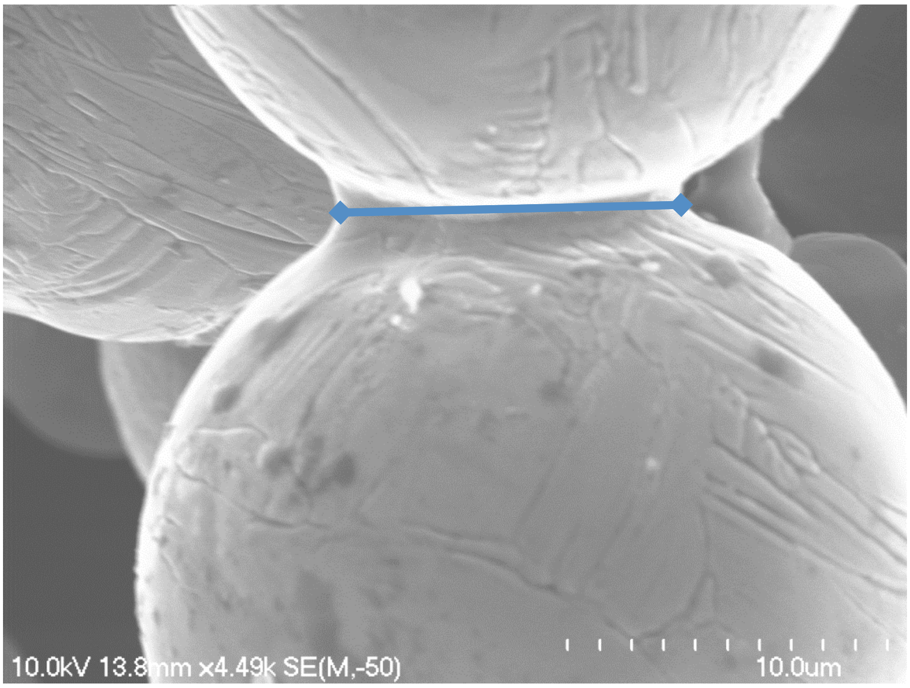

Figure 1.12: Neck size measured at the neck of the each blob

It was observed that the outer region of the blobs consisted of partially melted powder particles which were connected together by necks. The different features of the necks formed between the particles could be explained through the different isothermal conditions. The heat source from a highly focused laser beam is absorbed by the powder particles thus increasing the powder bed temperature. If the energy is sufficiently high enough, the laser fully melts the powder particles and forms a molten pool. This molten pool solidifies once the laser moves away. If there is insufficient heat the powder particles are only partially melted and a partially sintered region with porosity is created. This partially sintered zone consists of particles bound together by necks. A wider neck keeps the particles closer together compared with narrower necks. This could well be related to the formation of pores in the partially sintered region. The size and width of the necks may have a huge influence in determining the porosity of a part.

The boundary (Intermediate region)

In this study, the intermediate region of the cross-section of a blob is defined as the boundary separating the melted core and the outer low sintered region. Obviously, there is a visible boundary dividing these two regions. The boundary is not perfectly circular in shape as the infiltration occurred at the upper part and mostly at the lower part of the sectioned blobs. This phenomenon is related to the sintering mechanism in direct metal laser sintering where there is liquid pool formation. Most of the particles near to the inner region are covered by the molten pool. The molten pool is also visible at the outer region of a blob. It is possible that, due to the high isothermal condition and prolonged laser strikes, the molten pool splashes out of the inner region and infiltrates the powder particles underneath.

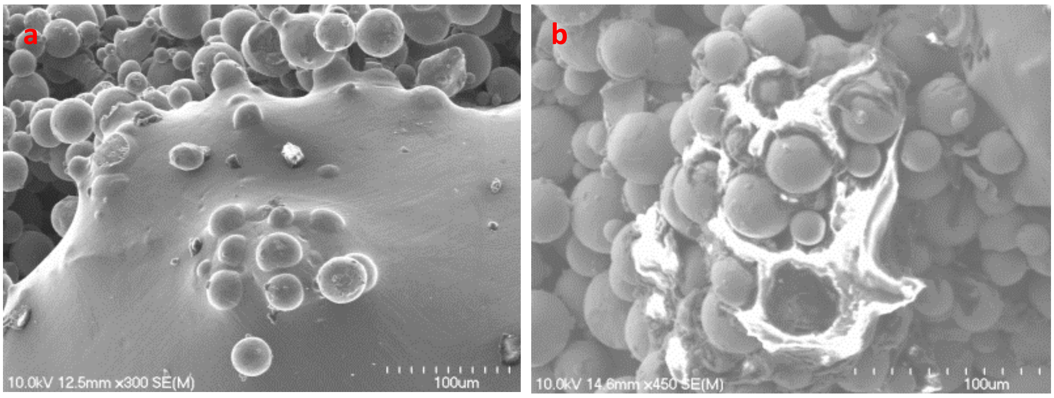

Figure 4.13: Particles in the intermediate region where the melted core and the sintered particles are divided. (a) & (b) are SEM images of a blob made using a 200W laser strike.

The images above show the metallic powder particles after they have been subjected to a high isothermal condition located near to the core. The temperature in this area is above the titanium melting temperature where most of the particles are fully melted. The molten pool infiltrates the particles near to it and fuses them together. There are also agglomerates of powder particles visible at locations near to the molten pool. The molten pool from the core area splashes to the nearby location due to the high energy density and when the molten pool solidifies, it holds the powder particles together to form a bunch of particles with a porous structure. These solid particles are weakly bonded and are normally seen near to the melted core.

A prominent feature in Figure 4.13, where the weakly bonded particles are located, is the size and shape of the pores formed due to partially melted particles. The width of pores and necks are identical. For similarly sized powder particles, the pore size and shape is homogenous. This probably indicates that the particles are located at the same temperature line or contour. The temperature is just high enough to cause the surface to melt and attract the surrounding particles.

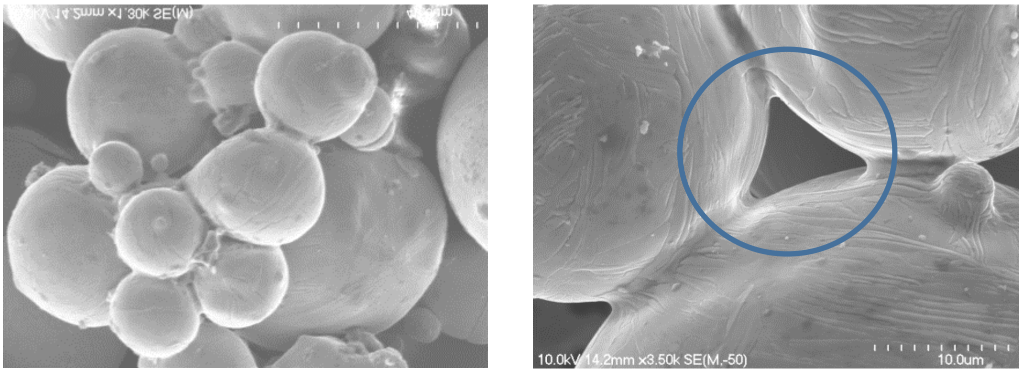

Figure 4.14: Agglomerated powder particles and pore structure.

Measurements were performed to quantify the neck width using SEM images, such as those shown in figure 4.14. Measurements were taken from random spots outside the melted core. It can be seen that, there are distinct differences between the ways that the particles fused together to leave porosity at the outermost circular region of the blobs. It was observed that in this area, the neck formation is only reached at an early stage of neck growth. This is indicated by the concave necks formed between adjacent particles. However, near to the melted core, the degree of sintering was much higher. The particles in this area have formed a fully coalesced structure. This observation is in agreement with a theoretical sintering model reported in the literature [8], which describes a mechanism in which particle penetration starts from the initial point of contact and is accompanied by neck build up. The experimental work in this study was used to describe the effect of laser power on the degree of sintering. With higher laser power and therefore higher energy density, a greater degree of sintering is observed. This greater degree of sintering was characterised by a greater neck width and smaller pore size.

4.4 Heat transfer Analysis

Two methods were selected to describe and explain the heat transfer during DMLS. The analytical solutions were obtained by utilizing MATLAB version 6.5 software with a mathematical model and a numerical model. For this analysis, a few assumptions and simplifications were made such as a decision to keep the thermal properties of titanium alloys constant throughout the laser interaction. The second method which was explained in detail in chapter 2 used a numerical solution by executing the MATLAB laser tool program

4.4.1 Temperature profile and evolution using the mathematical model

The aforementioned mathematical solutions were used to describe the temperature profiles and their evolution during DMLS. The results were analysed and plotted.

Laser power(W)	**Maximum heat flux (W/m²)**	**Time for surface to melt (s)**
20	3×10^{9}	0.1161×10^{-3}
40	5×10^{9}	0.0402×10^{-3}
60	7.6×10^{9}	0.0181×10^{-3}
80	10×10^{9}	0.0104×10^{-3}
100	12.7×10^{9}	0.0065×10^{-3}
120	15.3×10^{9}	0.0045×10^{-3}
140	17.8×10^{9}	0.0033×10^{-3}
170	20.4×10^{9}	0.0025×10^{-3}
180	22.9×10^{9}	0.0020×10^{-3}
200	25.5×10^{9}	0.0016×10^{-3}

Table 4.9: Time for surface to melt (only the time to melting is used)

Table 4.9 shows the laser power and its corresponding heat flux. It is clear that a higher laser power causes a higher heat flux and a shorter time for the surface to melt. At 20 W, the heat flux generated was 3×10^{9} Wmm^{-2} which is high enough to melt any metallic powder particles within a fraction of a second. Based on this calculation, it takes only 0.1161×10^{-3} sec to melt the Ti6Al4V powder. Obviously, an increase in the laser power increases the heat flux generated and this increases the surface temperature. For standard operating parameters, the laser power used is in the range of 170W to 200W. A high laser power input is normally used because it gives a bigger processing window. This means that the powder needs less time to melt or only requires a short exposure time with a higher laser power thus allowing the scan speed to be increased considerably.

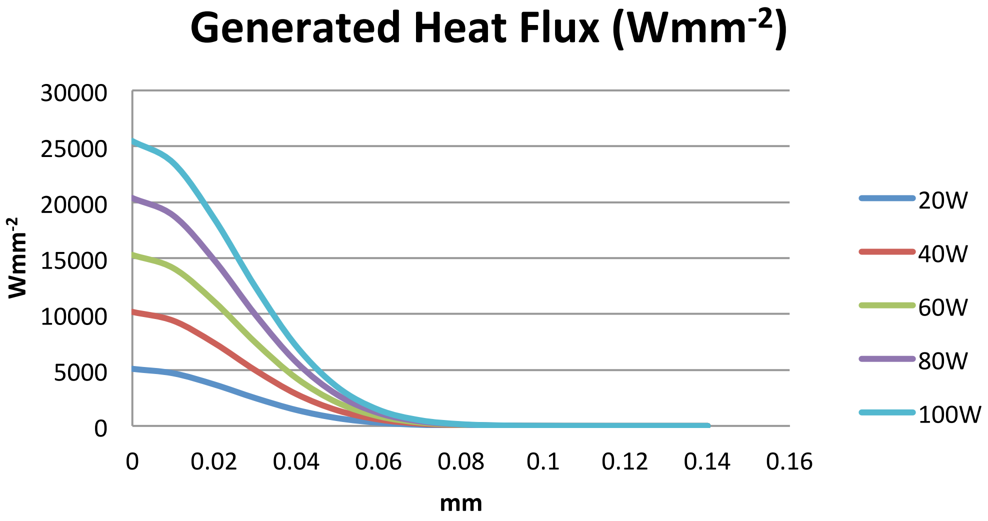

Figure 4.15: Heat flux generated within the beam radius (Wmm^{-2})

The heat flux generated on the powder bed surface is linearly proportional to the laser power. The graph in figure 4.15 shows the variation in heat flux generated with increasing laser power up to 100W. A 20W laser power creates 5000 Wmm^{-2} heat flux on the surface of the powder bed subjected to a stationery Gaussian laser beam profile. At 100 watts laser power, 25000 Wmm^{-2} heat flux is produced which causes the powder to melt within 0.0065×10^{-3} seconds. The value of time to melt could be used to determine the appropriate exposure time or the optimised processing parameters for a particular material.

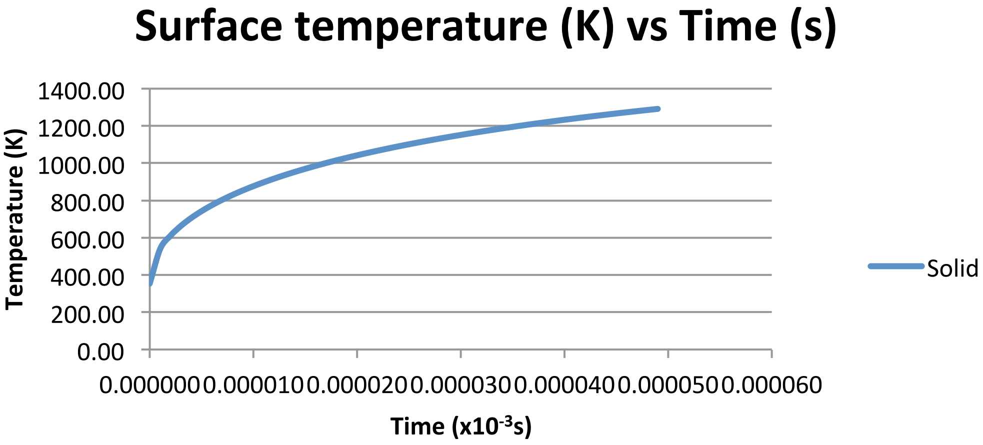

Figure 4.16: Temperature in Solid (blue)

Figure 4.16 is a plot of solid temperature versus time. The equation used to produce the data for these plots is explained in chapter 2[9]. The graph shows that the temperature in solid increases significantly within a few microseconds. It shows an increase in temperature on the powder bed as the process continues. If the maximum temperature is above the melting temperature then the powder is melted by the power of the laser beam. If the maximum temperature is below the melting temperature then the powder will remain solid or only partially melt.

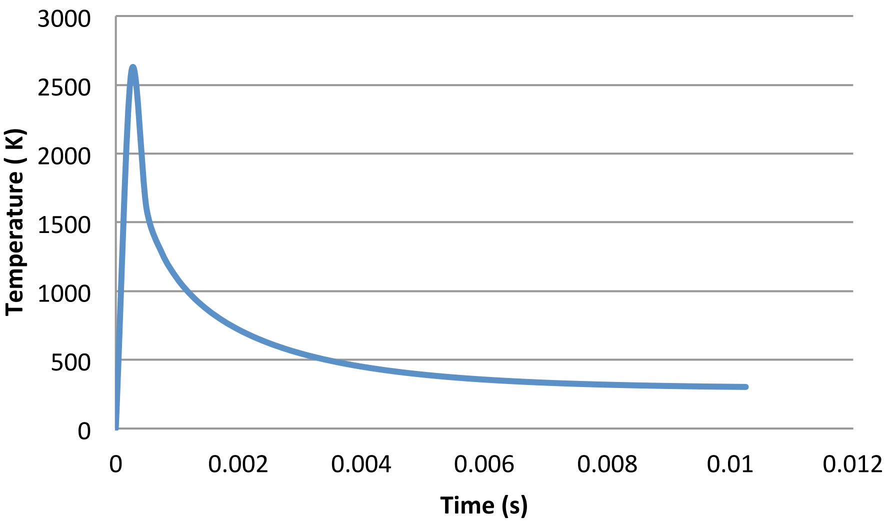

Figure 4.16a: The surface temperature of the powder bed for 20W within 0.01s

Table 4.10 also shows the effect of the laser power and hence the magnitudes of the heat flux on the maximum temperature in the powder, with respect to time. It is clear that the maximum temperature obtained is above the melting point of the powder, thus creating a molten pool. The experimental results show that the 20W blob has a small solidified liquid pool area. The temperature time plot in Figure 4.16a shows that the temperature drops rapidly after the laser heat supply is taken away, regardless of the laser power used. Heat conduction is the likely cause of a slower rate of temperature fall. As the heat is spread homogenously in the powder bed via conduction, it helps to create an even temperature over the penetration depth.

4.4.2 Numerical Method Solution

For the numerical analysis, a Gaussian power density distribution in the xy plane was used. The laser beam intensity is defined by the equation below[10];

$$I(x,y) = \frac{8P}{\pi d^2}\, exp\left[-\left(\frac{2\sqrt{2}}{d}\right)^2 .\,(x^2+y^2)\right] \qquad (17)$$

where P is the laser power and *d*(m) the beam diameter of the power density distribution. A simulation of the laser irradiation on the substrate was executed in MATLAB. The detail of the programming is explained in Chapter 2.The results are shown in the table below.

	Maximum heat flux (W/m^2)	**Maximum Surface temperature(K)**		
		0.001s	**0.1s**	**10s**
20W	$5x10^7$	350K	1500K	2000K
60W	$14x10^9$	1000K	4500K	6000K
100W	2.5×10^{10}	1500K	7000K	10000K
160W	4×10^{10}	2500K	11500K	14000K
200W	5.5×10^{10}	3000K	14000K	18000K

Table 4.10: Maximum surface heat flux and temperature with corresponding laser power

Table 4.11 shows the maximum heat flux generated with respect to time. At 20W, the maximum surface heat flux is 5 x10^7 Wmm^{-2} with an associated rapid temperature increase from 1000K to 2000K within 10 sec exposure time. Above 20W, the temperature is well past the melting and vaporisation temperature. This is the reason why most of the blobs show a small hole on the top surface as a result of the massive temperature rise during the 10 sec irradiation period. At 200W, the maximum temperature during a 10 sec exposure was 18000K. Due to this high temperature, smoke was seen in the building chamber at the end of the 10 second exposure time. There was a presence of smoke accompanied by a small fire for laser powers above 160W. The presence of smoke and possibly a fire at such high temperatures during the laser sintering process must be avoided as this could cause deterioration of the lenses and the machine parts in the building chamber.

Nevertheless, in a normal operating procedure a high laser power is preferable. This is because; a high laser power provides a bigger processing window, particularly by enabling faster scanning speeds to be used. This reduces the processing time and fabricates fully dense parts. The data in table 4.11 gives the optimised laser power with respect to exposure time. If one needs to use 200W laser power, the exposure time must be less than 0.001 second as this is sufficient enough to melt the powder particles.

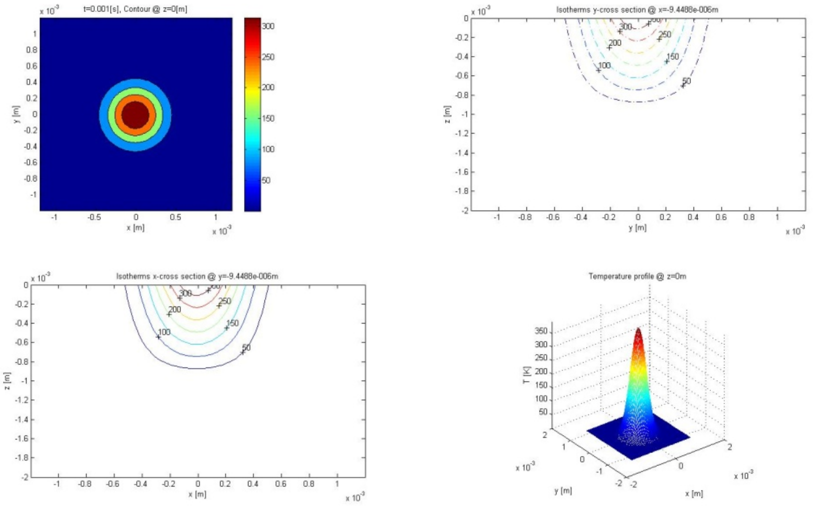

Figure 4.17: 20W laser exposure for 0.001sec (see appendix for enlarged image)

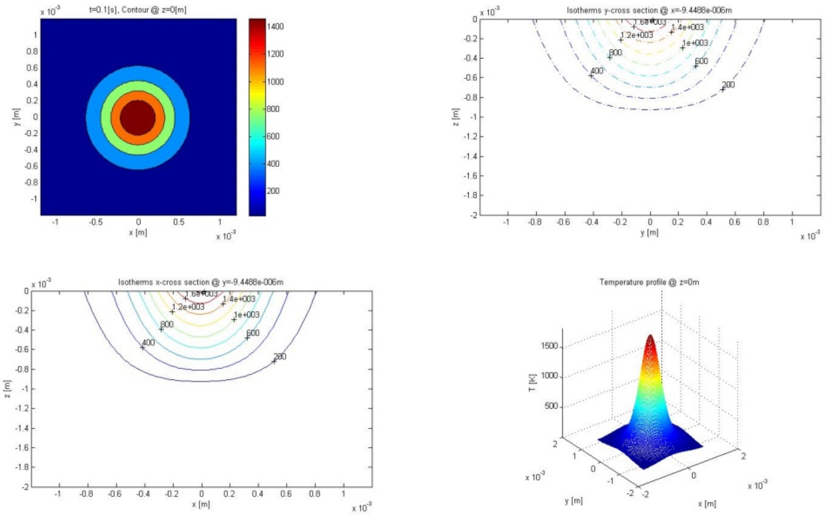

Figure 4.18: 20W laser exposure for 0.1sec (see appendix for enlarged image)

Figure 4.17 and 4.18 illustrate four different views of temperature distribution and penetration depth simulated during the DMLS process. At the top left is the radial distribution of the temperature generated due to a surface heat flux of 20W for 0.001sec. The top right view shows the y component distribution and at the bottom left is the z-component which represents the heat penetration depth with respect to the isothermal contour lines. In this simulation, it is clear that there is a temperature increase with longer exposure times. The peak surface temperature increased from 300K to 1500K within a fraction of second. The penetration depth also spread rapidly from 400µm to 800µm between 0.001 sec and 0.1 sec.

The simulation was further extended to 10sec in order to mimic the experimental results (figure 4.19). After 10 sec, the predicted maximum temperature for a 20W laser power is 2000K, which is below the melting temperature for Ti6Al4V. However the experimental result showed that there is a melted core on the 20W blob. This suggests that the simulation program slightly underestimates the maximum temperature and penetration depth which might be due to the constant thermal properties used in the calculation. It is possible that as the powder changes to liquid and then back to solid, the thermal conductivity changes. A solid has a larger thermal conductivity than powder particles and therefore spread the heat more effectively.

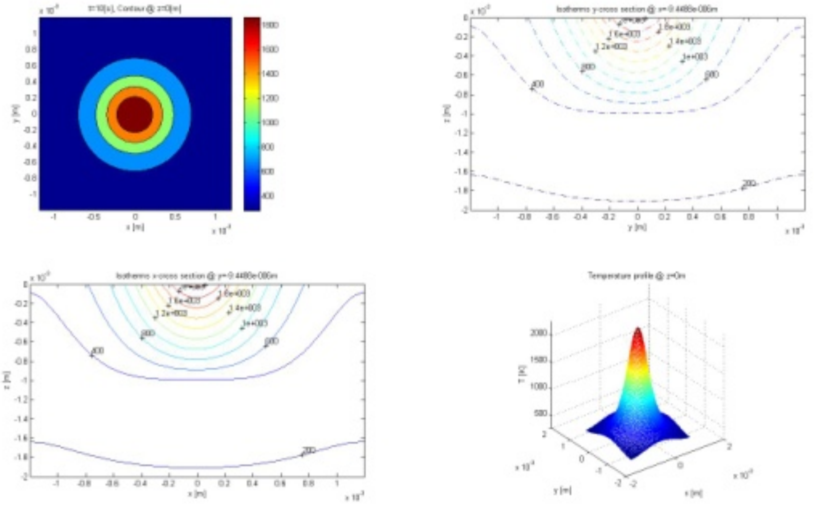

Figure 4.19: The temperature simulation of 20W laser irradiation for t =10s (see the appendix for an enlarged image)

It is observed in figure 4.19 that the temperature profiles and the penetration depth continuously increase with time. There is a larger variation in heat distribution within the innermost circle which lies within the diameter of the laser beam. The diameter of the beam was set at 100µm for the range of laser power applied in this simulation. A closer observation shows that the diameter of the innermost circle expanded to nearly 800µm and the heat penetration depth reached 1.8mm within 10 seconds. As shown in Table 4.11, there is a temperature rise as the power input increases from 20W to 60W, whereas differences in the temperature profile in the innermost regions and surroundings were possibly due to a secondary effect as a result of heat transfer by conduction across the powder bed.

The simulation result is comparable to that obtained from the mathematical model. The results for the predicted temperature profile from the mathematical model are slightly higher than those obtained from the numerical method. However, a comparison was only made for a low laser power and short exposure time as the mathematical model is not able to accurately process a high laser power for prolonged periods. Based on the experimental results, it seems as though the simulation slightly underestimated the temperature profile and penetration depth. This was expected, based on prior assumptions made about using independent thermal properties in the simulation, in order to keep a closed loop analytical solution. The heat spreads to the surrounding powder particles by heat conduction and this depends on the thermal properties i.e thermal conductivity, specific heat and diffusivity. In addition, the absorption value used in this calculation was 0.27, the lowest value for titanium powder. The lowest value of absorption used is meant to compensate for the constant thermal properties of the material. However, the isothermal contour generated by the numerical simulation gives a good correlation with the melted region shown in the experimental results. The simulation also shows good agreement with the surface temperature that causes the powder particles to melt.

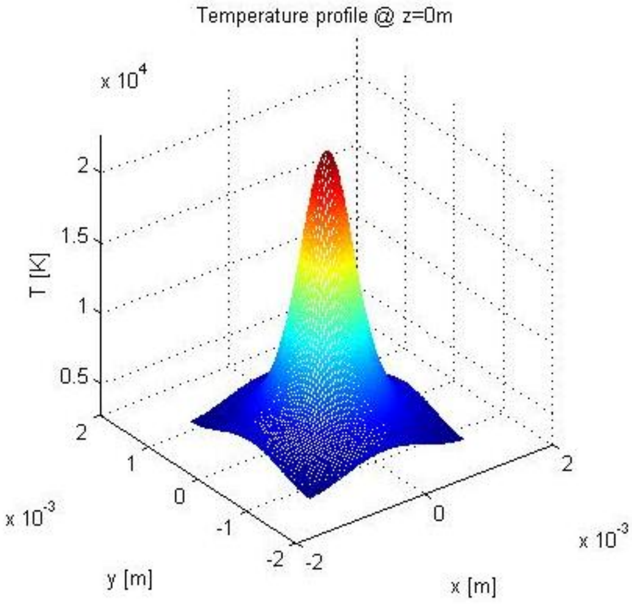

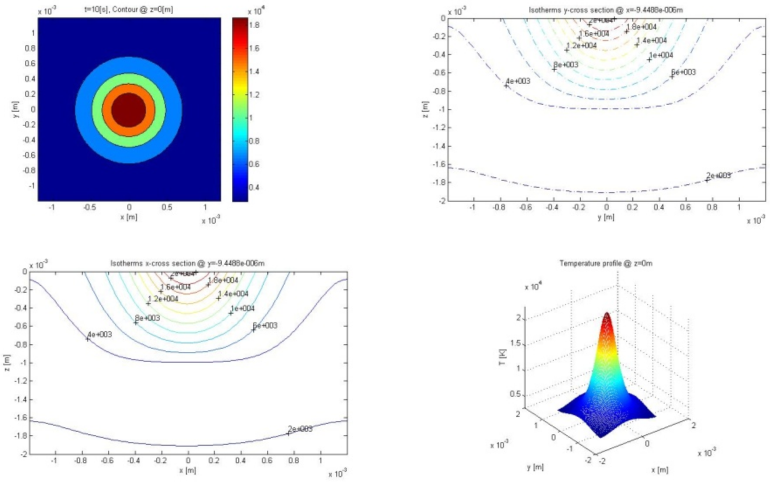

Figure 4.20: Peak temperature and isothermal conditions for 200W laser power exposed for 10sec (see appendix for enlarged image)

The maximum temperature and the heat penetration depth for a laser power of 200W, is shown in figure 4.20. The simulated maximum temperature is nearly 18000K which is too high for any processing condition. Based on the mathematical model, at 200W, the beam only needs 0.0016ms to melt the powder particles and in the simulation the temperature will reach 3000K after 0.001 sec. For the outermost isothermal contour of the heat affected area, the temperature is 2000K and the penetration depth nearly 2mm.

4.4.3 Discussion

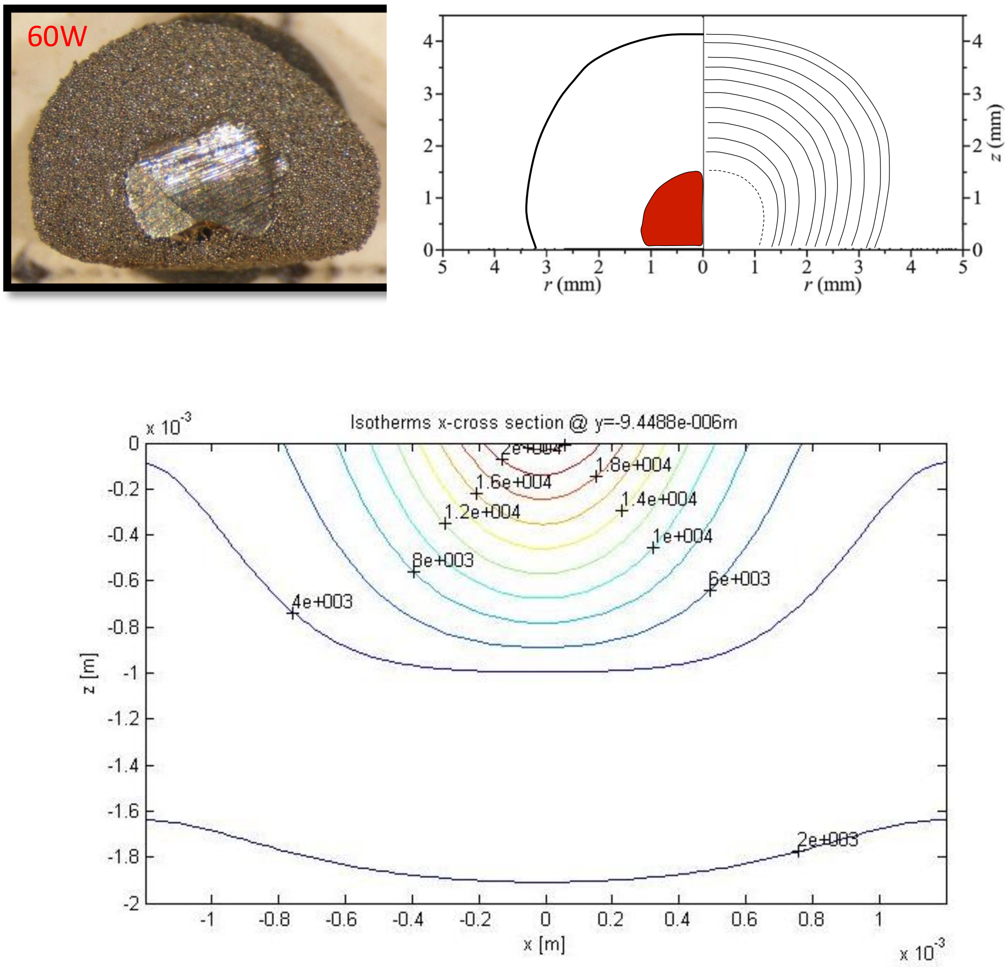

Figure 4.21: Experimental and Simulated results of the temperature distribution

Both the mathematical and numerical models used in this work employed a one dimensional heat conduction equation to solve the heat transfer in DMLS. A few assumptions were made so that the temperature-dependant material properties that cause the non-linearity in the equation can be solved. The mathematical model gives a good prediction of the temperature evolution in the liquid and solid during the laser–powder interaction. It also shows that there is sufficient time to melt the powder so that appropriate processing parameters can be determined. The numerical method utilising the MATLAB laser toolbox programme gave more detailed three dimensional information. The simulation programme established in MATLAB successfully described the temperature distribution and the isothermal conditions corresponding to variations in laser power.

Both theoretical and experimental measurements showed that the powder bed temperature, laser power and scan speed are the parameters that have the most significant influence on the thermal history of the laser sintered part. The heat source, which is the laser beam, was assumed to be the only surface heat flux and from this the temperature distribution can be explained. The derived mathematical and numerical solutions were compared with the experimental results for the sintering of Ti6Al4V powder. The isothermal contours gave a slightly lower value for the temperature of the melt pool at each of the laser power inputs used. The mathematical model gives a good estimation of the temperature evolution in the liquid and solid and also the time for the powder to melt and vaporise.

The influential material properties in determining the thermal history during laser sintering were the powder thermal conductivity, thermal diffusivity, specific heat and absorption coefficient. Both techniques which is based on mathematical and numerical solutions also confirmed that there is a significant powder bed surface temperature difference when the laser power is varied. It shows that as the energy density absorbed by the powder increases, the as sintered structure formed from a motionless laser beam, has bigger blobs with a bigger melted core.

4.5 Microstructural Characterisation

As a consequence of the building condition and strategy used, DMLS of metallic powder involves a complex solidification process which leads to a unique type of microstructure. A distinguishing feature of this process is in the predominantly downward heat flow caused by the laser beam, which irradiates the previously solidified powder and substrate. The material is therefore continuously heated up, with each laser beam pass, to above or below the beta transus temperature. Fig 4.22 shows the melted zone (core region) in a cross section of the blobs.

4.5.1 Optical Images

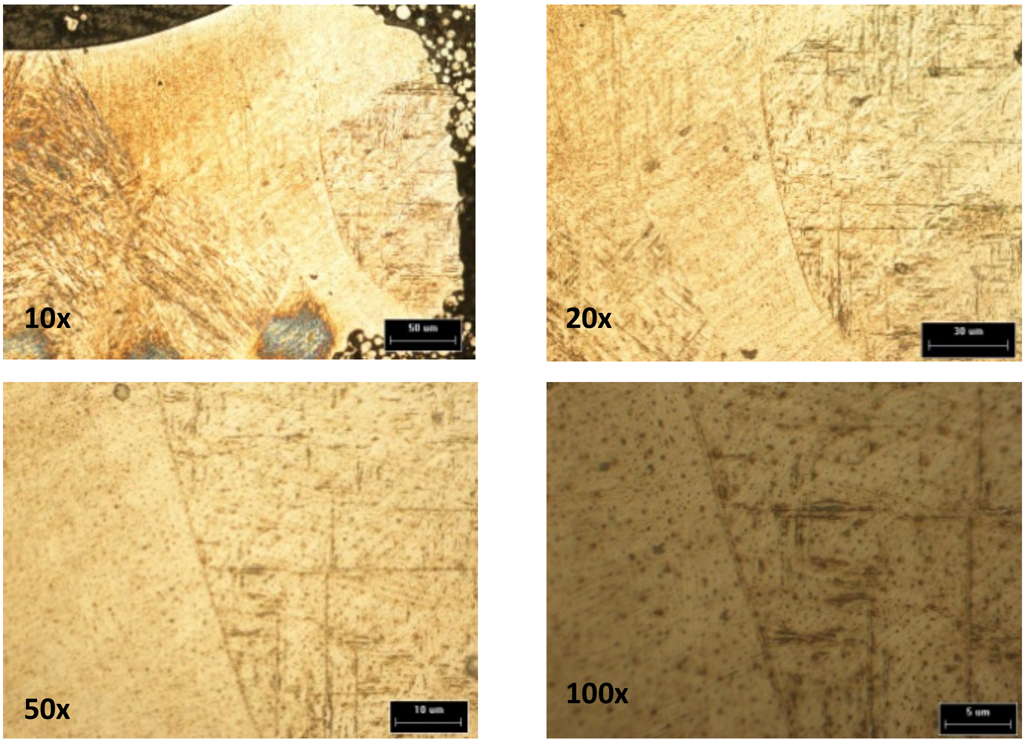

Figure 4.22: Optical images of 100W blob with different magnifications

As shown in Fig 4.22, at 100W to 200W with 10 second exposure, the interaction produces a structure like a ball, consisting of sintered particles. All of the blobs have similar surface microstructure but the size of the blobs increased as the laser power increased. In the micrographs in Fig 4.22 there are regions showing a fine and course microstructure. Near to the beam spot, the region is bright. Far from the beam spot, the microstructure is a courser acicular structure. When the laser power exceeds 160W the boundary becomes more difficult to see.

The DMLS microstructure in this particular experiment was characterised by a fine and coarse alpha-beta microstructure. The fine alpha, as a result of the fast cooling rate had transformed to alpha prime or a martensitic structure with an acicular morphology. The colonies of alpha prime (α’) with a needle like structure are mainly arranged with a 45˚ orientation to the beam axis.

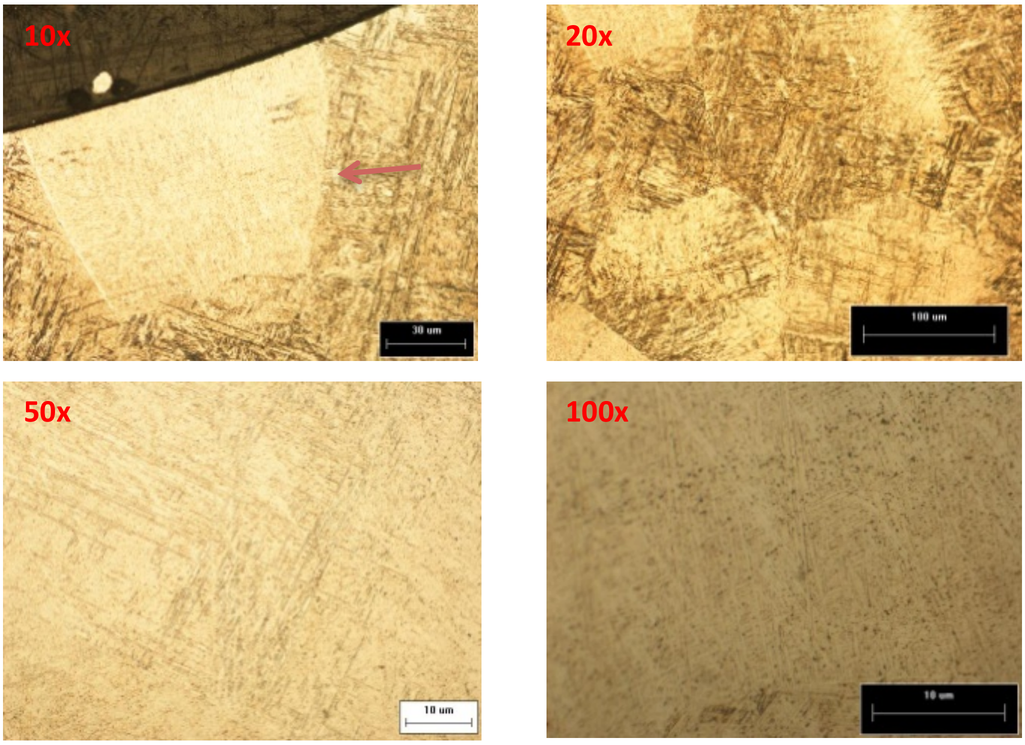

Figure 4.23: 120W blob surface texture at different magnifications

Figure 4.22 and 4.23 show a fine and a very coarse alpha-beta structure with an acicular morphology. The prior beta grain boundaries are outlined by the alpha phase.

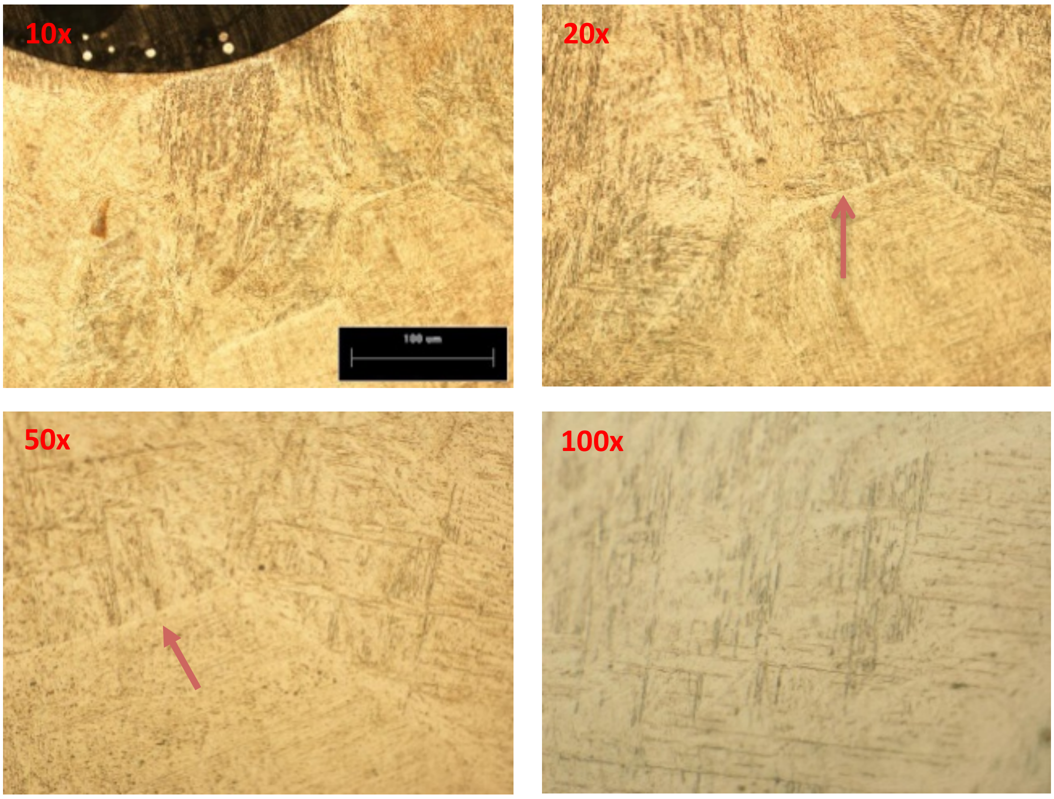

Figure 4.24: The arrow shows the α grain boundary on the surface of 140W blob.

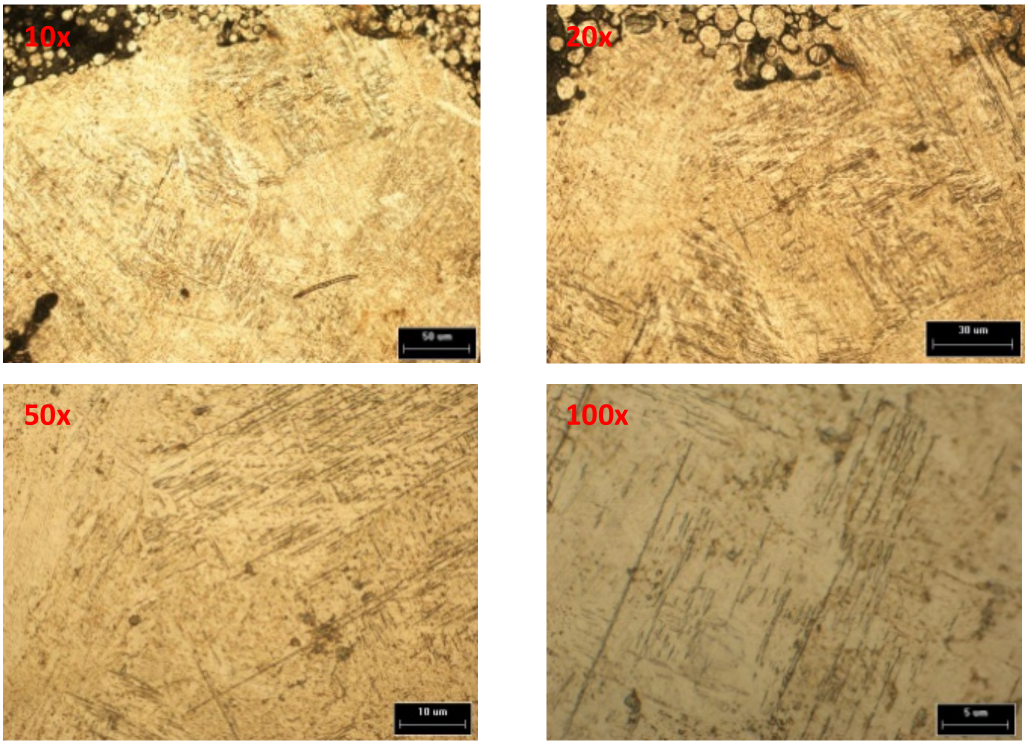

Figure 4.25: 160W blob – The grain boundary disappeared when higher laser power was used.

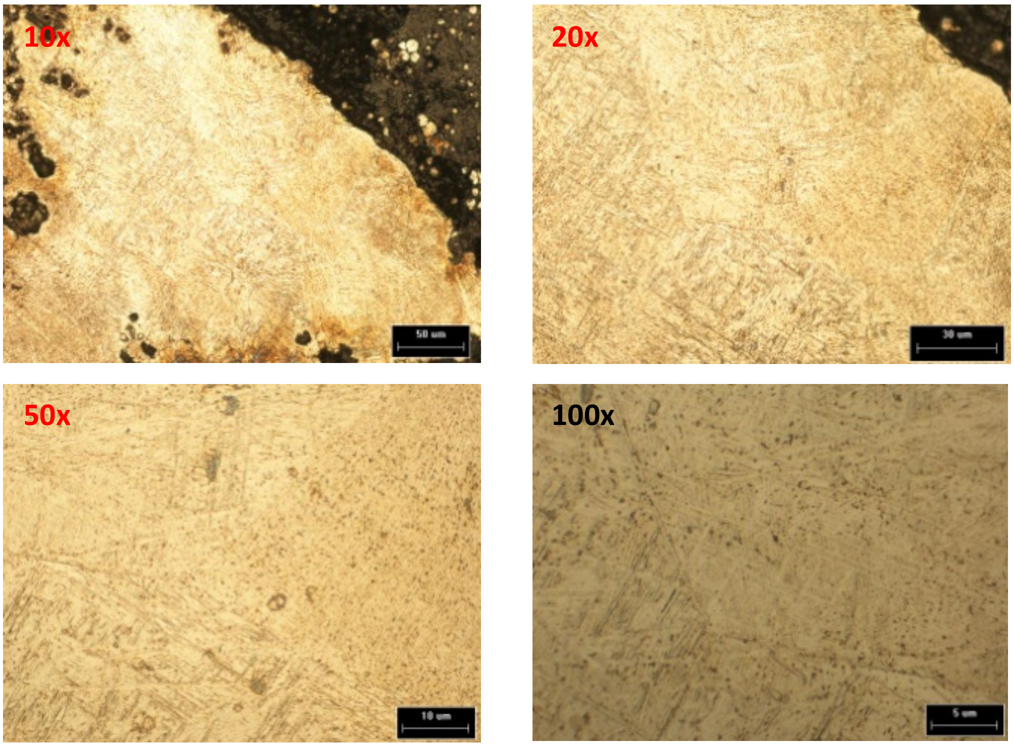

Figure 4.26:180W blob cross section surface

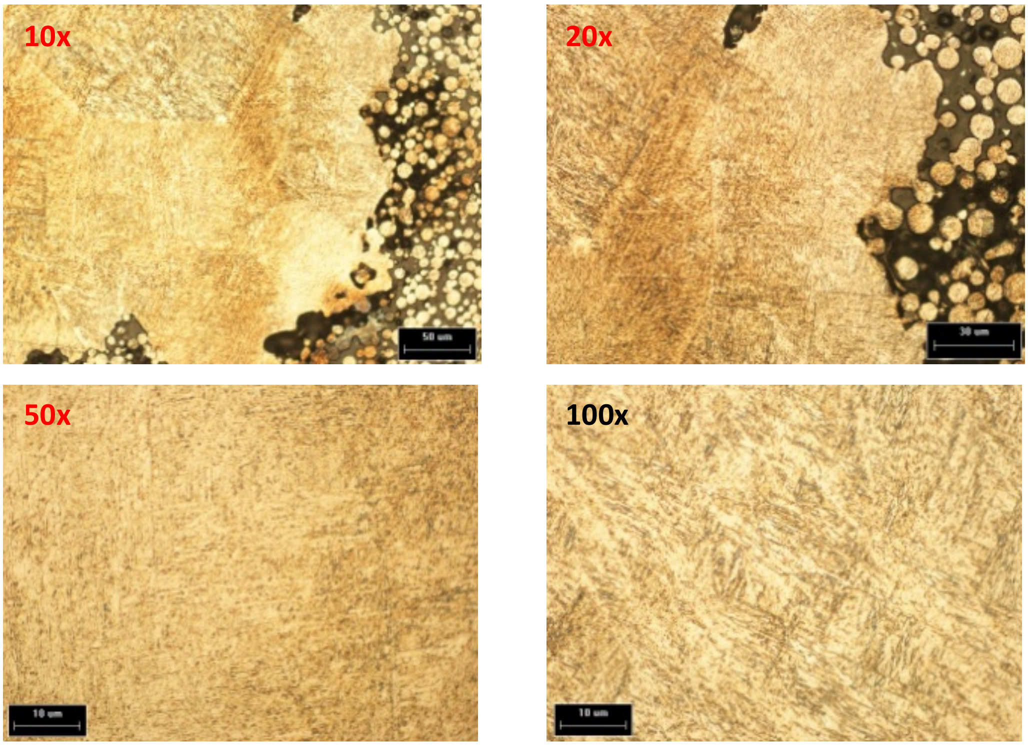

Figure 4.27:200W blob cross section surface

At a laser power above 140 W the alpha grain boundaries disappeared. The microstructure on the surface becomes more uniform in size and orientation and most of the surface was covered with a coarser lamellar structure.

4.5.2 SEM Images

Figure 4.28 shows typical macro morphologies of Ti6Al4V obtained from the DMLS process. The images show the surface of the blobs for different laser power of 140W, 120W and 100W respectively. It can be seen that the microstructure is coarser for blobs formed at higher laser power. The microstructure consists of a typical basket-weave structure with long alpha (α) plates which are oriented at 90˚ to each other. At 140W, the colony structure becomes visible in the overall basket-weave structure and each colony includes several parallel α and β laths, whose size depend on the laser power.

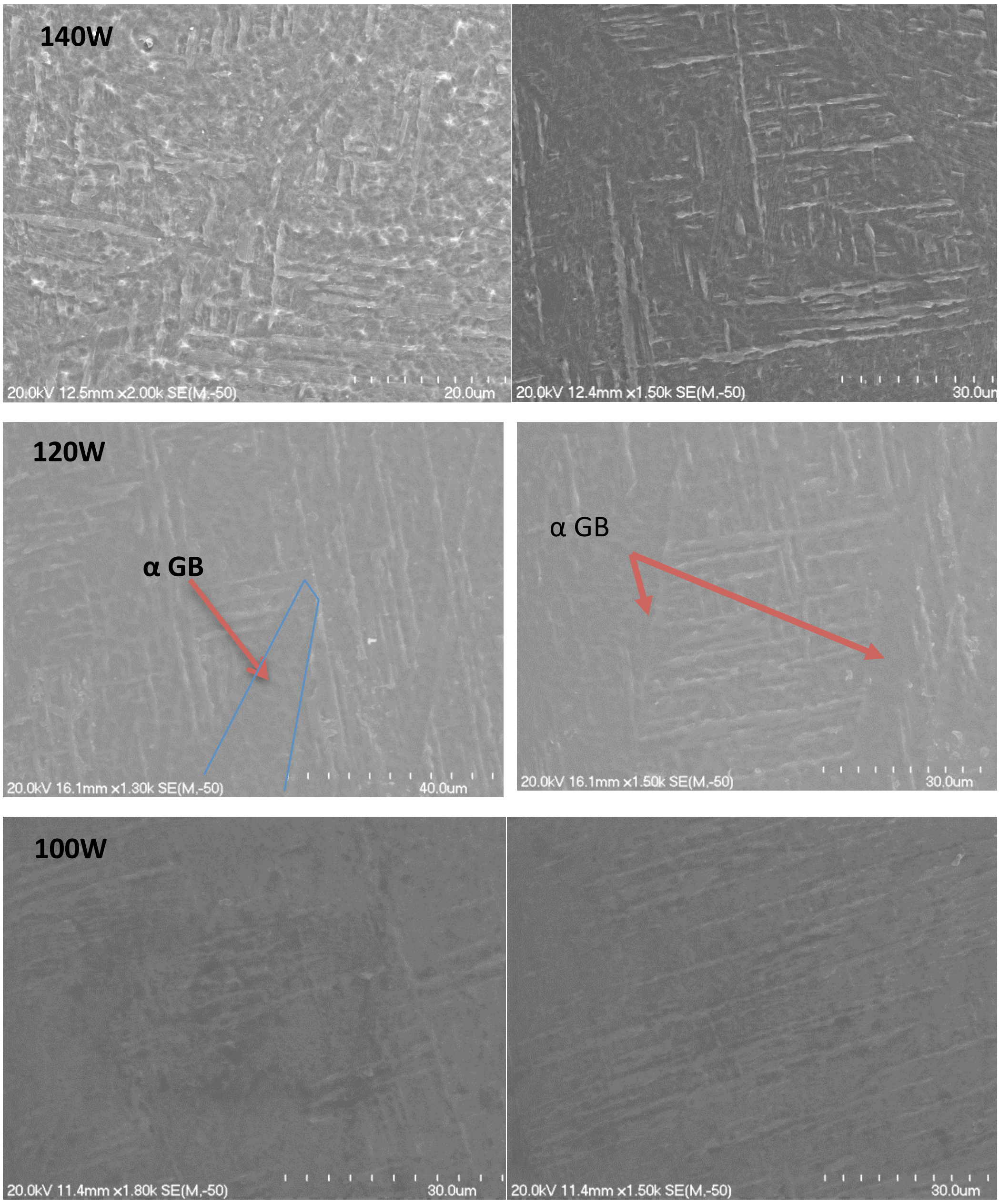

Figure 4.28: SEM images of the blobs showing the increase size of α and β laths with increased laser power

The width and length of the α /β laths also vary with laser power. At 100W, the α and β laths are thinner and longer than at 140W. The microstructure is also coarser at 140W than at 100W. It is suggested that at higher laser power, the microstructure becomes coarser. In the individual blob, the α lath width and length also vary at different locations, with the laths tending to be thinner at the top or near to the beam spot than at the bottom. The width of the α platelets ranges from 1 to 2µm. A comparison of the images in Fig 4.28 shows that there is a significant grain coarsening at higher laser power, and this is most likely caused by a slower rate of cooling as a result of a higher applied power density.

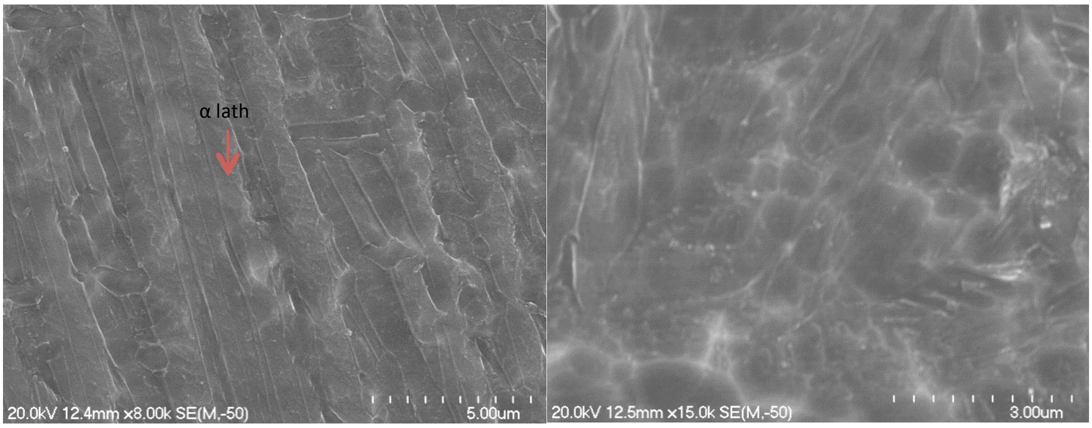

Figure 4.29: increased size of α and β laths with increased laser power

On average, the lamellae width is between 1µm to 4µm and 1 to 6µm for a laser power of 100W to 140W respectively (fig 4.29). This shows that the laser power or the energy density absorbed by the powder influences the size of the lamellae.

4.5.3 Porosity

When investigating the cross-section of the blobs, two types of porosity were found: flat pores and spherical pores. The formation of spherical balls could be due to a high volumetric energy density during the laser sintering process. The surface tension would try to minimise the energy by reducing the surface area to that of a sphere and create a balling effect. The formation of pores might also be because of the presence of hydrogen in the powder. At high temperature above the melting point, hydrogen would have a natural tendency to bubble out from the surface of the melt pool leaving behind spherical pores. Some porosity can be seen in Fig 4.30. When the laser power is increased to 160W, the pores disappear and the microstructure becomes nearly fully dense.. Porosity might also arise from the presence of trapped Argon gas in the powder bed.

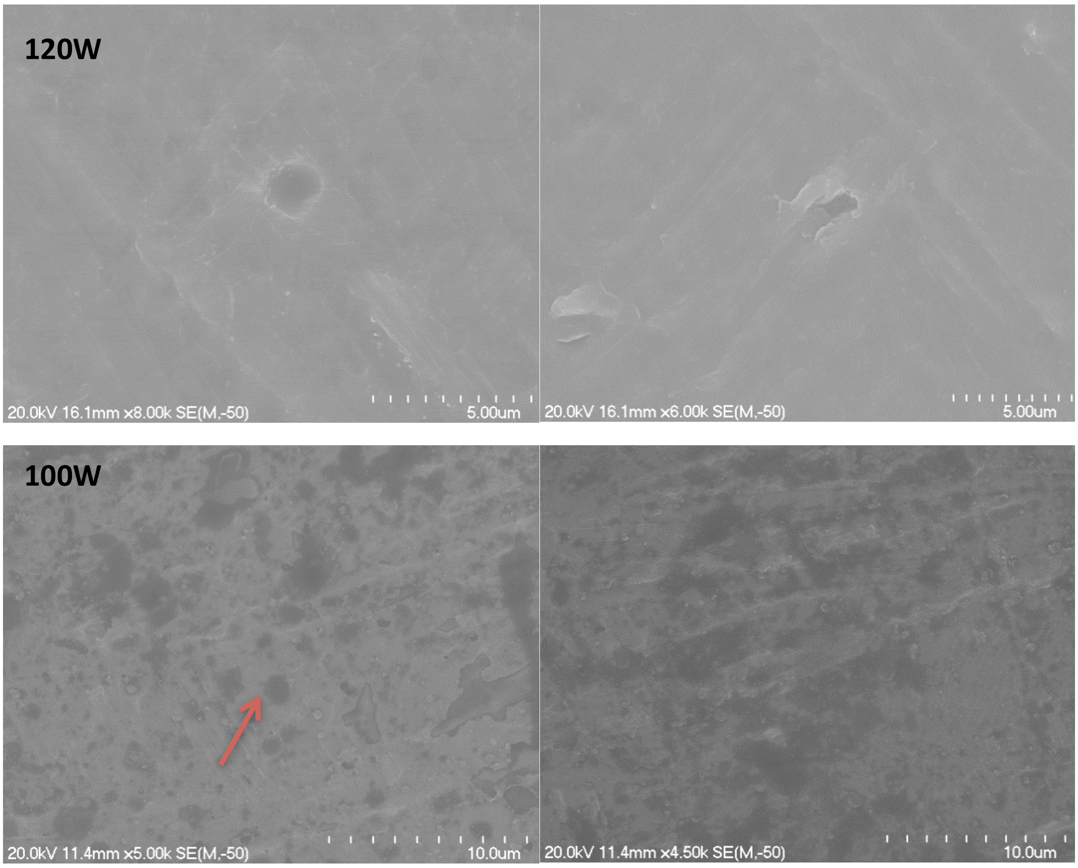

Figure 4.30: micrographs of the 100W and 120W surfaces. The black spots show porosities.

Higher magnification SEM images were taken to observe the porosity. Those microstructures produced using very low power (100W) show large amounts of porosity with interconnected pores. The highly porous structure found at very low power is associated with incomplete melting or partial melting of the powder particles where many black spots can be seen. The structure may consist of loosely bound particles which are melted together to form the interconnected porosity as seen in Fig. 4.30 and Fig. 4.31 The micro-porosity observed on the surface of blobs formed at 140W may be associated with shrinkage occuring during solidification, or with the presence of entrapped gases from the atmosphere or shrouding environment, particularly from the argon gas. There was no work done in this research to justify the above statement and the comment is based on other associated work[11]. The size of the pores found in blob’s formed at 140W are in the range of 2µm to 6µm.

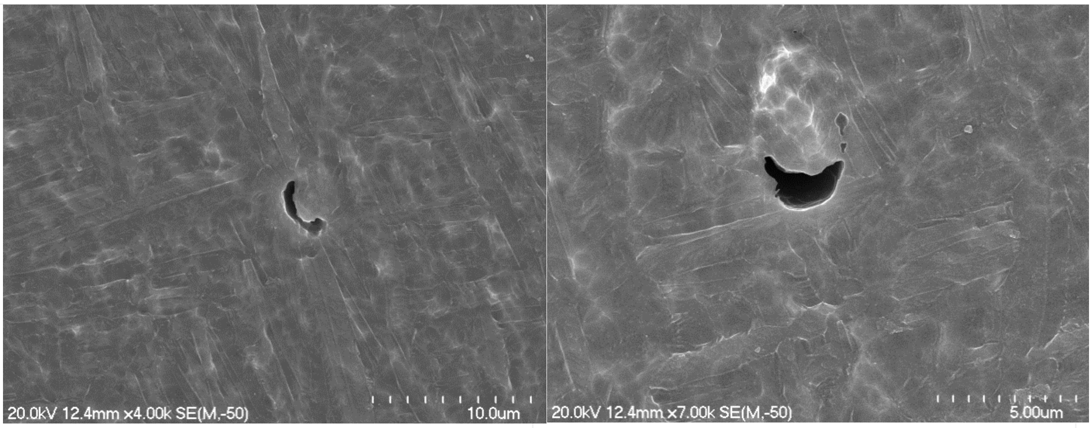

Figure 4.31: pore size and morphology

4.5. 4 Microhardness

Vickers microhardness testing was carried out using a LECO microhardness LM700 tester with a weight of 50g for 15seconds. For each sample, an average of ten measurements was recorded. It is evident that the Vickers hardness increases with an increase in laser power. It is also evident that a different texture on the surface of a blob provides slightly different Vickers hardness. The Vickers hardness is lower on the finer or brighter surface compared to the coarse and darker surface. It is worth mentioning that the effect of martensite decomposition, due to differences in temperature distribution, may cause differences in the texture of the surface area thus resulting in hardness changes [12].

Table 4.11: Vickers Microhardness with Variations in Laser Power

Specimens	**HV**
100W	311 ± 12.2
120W	305 ± 14.7
140W	295 ± 33.6
160W	310 ± 36.1
180W	346 ± 7.4
200W	351 ± 11.6

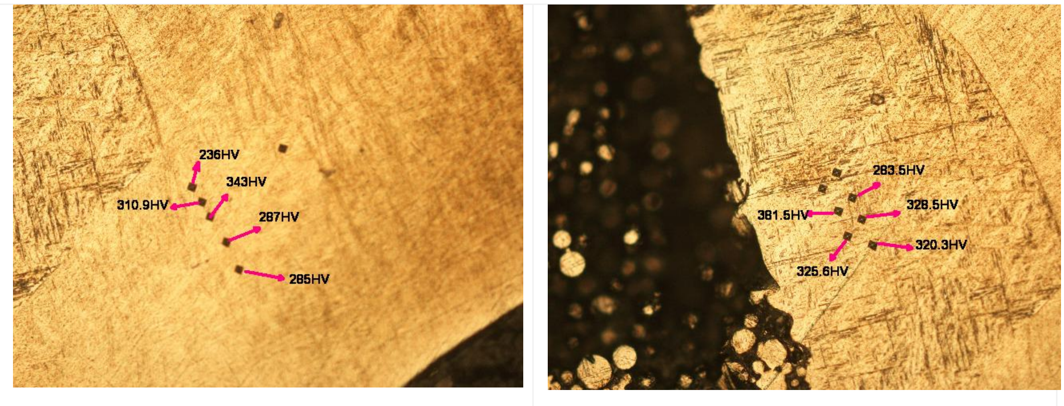

Figure 4.32: Microhardness on 100W polished surface at different textures

The slightly lower hardness values found in the brighter regions in the micrographs derive from a finer, needle like acicular structure. Five measurements were taken in each region and the average was calculated. The darker region with a coarser microstructure gave slightly higher hardness values compared to the lighter region.

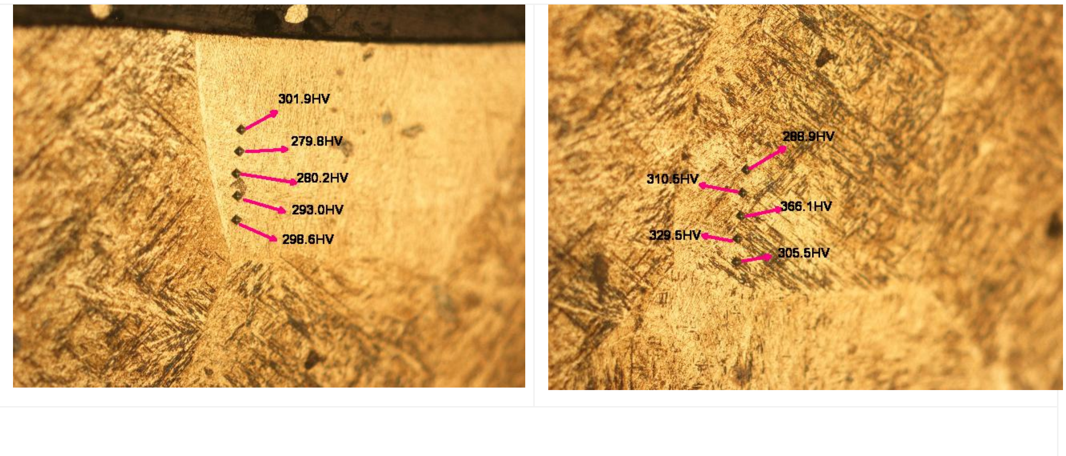

Figure 4.33: Microhardness on 140W polished surface at different textures

4.5. 5 XRD Characterisation

In order to identify the phases and determine the solidification texture, the polished and etched surface of individual blobs were characterised using X-ray diffraction (XRD). The identification of phases from the diffraction pattern is based upon the position of diffracted lines/peaks and their relative intensities. The diffraction angle which is 2ϴ is determined by the spacing d, between a particular set of planes. In this calculation Bragg's equation was used,

$$n\lambda = 2d\sin\Theta \tag{18}$$

Where λ is the known wavelength of the X –ray source, n is an integar value, d is the inter-planar spacing and 2ϴ is the diffracted angle.

The results of an XRD analysis are shown in figure 4.34. As can be seen, the only constituent in microstructure of a powder particle is the hexagonal close-packed (hcp) phase. The hcp pattern can be attributed to both the α phase and α' martensite. This is because they both have the same crystalline structure and very similar lattice parameters. With respect to the chemical composition of the Ti6Al4V alloy and the bespoke rapid cooling rates of DMLS process used in this experiment, it fits well the alpha prime martensite.

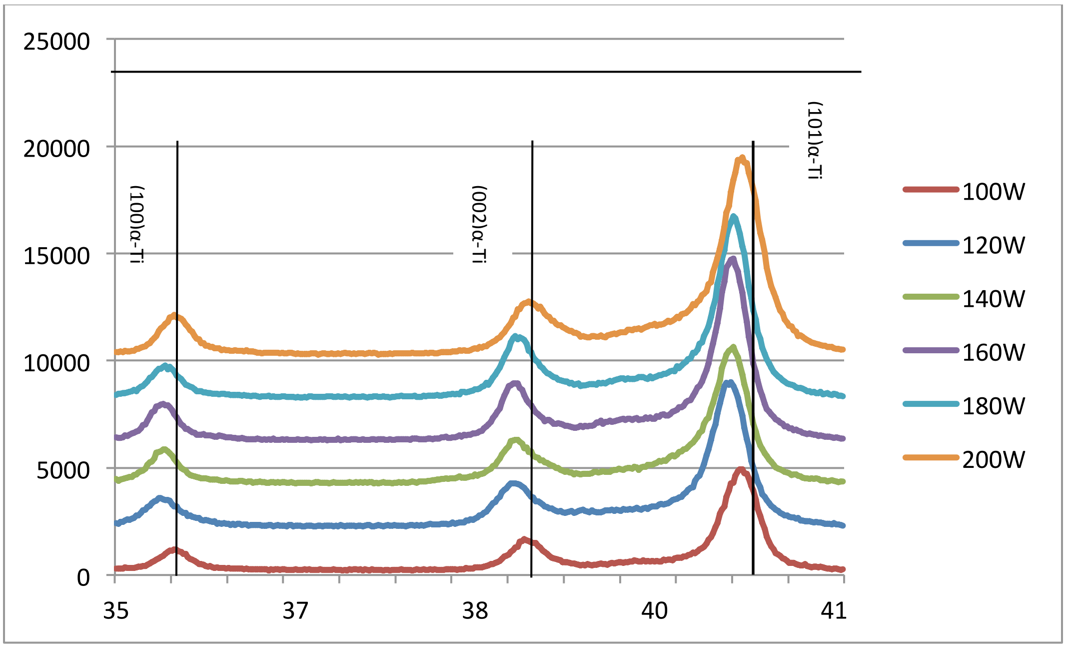

Figure 4.34: XRD data of the blobs (100W to 200W)

Figure 4.34 shows an enlarged view of an XRD pattern for 2ϴ = 35.0^{o}-41.5^{o} for as built blob's produced with various laser power inputs. Since there is no JCPDS standard for this material and the known results from the literature are not sufficiently numerous for a detailed comparison, the results are fitted to those reported for the hexagonal α-Ti (JCPDS file #44-1294) and for the cubic β-Ti (JCSPDS file #44-1288). From this qualitative fitting, the as built blob was indexed as shown in Table 4.12.

The hcp or α phase is textured on the (1 0 0) and (0 0 2) planes. The β phase which is characterized by the (110) is not observed. There are two possible causes for the disappearance of the β peaks. Firstly, it is probably due to the massive transformation of β to α and secondly it is possible that the neighbouring broadened α peaks submerged the residual β peaks and made them unobservable [13]. The results show a significant peak shift in the α phase for when a laser power of 100W to 180W was used, suggesting that there is lattice distortion with increasing laser power. It is well known that this lattice distortion correlates with the internal stress.

Finding the interplanar spacing and lattice parameter for each peak

The first peak in Fig 4.34 which results from diffraction by (100) planes occurs at 2ϴ =35.53˚. The corresponding interplanar spacing for this set of planes based on Bragg's law is equal to

$$d_{100} = \frac{n\lambda}{2\sin\theta} = \frac{(1)(0.1542\ \mathrm{nm})}{(2)\left(\sin\frac{35.53^\circ}{2}\right)} = 0.2525\ \mathrm{nm}$$

by using the diffraction peaks in the above figure, the a and c values for a hexagonal unit cell were calculated as follows;

	2ϴ	d-spacing	Intensity	hkl-α	c/a 1.633	a	c
100W	35.53	0.2525	1199	100	1.601	0.2916nm	0.4674nm
	38.45	0.2328	1670	002			
	40.57	0.2222	4942	101			
120W	35.39	0.2534	1593	100	1.584	0.2926nm	0.4635nm
	38.53	0.2335	2279	002			
	40.49	0.2226	6997	101			
140W	35.45	0.2530	1865	100	1.590	0.2921nm	0.4645nm
	38.59	0.2331	2308	002			
	40.51	0.2225	6630	101			
160W	35.43	0.2532	1974	100	1.589	0.2924nm	0.4646nm

	38.59	0.2331	2947	002			
	40.51	0.2225	8759	101			
180W	35.45	0.2530	1756	100	1.590	0.2921nm	0.4645nm
	38.57	0.2332	3132	002			
	40.51	0.2225	8740	101			
200W	35.53	0.2525	2130	100	1.594	0.2916nm	0.4647nm
	38.69	0.2325	2755	002			
	40.59	0.2221	9467	101			

Table 4.12: Indexing the XRD data

$$\frac{1}{d^2} = \frac{4}{3}\left(\frac{h^2 + hk^2 + k^2}{a^2}\right) + \frac{l^2}{c^2} = \frac{4\,sin^2\Theta}{n\lambda^2}$$

$$sin^2\theta = \frac{\lambda^2}{3a^2}(h^2 + hk^2 + k^2) + \frac{\lambda^2}{4c^2}(l^2)$$

$$sin^2\theta = A\,(h^2 + hk^2 + k^2) + Bl^2$$

The constants A and B are set as: $A = \frac{\lambda^2}{3a^2}$ and $B = \frac{\lambda^2}{4c^2}$

for (1 0 0) with the diffraction at 2Θ = 35.53˚ and d spacing of 0.2525nm

$$sin^2\frac{35.53}{2} = A(1)$$

$$A = 0.0759$$

for (101) with diffraction at 2Θ =40.57˚

$$sin^2\frac{40.57}{2} = A(1) + B(1)$$

$$0.09814 = 0.0759 + B$$

$$B = 0.0222$$

The ratio

$$\frac{c}{a} = \sqrt{\frac{3A}{4B}}$$

$$\frac{c}{a} = \sqrt{\frac{3(0.0759)}{4(0.0222)}}$$

$$\frac{c}{a} = 1.601$$

Then consider the plane spacing equation for the hexagonal crystal structure

$$\frac{1}{d^2} = \frac{4}{3}\left(\frac{h^2 + hk^2 + k^2}{a^2}\right) + \frac{l^2}{c^2} \tag{20}$$

for (1 0 0) the lattice parameter

$$\frac{1}{d^2} = \frac{4}{3}\left(\frac{1}{a^2}\right)$$

$$a = \sqrt{\frac{4}{3}(0.2525)}$$

$$a = 0.2916\, nm\ and\ c = 1.603(0.2916) = 0.4674 nm$$

4.3.3.6 Discussion

In this experiment, a 10mm powder bed was deliberately used so that the influence of the solid substrate is negligible. The heat loss through substrate is more efficient since a solid substrate such as a pure titanium platform is a good conduction medium. Without the substrate, the heat loss is through radiation and convection in the powder bed which is less effective and much slower compared with a substrate. Therefore, the temperature gradient in the powder bed becomes increasingly large with higher laser power and this changes the solidification mechanism. With higher power and a less effective heat loss mechanism, the temperature increase in a part being built becomes very high and this creates a coarser overall microstructure with α grain boundaries that become less distinct and effectively disappear. This explains the aforementioned SEM images where the grain coarsening was observed when higher laser power was used

A metallographic analyses of the surface of blobs by optical and SEM shows that the melted zone consists of an α+β structure with prior-beta grains. The heat conduction determines the prior β grain size in Ti6Al4V produced using DMLS. A finer microstructure was observed at the upper part of the melted core, indicating that the top part solidified faster than other areas. A Fully lamellar microstructure with different elongated lamellar sizes inside the melted core was also observed. This could be attributed to the high energy density within the laser melt which led to a high temperature gradient which promoted rapid cooling. XRD analysis confirms the presence of an α′ martensite in the microstructure. Heat transfer analysis confirms that the process generates a high surface heat flux which is proportional to the laser power. A high laser power gives a high energy density that causes the powder particles to melt and form a melt pool. A molten pool is observed at a laser power as low as 20W. A numerical solution gives a good indication of the temperature distribution on the powder bed even though the estimated penetration depth was lower than the experimental result. This is explained by the assumption of constant thermal property values for the powder .

The microstructure of the blobs had two characteristic regions, one which appeared brighter and consisting of very fine acicular needles and the other which appeared darker with a coarser needle like structure. The morphology of the lamellar structure consisted of acicular needles with a basket-weave pattern. Some of the acicular needles appear to be entangled as a result of competitive growth. Basket-weave patterns are associated with slower cooling rates. In this work this could be satisfactorily explained by the loose powder of 10mm thickness, which acted as a less effective heat sink compared with a solid substrate. Porosity was observed in blob's produced at laser power less than 140W. The pores were characterised as having flat and spherical features with the size ranging from 2µm to 6µm. The micro-porosity observed may be associated with shrinkage which occurs during solidification or with the presence of entrapped gases from the atmosphere or argon gas from shrouding environment [11, 14]

It has been shown that the Vickers hardness increases with an increase in laser power. The blobs had different microstructures associated with them as a result of the different rates of heat conduction occurring in the powder bed. This also indicates that a different powder packing density existed on the powder bed. The heat transfer on the powder bed is largely by conduction between the particles and also by radiation through the gap [15]. A good powder packing density provides more efficient heat conduction and heat loss and this leads to a formation of different textures on a blob's surface. It was observed that different textures on a blob surface have slightly different Vickers hardness. The Vickers hardness was lower for the finer microstructure compared with the coarser. It is likely that the extent of martensite decomposition due to differences in temperature distribution may cause differences in the surface microstructure which gives variations in hardness [12].

References

1. Gu*, X.Y.a.P., *A review of rapid prototyping technologies and systems.* Computer Aided Design, 1996. **28**(4): p. 307-318.
2. Levy, G.N., R. Schindel, and J.P. Kruth, *Rapid Manufacturing and Rapid Tooling with Layer Manufacturing (Lm) Technologies, State of the Art and Future Perspectives.* CIRP Annals - Manufacturing Technology, 2003. **52**(2): p. 589-609.
3. N.P.Karapatis, J.P.S.V.G.a.R.G., *Direct Rapid Tooling: a review of current research.* Rapid Prototyping Journal, 1998. **4**(2): p. 13.
4. Ryan, G., A. Pandit, and D.P. Apatsidis, *Fabrication methods of porous metals for use in orthopaedic applications.* Biomaterials, 2006. **27**(13): p. 2651-70.
5. Atsuko Shimosaka, Y.U., Yoshiyuki Shirawa, Jusuke Hidaka, *Sintering Mechanism of two spheres forming a Homogenous Solid Solubility Neck.* KONA, 2003. **21**(2003): p. 15.
6. Mercelis, P. and J.-P. Kruth, *Residual stresses in selective laser sintering and selective laser melting.* Rapid Prototyping Journal, 2006. **12**(5): p. 254-265.
7. N.W. Klingbeil, J.L.B.R.K.C., C.H. Amon, *Residual stress-induced warping in direct metal solid freeformfabrication.* International Journal of Mechanical Sciences, 2002. **44**: p. 57-77.
8. Rosenthal, D., *The theory of Moving Source of heat and its applications to metal transfer.* Trans. ASME, 1946. **43**(11).
9. Z.H. Shen, S.Y.Z., J. Lu, X.W. Ni, *Mathematical modeling of laser induced heating and melting is Solids>.* Optics & Laser Technology, 2001. **33**(2001): p. 533-537.
10. Romer, G.-w., *Matlab Laser Toolbox User Manual*, 2010.
11. J.-P. Kruth, M.B., E.Yasa, J. Deckers, L. Thijs, J. Van Humbeeck, *Part and material properties in selective laser melting of metals.* 16th International Symposium on Electromachining (ISEM XVI): p. 12.
12. Chlebus, E., et al., *Microstructure and mechanical behaviour of Ti—6Al—7Nb alloy produced by selective laser melting.* Materials Characterization, 2011. **62**(5): p. 488-495.
13. Gu, D., et al., *Densification behavior, microstructure evolution, and wear performance of selective laser melting processed commercially pure titanium.* Acta Materialia, 2012. **60**(9): p. 3849-3860.
14. J Dutta Majumdar, A.P., Z Liu, I. Manna, L. Li, *Microstructure characterisation and process optimisation of laser sintered rapid fabrication of 316L stainless steel.* Applied Surface Science, 2005. **247**(2005): p. 8.
15. N.K Tolochko, S.E.M., N.V Sobolenko, Yu V. Khlopkov, I.A Yadroitsev and V.B Mikhailov, *Main relationships Governing Laser sintering.* Journal of Advanced Materials, 1995. **2**(2): p. 151-157.

Chapter 5: Single track & single layer formation

A 3D solid part built using the DMLS process consists of many individual single tracks which form the 2D cross-section of a layer. These 2D layers are stacked up together to create a 3D part. The purpose of this experiment is to investigate the geometrical behaviour of these individual single tracks. This experiment was also performed to investigate the consolidation mechanism between the powder and the substrate on the first synthesized layer. The investigation is supported by a numerical model which simulates the heat transfer.

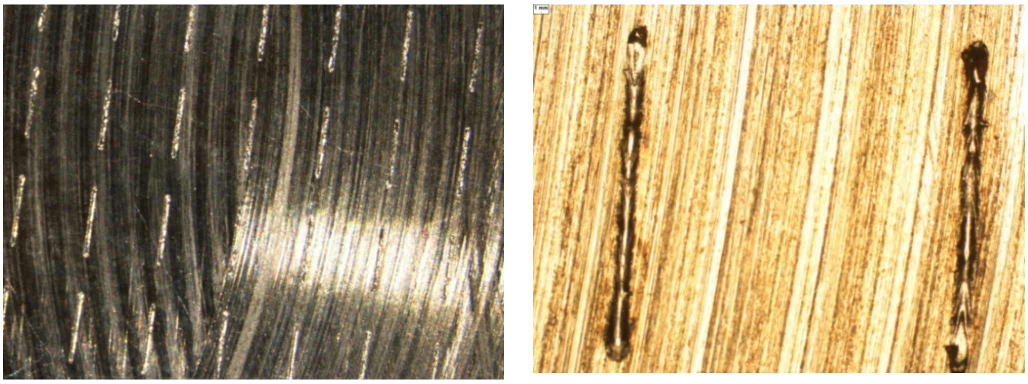

Figure 5.1: A Synthesized single track on the Ti substrate

5.1 Introduction

The selective laser sintering/melting process employs a layered manufacturing principle where each layer consists of individually scanned tracks. These individual tracks form two dimensional layers which are fused together to form a 3D part. Good inter-track and inter-layer bonding leads to good mechanical properties [1]. This bonding is controlled by the machine parameters which determine the heat transfer and heat distribution on the powder bed.

The factors affecting the heat distribution in DMLS are the heat source, which is the laser, and the heat affected zone in the powder bed. Therefore the heat transfer mechanism in DMLS can be studied through the optical properties of the laser beam and the thermal behaviour in the powder bed. The optical properties of the laser govern the degree of energy transfer and absorption by the powder bed, whilst the thermal behaviour in the powder bed is related to the heat source and includes conduction, convection and radiation.

5.2 Processing Conditions

5.2.1 Material & Machine parameters

The Ti6Al4V alloy powder was supplied by EOS and this had an average particle size of 40µm. The experiment was carried out using an EOSINT M270 extended version machine which provides a vacuum environment which can be filled by argon as a protective gas. The source of the radiation is a continuous mode Ytterbium fiber laser operating at the wavelength of 1.06µm with the maximum laser power of 200W. A small Titanium plate of 10mm thickness was utilized as a substrate/platform.

In this experiment, the scanning strategy was set for scanning along the X direction only. The scan spacing, which determines the amount of overlap between adjacent scan lines was set at 100µm in order to get optimum bonding, which aids densification. The layer thickness, which is the layer of newly deposited powder, was set at 30µm. After completing the sintering process on the X-Y plane, the sintered layer is lowered and a fresh layer of powder is deposited. In all cases the top surface of the newly deposited powder is assumed to be flat.

The machine parameters used in this experiment are shown below;

parameter	**Value**
Laser power	170W
Scan speed	1250mms-1
Scan spacing	0.1mm
Layer thickness	30µm

Table 5.1: Processing parameters for a single track and layer

5.2.2 Individual Single tracks

In order to identify each of the individual laser tracks, a 2mm scan spacing was set in the X and Y direction with a 60 degree rotation angle. Many individual single tracks were produced by the 170W laser power with a 1250mms^{-1} scan speed. The thickness of the deposited powder layers was 30µm and the length of the scan line was 2mm for all tracks. The width of the tracks, the area of powder consolidation and the melted depth were analysed.

5.2.3 Single layer formation

For single layer formation, each laser strike was controlled manually to make sure that the laser stopped once the first layer was completed. The scanning strategy was modified to give a one direction scanning path only in the Y direction. The alternate X and Y scanning strategies were unmarked. The overlap was set to zero which means that there was no gap or space between the single tracks and the width of the scanning line was controlled by the focused beam. A 10mm x 10mm rectangle was created using the CAD software and this data was sent to the machine. The machine was stopped once the first layer had been completed.

5.2.4 Individual track on the re-melted layer

The first set of parameters was used for this experiment. Firstly, the laser was set to scan a cube with dimensions of 15mm x15mm x 10mm. After a few layers were completed, the machine was stopped and the scanning parameters were changed and the laser was set to scan an individual track on the previous layer. This means that the previous layer was now acting as a substrate. The only difference is that the substrate is now made from re-melted Ti6Al4V powder instead of pure Ti. The individual tracks were then analysed.

5.3 Geometrical characteristics of laser induced melting

The geometrical features of a single track and a single layer were studied in this section. The s are divided into two areas; firstly the laser induced melting on the first layer and secondly on the re-melted layer. The size and morphology of the as built single track was measured and analysed according to the scanning parameters. The surface was checked for any visible cracks or other defects.

5.3.1 Laser induced melting of a single laser track

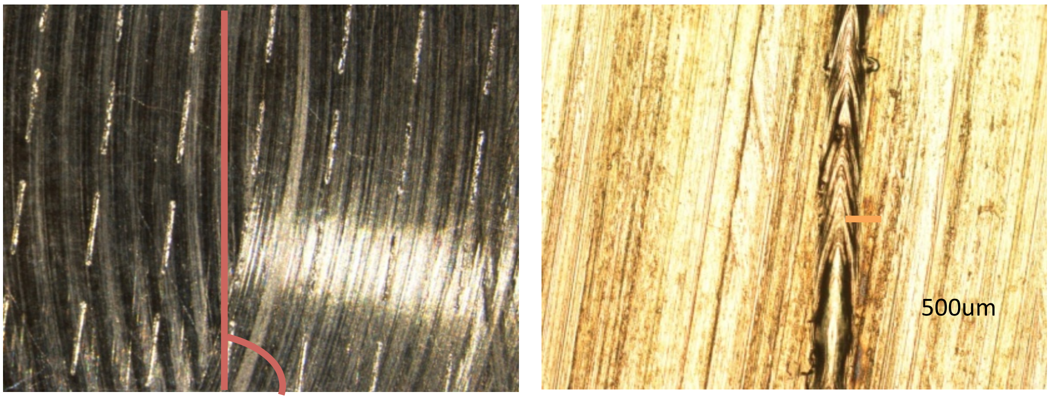

Figure 5.2 Laser induced melting on a Ti substrate

Figure 5.2 shows the laser –powder interaction on the first layer. It is noted that on the first layer, the laser not only melts the powder but also melts the substrate and forms an elongated molten track. When the laser strikes onto the first layer of a thin powder bed, it causes splashing in most of the powder which directly exposes the laser to the substrate. The tracks have a uniform width of 90µm±15, which is the beam diameter and a scan length of 2mm. The melted depth was measured at less than 20µm.

This is evidence that, under these processing parameters, the energy density is sufficient to melt the substrate and create a joint substrate-powder molten pool. It also suggests that on the first layer, there is a larger volume of powder so that a higher laser energy density is required to create a better joint between the molten pool of the substrate and the metallic powder. This confirms the normal practice where the first layer has to be scanned twice to achieve good interlayer bonding.

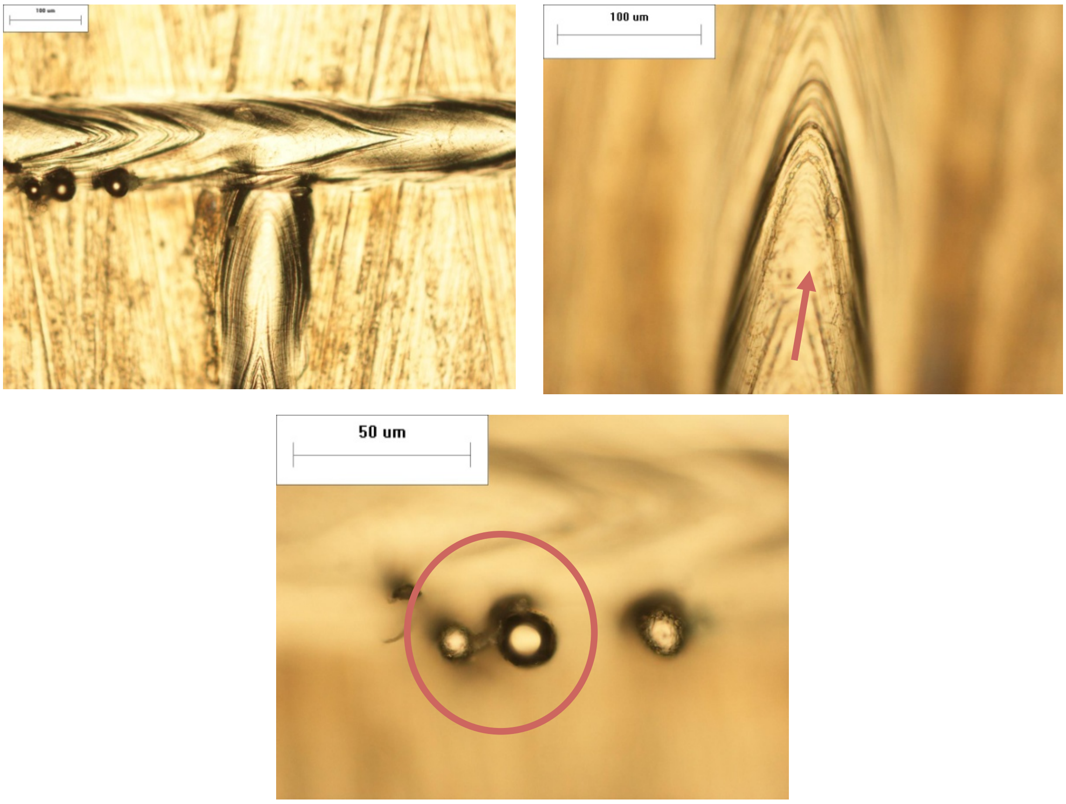

Figure 5.3: Optical images of individual tracks

From the optical images in figure 5.3, the width of an elongated individual track is consistent throughout the scanning line. However, at each end, the elongated track had shrunk and produced a narrow tip feature suggesting a solidification front. Not many powder particles could be seen along the tracks. The powder particles are weakly bonded and can be easily removed with minimum force. The rippled texture on a melted track suggests the scanning direction of the laser beam. The laser energy in this experiment successfully formed continuous individual tracks on the substrate. There are no visible cracks on the solidified track. This was measured using the optical microscope measurement tools. The details of this measurement are explained in chapter 2.

At a higher magnification (figure 5.4), the SEM images provide more information. The laser selectively melts the powder according to the predefined scanning pattern which, in this case, is a 2mm single line. The width of the individual track is consistent at 90µm±15µm and the length of the track is 2mm. It can be seen that most of the powder particles had melted and were embedded in the substrate. The substrate’s surface is left with visible individual tracks featuring dented/marked or rippled lines which show that the energy input had not only melted the powder but was high enough to penetrate the substrate.

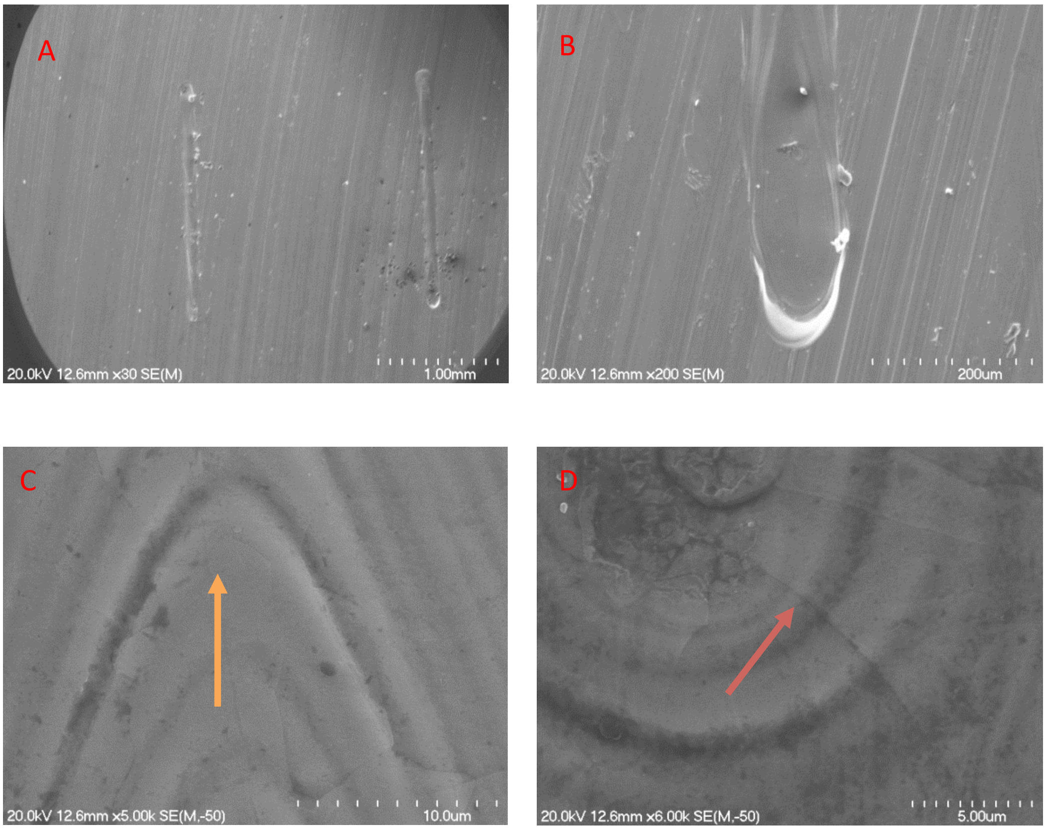

Figure 5.4: SEM images of an individual track

At one end of a track, tiny cracks were visible on the track floor (Figure 5.4D). These cracks might have formed at the place where the highly focused beam first struck the thin powder bed. Since the energy density was high, the highly focused laser beam splashes the powder particles and hence directly exposes the laser beam to the surface of the substrate.

5.3.2 Laser induced melting of a single layer

The result showed that the laser scanned the powder bed according to the CAD data and followed the predefined scanning strategy. No visible gaps could be seen in the newly sintered layer and all the spaces in the 20mm x 20mm area were occupied by a single laser track. This indicates that the first layer was built successfully. As shown in above figure, the single layer consisted of many individual tracks which are continuous and have a consistent size. The individual single tracks exhibited the same features discussed in the previous section.

A prominent feature in the formation of a single layer is at the meeting point of individual tracks. Even though the scanning strategy parameters were modified, the machine calculates how to scan the 400 mm^2 area. The surface looks rough and wavy and each of the individual tracks is noticeable. At the meeting point of the ends of individual tracks, the molten ends of a track create an uneven and non-uniform surface.

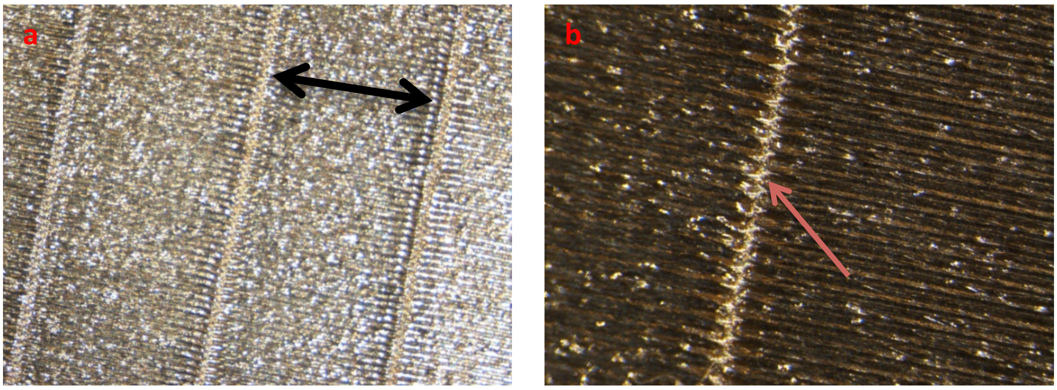

Figure 5.5: Single layer formation. (a) The arrow shows the laser stripe width of scanning strategy for this particular layer and (b) the laser end point.

The optical micrographs show that the molten pool in the elongated tracks, where the tracks join, has a uniform width with no overlaps. The track size shrank at the end of its scanning point and created a space between the individual tracks. A better manipulation of the scanning strategy might be the solution for this issue. The scanning strategy in each layer is different; it might therefore be the case that the one can cancel the other so that the surface effects of a previously sintered layer would be minimal. In other words, the rippled texture created in a previous layer is cancelled by the new scanning pattern on the next layer.

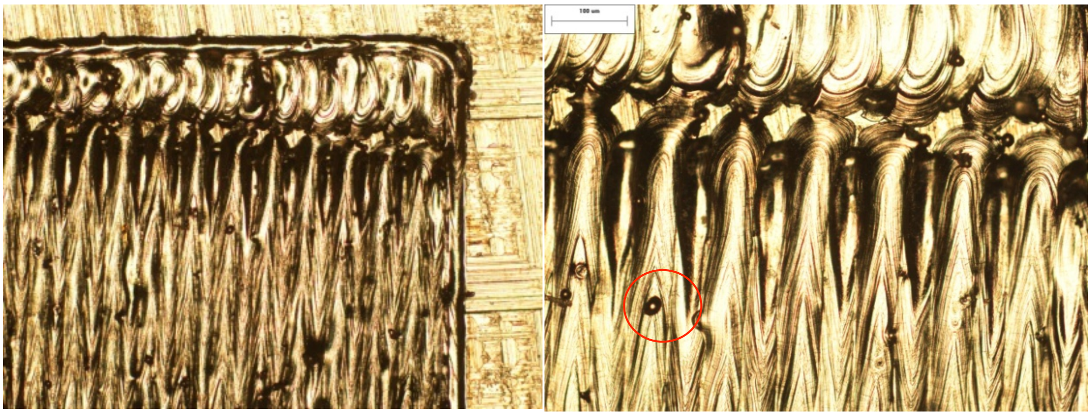

Figure 5.6: Optical micrographs of single layer formation (scale is 100µm)

One of the particularly important features of a newly formed layer is that it should be flat and uniform so that the next thin layer of powder can be spread evenly. There are many weakly bonded particles along the individual tracks and at the intersection points. There are also many individual particles and agglomerated particles and inter-agglomerated particles on the layer. As these particles are weakly bonded they easily get thrown off the track while the roller blade deposits a new powder layer.

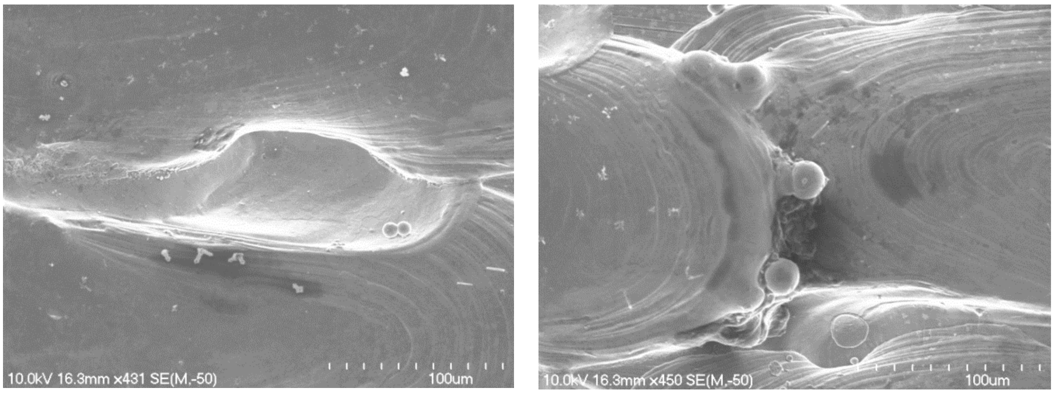

Figure 5.7: Weakly bonded powder particles on a single layer

Under the optical microscope, the black spot circled in figure 5.6 is actually an un-melted powder particle. The SEM images confirmed that all of the individual tracks are continuous with uniform size and shape. The size of the individual molten tracks formed on metallic powder is slightly wider than the ones formed on the substrate from the same material. This is possibly due to the fact that not only the powder in the laser irradiation zone involved in the formation of this individual molten track but also the powder from an adjacent track and area [2].

The height of the molten track does not exceed the powder layer thickness which was measured at 20µm±7.5µm as shown in Fig 5.8 There were no cracks or holes visible on the single layer

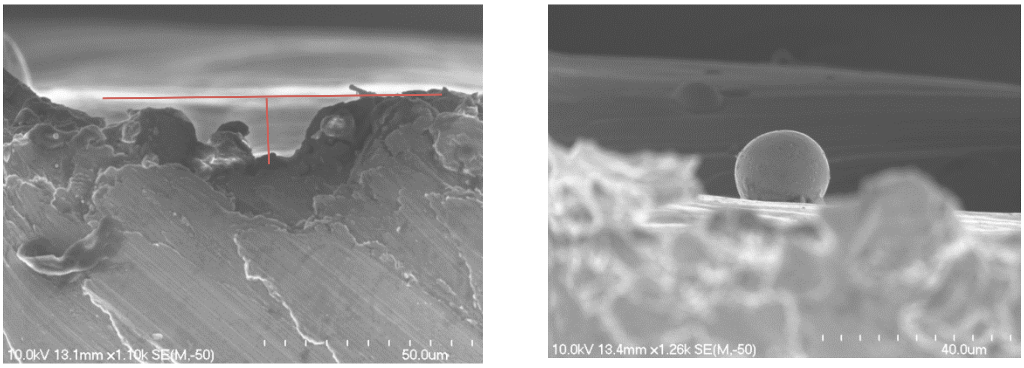

Figure 5.8: SEM images of a single layer melted depth and the unmelted particles

5.3.3 Laser induced melting on the re-melted layer

In this experiment, an individual track built on a previously solidified layer was analysed. These 2mm individual lines were scanned to be 5mm apart so that each of them is easily noticeable.

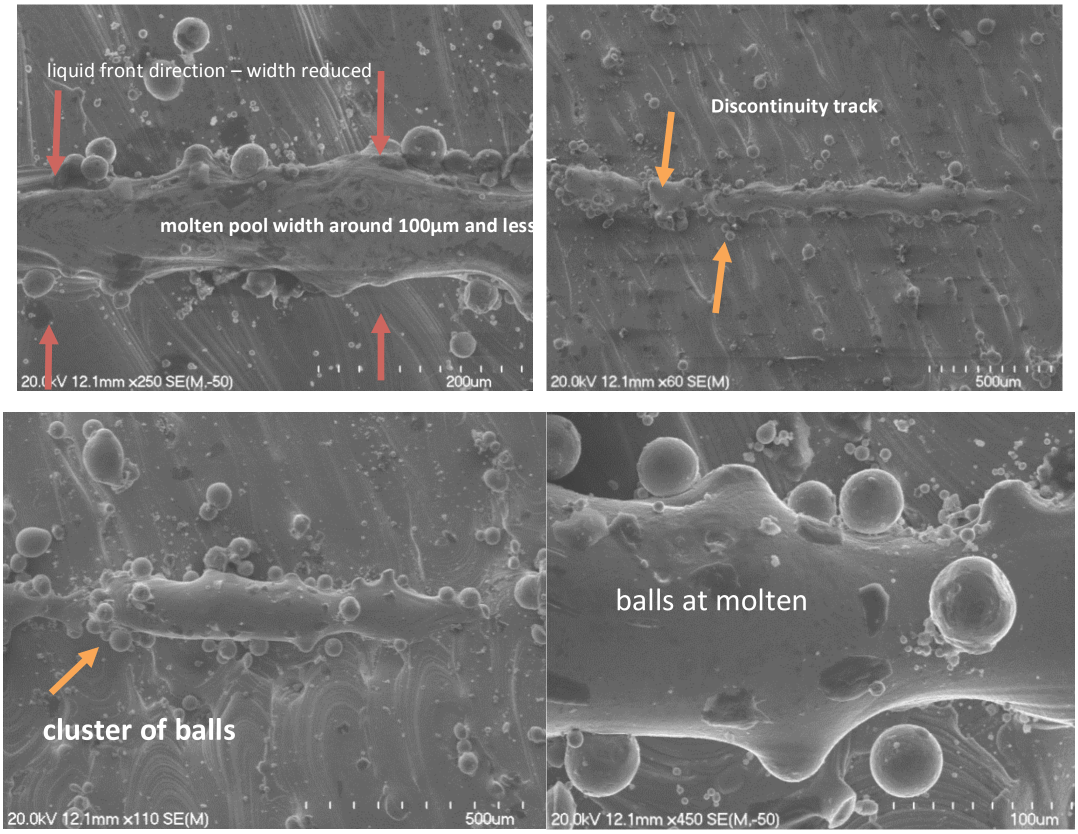

Figure 5.9: SEM images of individual tracks built onto the solidified layer.

The results show a few distinct characteristics. The individual tracks were built accordingly to the predefined scanning pattern. The size, length and pattern of these individual tracks conformed to the scanning strategy. However there is an inconsistency in the structure of these 2mm molten individual tracks. The width of the track is not uniform along the 2mm scan line, which is probably due to an inhomogeneous packing density of the powder bed. The solidified track's width was about 100µm±20µm, but a few tracks were less than 80µm and some were measured to be about 115µm.

As shown in figure 5.9, fragmentations of the molten track occurred. This is one of the drawbacks caused by a problem known as the "balling effect". Under the effect of surface tension, the elongated molten tracks have a tendency to ball up to create a droplet structure rather than a continuous molten track. The elongated molten track also shows a cluster of balls formed within the scan line and partially melted powder particles along the track. These partially melted particles are weakly bonded to the molten track. A molten track formed individually and separately with a gap has different characteristics compared one formed with no gap. It is therefore worthwhile mentioning that an adjacent molten track provides more stability to a newly formed track. The instability of the molten track causes discontinuity and fragmentation of the track.

5.4 Heat transfer Analysis for Single layer formation

An investigation into the temperature field distribution during DMLS is discussed in this section. The effects of the processing parameters on the temperature field distribution were studied using a 3D simulation model developed in MATLAB and which is based on finite element theory. A few assumptions were made in order to avoid non-linearity of the system. The model used the exposure time or laser-material interaction time and the surface heat flux to predict the temperature distribution and the isothermal contours of the heat penetration depth. The thermal properties of the substrate used in this experiment were based on the standard bulk titanium thermal properties, as explained in an earlier chapter. The thermal properties were kept constant throughout the simulation. The objective was to predict the effects of exposure time or interaction time on the temperature field during the laser sintering process.

The exposure time is defined as the ratio of the laser beam diameter to the scan speed[3]. In this case, the laser beam diameter was 100µm and the scan speed was 1000mms^{-1}, which gives an exposure time of 0.0001 second. In this study two different exposure times were used; 0.001 second and 0.1 second. This is sufficient to show the effect of exposure time on the temperature distribution and the heat penetration depth, which is the main purpose of this simulation. The laser is assumed to have a Gaussian distribution and generates the surface heat flux homogenously along the x, y axes.

5.4.1 Temperature distribution

During DMLS, the laser irradiates the powder and the heat transfer through the open pores delivers sufficient energy to fuse the powder particles together. As shown in figure 5.10, the laser irradiation causes the powder bed temperature to increase rapidly. With the aforementioned processing conditions, the maximum surface heat flux after 0.001 sec is 5x10^{10} Wmm^{-2}. This gives a peak temperature of 3000K. At this point, the radial temperature distribution has grown extensively from the diameter of the laser beam, which is 100µm, to more 400µm. The heat penetration depth is near to 800µm. The isothermal lines indicate that the powder layer below 200µm has reached the melting point and the heat affected zone has expanded to less than 800µm. The powder particles within the heat affected area (HAA) would be fused together since the temperature is below the melting temperature of Ti6Al4V.

The simulation was further extended to a 0.1 second exposure time. This is reasonably achievable during DMLS by slowing the scanning speed. It is noted that with a longer exposure time, there is a very large increase in surface temperature which reaches 14000K. In fact, vaporization and plasma formation occur at this temperature and this block the incident laser power and absorbs a portion of the laser energy. These effects were ignored in this work. The model gives a good indication of the effect of processing parameters on temperature distribution, as one need to be able to control the laser exposure time within the standard processing window.

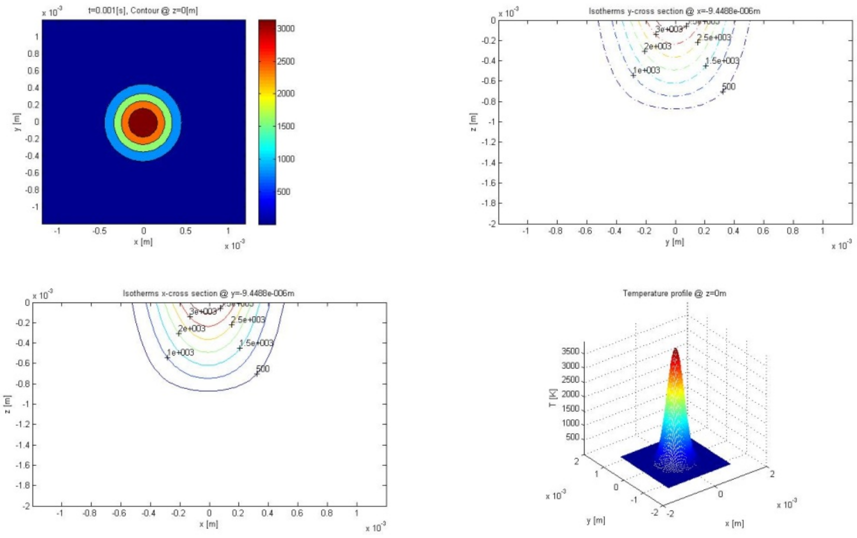

Figure 5.10: Temperature field and melting depth after 0.001sec laser irradiation (see appendix for enlarged image)

5.4.2 Melt depth

In this study the melt depth formed due to a different laser exposure time was investigated. Prior to laser irradiation, the surface temperature increases rapidly and forms a molten pool which solidifies when the laser moves away or is switched off. The size and depth of the solidified molten pool is temperature dependant and a longer exposure time increases the interaction between the laser and material. This increases the surface heat flux and subsequently the heat affected zone in the powder bed. At 0.001sec, the peak temperature recorded was 3500K which is well above the melting point of Ti6Al4V (fig 5.10). The isothermal lines corresponding to the generated temperature along the z-axis shows that the affected area within the melting temperature of the titanium alloy is even less than 200µm. With a 0.1 second exposure time, the line expands to more than 600µm. However, it is important to remember that the penetration depth is overestimated by this model, because the thermal properties used in this model were kept constant and do not reflect the temperature dependant thermal properties of the material during laser sintering process (fig 5.10). Furthermore, as mentioned earlier, this model used a slightly longer exposure time (0.001s) compared to the experimental condition (0.0001s). In laser sintering, where a high energy density is used, a fraction of second may have a huge effect on the process. Nevertheless, the model shows good agreement with the experimental results and explains the effect of laser exposure time on the temperature field and the penetration depth. It is therefore crucial to find the right combination of processing parameters so that sufficient exposure time is given for ideal laser-material interaction.

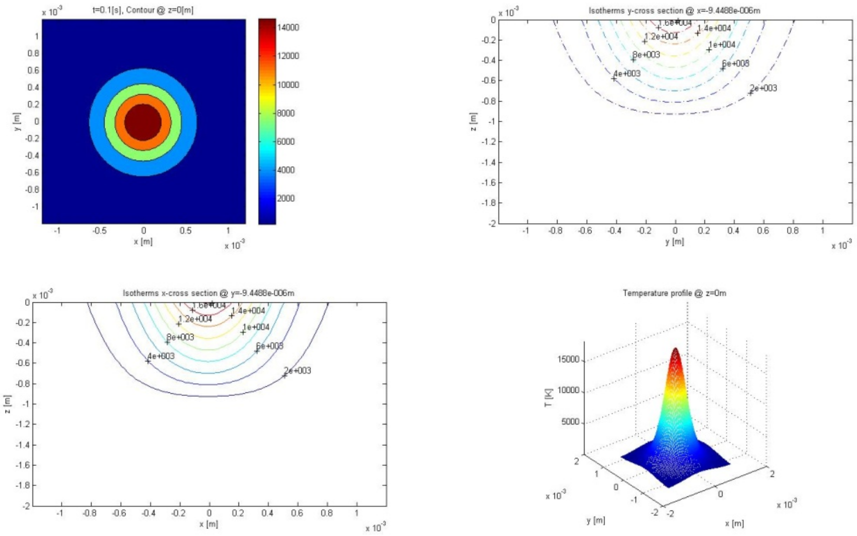

Figure 5.11: Temperature field and melting depth after 0.1sec (see appendix for enlarged image)

5.5 Discussion

The analysis of single track formation on a substrate and on a re-melted layer showed that both situations have identical features. Under the specific processing parameters used, the laser power supplied was sufficient to not only melt the powder particles but also to melt the titanium substrate. The depth of penetration into the substrate is believed to give an additional stabilizing effect for the sintering of good molten tracks. Substrate or previous layer remelting should be controlled in a way that it is not too excessive so that the geometry of the tracks is preserved and at the same time providing good interlayer bonding which is crucial for good mechanical properties.

A single track formed on a solidified layer was wider than the molten zone on a substrate of the same material. This is because powder has a higher absorptivity and a smaller thermal conductivity compared with the bulk material. The depth of a molten track represents the degree of penetration into the substrate and this generally does not exceed the thickness of the powder layer, which is 30µm. It is worth mentioning that in the first layer the apparent density of the deposited powder was very low and therefore the laser beam not only interacts with the powder but is also directly exposed to the substrate. Therefore substrate remelting and an adjacent solidified track contribute to the formation of regular and continuous molten tracks. When the energy is not sufficient to melt the substrate, the stabilizing effect of substrate penetration disappears and therefore irregular and fragmented molten tracks are visible. The formation of droplets, known as a balling effect, occurs because of the instability state of the molten pool.

Many have agreed that, laser power, scan speed, scan spacing and layer thickness have a great influence on the laser sintered part [2, 4, 5]. Scanning speed determines how fast the laser moves over the powder bed. A higher scanning speed reduces building time but causes deterioration in the quality of final parts, which have higher porosity and poorer surface finish. It also determines the interaction time between the laser and powder. Scan spacing is the distance between two laser scanned tracks and the layer thickness is the distance between two consecutive layers. A smaller scan spacing than the laser beam spot diameter creates overlaps between tracks and a bigger scan spacing avoids overlaps, but causes a highly rippled surface. One can also use the exposure time to determine the process control and investigate the effects of this on the temperature distribution by dividing the laser beam spot by the scan speed. For that reason a simulation model was developed to look at the effect of laser exposure time on the temperature distribution and the heat penetration depth. The model indicates that a longer exposure time causes a wider heat affected zone and more importantly a change in a fraction of a second in exposure time has a huge effect on the temperature field due to a highly focused laser beam.

5.6 References

1. Yadroitsev, I. and I. Smurov, *Selective laser melting technology: From the single laser melted track stability to 3D parts of complex shape.* Physics Procedia, 2010. **5**: p. 551-560.
2. Yadroitsev, I., et al., *Factor Analysis of Selective laser melting process parameters and geometrical characteristics of Synthesized single tracks.* Rapid Prototyping Journal, 2012. **18**(3): p. 9.
3. Wiria, F.E., K.F. Leong, and C.K. Chua, *Modeling of powder particle heat transfer process in selective laser sintering for fabricating tissue engineering scaffolds.* Rapid Prototyping Journal, 2010. **16**(6): p. 400-410.
4. Marleen Rombouts, J.-P.K., Ludo Froyen, *IMPACT OF PHYSICAL PHENOMENA DURING SELECTIVE LASER MELTING OF IRON POWDERS.* Fabrication, Materials, Processing, Properties TMS (The Minerals, Metals & Materials Society), 2009. **1**.
5. Bo Song, S.D., Baicheng Zhang, Hanlin Lioa, Christian Coddet, *Effects of Processing parameters on microstructure and mechanical property of selective laser melted Ti6Al4V.* Materials and Design, 2012. **35**: p. 5.

Chapter 6 –Microstructure & mechanical properties of DMLS parts

6.1 Introduction

Laser energy density (LED) for a given material is the key factor that affects the quality of a part fabricated via DMLS[1, 2]. The laser energy density is in proportion to laser power and scan speed. According to this relationship, increased laser power or a decrease in scan speed increases the energy density. A high energy density results in fully melted particles and therefore better density. However, once the powder is fully molten, there is little benefit in increasing the energy density any further. It was reported that there is a processing window where optimized laser power and scan speed produces full density part[3, 4]. However, too much energy causes deterioration and decreases the part density [5].

A better understanding of the process is necessary to deal with the aforementioned problems. Many have agreed that DMLS is a complicated process and requires a thorough investigation in order to simulate and find mutual links between processing parameters and the properties in an end part[2, 6, 7]. Processing parameters such as laser power, beam spot diameter, scanning velocity and material properties, such as absorptivity, conductivity and building conditions have an effect on the process. As a whole these parameters play a large role in determining the microstructural evolution during the DMLS process. Literature review shows that much research work has been done to investigate the influence of processing parameters on properties such as tensile strength, surface roughness and relative density of laser sintered products[1, 8, 9]. Also there have been feasibility studies on the DMLS process for use in applications such as in automotive, aeronautical and biomedical [10-14]. However, research on microstructural characterization in general is quite limited, especially for reactive materials like titanium [9, 15].Therefore this research presents a description and explanation of the microstructures in a Ti6Al4V alloy formed during the DMLS process as a result of changes in the scanning speed .

6.2 Material & Method

The Ti6Al4V metallic powder used in this work is known as EOSTi64 gas atomized powder supplied by EOS. The powder was spherical and had a particle size between 45µm to 100µm in diameter. All parts were manufactured using an EOSINT M270 extended version machine under a high purity argon atmosphere containing no more than 100 parts per million oxygen. The machine is equipped with a 400W Yb:YAG fibre laser which had a focused spot size of 100µm. Small cubes (10mmx10mmx15mm) were manufactured using a constant laser power of 200W and three different scan speeds, of 750mm/s, 1000mm/s and 1250mm/s. For each condition, two specimens were manufactured and these were described as S1, S2 and S3 respectively, corresponding to the different scanning speeds used. The layer thickness was kept at the default setting of 30µm for titanium powder.

Metallographic analysis was performed on the top and side surface of the cubes by mounting them in epoxy. Grinding was done using 320, 600, 1200, 2000 and 4000 grade silica paper to remove the scratches cause by the sectioning. The final polishing was done using a diamond cloth with a silica colloidal as a suspension. Samples were etched using Kroll's reagent and the microstructures were examined using an Olympus microscope and Scanning Electron Microscope (SEM) for higher magnifications. The Vickers hardness test was performed on a polished surface using a LECO hardness tester with analysis parameters set at 50g with 15s dwell time. An average of ten indents were taken for each condition.

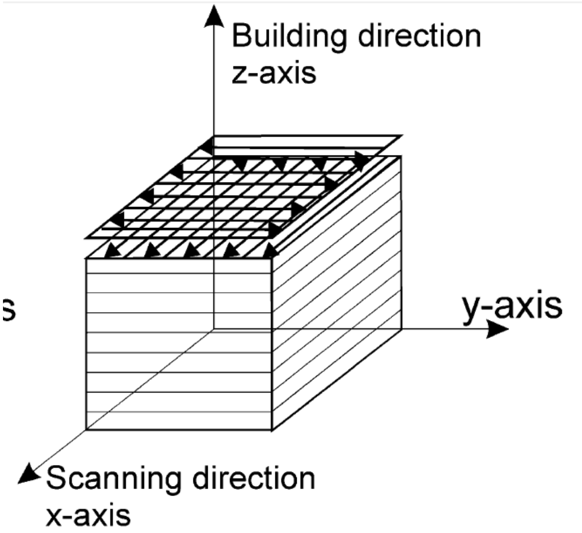

Figure 6.1: Surface for metallographic analysis. The top view indicates a cross-hatching technique using zig-zag vectors

In this research, a full factorial design was not used since the goal of this investigation was to explain the influence of scan speed on the microstructure rather than to find optimized processing parameters for this material. There are two types of energy density calculations; one is known as linear energy density (LED), which only considers laser power and scanning speed. The other is Volume Energy Density (VED) where hatch spacing and layer thickness are taken into account.

Processing Condition

	S1	S2	S3
Laser power	$200W$	$200W$	$200\,W$
Scan Spacing	$100\mu m$	$100\mu m$	100µm
Scan Speed	750mm/s	1000mm/s	1250mm/s
Layer Thickness	$30\mu m$	$30\mu m$	$30\mu m$
Spot diameter	$100\mu m$	$100\mu m$	100µm
Oxygen Level	$< 0.04\%$	$< 0.04\%$	$< 0.04\%$
Temperature	80°C	80°C	80°C
Energy Density	88.9 Jmm^{-3}	66.7 Jmm^{-3}	53.3 Jmm^{-3}

Table 6.1: Processing conditions for each group

6.3 Microstructural Characterisation

Ti6Al4V is an α/β titanium alloy whose microstructure is strongly dependent on cooling rate, particularly quenching from the β phase. In DMLS fabrication, where parts are built layer by layer, the material is heated and re-heated continually with each laser beam pass to above or below the β transus temperature[16]. Thus the changes occurring in the layered alloy structure may be complex to a degree depending on the thermal history.

In DMLS, the microstructure derives from the melting and solidification of a molten pool. Solidification is a transformation of an alloy melts into a solid piece of the alloy, which involves crystallization of the liquid phase, segregation of impurities and alloying elements, liberation of dissolved gases, formation of shrinkage cavities and porosity. Grains form as a result of solidification or other phase transformation processes. A grain is a small region of in a metal which has a continuous crystal lattice orientation. Each grain represents a small single crystal and its shape and size change with thermal treatment processes [17].

6.3.1 Parallel to the building direction

A side surface (parallel to the building direction) of a cube shows many layer bands (bunches of columnar grains) with a fine acicular morphology. The width of the layer bands is roughly 30µm which reflects the predefined layer thickness of the deposited powder. Light and dark colour tones were observed on the etched surface of cross-sections. In the dark area, a very fine, acicular structure with a herring bone appearance can be seen inside the elongated grains which are oriented parallel to the building direction. It is suggested that this is due to the high temperature gradients deriving from the DMLS process.

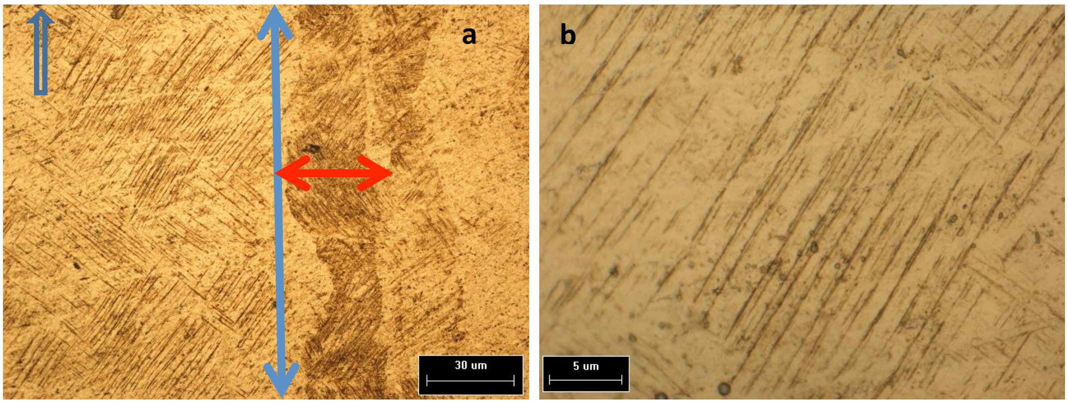

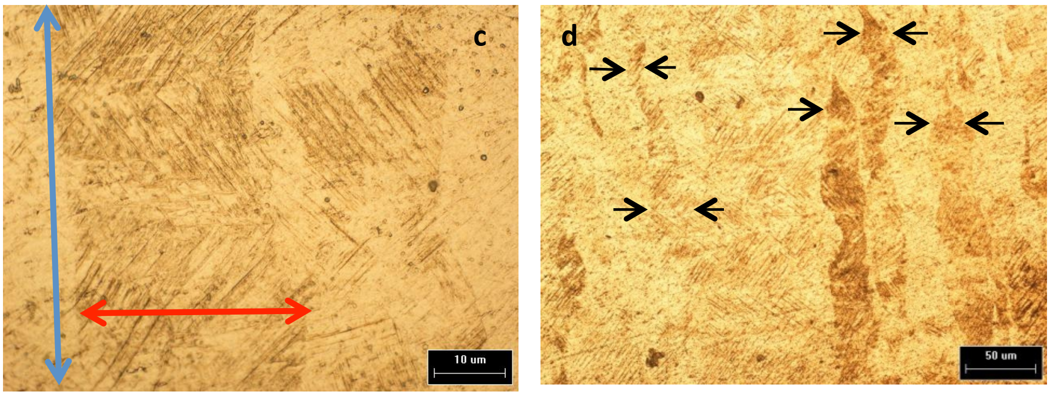

Figure 6.2: S1 polished surface obtained at scan speed of 750mm/s (a-d)

Figure 6.2 shows a side view of the deposited powder at a scan speed of 750mms^{-1}. Columnar grains with a distinctive herringbone structure, with changing orientation within them are visible throughout the entire field of view. The width of the columnar grains is in the region of 50µm to 75µm and are bigger at the bottom compared with the top (figure 6.2d).

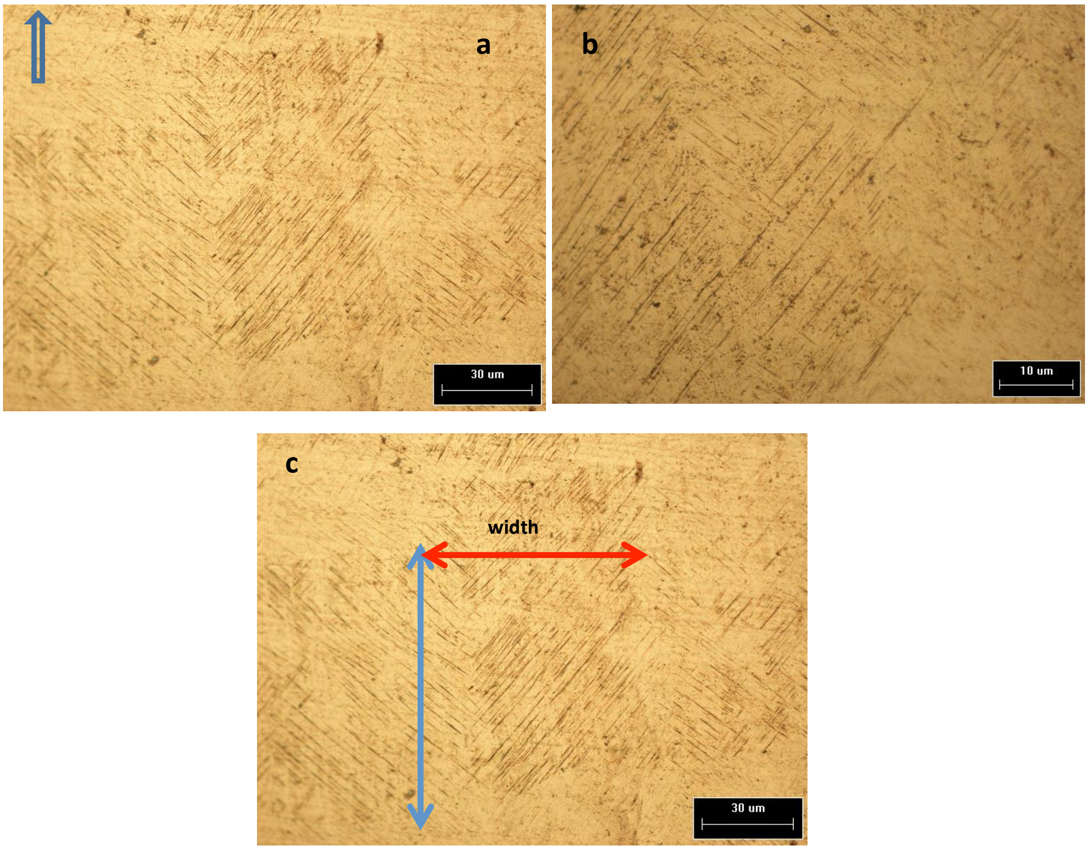

Figure 6.3: The optical images of S 2 polished surface with scan speed of 1000mms^{-1}(a-c)

Figure 6.3 shows the macro-morphologies in sample S2 which was made using an increased scanning speed (1000mms^{-1}). A similar texture to that in sample S1 can be seen, where the entire surface is dominated by slightly thinner columnar grains with a herringbone texture, compared to those in sample S1. The width of the columnar grains in this group is in the region of 40-55µm. The texture, which maintains a more consistent orientation through the layer thickness, is clearly visible. Only a few columnar grains can be seen in this group. The acicular structure within the columnar grains has an orientation of ±45˚ to the building direction.

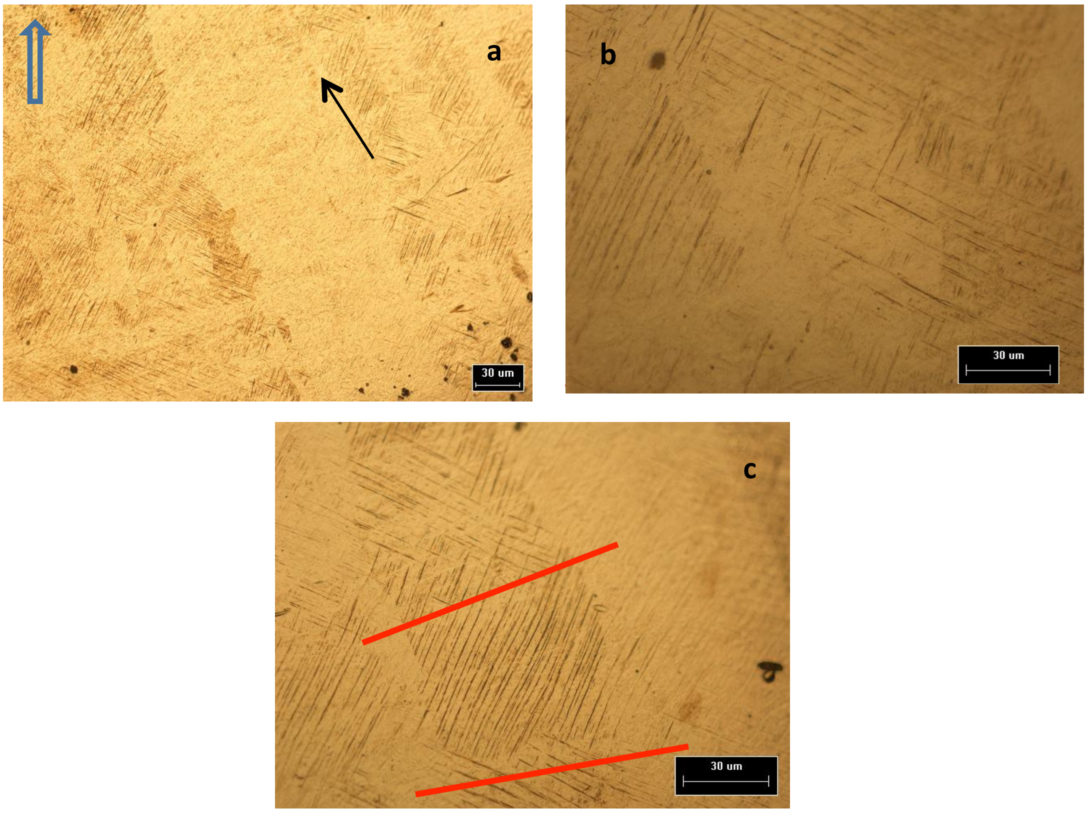

Figure 6.4: The optical images of S3 polished surface obtained at the scan speed of 1250mms^{-1}(a-c)

Figure 6.4 shows the columnar grains in a specimen from group S3. The columnar grains are still visible on the entire surface. The columnar grains in this group have more irregular sizes and they are more visible at the centre than at the edge of a cube. The width of the columnar grains ranges from 30µm to 40µm which is lower than for the other groups. It was also observed that at this scan speed, the columnar grains were tilted at an angle of about 20˚ from the bottom to the top surface. The bunch size of the columnar grains is also bigger at the bottom. In general only columnar grains were observed in a side surface. They grew across several layers creating many layer bands parallel to the building direction. During the laser scan, the tops of the grains in the previous layer can be partially re-melted so that they can undergo epitaxial growth into the next layer, thus generating the columnar grains across several layers. Inside a columnar grain, long thin, narrow and parallel needle-like acicular laths are present. Most of the acicular needles lie at ±45˚ to the building direction.

6.3.2 Perpendicular to the building direction

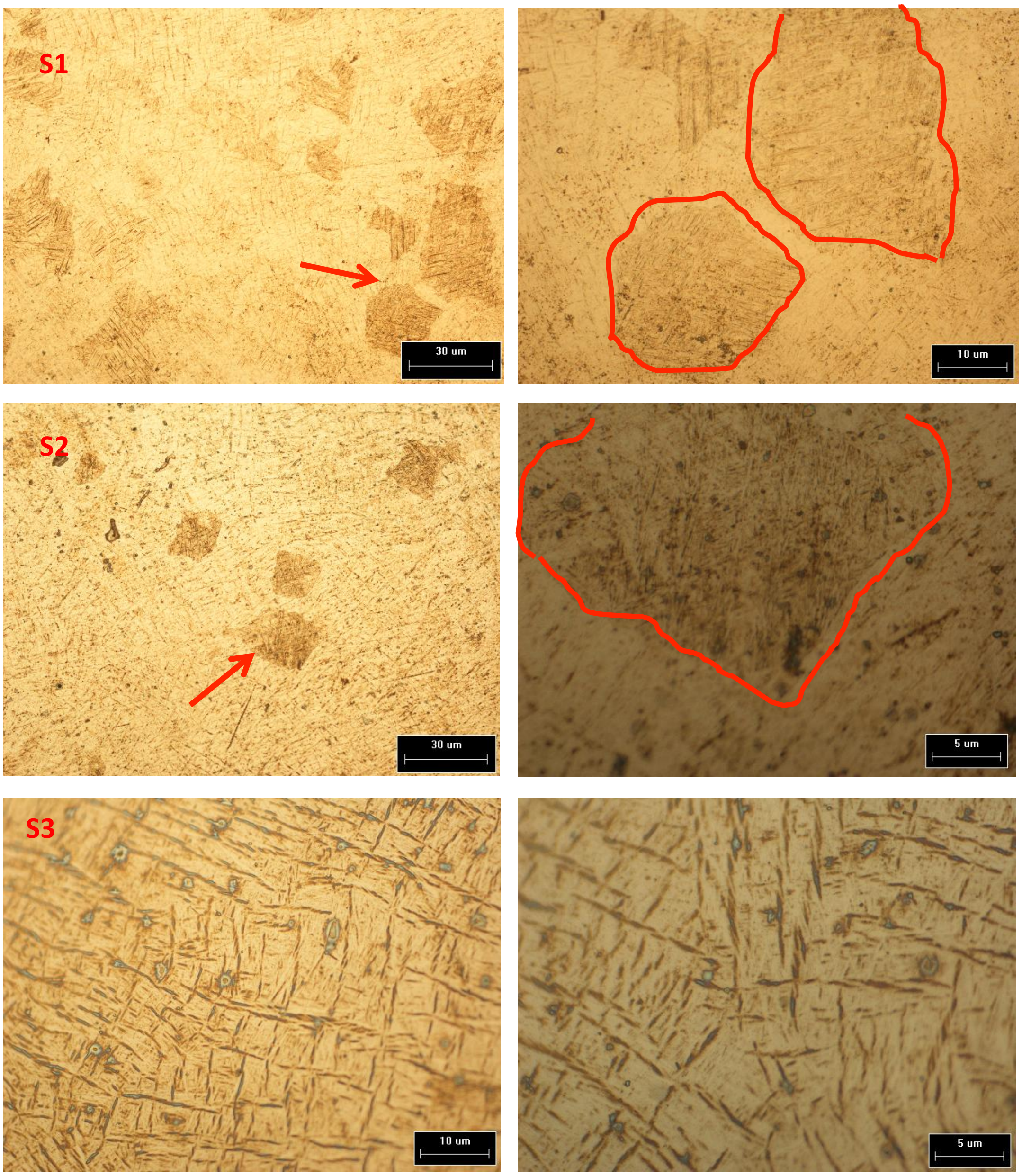

Figure 6.5: Top view for S1(750mm/s), S2(1000mm/s) and S3(1250mm/s)

The top view of a DMLS part is characterised by elongated grains oriented according to the scanning strategy which controls the direction of the heat flow. The elongated grains appeared as a grid pattern based on the predefined scanning strategies of the laser movement. In S3, the entire surface was covered with the elongated grains with grid pattern texture corresponding to the scanning vectors. On the other hand, for S1 and S2, the surface appeared to be very smooth with a very fine texture mostly at the edges of the specimens. As the scan speed reduces, many dark areas caused by preferential etching are visible on the top surface (1250mms^{-1} to 750mms^{-1}). These areas are mostly located near to the centre of the specimens. In the darker areas, there the structure is acicular, with a needle-like morphology similar to that seen in a side view. The arrangement of these acicular needles in the preferentially etched areas on the top surface is more random with a more complex basket-weave structure compared to the side view (as marked in figure 6.5). This more random orientation is possibly caused by a change in chemical composition of the alloy, which is brought on by Al segregation caused by the rapid solidification resulting from a higher energy input.

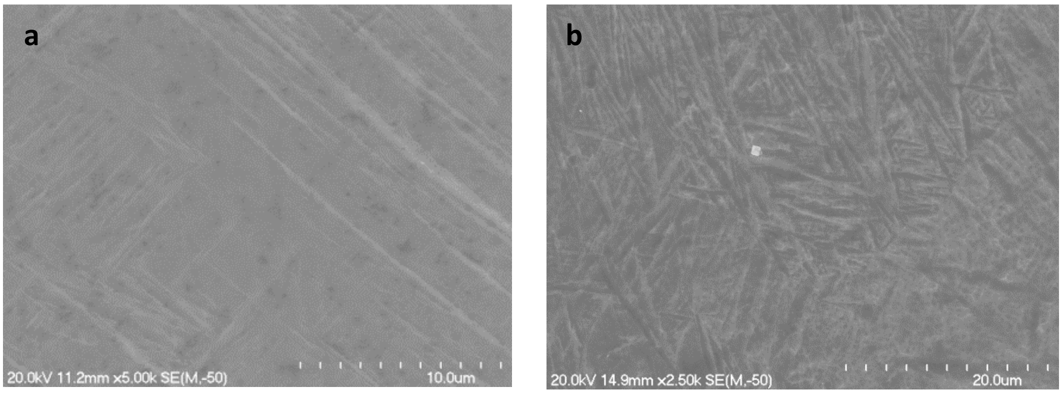

Figure 6.6: SEM micrographs of a side view (A) and top view (B) of S1

SEM micrographs show the presence of long thin elongated grains with an acicular or needle like morphology (figure 6.6). In a side view, the acicular needles appear as parallel bundles with similar orientation (columnar texture). A top view shows a basket-weave structure with irregular, randomly oriented acicular needles. In general, as the scan speed reduces, the microstructure becomes coarser with the α laths becoming thicker.

The darker areas identified in figure 6.5 in specimens made using a lower scanning speed, represents the melt pool boundary, where the melting temperature is reduced through possible Al segregation. This dark zone is more intense at lower scanning speeds compared to those found in specimens made using a higher scanning speed. This is probably due to the preferential etching of the intermetallic Ti_3Al phase which can form as a result of Al segregation. This is similar to work done by Pedersen [18]. It has been reported that in zones with a 25% Al concentration, a Ti_3Al phase will precipitate when the temperature reaches 500-600˚C. Therefore, when a higher amount of heat is supplied by lowering the scan speed, the material will reach higher temperatures and more material will remain longer at this higher temperature, thereby increasing the volume of precipitation[18].

6.3.3 XRD Characterisations

X-ray diffraction analysis was performed on the x-y plane of S1, S2 and S3. Results of the XRD analysis are shown in Fig 6.7. In this figure, a typical XRD diffraction pattern for the titanium alloy Ti6Al4V was obtained for a full scan from 30 - 90˚. Diffraction peaks corresponding to the hexagonal close-packed (hcp) Ti (JCPDS Card No. 893725) were generally detected in laser DMLS specimens. It can be seen that the only constituent of the laser sintered part was a hexagonal close-packed (hcp) phase. The hcp pattern can be attributed to both α and α' martensite, since they have a similar crystalline structure and very similar lattice parameters. However, with respect to the high laser energy density and rapid cooling rates, the microstructure obtained is undoubtedly α' martensite. Here the standard diffraction peaks for hcp Ti (α phase) located at 2Θ = **38.45˚** and 2Θ = **40.18˚** were taken for comparison. At a relatively low scan speed (750mms^{-1}) which results in high energy density, the 2Θ locations of the hcp Ti diffraction peaks of a DMLS part were shifted to the right (**38.67˚ and 40.61˚**). As the scan speed increases to 1000mms^{-1}, the 2Θ locations of the diffraction peaks again shifted to higher 2Θ (**38.72˚, 40.61˚**). According to the standard (JCPDS Card No. 893725) these diffraction peaks are associated with a martensitic phase. A significant shift of 2Θ to a value was detected at a scan speed of 1250mms^{-1} at 2Θ = **38.81˚** but not at 2Θ=**40.55˚**. The diffraction peaks for the alpha prime or martensite phase became considerably broadened and the intensity showed a significant decrease, suggesting a fine microstructures.

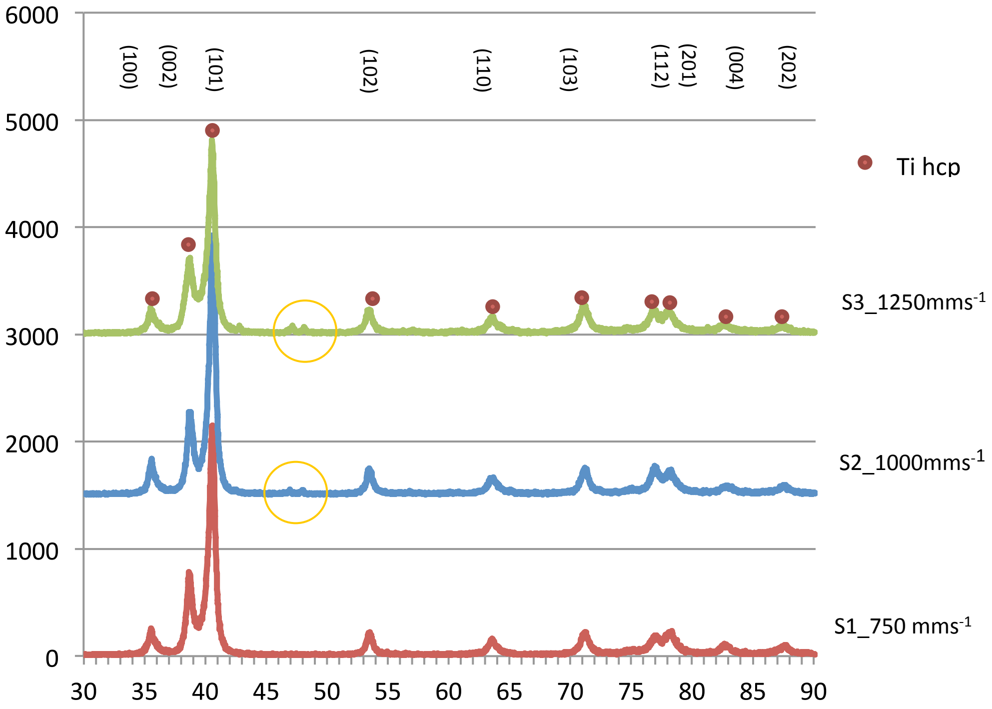

Figure 6.7: XRD spectra of laser sintered titanium alloy parts at different scan speed

	Ti		S1(750mms^{-1})		S2(1000mms^{-1})		S3(1250mms^{-1})	
2Θ	38.45	389	38.67	781	38.81	778	38.72	717
2Θ	40.18	923	40.61	2152	40.61	2425	40.55	1810

Table 6.2: XRD diffraction data for S1, S2 and S3

6.3.4 Discussion

Changing the processing parameters particularly the four crucial parameters i.e laser power, scan speed, scan spacing and layer thickness has an effect on the microstructure [19, 20]. In this study, the influence of scan speed was studied. The above metallographic analysis indicates that a lower scan speed results in coarsening of the microstructure. A low scanning speed also results in grains that are better aligned with the building direction. Hardly any porosity was seen using optical and SEM microscopy for all of the investigated groups. Another important observation at lower scan speed was the formation of columnar grain growth which indicates that the re-molten depth is bigger at lower scan speed.

The microstructure consists prior β columnar grains with an α+β structure consisting of α platelets with an acicular (plate-like) morphology. From this study, it has been observed that the scanning speed has a strong effect on the shape and size of the columnar grains. A low scanning speed (< 1250mms^{-1}) gives a high energy density and the width of the columnar grain is bigger. At a higher scanning speed (S3) the columnar grains are smaller and somewhat tilted relative to the building direction. The width of the columnar grains for all groups is in the region of 30µm to75µm which is near to the size of the scan track and layer thickness.

The herringbone pattern was caused by the alternate scanning directions. If the laser beam moves from left to right , the acicular structure is slanted as ///, and from right to left, the grains are slanted \\\. This relation suggests that the heat transfer direction plays a large role in the determination of the grain orientation[21]. The XRD data revealed the presence of the alpha prime martensite phase in the sample. The martensitic regions extend through the build with preferential planes of crystallographic growth arranged at a 45˚ angle to the building direction or z axis. The XRD data also showed the presence of the β phase in S2 and S3 but not in S1 (circled in fig. 6.7). With the higher energy density in S1, there is more decomposition of the β phase

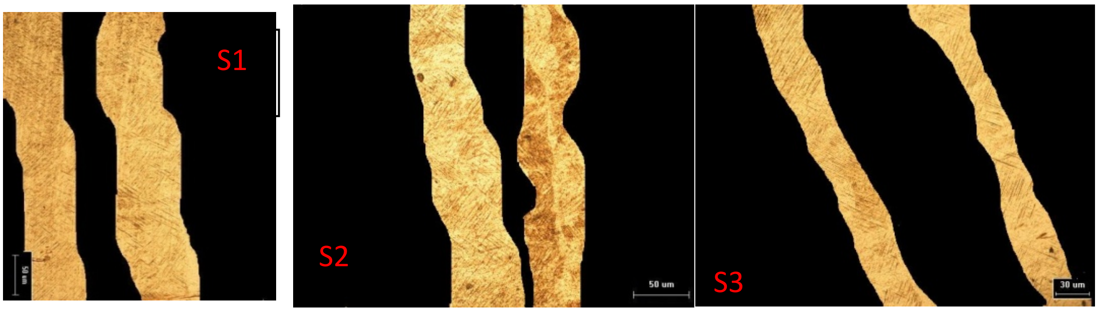

Figure 6.8: columnar grains of S1(750mms^{-1}), S2(1000mms^{-1}) and S3(1250mms^{-1})

The highlighted structure in Figure 6.8 is columnar growth in which the alternating herringbone structure indicates the change of scanning direction during the DMLS processing. The darker etched features indicate that the melt pool boundaries in the side views are more intense in S1 & S2. The occurrence of these bands allows one to estimate the actual re-molten layer thickness, based on vertical separation. It has been suggested that these bands become visible due to preferential etching of the intermetallic $TiAl_3$ phase. Due to the fast solidification, zones rich in Al are formed. The $TiAl_3$ phase will precipitate when the temperature reaches 500-600˚C, since the solubility of Al in Ti is very low

[21]. When a higher energy density was applied, the material reached a higher temperature and more material remained longer at temperature. This increases the volume of precipitation.

Ideally, pure Ti exhibits an allotropic phase transformation at 882˚C, transforming from a body-centred cubic (bcc) crystal structure (β phase), which is stable at higher temperature to a hexagonal (hcp) crystal structure (α phase), stable at lower temperature[18]. DMLS causes the powder particles to completely melt and solidify as a result of a high working temperature and fast cooling rate. The high heating/cooling rates in DMLS have been reported to be between 10^3 to 10^8 Ks^{-1} leading to a possibility of non-equilibrium phases [22]. Essentially, the laser scan speed influences the phase transformation by changing the degree of under-cooling and the solidification rate. At low scan speed, the input laser energy density (LED) during track by track scanning is relatively high, leading to an elevated thermalization of the energy and attendant residual stresses. Because of this thermal history, DMLS parts have a distinct and different microstructure compared with other manufacturing means. The microstructure consists of columnar grains with an acicular (plate-like) morphology. The acicular needles are attributed both to the α phase and the α’ martensite phase and are long, narrow with parallel orientation.

Mechanical properties

In this section, the variation in mechanical properties with laser parameters was investigated. It is known that the mechanical properties of a laser sintered part are determined by its microstructure. This is determined by the processing parameters and associated thermal history[23]. DMLS is an additive layer manufacturing process which is different from other, more conventional manufacturing techniques where subtractive processes are utilized. Therefore the microstructure of a DMLS part may differ from those fabricated using conventional tools since the process and thermal history are different. Hence the question arises, how good are the mechanical properties of titanium alloys fabricated through DMLS and are they competitive with those made using more conventional processing.

6.4 Tensile properties

Three groups of tensile specimens were built with different scan speed and scan spacing so that the influence of both parameters could be investigated. As discussed before, the scan speed determines the exposure time between the laser and the material. By increasing the scan speed, the energy density is reduced and by reducing the scan speed the energy density increased. The scan spacing is the distance between the laser scanned tracks. This parameter controls the overlaps between the scanned tracks. A small scan spacing creates big overlaps and bigger scan spacing creates small overlaps. A total of 27 flat dog-bone specimens were fabricated and divided into three main groups; G1, G2 & G3 with varies scan speed 1250mms^{-1}, 1000mms^{-1}, and 750mms^{-1} respectively. The groups were further divided into three subgroups (G1S1, G1S2 & G1S3) with different scan spacing 0.05mm (S1), 0.08mm (S2) and 0.1mm (S3). Each subgroup has three (3) specimens.

The results are shown below:

Scan speed(mm/s)	**0.05mm scan spacing**			**Average Yield strength MPa**	**Energy density J/mm^{-3}**
1250	1027	1029	1024	**1026**	**106.7**
1000	963	1035	1033	**1010**	**133.3**
750	1056	1069	1061	**1062**	**177.8**
	0.08mm scan spacing			**Avg YS (MPa)**	
1250	1028	1024	1020	**1024**	**66.7**
1000	1023	1018	1022	**1021**	**83.3**
750	1084	1090	-	**1087**	**111.1**
	0.1mm scan spacing			**Avg YS (MPa)**	
1250	1070	1068	1065	**1068**	**53.3**
1000	1030	1037	1035	**1034**	**66.7**
750	1081	1084	1095	**1087**	**88.9**

Table 6.3: Yield strength of different groups

Table 6.3 shows the variation in tensile strength for different group variations in scan spacing and scan speed. The results show that when the scan speed was reduced or when the interaction time was longer by 20%, the tensile strength increased slightly. There was not much difference when the scan speed was reduced from 1250mms^{-1} to 1000mms^{-1} at the same scan spacing. However, as the scan speed was lowered to 750mms^{-1}, the tensile properties showed a positive rise. The yield strength correlates well with the energy density. As can be seen, a higher energy density gives material with higher yield strength. The highest average yield strength was recorded at 1087MPa when the lowest scan speed (750mms^{-1}) and smallest scan spacing (0.1mm) were used. It is worth mentioning that there is an upper limit to the energy density. Too much energy has no benefit on the yield strength.

Young’s modulus is defined as a measure of the stiffness of an elastic material for a given geometry. It is also as the ratio of the stress over the strain along an axis. It was found that, at constant scan spacing, a slight reduction (20%) in scan speed causes a positive increase in the stiffness. The highest modulus is 120GPa for a scan speed of 750mms^{-1} and a scan spacing of 50µm. The lowest modulus is 66GPa at a scan speed of 1250mms^{-1} and with a 100µm scan spacing. The latter laser scanning condition gave a large variation from 66GPa to 100GPa in measured modulus. This is likely to be because of higher levels of porosity with increased scan seed and scan spacing. It is also apparent that in general, a bigger gap between tracks, gives reduced modulus value. For this condition, the energy density per track is reduced compared with a track with smaller scan spacing. It indicates that with a smaller overlap an area of the track was exposed more to the laser beam.

Scan speed (mm/s)	**0.05mm scan spacing**			**Average Modulus (GPa)**	**Energy Density Jmm^{-3}**
1250	98	77	81	85	**106.7**
1000	87	103	90	93	**133.3**
750	77	120	81	93	**177.8**
	0.08mm scan spacing				
1250	76	77	94	82	**66.7**
1000	95	83	93	90	**83.3**
750	67	100	-	84	**111.1**
	0.1mm scan spacing				
1250	66	82	100	83	**53.3**
1000	95	91	97	94	**66.7**
750	108	89	86	94	**88.9**

Table 6.4: Young’s Modulus for different scan speed and scan spacing

Scan speed(mm/s)	**0.05mm scan spacing**			**Average strain (%)**
1250	4.2	4.6	4.6	4.47
1000	1.7	3.4	4.4	3.17
750	2.8	2.7	3.0	2.83
	0.08 scan spacing			

1250	4.6	4.5	4.4	4.1
1000	4.4	4.3	3.3	4.1
750	4.2	3.7		2.8
	0.1 scan spacing			**Average strain (%)**
1250	4.8	4.3	3.2	4.5
1000	3.8	4.3	4.2	4.1
750	2.2	2.5	3.8	2.83

Table 6.5: Strain (%) of different groups

The ductility of the laser sintered parts was determined by elongation to fracture in a tensile test. The results from this work indicate that high tensile strength correlates with low ductility. The highest elongation was 4.8% elongation to fracture for a scanning speed of 1250mms^{-1} and a scan spacing of 0.1µm. The lowest was 2.2% at a scanning speed of 750mms^{-1}. It is noted that the ductility was reduced when a lower scan speed or a higher energy density was used. From this experiment, a combination of highest scanning speed with the lowest scan spacing gave the highest elongation to fracture. The result indicates that both scan speed and scan spacing influence the mechanical properties. In general the data presented shows a small positive trend as there are two variables used in this experiment. These two variables may cancel one another out and therefore the effect is minimal.

	Table – Tensile Properties						
	Scan Speed (mm/s)	**Scan Spacing (mm)**		quantity	Avg Ultimate Tensile Strength(MPa)	Avg. modulus (GPa)	Avg. Elongation (%)
Group 1	1250	1	0.05	3	1031	85	4.47
		2	0.08	3	1025	82	4.50
		3	0.1	3	1071	83	4.10
Group 2	1000	1	0.05	3	1010	93	3.17
		2	0.08	3	1024	90	4.00
		3	0.1	3	1039	94	4.10
Gr	750	1	0.05	3	1062	93	2.83

		2	0.08	3	1087	84	2.83
		3	0.1	3	1088	94	3.95
ASTM F 136-02-a (Oxygen level <0.13)					795	110	10
ASTM F 1108-04 (Oxygen level <0.20)					758	110	8

Table 6.6: The Overall tensile properties of each group

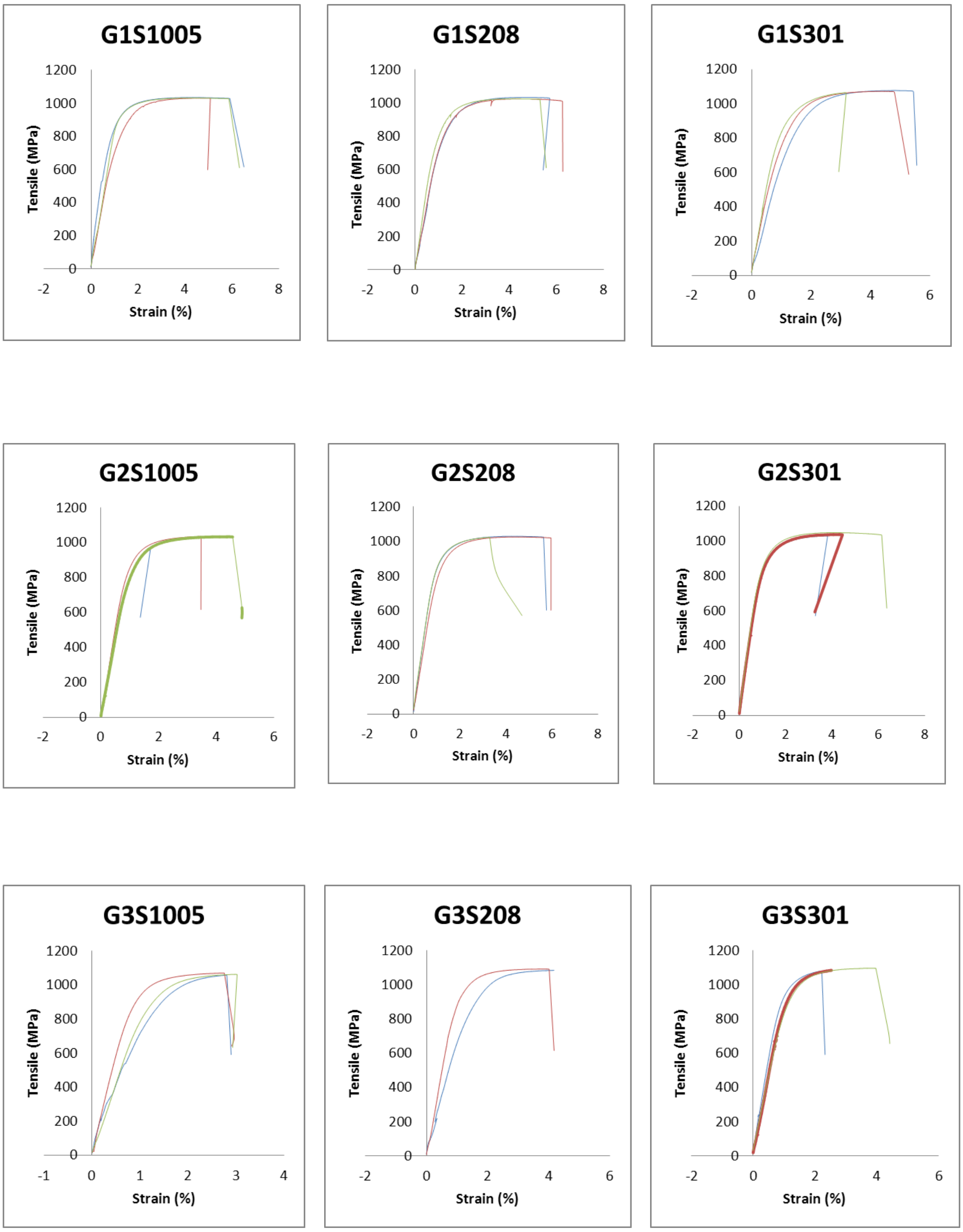
G1S1005
G1S208
G1S301
G2S1005
G2S208
G2S301
G3S1005
G3S208
G3S301

Figure 6.9: Stress vs strain graph for group 1, 2 and 3

The above table gives an indication of the influence of scan speed and scan spacing on the mechanical properties of part fabricated via DMLS. According to the energy density equation, there are four important processing parameters which determine the success of making a good laser sintered part. Scan speed, which is the velocity of a laser beam moving on the powder bed and scan spacing, which is the gap between the tracks. From the table, it was found that the mechanical properties of a DMLS part are dependent on scan speed and scan spacing. The tabulated data shows that the tensile strength of a laser sintered part exceeds the ASTM standard (Table 6.6) but below the standard for elongation. However, a better elongation can be achieved by increasing the scan spacing or by using the right combination of these two variables.

Figure 6.9 shows typical stress-strain curves for parts processed at laser speeds of 1250mms^{-1}, 1000mms^{-1} and 750mms^{-1} with corresponding scan spacing of 50µm, 80µm and 100µm respectively. It is clear that unlike its effect on ductility, a reduced scan speed has no pronounced effect on the tensile strength and elastic modulus. The result is in good agreement with predictions from the energy density equation[1]. According to this equation, the energy density increases with reduced scan speed thus increasing the surface temperature of the powder. Higher energy density results in a larger number of melted particles leading to a higher part density. However, once the powder is fully molten, there is minimal benefit to be gained from increasing the energy further. It can be seen that even at the slowest speed, the strength is almost the same as that achieved for a higher scanning speed, but the ductility drops to a very low level. The result also indicates that the tensile strength of a DMLS part at room temperature is comparable with those for Ti6Al4V, given in the ASTM the standard. Therefore, the tensile properties of DMLS parts are good enough to meet the needs of many engineering applications.

6.4.2 Fracture Surface

In this section, the fracture surfaces of broken tensile specimens, built using different processing parameters, is investigated. The fracture surface of a DMLS part, as shown in the figures 6.10 to 6.12, confirms a mixed mode fracture behaviour. Fractured parts were characterised by SEM and characteristic features could be seen for each of the scanning speeds. The fractured surfaces contained small, shallow dimples and quasi-cleavage fracture. As shown in figure 6.10, there is evidence of ductile dimples and an indication of weakly bonded powder particles at lower magnification. A quasi-cleavage fracture appearance is apparent at higher magnification.

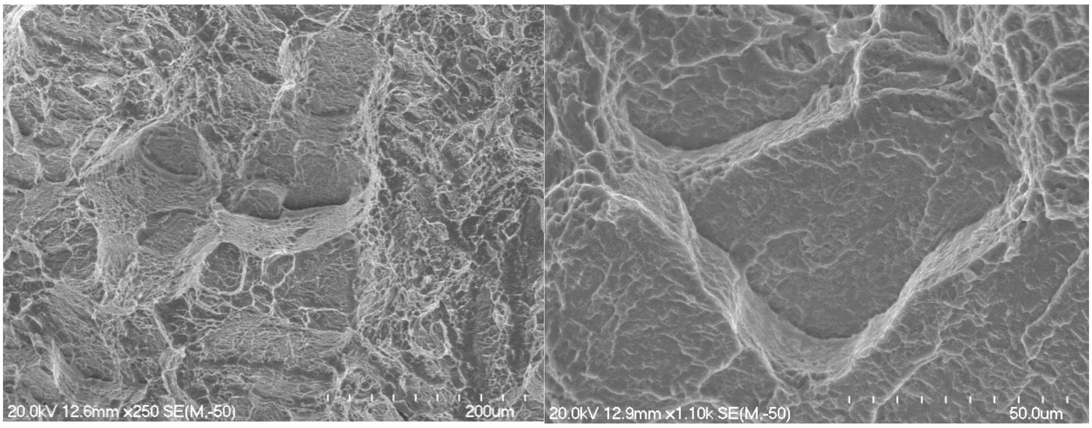

Figure 6.10: Fracture surface of G1(1250mm/s)

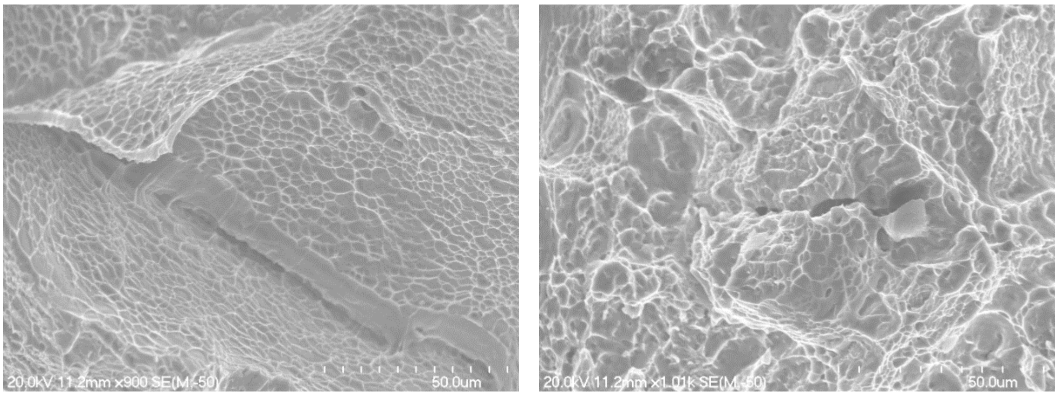

Figure 6.11: Fracture surface of G2 (1000mm/s)

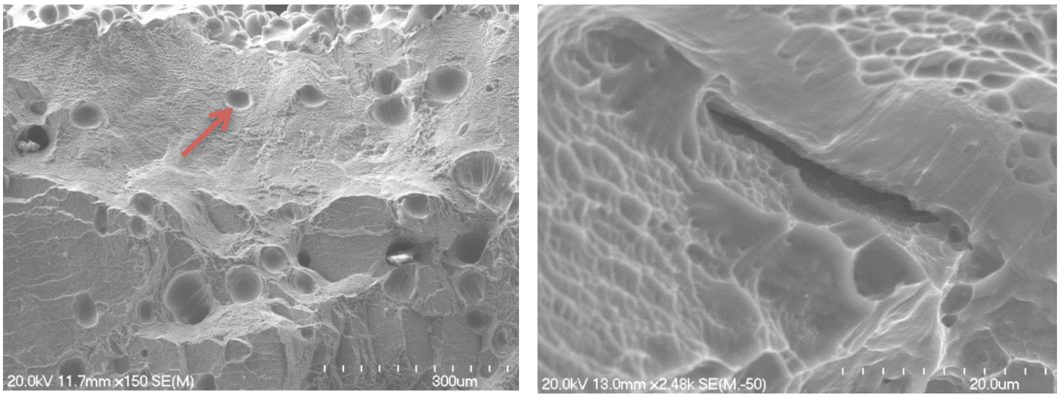

Figure 6.12: Fracture surface of G3 (750mm/s)

Overall the fracture surface shows a brittle appearance. In figure 6.12 there appears to be more evidence of ductile dimples, compared with fig. 6.10, within a generally flat fracture surface. As shown is figure 6.10 and 6.11, when the scan speed was reduced 20% to 1000mms^{-1}, the presence of micro cavities on the fracture surface are pronounced. Specimens from group 1 processing have bigger and deeper dimples. The fractured surface for specimens from Group 3, where the scan speed was reduced to 750mms^{-1}, exhibit more distinct brittle features compared to the other two groups. Certainly, there were many micro pores and micro-cavities in the size range of 1 to 10μm on the facture surface. The dimples were also increased in size. Theoretically, the micro pores play a role as crack initiators. During the tensile test, the micro cracks can act as stress raisers which can cause crack propagation.

The fabrication of parts by DMLS is a process based on the stability of the continuous melting pools in a single track. When a lower scanning speed is used, the longer exposure time to the laser beam may disturb the stability of the continuously melting pools. The molten pools produced by the scanning laser are essentially equal in size and shape due to a focused laser spot and uniform layer thickness. According to the laser energy density relationship, an increase in the energy density may create bigger molten pools and cause irregularities in the continuous molten pool. The DMLS process involves high cooling rates. This produces a finer grain size which contributes to a high tensile strength. However, the presence of micro pores and some poorly fused particles, due to instability in the molten pool reduces the resistance to fracture.

6.4.3 Vickers Hardness

Microhardness testing was performed on rectangular blocks built using DMLS. The blocks were built with variations in scan speed and the hardness of cross-sections was measured using a Mitutoya Hardness tester with a 50g load and a dwell time of 15s. Table 6.7 gives the effect of laser scan speed on the hardness. The results show that hardness increases with a reduced scanning speed. However, at the highest scanning speed of 1250mms, the hardness is still very high.

The calculated hardness is shown in table 6.7.

Scan speed	Scan spacing	Hardness (HV)
1250mms^{-1}	0.1mm	321 ± 12HV
1000mms^{-1}	**0.1mm**	**338** ±15HV
750mms^{-1}	**0.1mm**	**370** ± 12HV

Table 6.7: variation in hardness with scan speed

The microhardness shows a reduction in hardness with reduced scan speeds. Even though only a minimal effect is recorded through the hardness data, it is suggested that the scan speed has a considerable effect on a laser sintered part. At 1250mms^{-1} scan velocity, the parts were built successfully with good mechanical properties which conform to the ASTM standards.

Refering Table 6.6, it is stated that the oxygen levels given in the two ASTM standards are below 0.13% and 0.20% respectively. During DMLS processing, the oxygen level in the building chamber was kept below 0.04% by flushing argon gas continuously at 40 litre per min. The presence of oxygen not only increases the surface tension of the molten pool causing a balling effect but can also cause burning which deteriorates the DMLS part.

6.5 References

1. Simchi, A. and H. Pohl, *Effects of laser sintering processing parameters on the microstructure and densification of iron powder.* Materials Science and Engineering: A, 2003. **359**(1-2): p. 119-128.
2. Bo Song, S.D., Baicheng Zhang, Hanlin Lioa, Christian Coddet, *Effects of Processing parameters on microstructure and mechanical property of selective laser melted Ti6Al4V.* Materials and Design, 2012. **35**: p. 5.
3. Kumar, J.-P.K.a.S., *statistical analysis of experimental parameters in SLS.pdf.* Advanced Engineering Materials, 2005. **7**(8): p. 6.
4. Mukesh Agarwala, D.B., Joseph Beaman, Harris Marcus and Joe Barlow, *Direct Selective Laser Sintering of Metals.* Rapid Prototyping Journal, 1995. **1**(1): p. 11.
5. Simchi, A., *Direct laser sintering of metal powders: Mechanism, kinetics and microstructural features.* Materials Science and Engineering: A, 2006. **428**(1-2): p. 148-158.
6. Ruidi Li, Y.S., Jinhui Liu, Huashan Yao, and Wenxian Zhang, *EFFECTS OF PROCESSING PARAMETERS ON THE TEMPERATURE FIELD OF SELECTIVE LASER MELTING METAL POWDER.* Powder Metallurgy and Metal Ceramics,, 2009. **48**(3-4(466)): p. 10.
7. Deckard, J.D.W.a.C.R., *Advances in Modelling the effects of Selected Parameters on the SLS process.* Rapid Prototyping Journal, 1998. **4**(2): p. 11.
8. Glardon, R., et al., *Influence of Nd:YAG Parameters on the Selective Laser Sintering of Metallic Powders.* CIRP Annals - Manufacturing Technology, 2001. **50**(1): p. 133-136.
9. Yasa, E., J. Deckers, and J.-P. Kruth, *The investigation of the influence of laser re-melting on density, surface quality and microstructure of selective laser melting parts.* Rapid Prototyping Journal, 2011. **17**(5): p. 312-327.
10. Murr, L.E., et al., *Next-generation biomedical implants using additive manufacturing of complex, cellular and functional mesh arrays.* Philos Transact A Math Phys Eng Sci, 2010. **368**(1917): p. 1999-2032.
11. Ponader, S., et al., *In vivo performance of selective electron beam-melted Ti-6Al-4V structures.* J Biomed Mater Res A, 2010. **92**(1): p. 56-62.
12. Balla, V.K., et al., *Porous tantalum structures for bone implants: fabrication, mechanical and in vitro biological properties.* Acta Biomater, 2010. **6**(8): p. 3349-59.
13. Bertol, L.S., et al., *Medical design: Direct metal laser sintering of Ti–6Al–4V.* Materials & Design, 2010. **31**(8): p. 3982-3988.
14. Sebastian Storch, D.N., Guenther Schaefer and Rolf Reiter, *SLS qualifying analysis of metal based powder systems for automotive application.* Rapid Prototyping Journal, 2003. **9**(4): p. 12.
15. Murr, L.E., et al., *Microstructure and mechanical behavior of Ti-6Al-4V produced by rapid-layer manufacturing, for biomedical applications.* J Mech Behav Biomed Mater, 2009. **2**(1): p. 20-32.
16. G Lutjering, J.C.W.a.A.G., *Microstructure and Mechanical Properties of Titanium alloy: Titanium.* Springer Science and Business Media, 2007. **35**.

17. Darmadi, D.N., J.Tieu, A.Kiet, *Analytic and finite element solutions for temperature profile in welding using varied heat source model.* World Academy of Science, Engineering and Technology, 2011. **81**: p. 154-162.
18. Pedersen, R., *Microstructure and Phase Transformation of Ti6Al4V*, in *Department of Applied Physics and Mechanical Engineering, Division of Engineering Materials*2002, Lulea University of Technology.
19. Klingbeil, J.B.a.N., *The Role of Process Variables in Laser-Based Direct Metal Solid Freeform Fabrication.* Journal of Manufacturing, 2001.
20. Yadroitsev, I., et al., *Factor Analysis of Selective laser melting process parameters and geometrical characteristics of Synthesized single tracks.* Rapid Prototyping Journal, 2012. **18**(3): p. 9.
21. Thijs, L., et al., *A study of the microstructural evolution during selective laser melting of Ti–6Al–4V.* Acta Materialia, 2010. **58**(9): p. 3303-3312.
22. Gu, D., et al., *Densification behavior, microstructure evolution, and wear performance of selective laser melting processed commercially pure titanium.* Acta Materialia, 2012. **60**(9): p. 3849-3860.
23. Nikolay K. Tolochko, T.L., Maxim K. Arshinov, Andrey V.Gusarov, Victor I. Titov and Ludo Froyen, *Mechanism of selective laser sintering and heat transfer in Ti Powder.* Rapid Prototyping Journal, 2003. **9**(5): p. 13.

Chapter 7: Design and Fabrication procedure for a Customised Titanium Implant

Introduction

In previous chapters, the effects of processing parameters such as laser power, scanning speed and scan spacing on the microstructure and mechanical properties were analysed. The knowledge about the role played by each of the DMLS processing parameters was used to improve process understanding as well as to allow one to appropriately select the right set of processing parameters to achieve specific properties in a part to be built. It can be concluded that the properties of laser sintered parts depend strongly on each single laser melted track and each single layer as well as on the connection between them. A sufficient laser energy density, which is strongly influenced by laser power, is imperative to allow an ideal interaction between the laser and material where fully dense or porous parts can be built successfully. The relationship between texture evolution and a specific energy density used for manufacturing a fully dense part was investigated. This was done to find out which microstructural features can be tailored during the laser sintering process.

For biomedical implants, it is not necessarily better to have a fully dense part but a good combination of a porous and dense structure is required [1-3]. It is difficult and sometimes impossible to fabricate customised bone implants with complex shapes by means of cutting, sheet forming and casting, and furthermore to tailor the structural properties to a specific requirement. This chapter illustrates a new design method and fabrication procedure for making craniofacial implants by employing the manufacturing processing knowledge gathered from the previous chapters with a 3D medical imaging processing technique.

In the first section, the fabrication framework is presented which begins with the CT scan data acquisition and data manipulation. This includes the data transfer from 2D radiography images to 3D solid data using specific medical imaging software. The second section develops a technique for making porous structures through CAD software. Finally, a novel design procedure for a patient specific porous implant is presented, which takes into consideration its' aesthetic and functional requirements by utilizing a predefined unit cell lattice structure developed through appropriate software.

7.1 The development of a customised craniofacial implant

A flow chart of the fabrication technique for a customised craniofacial implant is shown in Table 7.1. CT scans or CAT scans, stands for computed tomography (CT) or computed axial tomography (CAT). It uses an x-ray technology to take multiple cross-sectional views of the human body. Compared to other x-rays methods, a CT scan is capable of obtaining clearer images of organs, bones, soft tissues, blood vessels and other internal organs. Basically, a CT scan is used as a reference for designing new patient specific implants. Therefore for each new implant, the patient needs to go through this process so that a customised design can be made. The customisation is based on the anatomical data obtained directly from the CT scan data which includes the size, shape and morphology of the affected bone. The availability of commercial medical imaging software such as MIMICS and MAGICS provides great assistance in generating and manipulating 3D medical surface data from 2D CT multiple cross-sectional images.

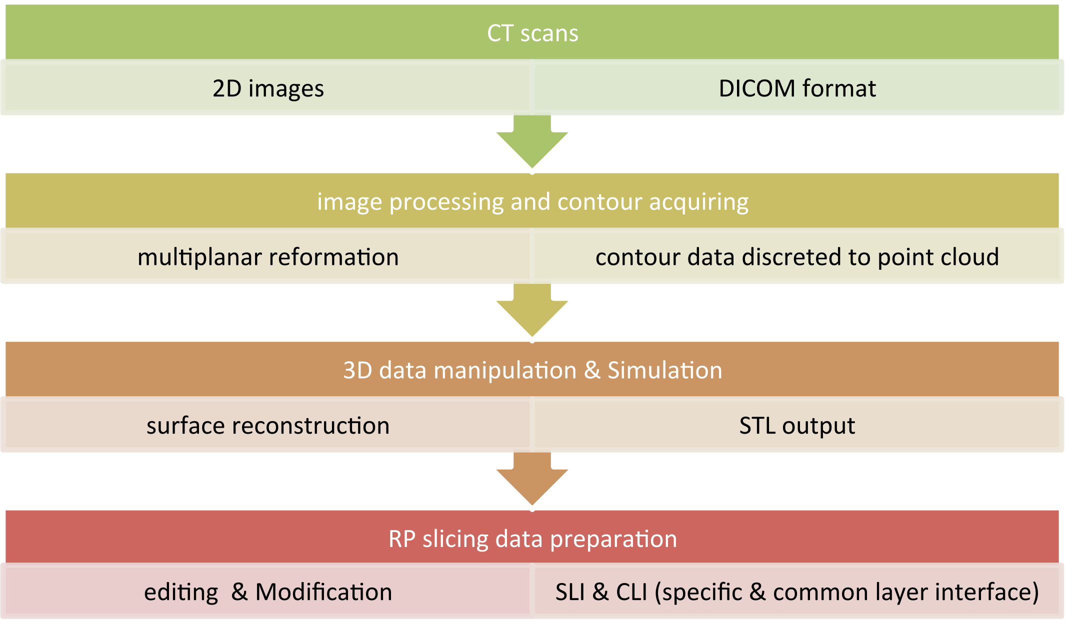

Figure 7.1: Image processing work flow

DICOM stands for Digital Imaging and Communication in Medicine (www.materialise.com). DICOM is a standard for handling, storing, printing and transmitting information in medical imaging, which includes file format and a network communication protocol. It allows image processing software for receiving and retrieving patient data directly from the scanner so that the communication between two different systems can be established. DICOM has been widely adopted by hospitals particularly in picture archiving and communication system (PACS)

7.1.1 Digital Data Preparation

A patient's CT scan data, with cranial defects and mandible deformities obtained from a scanner, were manipulated using MIMICS software in order to produce segmentation of the bony structure for each tomography slice. The 2D segmented slice data was converted to 3D data, mainly for better visualisation and manipulation. Now the data is saved as *.mcs* which is the specific format for MIMICS software. In MIMICS, suitable thresholding values were assigned to separate the regions of interest, which are the affected cranial and mandible bones. At this stage, much work is done on the 2D cross-sectional data as this allows faster processing of more accurate data selection. With appropriate thresholding values, MIMICS generates a 3D anatomical part from the multiple 2D cross-sectional data. Upon completion, the selected part is converted to STL format and transferred to another platform for further editing.

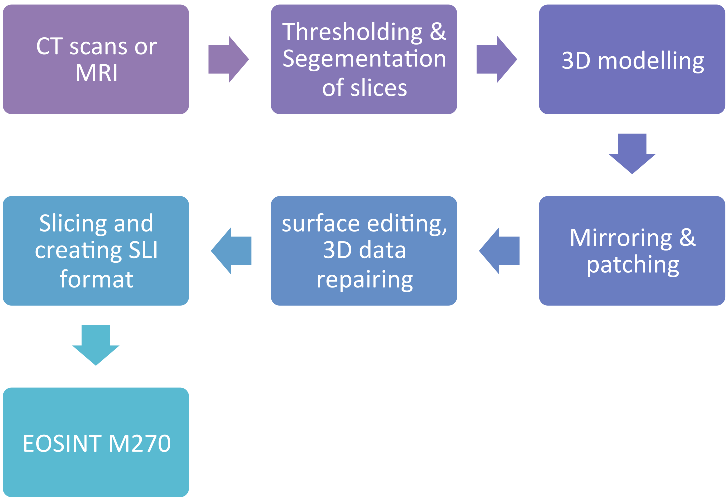

Figure 7.1a: Fabrication process flow

7.1.2 Data Conversion

The flow chart provides the data conversion platforms during the development of customised implants. These multiple platforms are associated with different type of software which will be explained in detail in a later section. Basically, in order to manipulate and fabricate a craniofacial implant, this software and its particular file format are needed. As far as data transferring is concerned, these software are inter-related and were developed by Materialise and EOS for this specific task.

Figure 7.1b: Software and its required format

7.1.3 CT Scan Data (DICOM specification)

CT Images are a pixel map of the linear X-Ray attenuation coefficient of tissue. The pixel values are scaled so that the linear X-ray attenuation coefficient of air equals -1024 and that of water equals 0. This scale is called the Hounsfield scale after Godfrey Hounsfield, one of the pioneers in computerized tomography. Using this scale, fat is around -110, muscle is around 40, trabecular bone is in the range of 100 to 300 and cortical bone extends above trabecular bone to about 2000. In this study a trabecular and cortical were used for the modelling. The pixel values are shown graphically by a set of gray levels that vary linearly from black to white.

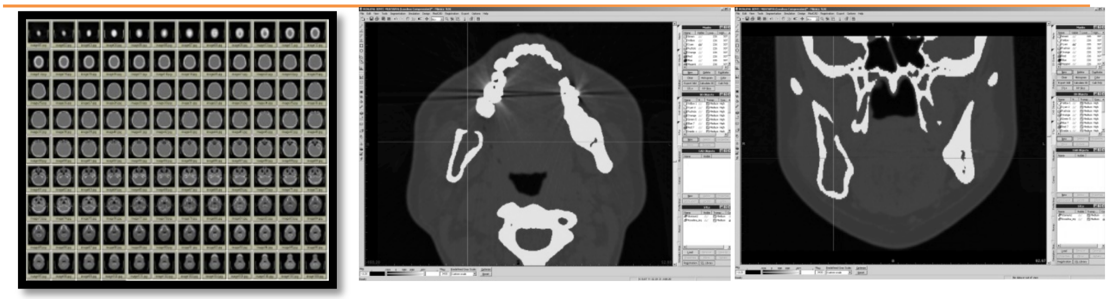

Figure 7.2: CT scans images of an infected mandibular due to ameloeblastama

The mapping of pixel values into gray levels is specified by a level and a width. A gray scale is centred about its level. For example, a level of 0 specifies that water will be displayed as mid-gray. The extent of the gray scale is specified by its width.

The default gray scale used by MIMICS allows you to see the full range of tissue from air in the maxillary sinus to the densest of cortical bone, but subtle differences in the soft tissue cannot be visualized. If we narrow the gray scale, we can get a better visualisation of the subtle differences in the soft tissue or trabecular bone, but at the cost of forcing cortical bone to be in one gray level: white. Narrowing the gray scale can help us to locate the mandibular canal if it is not easily seen with the default gray scale. For data transfer specification, uncompressed DICOM data is required in which the images are prepared in three different layouts consisting of axial, coronal and sagittal. The preferable setting for the CT scans is as shown below;

Scan Parameters	
Mode	Spiral Scan
Volt	120kV;140mA
Slice thickness	0.6 to 1mm
Rotation time	1sec
Field of view	21cm
Pitch	1
Rotation increment	1mm

Table 7.2: CT scan specification

MIMICS software is an image-processing package with 3D visualization functions that interfaces with all common scanner formats. In this study, MIMICS is used as an interactive tool for the visualization and segmentation of CT images and 3D rendered objects. A non-invasive imaging technique scan of the defect region was taken and appropriately loaded into MIMICS software. The images were sequentially stacked upon each other and information related to the imaging parameters such as slice thickness, pixel resolution were entered into the system. Generally, in the medical field, MIMICS software can be used for diagnostic, operation planning or rehearsal purposes. It provides a very flexible interface for rapid prototyping systems since distinctive segmentation of objects can be created.

7.1.4 Thresholding & Segmentation in Mimics

MIMICS provides a flexible interface for quickly calculating a 3D model of the region of interest with a thresholding method. Subsequently, we can set the parameters for resolution and filtering. Information about height, width, volume and surface is available for every 3D model. Thresholding means that the segmented object will contain only those pixels of the image with a value higher than or equal to the threshold value. Sometimes an upper and lower threshold is needed; the segmentation mask contains all pixels between these two values. A lower threshold value makes it possible to select the soft tissue of the scanned patient. With a higher threshold, only the very dense parts remain selected. Using both an upper and lower threshold is needed when the nerve channel needs to be selected.

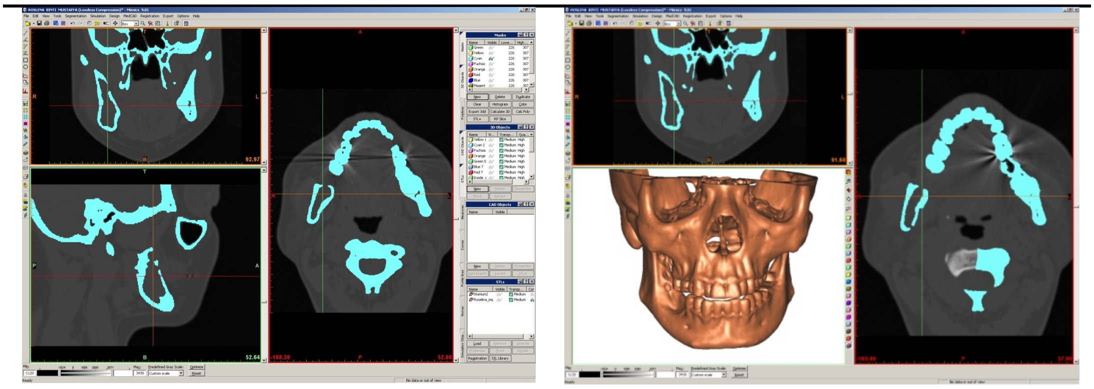

Figure 7.3: The area of interest (segmentation) is selected through a thresholding technique

One of the important things in modelling is to assign the correct thresholding value. Generally, if one's objective is to have a nice looking model, a lower threshold value is recommended since it will result in a model with fewer holes. On the other hand, when the model serves for modelling prosthesis a higher threshold value is preferred. The choice of a threshold is obviously very crucial and a very difficult decision.

Name	Lower threshold	Higher threshold
Bone (CT)	226	**3071**
Soft tissue (CT)	-700	**225**
Enamel (CT, Adult)	1553	**2850**
Enamel (CT, Child)	2042	**3071**
Compact Bone (CT, Adult)	662	**1988**
Compact Bone (CT, Child)	586	**2198**
Spongial Bone (CT, Adult)	148	**661**
Spongial Bone (CT, Child)	156	**585**
Muscle tissue (CT, Adult)	-5	**135**
Muscle Tissue (CT, Child)	-25	**139**
Fat Tissue (CT,Adult)	-205	**-51**
Fat Tissue (CT, Child)	-212	**-72**
Skin Tissue (CT, Adult)	-718	**-177**
Skin Tissue (CT, Child)	**-766**	**-202**

Table 7.3: Thresholding values for bones and tissues

A solution to this threshold problem may be to work with different thresholds for different regions. Table 7.3 shows the predefined threshold values for segmentation. The segmentation and the morphology operation are easier to run at this stage since all the images are well connected to each other. These multiple 2D cross-sectional images with the same thresholding value are stacked together to form 3D surface data representing the selected parts or organs. In the case of a cranial defect, the full skull data was transferred and for an infected mandible, only the mandible was converted to *.stl* format data. The next step is editing and repairing of the 3D surface data in MAGICS before designing the implant.

7.1.5 Mirroring technique & Fixing in Magics

After segmentation, a mirroring technique is used to get the good data for the implant. This means, based on the location of the defects, the good area, surfaces or region on the other side is mirrored to retain the same size, shape and morphology of the new implant. An axis of symmetry is identified based on the virtual model even though a human cranial structure is not perfectly symmetrical and there may be some asymmetry which will result in an imperfect match. As for the mandible, since only half of the mandible was affected by the disease, the mandible was cut into two parts through the middle to separate the good side and the affected area. The affected side was removed and the good side was mirrored. Removing unwanted triangles which represent the unwanted surfaces has to be done manually by deleting the unwanted surfaces or triangles. As shown in figure 7.4, the manipulation and 3D surface editing is done using MAGICS software.

The mirrored file normally has unwanted surfaces or triangles from the mirroring process. Therefore, MAGICS was used to remove all these unwanted surfaces. These surfaces consist of small triangles. As for the new cranial flap, only the outer surface was required as a reference for the new frontal implant and it is the same for the mandible implant. The outer or inner surface represents the outline or reference for the new implant. Therefore, all the surfaces beneath the mirrored part and the surfaces inside the mandible were removed accordingly.

7.1.6 Generating 3D data & simulation In MAGICS

Once the size and shape of the new implant are confirmed, thickness was assigned to the part so that solid data can be generated. As for the frontal implant, the outer surface is selected and 1mm thickness is applied uniformly. It is more difficult for the mandible due to its morphological complexity compared to the frontal implant. Therefore for the mandible, a region by region method was used in order to get a smooth and uniform thickness throughout the mandible. The region or area where the surfaces meet together and which forms a crooked new surface was removed properly and replaced with a smooth surface. This was done by selecting individual triangles on the part and removing them manually.

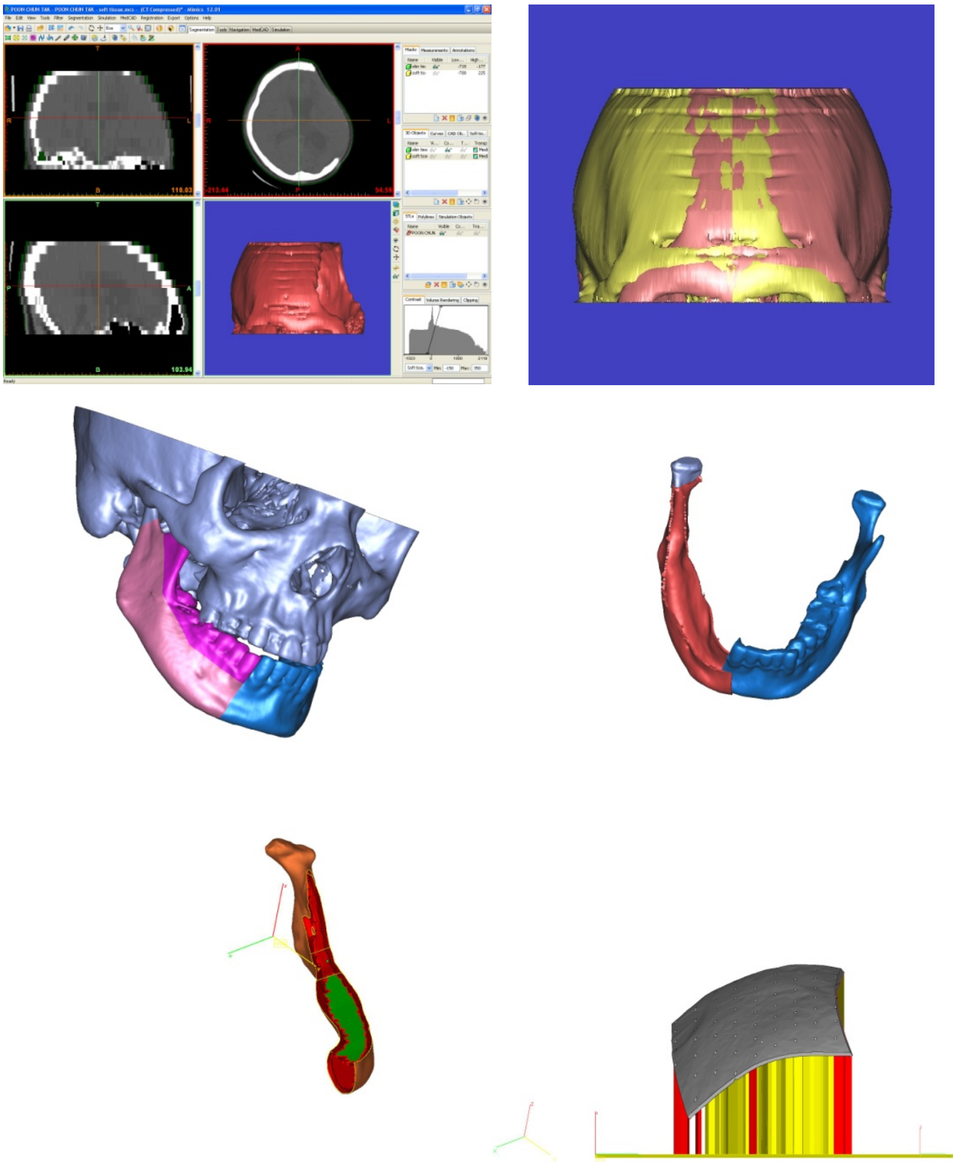

Figure 7.4: CT scan images and simulation in MAGICS software

Finally, both implants were checked for unwanted surfaces prior to the applied thickness. A simulation was performed in MAGICS to analyse how the new implant fits the patient’s bone. The part was first orientated in the same plane and axis. Both the patient’s skull and mandible were brought to the original position which is at 10, 10, 10 in x, y, z respectively. A translation function was used where quantitative movement of the part can be done. The new implant was fitted to the patient’s skull and mandible with 0.5mm tolerances given prior to the fabrication process. This is due to the probability that the final parts may require deburring or machining to remove sharp edges. The size and shape were checked accordingly so that the cosmetic and functional requirements were fulfilled.

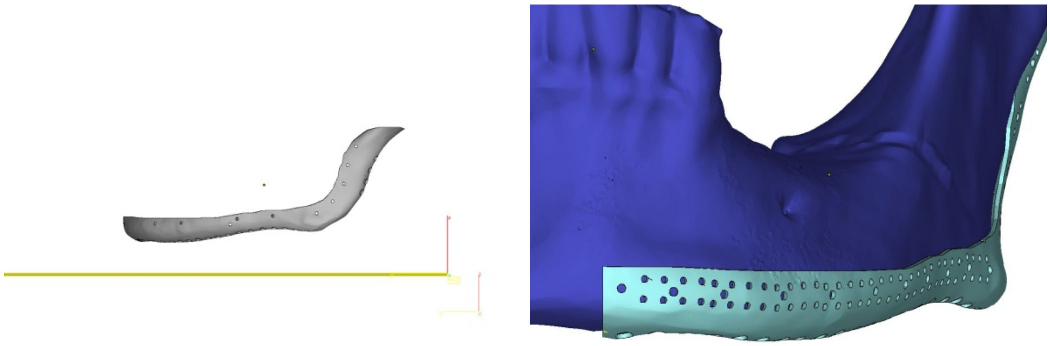

Figure 7.5: mandible implant with the titanium mandible tray assembly

7.2 Designing a porous structure via a virtual puncher

Two design methods were used in this research work for manufacturing porous cranial and mandible implants. The first method used in this study is time consuming and involves lengthy steps. This was done by employing basic CAD functions. The procedure has certain limitations in relation to design complexity and also accuracy, since the placement of the virtual puncher on the desired location is sometimes impossible. The second method provides a more innovative and simpler approach where a predefined unit cells function was used to attach a complex lattice structure onto the desired part or regions.

7.2.1 Virtual tooling or puncher

The first method uses CAD software to create a 3D virtual tooling or puncher. This puncher was then integrated with the 3D implant data for the mandible and the cranial flap. It is necessary to have both the puncher and the implants in the same data format. In this case, an stl format was used. Apparently, MIMICS was used to convert the implant data to stl , Solid works was utilised to design the virtual puncher and finally, MAGICS was used as the STL editor where mirroring, fixing and assembly were done.

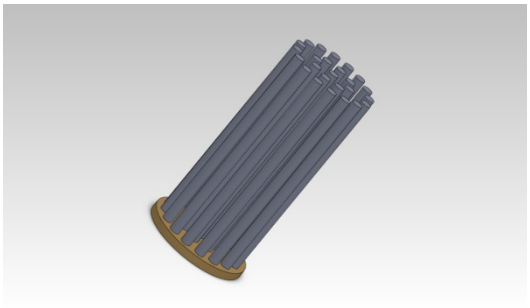

Figure 7.6: Virtual Puncher design in Solidworks

The puncher has many cylindrical features with two sets of diameter, 500µm and 1000µm respectively. The file was then converted to STL format and transferred into MAGICS software so that it could be assembled with the new 3D implant data. The puncher was placed at regions of interest on the implant's surface where a porous structure was required. In the case of the cranial flap, the surface was made porous by creating many holes. These holes are based on the size of the cylindrical feature on the puncher. A subtractive Boolean operation was used, thus leaving many holes of a circular shape on the new implant surface. These steps were repeated till the hole covers the entire area.

As for the new mandible, it was designed to have a thin wall with an approximate thickness of 0.5 mm. A series of 500µm and 1000µm holes were placed on the wall respectively and 2mm holes on the bottom of the mandible. The same procedure was used to create those holes where a virtual puncher was created and a Boolean operation was used. This process consumes time as it is difficult to locate correctly the virtual puncher on the intended surfaces. On top of that it involves a huge amount of data to manipulate and process. Once the design is ready, the file was saved as STL and sent to EOS Tools software for slicing and support generation.

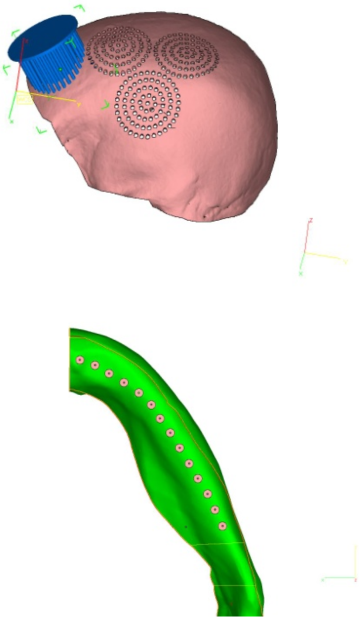

Figure 7.7 shows where the virtual puncher intersects the cranial flap and then a Boolean operation was used to create holes on the surface. This assembly work was done in MAGICS.

A series of 2mm holes were placed on the bottom of the mandible tray for fixation. 500µm and 1000µm small holes were randomly placed on both sides of the wall to create pores

Figure 7.7: A Boolean operation is used to create the pores on the mandible.

7.2.2 Creating a support structure

One of the crucial steps in DMLS is creating support structures and identifying the optimum part orientation[4]. The support structures are required before a part can be fabricated or sent to the machine. This was performed using the MAGICS RP Tools. For creating a support structure, there are a few things that need to be considered;

1. Surfaces which need to be supported.
2. How to remove the support structure after completion of the part.
3. The surface which needs to be preserved – in the case of a mandible implant, the outer surface was preserved by having the support structures in the inner surface.

Basically, all the downward surfaces which have build angles of more than 45° require a support structure. Removing the support structure is a tedious job and is time consuming, especially for tiny parts with a complex internal structure. On top of that, a support structure leaves marks and causes a rougher surface which normally requires post processing work.

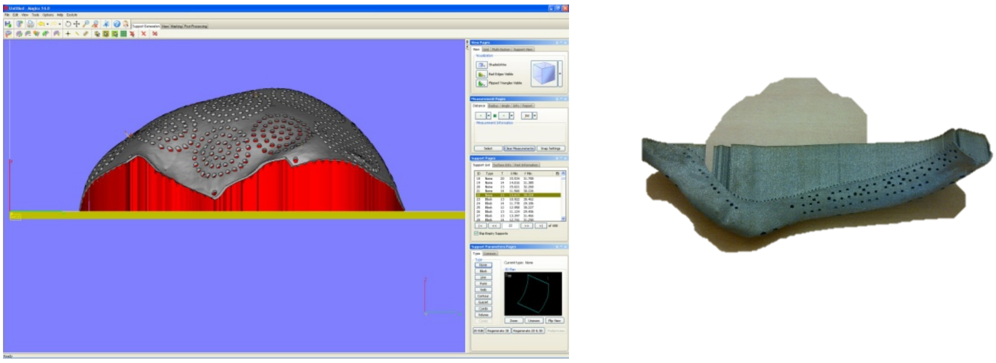

Figure 7.8: support structure on the implants

processing 2 hr 40mins

- processing conditions as illustrated above
- average 15min/mm

powder consumed 300g

- powder consumed
- volume of the mandible tray 1061.795mm^3

cost £461.98

- including man hour for design, processing & post treatment, overhead rate, data preparation, data alteration (support, slicing, fixing), VAT

post processing 1 hr

- removing part from platform, removing support structure, thermal stress relieved (wire cutting, grinding)

7.2.3 Results & Discussion (mandible & frontal implants)

The mandible and frontal implants were successfully built using the direct metal laser sintering technique. No post treatment was required and the part has good surface quality with accurate dimensions and geometry which conformed to the 3D digital data. Cracks and the common stairs effect due to layer by layer fabrication were not visible. Measurements confirmed that the as built specimen was in accordance with the CAD data. The mandible was fabricated in two hours forty one minutes at a cost of £384.98 (excluding VAT). It has a building height of 28.44mm. The building speed for this fabrication was 15mins/mm.

Figure 7.9: The frontal and mandibular implant

7.2.4 Utilising unit cells in MAGICS

Another method used in this study to produce a porous implant was by utilising a specific unit cell structure. Different unit cells were selected in order to vary the porosity of a part and investigate the manufacturing capability of building a complex internal structure controlled by the size and design of the strut (Table 7.4).

This application is available in an upgraded version in MAGICS v17 software. MAGICS software, as discussed earlier, enables you to import a wide variety of CAD formats and to export files ready for rapid prototyping, tooling and manufacturing. Its applications include repairing and optimising 3D models; analyzing parts; making process-related design changes on your STL files; designing fixtures; documenting your projects; production planning and much more. In the upgraded version of MAGICS software, it has a library of unit cells with porous structures as shown in Table 7.4. The default unit cells have calculated volumes and porosity. The size of a structure and its porosity can be defined through the size of the struts in the x, y and z directions or the size of the pores in a unit cell respectively. There are many unit cells in this library such as basic rectangles, cross X, Gstructure10 which can be selected based on the user preferences.

A Boolean operation was used to attach the selected unit cells on the intended area. The unit cells were defined by choosing the unit cell type with an appropriate strut size. The strut size determines the porosity of a part where the smallest strut size provides the highest porosity. A good graphic processing desktop is required to process this porous structure. If a complex or huge part was used, it will take a longer time to process. In this study, five unit cells were selected as shown in Table 7.4. Each of these unit cells has a type of strut and design. The strut size for this particular design was from 0.1 to 0.8mm and the unit cell in the range of 1mm to 2mm.

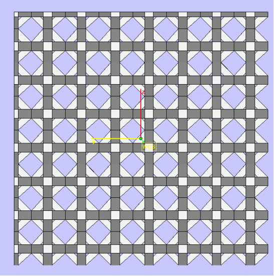		Pattern 1: G Structure10 Unit Cell: 2mm Strut dimension: 0.519mm Cubic's Volume: **999**mm^3
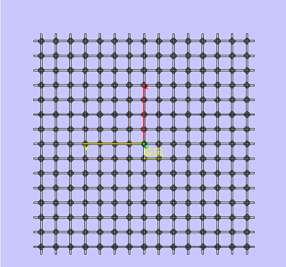		Pattern 2: Cross 3 Unit Cell Size: 1mm Strut dimension : 0.1mm Cubic's Volume: **155**mm^3
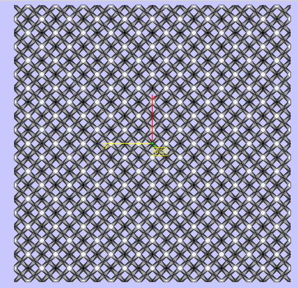	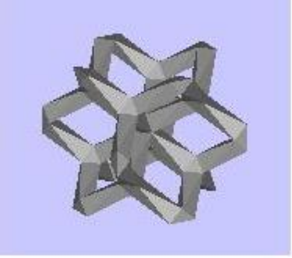	Pattern 3: Dode Medium Unit Cell Size: 1.2mm Strut dimension : 0.219mm Cubic's Volume: **423**mm^3
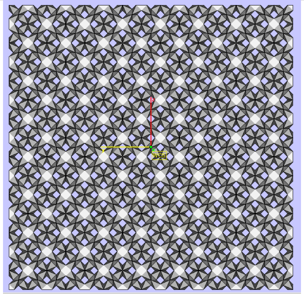	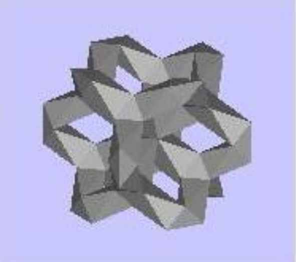	Pattern 4: Dode Thick Unit Cell Size: 1.6mm Strut dimension : 0.718mm Cubic's Volume: **832**mm^3
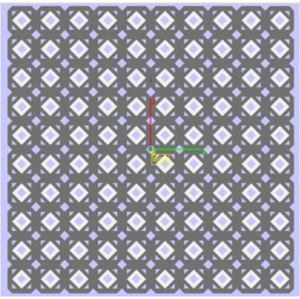		Pattern 5: Trunc Octa Light Unit Cell Size: 2mm Strut dimension : 0.48mm Cubic's Volume: **687**mm^3

Table 7.4 Design parameters for the cups

Item	Unit Cell	Cube Weight(g)	Cube design Volume (mm^3)	Cube measured Volume (mm^3)	Cube Density (gcm^{-3})
P1	GStructure10	5.10	999	1163	4.382
P2	Cross3	1.72	155	442	3.872
P3	DodeMedium	4.21	832	1210	4.344
P4	DodeThick	5.27	423	969	4.364
P5	TruncOctaLight	4.14	687	958	4.322

Table 7.5: The weight, volume and density of the cubes

The design steps to produce porous cubes by applying the unit cells in MAGICS software are shown below. With these functions, a lattice or lightweight structure, as discussed earlier in this chapter is not a problem at all. The four steps required before porous structure can be designed successfully. The processing time was longer for smaller strut sizes, which in this case is 0.1mm, since it consumes more structure per volume to analyse.

1. A file is converted to STL format.
2. If there is a combination of a solid and a lattice structure in one part, the part needs to be separated (not connected) and must be given different name before assembly.
3. Under Tool >create structure> choose structure> define other parameters for customisation> apply.
4. A Boolean operation is used to attach the unit cells on the part and subsequently remove the unwanted area.
5. The part was saved as STL and follows the normal fabrication procedure before send it to an RP machine i.e slicing

The parts were designed as 15mm cubes. The bounding volume of the parts is 3375mm^3. The average grain density of each cube is as shown in table 7.5, which is slightly lower than the theoretical density of fully dense Ti6Al4V (4.42gcm^{-3}). Table 7.5 also shows the actual weight and porosity values compared with those of the intended design values. The difference in values between the theoretical and experimental values can be attributed to the undulations on the surface and the possibility of having unsintered powder particles trapped in the structure.

The porosity is given by the equation:

$$P_1 = \frac{V_1 - V_2}{V_1} \tag{19}$$

where P is porosity, V_1 is the bounding volume, V_2 is the material volume. The density of a cube was calculated using gas pycnometry. Three readings were collected per unit cube and an average was used. The details of this measurement are explained in chapter 3.

The amount of porosity varied in each cube in accordance with the selected unit cell structure. This is controlled via the size of the struts; by reducing the strut size and the pore size is increased. Therefore the calculated surface area decreased with an increase in porosity. A correlation between the porosity of the cubes and pore volume is shown in table 7.6. The porosity values calculated using gas pycnometry are lower than the theoretical design values determined by the software. The designed parts are assumed to have a flat smooth surface for calculation of porosity values.

Unit Cell	**Theoretical Pore volume (mm^3)**	**Experimental Pore Volume**	**Theoritical Porosity (%)**	**Experimental Porosity (%)**
G structure 10	2376	2212	70.40	65.5
Cross_3	3220	2933	95.41	86.9
DodeMedium	2952	2406	87.47	71.3
Dode Thick	2543	2165	75.35	64.1
TruncOctaLight	2688	2417	79.64	71.6

Table 7.6: The pore volume and porosity of the 15mm cubes ($3375mm^3$)

Internal Characterisation

Pore size distribution, surface area, pore connectivity were studied using optical and SEM images. The images show that interconnected pores were built successfully and distributed evenly. The struts were well formed without any discontinuity throughout the internal regions. There is still evidence of residual powder particles trapped within the structure. This is seen in G structure10 (P1), DodeThick (P4) and TrunOcta(P5). There was no evidence of residual powder particle lodged within the pore spaces in Cross_3.

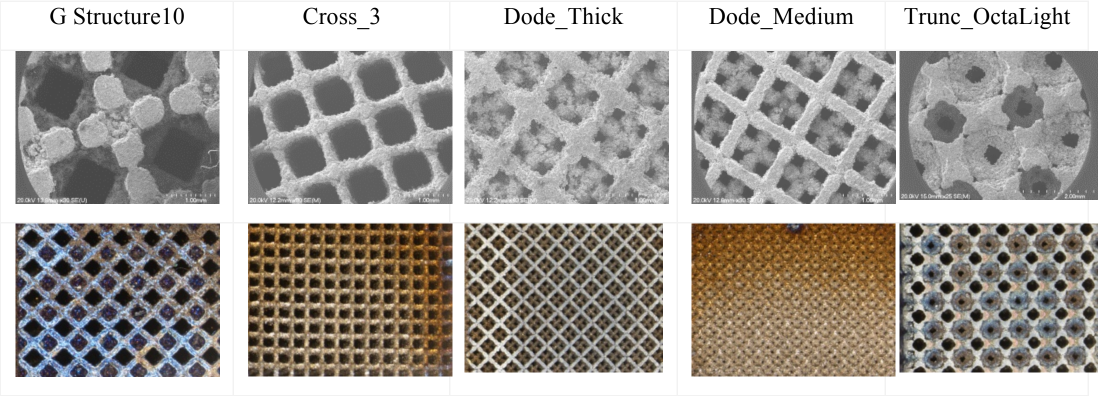

Figure 7.10: Optical and SEM images of the cubes showing the detail of the structure built for each of the CAD files

Compression Testing

The cubes with different structures were compression tested and the data was used to plot Load/displacement graph

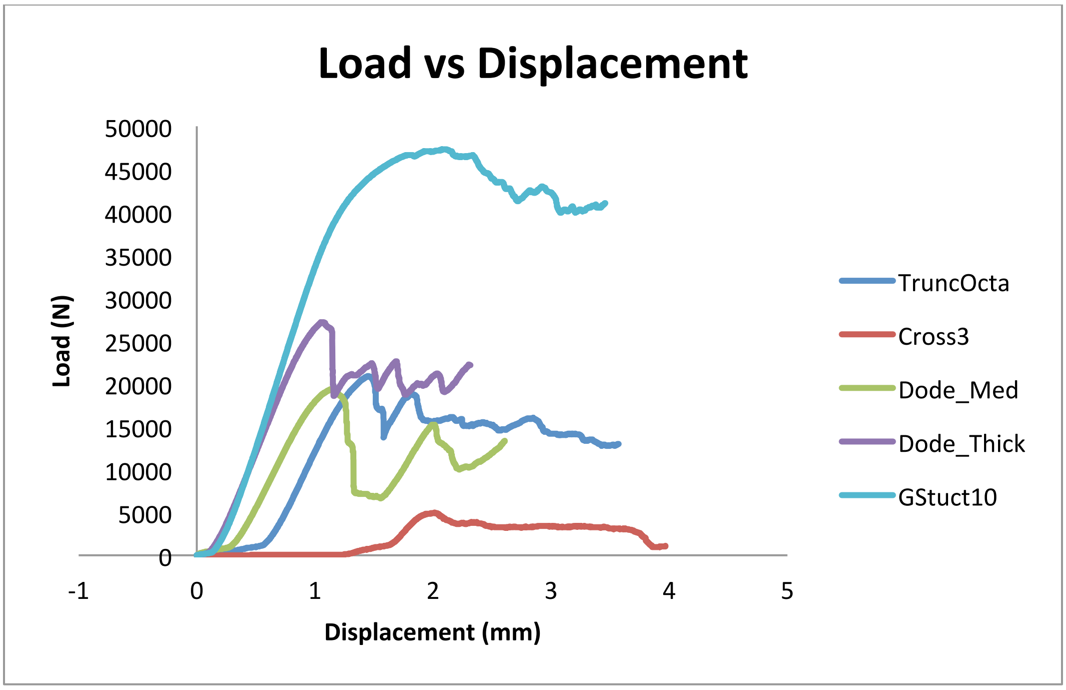

Figure 7.11: Load-displacement average curves for different unit cell structures

Three cubes for each unit cell structure were compression tested. The Load/displacement curves were consistent for all of the specimen types which indicates repeatability of results for each of the fabrication processes and consistent reproduction of the internal structure of the as built parts.

Unit cell	Porosity (%)	Maximum Load(N)	Displacement (mm)	Modulus (MPa)	Stiffness (Nm)	Maximum load to density ratio
P1(GStruc10)	65.5	41029	3.46	2893	11.6	9.36
P2(Cross3)	86.9	4725	3.97	877	1.2	1.22
P3(DodeMed)	71.3	19232	4.3	1887	3.3	3.22
P4(DodeThick)	64.1	27148	2.41	2284	9.3	5.15
P5(Trunc)	71.6	20558	2.89	1995	4.9	4.96

Table 7.7: Maximum load, stiffness value and performance indication ratio for the titanium cubes

The variation of maximum compressive load and stiffness with a variation in porosity is depicted in Table 7.7. As predicted, both the compressive load and stiffness decrease with an increase in the porosity. There is a more significant drop in compressive load compared to the stiffness due to the variations in design. The cube with pattern 1 (Gstructure10) shows the highest compressive load and stiffness while pattern P2(cross3) with the smallest strut size has the lowest stiffness and compressive load. P3 (DodeMedium) and P4(DodeThick) have a similar unit cell structure but slightly different strut sizes. This contributes to a small variation in porosities but a significant drop in compressive load. P3 and P4 have slightly decreased porosities when the strut size is increased from 0.2µm to 0.7µm respectively. This suggests that the mechanical properties are not only dependant on the strut size as well as the porosity but also on the shape of the unit cell. It was observed that cubes with a smaller strut size tended to fail at lower loads. This reflected the experimental results given in the previous chapter, where discontinuity and fragmentation occurred due to single track beam exposure. The width of a single track was 90µm, which is the same as the beam spot size.

In this study, 15mm cubes were successfully laser sintered using the EOS Ti6Al4V powder. The cubes were sintered to give different unit cell structures in order to create variation in porosity and mechanical properties. Cubes with porosities ranging from 65.5% to 86.9% and with a maximum load of 45kN to 1kN respectively were successfully fabricated. The weight of the fabricated cubes is in the range of 1.72g for the Cross3 design to 5.27g for the Dode Medium. The performance of each structure can be assessed by the maximum compressive load to density ratio. The value of this ratio for the different structures shows that unit cell P1 with a G structure 10 unit cell has the best performance. This is because P1 has a relatively high porosity and highest stiffness while maintaining a high strength. In addition, this design was built successfully with no defects or collapsed structure.

7.2.5 Design parameters for Acetabular cup

Five acetabula cups with a porous structure were built using the bespoke procedure. The acetabula cup was designed in two parts, consisting of outer and inner parts, using Solidworks. The outer part with a surface volume of 6027mm^3 was attached with five types of unit cell. The unit cell parameters are shown in Table 7.4 and discussed earlier. It is worth mentioning that the cups have standard features but it was rescaled slightly to suit the production and budget in this research work. The main purpose of this work was to investigate the capability of the DMLS machine to fabricate a complex internal structure in one step. This section explains the fabrication framework and the influence of the part geometries on the fabrication procedure.

The design parameters used in this research work are shown in table 7.8. Five different unit cells were selected with a calculated porosity. This was to make sure that multiple design parameters were selected which incorporated different size values for thin struts in the x, y and z direction. Theoretically, the thinner the strut size, the higher the porosity. However, one needs to consider the processing parameters before determining the design parameters. For example, the smallest laser beam spot size is 100µm diameter; therefore the strut size cannot be smaller than that. All of the cups were built without any support structures. These two parameters set the design and process parameters.

All cups were built simultaneously on one platform with similar processing parameters. A 50Jmm^{-3} energy density was used with a combination of 200W, 1250mms^{-1} scan speed, 100µm scan spacing and 30µm layer thickness. The part building height was used to set the right orientation and to determine the amount of powder needed to fabricate each cup. Good orientation avoids unnecessary support structures and could optimise the building time. It also helps to build parts successfully by reducing the building height and the risk of a possibility of collapse. Finally, the part properties are used to run a cost analysis as this will determine the production time, man-hour needed and the amount of powder used. The bespoke set of processing parameters and building conditions used for manufacturing these cups were established from the previous chapters. This is considered as the optimized parameters for building a solid titanium alloy part without the influence of part geometries. In this section, the optimized processing parameters were tested with complex internal structure and geometries.

Design steps

The design steps to create a porous structure are shown in Figure 7.12. The outer cup has a design volume of 6027mm^3 and the inner part 9072mm^3.

Acetabular Cup	Outer cup volume (mm^3)	Porosity (%)
G structure 10	1786	70.40
Cross3	457	95.41
DodeMedium	758	87.42
Dode Thick	1483	75.35
TruncOctaLight	1228	79.64

Table 7.8: Cup volume and porosities

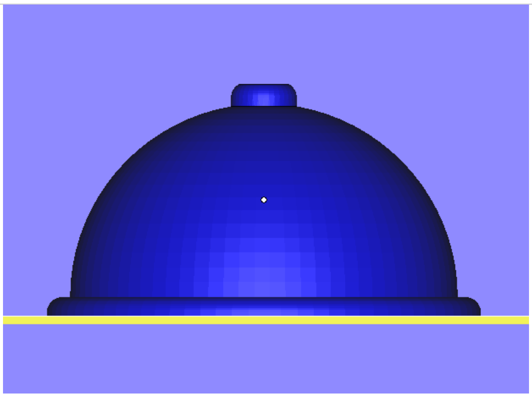	The inner part was imported into MAGICS. The part is orientated accordingly. This helps while doing part assembly and to make sure that the assembly part is all in the same location.
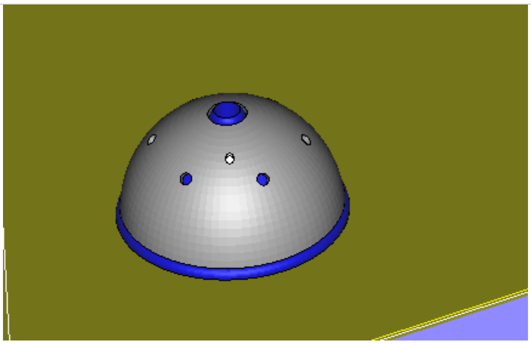	The outer part was imported into MAGICS in assembly mode. The part and position were verified. The outer part properties are Cup space Volume : 6027mm^3 Cup inner volume : 9072mm^2
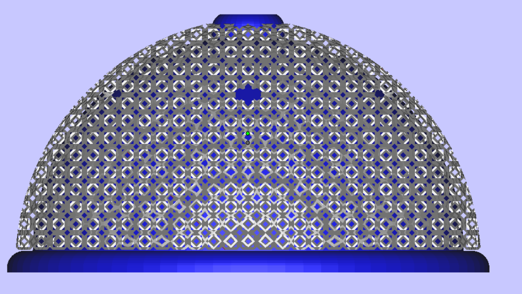	The outer part is selected and the lattice structure was attached to the part. The assembly part was saved as STL together with the inner part

Figure 7.12: Utilizing the unit cell structure on the acetabula cup

7.2.6 Processing conditions

The processing conditions are as shown below. Other important processing conditions such as skin/core parameters and scanning strategy follows the standard parameters. The parts were built on a 250mm x 250mm titanium platform in one step. The powder container was filled to a height of 200mm with EOS Ti64 powder. A high speed stainless steel roller blade was used to deposit the powder on the platform. Using the bespoke processing conditions, it took four and half hours to fabricate five acetabula cups. Related fabrication data is given below:

processing 4 $^{1/2}$ hour

- processing parameters as illustrated above
- average 15min/mm

powder consumed 500g

- powder consumed per acetabular cup
- volume of the cup

cost per cup £575

- including man hour for design, processing & post treatment, overhead rate, data preparation, data alteration (support, slicing, fixing)

post processing 4 hour

- removing part from platform, removing support structure, thermal stress relieved (wire cutting, grinding)

7.2.7 Results

Out of five cups, three were successfully built (P1,P4&P5), one built with many defects(P2) and one failed to construct the intended lattice structure. The result shows that only P1 and P5 have a high degree of lattice structure completion compared with P1 and P2. Sample P2 has struts in the size range of 0.4mm to 0.6mm. P3 with a DodeThick unit cell structure was about 80% completed and shows many discontinuity tracks and was unable to completely follow the intended lattice structure. P2 with the thinnest strut size and highest porosity shows many broken features and discontinuity tracks.

It is worth highlighting that the machine is able to fabricate at least 60% of recognisable lattice structure. P3 with a DodeMedium unit cell structure completely failed and the lattice structure is not recognisable on the cup surface. Cracks or any other defects were not visible on the internal surface of all the cups. It can be seen that, many agglomerated powder particles were stuck under the lattice structure and along the struts. The build took four and half hours to complete an approximate cost of £575 each.

This experiment shows the limit of DMLS in terms of the the smallest size that can be built and the influence of the shape or design. The strut size and the shape of the intended part also contributed to the successful printing.

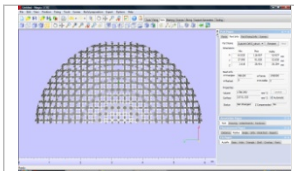	Pattern 1: G_Structure 10 Volume : 1786mm^3 Strut size : 0.56mm	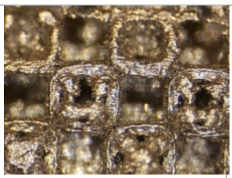	
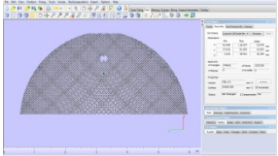	Pattern 2: Cross 3 Volume : 457mm^3 Strut size: 0.14mm	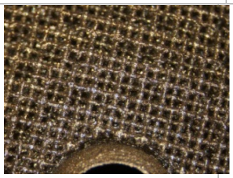	
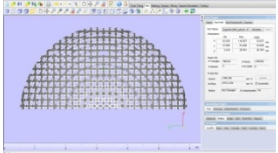	Pattern 3: Dode-Medium Volume : 758 mm^3 Strut size: 0.18mm	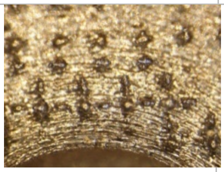	
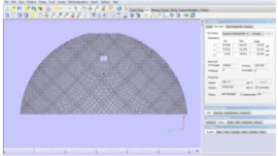	Pattern 4: Dode_thick Volume : 1483 mm^3 Strut size: 0.22mm	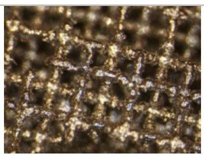	
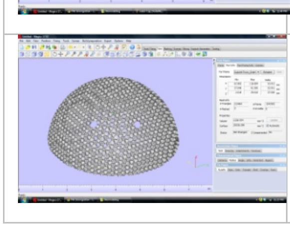	Pattern 5: Trunc_Octa_Light Volume: 1228mm^3 Strut size: 0.47mm	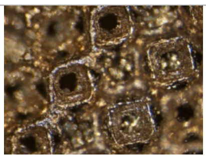	

Figure 7.13: Acetabular cup with lattice structure produced by DMLS

Discussion

Sophisticated 3D bio-modelling software and a direct metal fabrication technique has pushed the manufacturing of these synthetic implants to the next level. This methodology successfully fabricated complex shapes of a custom-designed mandible from CT scan data utilizing Ti6Al4V powder. This technique also added artistic value to maxillofacial and plastic surgery by restoring the affected cranio-bones with a strong similarity to a customised titanium implant. However specific software is needed in order to perform implant design. The previous version of MAGICS software had only basic design functions, therefore it was difficult and time consuming to perform any complex bio-modelling design tasks.

As shown earlier, the porous structure on the mandible implant used a manual approach while the porous acetabula cups were built with a fine scaled lattice structure. Creating porous or lattice structures by utilizing a unit cell structure has proved to be more practical and useful. This technique enables the user to precisely position the lattice structure at any desirable location thus controlling the density distribution. The design data can be easily manipulated and the strut size that determines the size of a unit cell is changeable. This technique shows a pronounced advantage in designing and manipulating lattice structure for biomedical applications. It significantly reduces time and provides better control of an implant structure

This study shows that, with this technique it is possible to successfully fabricate a porous structure with up to 70% porosity. However one has to carefully consider the part geometries and the minimum allowable strut size for each design. The recommended set of processing parameters for building a fully dense part from titanium alloy powder is; laser power in the range of 170 to 190W, scan speed in the range of1000mms^{-1} to 1250mms^{-1}, 100µm scan spacing and 30µm layer thickness .This brings to a specific energy density of 50Jmm^{-3}.

References

1. Bandyopadhyay, B.V.K.W.X.S.B.A., *Engineered Porous Metals for Implants.* Journal of Manufacturing, 2008. **60**(5): p. 4.
2. Cronskar, M., *The use of Additive Manufacturing in the Custom Design of orthopaedic implants*, in *Technology and Sustainable Development*2011, Mid Sweden University: Sweden.
3. David Bombac, M.B., Matija Krkovic, Radomir Turk, Anton Zalar, *Characterisation of Titanium and Stailess steel medical implants surfaces.* Journal of materials and Geoenvironment, 2007. **54**(2): p. 14.
4. Shi, I.G.a.D., *SLS fabrication parameters.pdf.* Rapid Prototyping Journal, 1997. **3**(4): p. 8.

Chapter 8: Discussion & Future recommendation

This research work, the first of its kind at the University of Waikato, was carried out to gain a better understanding of the laser sintering process and its application, particularly for customised implant fabrication. The experiments were design carefully so that the intricate laser-powder interaction that controls and influences the sintering/melting process could be explained. Apart from the important variables, this study also demonstrated the fabrication procedure, with respect to specific building and environment conditions utilizing a reactive material such as titanium, for biomedical applications. The work was also based on the invaluable experience gained in operating an EOSINT M270X DMLS machine. This provided a better understanding of the machine handling information and an insight into a real time production line. Various phenomena, including laser absorption, heat transfer, sintering/melting of the powder particles, presence of molten pool, rapid cooling and solidification, take place during a laser sintering/melting process. These have been analysed and explained. The significant contribution of this work is elucidated below;

1. Successfully establish the process-microstructure –mechanical properties relationship and what governs the part's integrity of DMLS process
2. Provide the methodology to determine the allowable processing parameters for fabrication of solid or porous part.
3. Develop a new fabrication procedure which gives better porosity and strength to cater biomedical implants requirements.
4. Develop new design and process methodology for utilization of complex unit cell structure via DMLS

8.1.1 The Process

The fabrication framework presented in Chapter 3 begins with the CAD data where a part is virtually crafted or designed. The intermediate phase is the preparation of computer aided manufacturing (CAM) data. At this stage, the CAD or design data is converted to stl format which is the most common CAM format. Later, the data was sliced at 30µm creating many of 2D cross-sectional slices.

Each of the layers was checked for redundancy, crossed and missing lines. Supports were created for all downward surfaces. This data is known as specific layer format (sli) and common layer format (cli). Finally, the data was sent to the machine for fabrication. It is worth highlighting that, a reasonable amount of knowledge and skill are required in order to correctly place the necessary support structure on the part and at the same time provide a simple way to remove it after completion. A support structure is not only beneficial for constructing downward surfaces but has a huge influence in dissipating high internal stresses efficiently at those regions where residual stresses are high[1-3].

There are two important physical preparations, the material and machine preparation, when using the DMLS route. In this study, EOS Ti64 alloy powder was used for all experiments. This powder has an average particle size of 37µm with most particles having a spherical shape and a relative density of 4.43gcm^{-3}. The building chamber temperature was kept constant at 80˚C during fabrication under vacuum. The oxygen level was controlled at below 0.01%per cm^{3} by flushing argon gas continuously at 10 litre per min. The processing parameters for most parts is 170W (skin), 190W (core) of laser power, 1000mms^{-1}(Skin) and 1250mms^{-1} (Core) of scan speed, 100µm scan spacing and 30µm layer thickness. This gives an average volume energy density of 50 to 70 Jmm^{-3} with a building rate of 10mm per hour.

A pure titanium substrate was used in most fabrications as it provides better heat conduction and exhibits good stabilizing effects. This was explained in the single laser spot and single track experiments on the substrate and re-melted layer respectively. The localised laser energy density not only melts the powder but penetrates the substrate underneath and creates a rippled surface. Without the substrate, the molten pool tends to ball up and form droplets rather than moving downward as shown in chapter 4. This experiment is also in a good agreement with single track formation on a remelted layer. With the same laser energy density a single track was characterised by discontinuity, inconsistent size and fragmentation.

The small mini plate used in this work facilitated a considerably faster preparation time, compared with the standard plate, in depositing a thin layer of powder particularly for the first five layers. It also speeds up the task of levelling the building platform, providing better powder distribution. Filling up the powder into the powder container is a time consuming and tiring task. The powder needs to be sieved manually using 63µm filter before it can be placed in the powder container.

8.1.2 The effects of processing parameters

The effect of laser power was explained in Chapter 4. When the laser strikes the powder bed for ten seconds a blob/droplet consisting of a melted and sintered structure was formed. The blobs were of different sizes depending on the laser power. These blobs all had similar feature, such as shape and structure. This suggests that there is a consistent heat transfer mechanism when the laser strikes the powder bed. The shapes obtained show that the molten pool has a tendency to ball up due to the surface tension rather than to flow or spread uniformly on the powder bed. This indicates that the laser power has a direct relation with the size of the melted or sintered structure. The size of the blobs correlates linearly with the laser power. The blobs show a bigger radial distribution compared to their overall height and this value changed drastically from an increase in laser power from 100W to 120W. This suggests that there is a greater heat distribution in the x,y plane compared with the penetration depth. The inner diameter (melted core) to outer diameter (sintered core) ratio is consistent at 1.6 for various laser powers suggesting a uniform heat distribution and good powder packing density in the powder bed. At 140W, a blob exhibits the highest melted to sintered ratio, a flat surface, and seamless boundary (no cracks visible) suggesting the stability of the molten pool and a smooth laser-material interaction.

Heat transfer in the powder bed was characterised by a high surface heat flux and high surface temperature. For 20W laser power, the surface temperature was well above the melting temperature of the titanium alloy. This proves that with sufficient energy density and appropriate exposure time, a molten pool can be formed. The mathematical model used in this study and the program develop in MATLAB are in good agreement with the structure of the individual blobs. The mathematical model gives valuable information for predicting the melting time and evaporating time. Nevertheless, the calculation was reported to be not accurate for long exposure time[4]. It is still useful, as one can see the influence of laser power and surface temperature during the sintering process. The model provides a good relationship between the laser power and surface temperature with the exposure time. It is worth mentioning that the exposure time can also be used to choose the appropriate processing parameters, instead of the energy density, by selecting a suitable scan speed and laser beam diameter. The numerical model developed in MATLAB successfully simulates the isothermal condition and the penetration depth during the laser sintering process, particularly for low laser power and short exposure time.

One of the particular interests in this experiment was to find out the relationship between the laser power and the as built structure. The results showed that the degree of sintering is dictated by the isothermal condition during the laser sintering process, where near to the melted core the inter-particle necks were characterised by both larger and smaller distances between particles. Far from the melted core, the necks are narrower and the distance between sintered particles is bigger. It is therefore possible to create porosity through different processing conditions or by manipulating processing parameters. In other words, with appropriate processing parameters, the DMLS process is not only capable of producing full density parts but parts with controlled porosities.

As far as the process-structure relationship is concerned, the fundamental mechanism of this laser sintering process relies on the inter-track and interlayer bonding. A solidified layer consists of many individual elongated or cylindrical tracks. The width of the elongated tracks obtained in this research is 90µm±15µm on a pure titanium substrate and 100µm±20µm on the re-melted layer. This is in agreement with a study which reported that a metallic powder has a high absorptivity but low thermal conductivity, which causes the width of the molten tracks to be slightly bigger than those made on a platform or substrate [5]. Inducing the powder bed with a volume energy density of 50.67

Jmm^{-3}, an elongated track was formed with a 5mm gap between them on the top of a previously solidified layer. The elongated track was characterised by fragmentation, discontinuity in the track and a cluster of powder particles along the track, suggesting instability of the molten pool. This is completely different to tracks formed side by side without any gap. Therefore, it is not advisable to have a huge gap between the tracks as it may potentially cause “balling” effects and prevent the formation of a smooth elongated track. It is important to highlight that the scanning pattern is crucial in promoting stability of a molten pool where heat and stresses can be spread efficiently via adjacent solidified tracks.

8.1.3 The microstructure and mechanical properties

The crystalline structures of DMLS processed titanium alloy parts fabricated under various energy density conditions exhibited a very fine acicular structure consisting largely of the α phase. The phase was further identified as α’ martensite by XRD. At low laser power, the microstructure was characterised by fine (bright) and coarse (dark) regions consisting of a needle like acicular structure with clear boundaries dividing the region. The cross-sectional surface of a blob has an interesting texture that explained the heat conduction in the powder bed. The coarse and fine textures on the surface suggesting different solidification rates.

As the laser power increased and consequently the laser energy density intensified, a microstructural transformation occurred and the structure changed into a relatively refined acicular structure. The same crystalline structure was also observed on a surface parallel to the building direction of a solid part. Due to the layer by layer solidification process, the cross section of a DMLS processed part showed columnar grains with visible layer bands suggesting a directional solidification. In these columnar grains, long thin, narrow and parallel laths of the acicular needles were present. Most of the acicular needles lie at ±45˚ to the building direction.

The effects of crucial processing parameters particularly the scan speed on the microstructure were also investigated. By decreasing the scan speed ($1250mms^{-1}$ to $750mms^{-1}$), the laser energy density increases and results in a finer microstructure. From the viewpoint of energy density, one can notice that, a low scan speed causes an increase in surface temperature and contributes to a larger degree of undercooling of the molten pool thus favouring the rapid growth of a refined microstructure. The significant grain refinement in the α phase or α’ phase was also confirmed by the presence of considerably broadened α’ diffraction peaks with a low intensity in the XRD analysis. This explains the process-structure relationships. Using the volume energy density formula, one can establish a direct relationship between the processing parameters with the size of the grain structure.

The fine acicular structure of a laser sintered part results in good mechanical properties. The refinement of the microstructure, due to higher laser power or by slower scan speed, gives rise to the mechanical properties found in laser sintered parts[6]. The microhardness testing performed on the surface of cross-sections of individual blobs indicates a positive raise with increase in laser power. This is in relation to the high energy density and larger degree of undercooling where a finer microstructure was observed. The lowest hardness of 305±12 HV was reported for a 100W blob and the highest hardness of 351±17HV was reported for blobs made at 200W. The tensile stress-strain curves for the as built blocks showed a low-strain hardening behaviour of the mean tensile strength was 1030MPa, a Young’s modulus of 90GPa with strain to failure of 4%. As seen in chapter 5, the differences in mechanical properties for different scanning speed has only a minimal effect on the properties[7]. However, it shows that even with a small changes in scan speed (20%) the ductility was most affected.

The fracture surface after tensile testing shows a common brittle behaviour confirming its low ductility. The fracture surfaces were characterised in part by ductile dimples, some evidence of cleavage and micro cavities. At a scan speed of 750mms^{-1}, more defects such as evidence of incompletely melted powder were observed and the surface was characterised by a mixture of smooth regions associated with intergranular fracture as well as shallow dimple features. Therefore, concerning the stringent biomedical structure requirements, it is necessary to optimise the process control and possibly apply further thermal treatments to compensate for the presence of porosity.

8.1.4 Biomedical Applications

The Direct Metal Laser Sintering process used in this work has demonstrated success in fabricating biomedical implants made from a titanium alloy. This method is capable of manufacturing complex shapes and the structure of a customised mandible and acetabula cup according to a patient's CT scan data and 3D CAD data respectively. The cup has a complex, fine scaled scaffold structure on its outer surface, which aims to improve osseointegration. One of the distinct advantages is that this technique allows the use of a complex internal structure to reduce weight while still maintaining its functional requirements. Compared to parts prepared by other manufacturing means, the DMLS method produces parts all with comparable mechanical properties but with limited ductility. This may be due to high oxygen content in the starting powder[8].

An important issue which arose during the design phase involved the porous or lattice structure on the implant. There are limitations and difficulties if the porous or lattice structure is designed with a combination of CAD software and basic MAGICS functions. Specific design functions are needed in order to attach a complex structure onto the implant data. As discussed in Chapter 7, the use of MAGICS unit cell structures was found to be very useful and essential for manipulating large amounts of stl data and attaching the intended porous structure. Out of five lattice designs, three were successfully manufactured through the DMLS method. The unsuccessful design was characterised by thinner struts less than 500µm wide. Struts with sizes more than 500µm were built successfully on the same building platform with similar building conditions. Based on this experiment, the optimised parameters used for most of the parts is not applicable for the acetabula cup with a thinner lattice structure.

In conclusion, DMLS proved to have significant advantages for producing customised parts with tailored structures and properties. However, it is important to emphasise that there is no one set of parameters for different kinds of design or structure. Each design, especially those with a higher degree of complexity, requires a thorough understanding of the building conditions so that specific process control can be established. This includes the specific energy density, the potential residual stresses, the need for a support structure and its location, a suitable scanning strategy, the use of a building platform or a substrate, the degree of design complexity, building height, the type of blade used for depositing powder and the powder packing density. Aforementioned factors play an important role in the DMLS process thus finding the right combinations, which includes all of the above factors, is of prime importance

8.1.5 Future work recommendations

Many important issues have been identified throughout this research work. Of particular interest are the variations in the processing parameters to produce specific microstructures and microstructural variations during the rapid melting and solidification process. The fundamental studies of laser-power interaction in this research work show that there is a significant influence of laser power and scan speed in determining the final microstructure. However, this research work had limited access to changing the machine parameters independently due to safety issues and the default factory setting of the machine itself. As a result, the parameters used in this work are within the permissible range set by the machine manufacturers. Defining the microstructural evolution during laser sintering in a more detailed quantitative manner, such as decomposition of the α' martensite and remaining β phase after rapid solidification, coupled with the thermal history corresponding to a variation in processing parameters should be a part of any future work. A deeper understanding of the structure property relationships may take additive manufacturing processes forward towards building parts that can be selectively tailored to desirable properties and more ironically which are not achievable by any other manufacturing means.

The thermal model developed using MATLAB should include the temperature dependent thermal properties. Even though the program will be more complicated and time consuming, the results may give a better prediction and accuracy. It is also meaningful and desirable if the thermal model not only simulates the temperature distribution but at the same time calculates the residual stresses in 3D dimensions during the fabrication process. This is because the residual stress in laser sintered parts is known to cause delamination and deterioration in a part’s integrity[9]. The direction of future work should progress along this line, as predicting and simulating the building condition prior to thermal distribution could eliminate the expense of a trial and error method used currently.

As discussed before, the processing parameters for a particular design and structure are determined by many factors. The next research direction should also rank all the factors that control the processing conditions for a specific application. This will provide essential information to a user in finding the right processing window. As an example, in many applications it is probably sufficient just to get the right energy density but in other cases it is probably crucial to locate the right support structure or perhaps to find the right building orientation. Therefore providing a method of selecting and emphasising the right factors should be the next priority.

8.2 References

1. M Cloots, A.B.S., K. Wegener, *Assesing New Support minimizing strategies for additive manufacturing technology*, in *Manufacturing Technology*: Austin.
2. Allen S, D.D., *Determination and evaluation of support structure in layered manufacturing.* Design Manufacturing, 1995. **5**: p. 10.
3. Ahmed Hussein, C.Y., Richard Everson and Liang Ho, *Preliminary Investigation on cellular support structures using SLM process.* manufacturing the future VRP, 2011.
4. Shin, S. and H. Chung, *Modeling of Melting, Evaporating, and Resolidifying Procedure in Laser-Induced Metal Processing.* Journal of Manufacturing Science and Engineering, 2009. **131**(2): p. 024501.
5. Simchi, A. and H. Pohl, *Effects of laser sintering processing parameters on the microstructure and densification of iron powder.* Materials Science and Engineering: A, 2003. **359**(1-2): p. 119-128.
6. Bo Song, S.D., Baicheng Zhang, Hanlin Lioa, Christian Coddet, *Effects of Processing parameters on microstructure and mechanical property of selective laser melted Ti6Al4V.* Materials and Design, 2012. **35**: p. 5.
7. Kumar, J.-P.K.a.S., *statistical analysis of experimental parameters in SLS.pdf.* Advanced Engineering Materials, 2005. **7**(8): p. 6.
8. Rombouts, M., et al., *Fundamentals of Selective Laser Melting of alloyed steel powders.* CIRP Annals - Manufacturing Technology, 2006. **55**(1): p. 187-192.
9. Mercelis, P. and J.-P. Kruth, *Residual stresses in selective laser sintering and selective laser melting.* Rapid Prototyping Journal, 2006. **12**(5): p. 254-265.

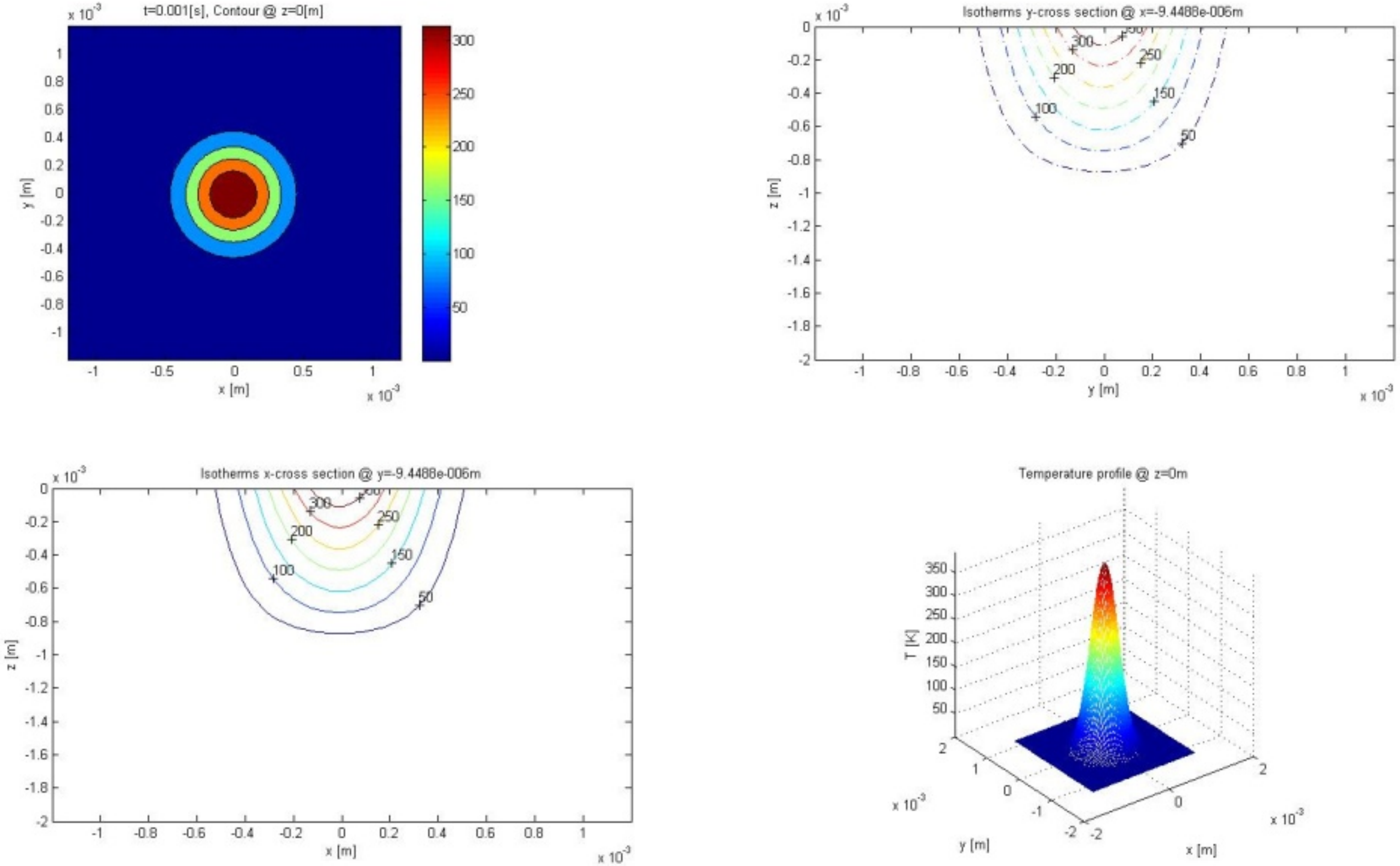

Figure 4.17 Temperature profile of 20W laser beam exposure on the powder bed for 0.001second

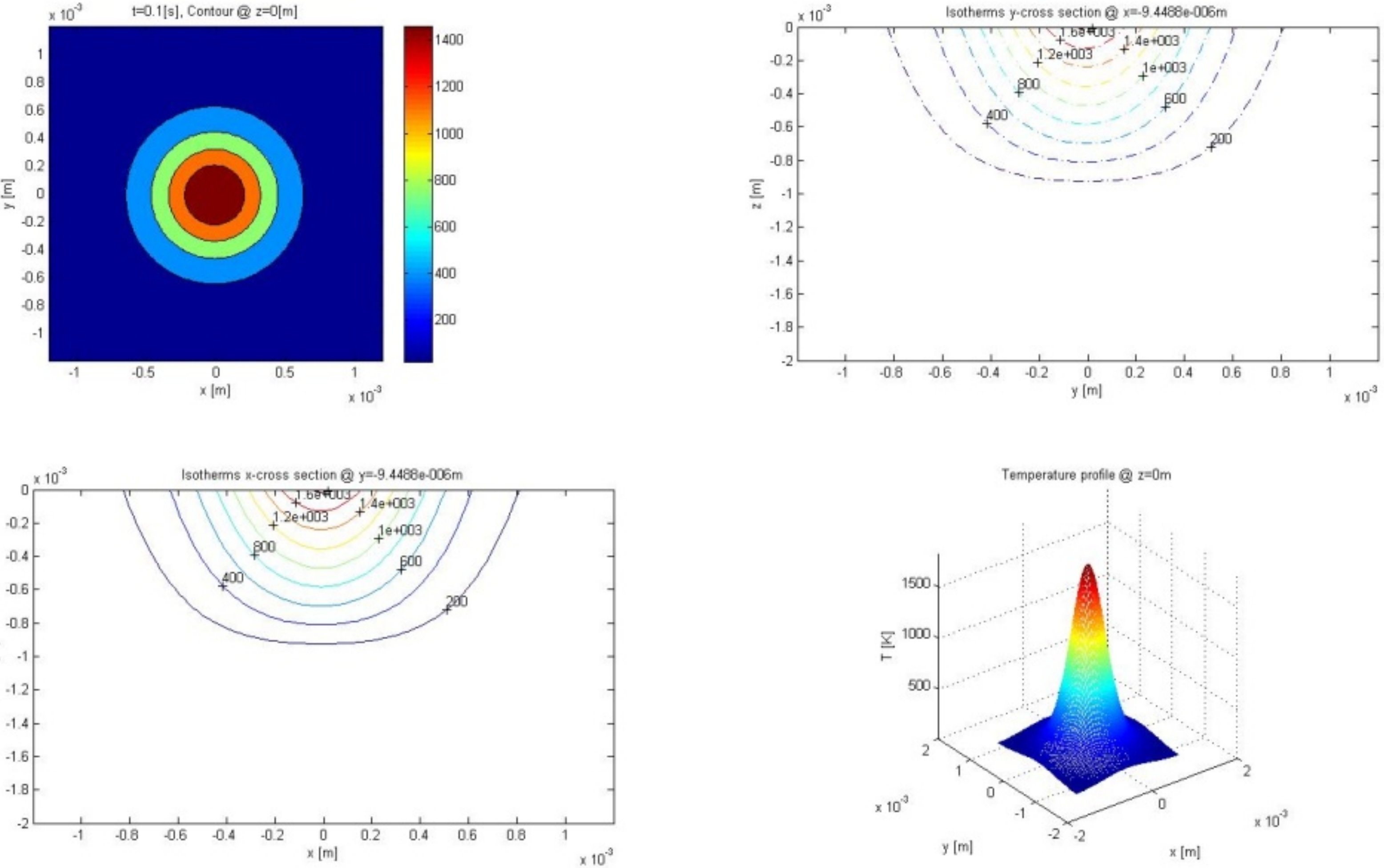

Figure 4.18 Temperature profile of 20W laser beam exposure on the powder bed for 0.001second

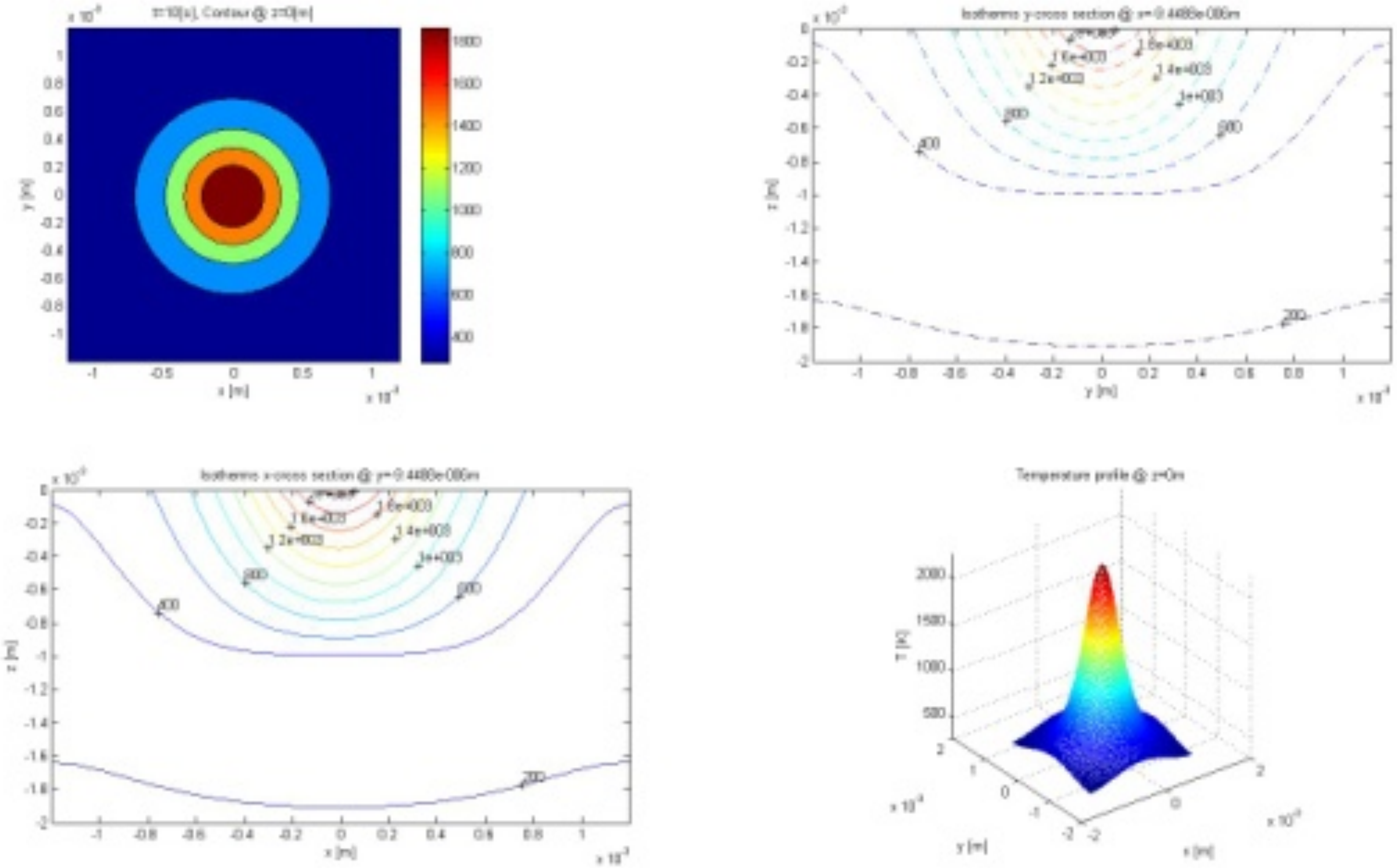

Figure 4.19 Temperature profile of 20W laser beam exposure on the powder bed for 0.1 second

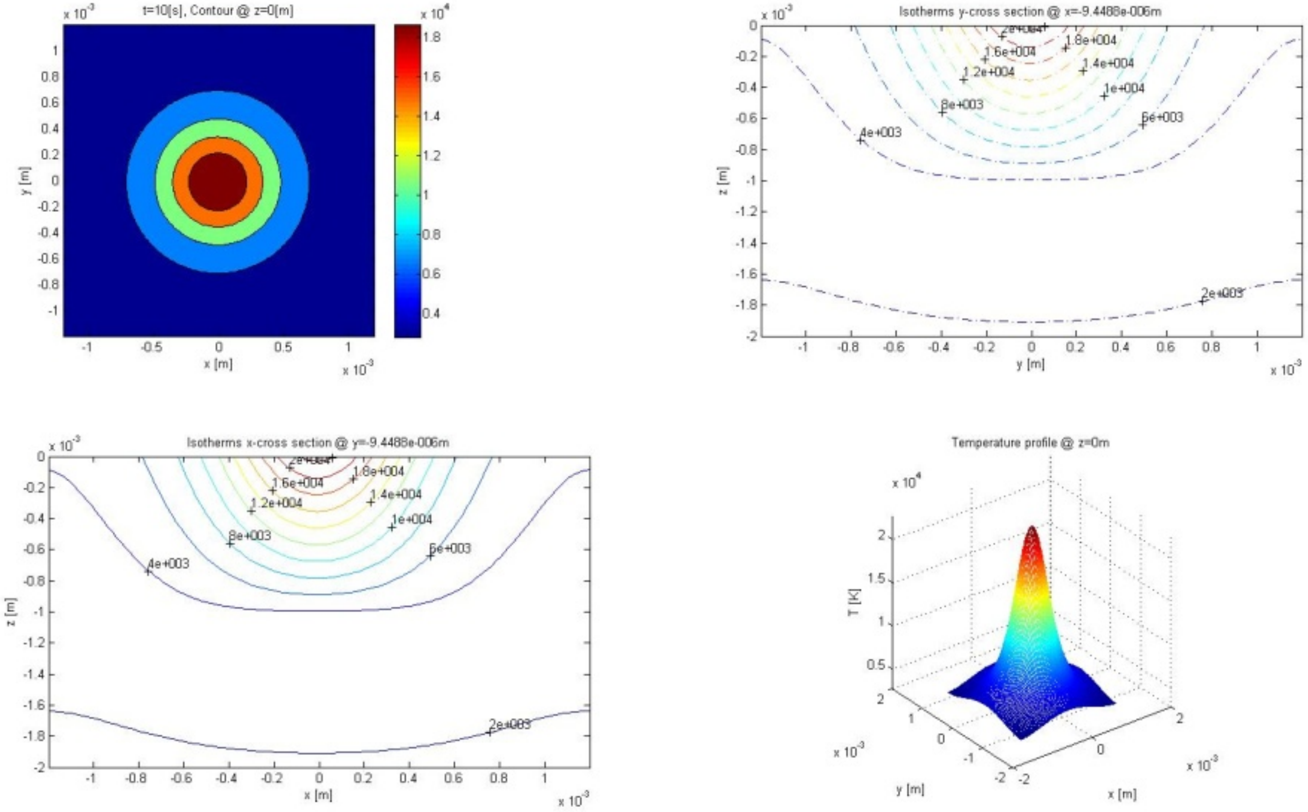

Figure 4.20 Isothermal condition for 200W laser power exposed for 10secs

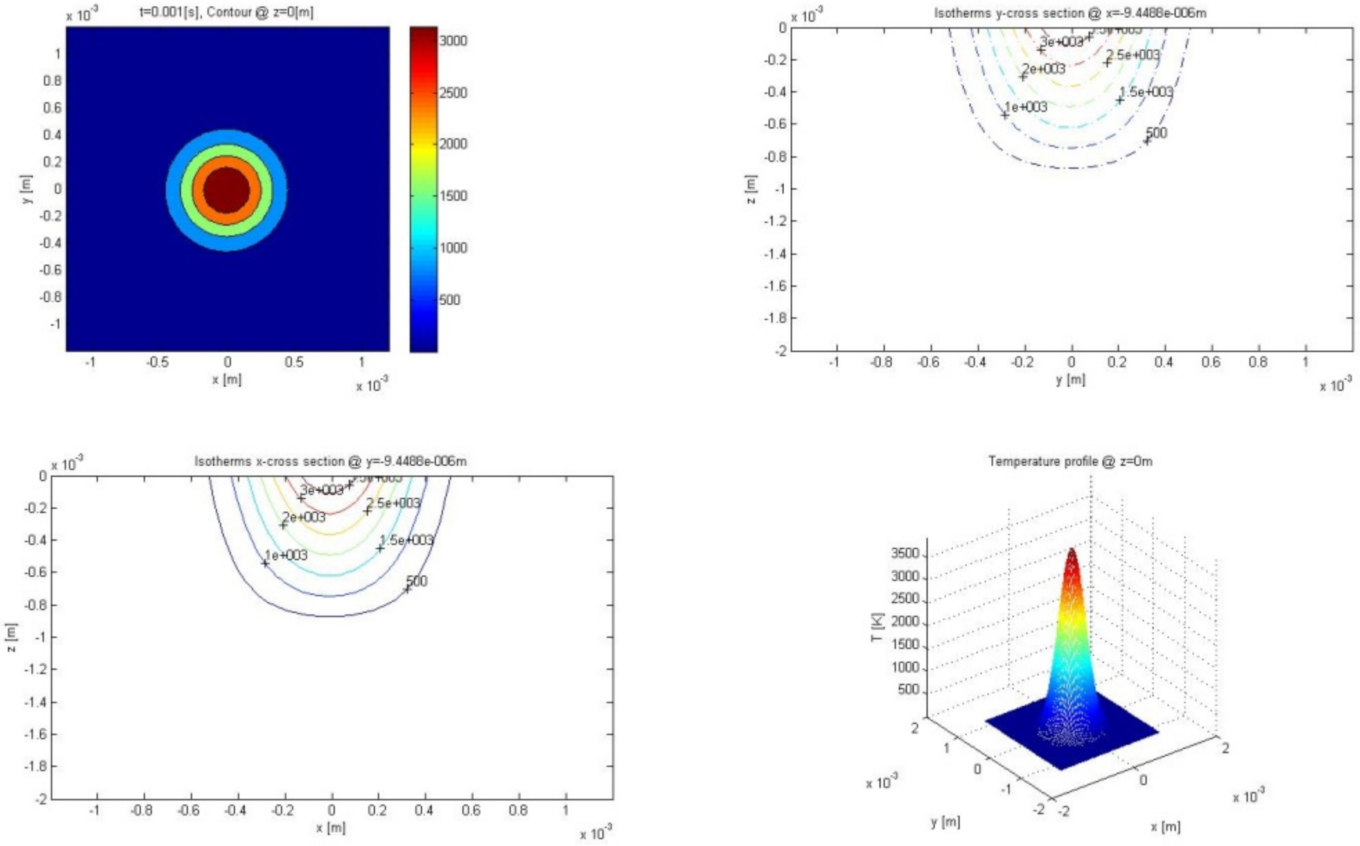

Figure 5.10 Temperature distribution and melting depth after 0.001 sec laser irradiation

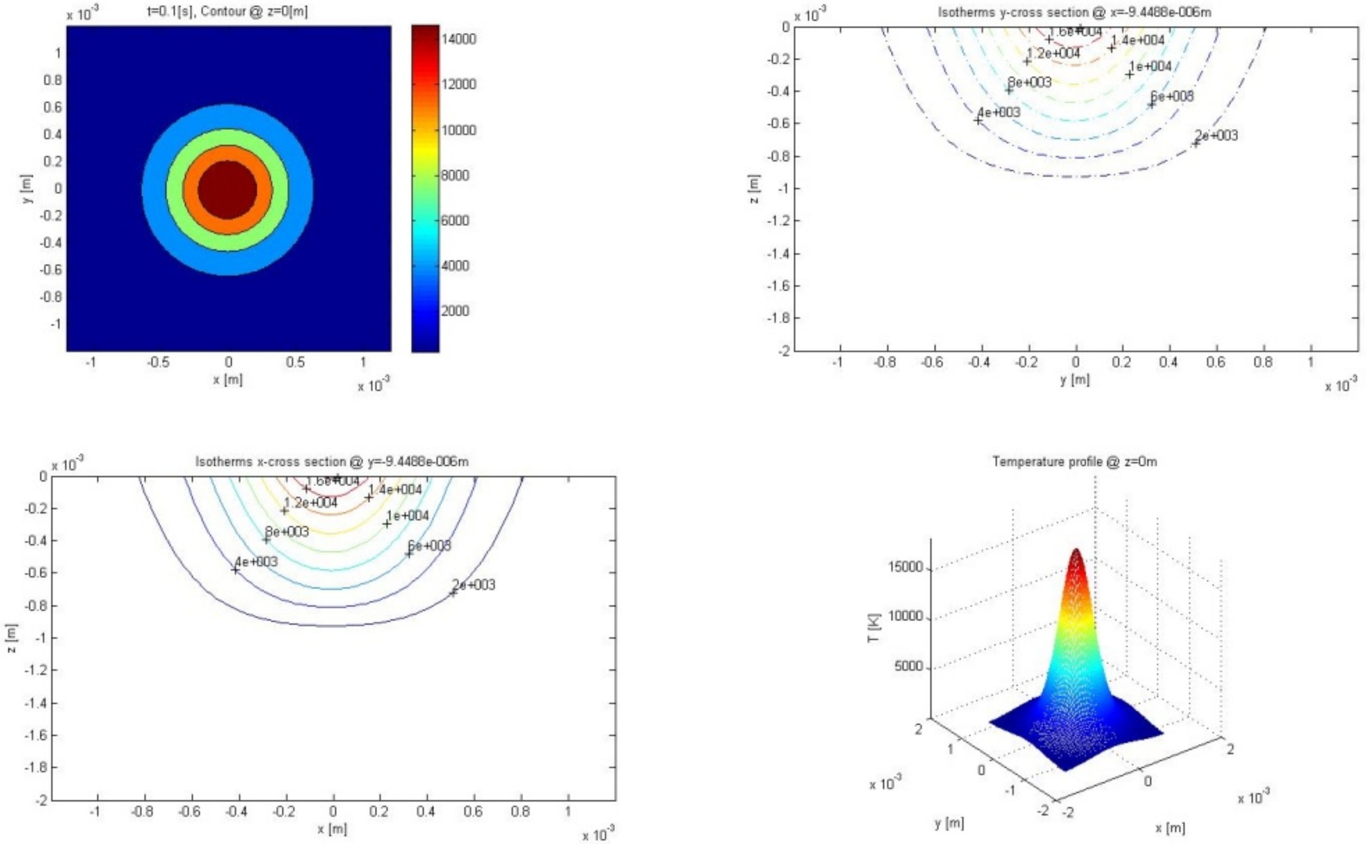

Figure 5.11 Temperature distribution and melting depth after 0.01 sec laser irradiation